Modelling and Quantification of Structural Uncertainties in Petroleum Reservoirs Assisted by a Hybrid Cartesian Cut Cell/Enriched Multipoint Flux Approximation Approach

Mohammad Ahmadi

Submitted for the Degree of Doctor of Philosophy

Institute of Petroleum Engineering

Heriot Watt University

Edinburgh

UK

April 2012

This copy of the thesis has been supplied on condition that anyone who consults it is understood to recognize that the copyright rests with its author and that no quotation from the thesis and no information derived from it may be published without the prior written consent of the author or the University (as may be appropriate).

Abstract

Efficient and profitable oil production is subject to make reliable predictions about reservoir performance. However, restricted knowledge about reservoir distributed properties and reservoir structure calls for *History Matching* in which the reservoir model is calibrated to emulate the field observed history. Such an inverse problem yields multiple history-matched models which might result in different predictions of reservoir performance. *Uncertainty Quantification* restricts the raised model uncertainties and boosts the model reliability for the forecasts of future reservoir behaviour. Conventional approaches of *Uncertainty Quantification* ignore large scale uncertainties related to reservoir structure, while structural uncertainties can influence the reservoir forecasts more intensely compared with petrophysical uncertainty.

What makes the quantification of structural uncertainty impracticable is the need for global regridding at each step of *History Matching* process. To resolve this obstacle, we develop an efficient methodology based on *Cartesian Cut Cell Method* which decouples the model from its representation onto the grid and allows uncertain structures to be varied as a part of *History Matching* process. Reduced numerical accuracy due to cell degeneracies in the vicinity of geological structures is adequately compensated with an enhanced scheme of class Locally Conservative Flux Continuous Methods (*Extended Enriched Multipoint Flux Approximation Method* abbreviated to *extended EMPFA*).

The robustness and consistency of proposed *Hybrid Cartesian Cut Cell/extended EMPFA* approach are demonstrated in terms of true representation of geological structures influence on flow behaviour. In this research, the general framework of *Uncertainty Quantification* is extended and well-equipped by proposed approach to tackle uncertainties of different structures such as reservoir horizons, bedding layers, faults and pinchouts. Significant improvements in the quality of reservoir recovery forecasts and reservoir volume estimation are presented for synthetic models of uncertain structures. Also this thesis provides a comparative study of structural uncertainty influence on reservoir forecasts among various geological structures.

Dedicated to my everything....Maryam

Acknowledgements

I am really grateful to my supervisor Professor Mike Christie. He provided me freedom to explore different ideas and meanwhile gave me insightful suggestions and guidance. I benefited a lot from all of the discussions and interactions with him. I am also indebted to my second supervisor Professor Margot Gerritsen for her invaluable hints on my PhD direction.

The uncertainty project sponsors BP, BG, ConocoPhillips and JOGMEC are especially appreciated for their financial support during my PhD studies.

Special thanks go to all my dear friends in Heriot-Watt University particularly the old and new members of Uncertainty Quantification Group (Monica, Vasya, Dan, Allanah, Linah, Yasin, Lorna, Simon, Asaad, Hamid). They made the life easier in Edinburgh for me away from my lovely wife.

Many appreciations go to the PhD external examiner Professor Michael Edwards and PhD internal examiner Professor Sebastian Geiger for reviewing thoroughly my thesis and providing me many helpful corrections for improving my thesis.

I take this opportunity to thank my family especially my parents, who always stand by me and share my joy and sorrow. Finally I express my sincere gratitude to my pure love, Maryam who gave me the motivation and confidence to do what I need to do. I love you Maryam!

Table of Contents

Chapter 1: Introduction **1**

1.1: Geological Structures…….1

1.2: Structural Uncertainties: Sources and Consequences…….4

1.3: Previous Works on Quantification of Structural Uncertainties……..8

1.4: Thesis Statement and Abjectives……..…11

1.5: Thesis Outline……...13

Chapter 2: An Overview of History Matching and Uncertainty Quantification **15**

2.1: History Matching.....16

2.1.1: Literature Review of Automatic History Matching.....17

2.1.2: Neighbourhood Algorithm.....20

2.2: Uncertainty in Reservoir: Sources and Quantification.....23

2.2.1: Methods for Uncertainty Quantification.....26

2.2.2: Neighbourhood Bayes Algorithm for Posterior Inference.....29

Chapter 3: Cartesian Cut Cell Method **33**

3.1: Introduction to the Family of Immersed Boundary Methods (IBM).....34

3.2: General Workflow for Reshaping Ill Cells.....41

3.2.1: The Interacting Data Structures.....41

3.2.1.1: The Grid.....41

3.2.1.2: The Interfaces.....41

3.2.1.3: The Reservoir Boundaries.....42

3.2.2: Finding Cells Defected by Imposition of Reservoir Boundaries...43

3.2.3: Determining the Relative Cut Cell/Boundary Configuration.....44

3.2.4: Splitting the Cells Volume.....45

3.2.5: Creating New Cells.....48

3.3: Treating Multiple Intersecting Boundaries.....54

3.3.1: Determining the Relative Fault-Cell Geometrical

Configuration.....56

3.3.2: Splitting the Cells Volume.....58

3.3.3: Creating New Cells.....58

3.4: Redefining Cell Connections.....63

3.5 Application of Cartesian Cut Cell Method for a Complex Set of Intersecting Structures…….69

3.5: Priorities of Cartesian Cut Cell Method over Corner Point Grid……73

Chapter 4: Extended Enriched Multipoint Flux Approximation Method 75

4.1: The Motivation for Using Multipoint Schemes to Approximate the Flux...76

4.2: Literature Review on Class of MPFA Methods and Related Techniques....81

4.3: Extended EMPFA for General 2-D Quadrilateral Cells.....91

4.3.1: Bilinear Potential Approximation.....91

4.3.2: Bilinear Approximation of Potential Gradient.....92

4.3.3 Flux Reconstruction on Sub-volume Faces.....94

4.3.4: Enforcing the Full Flux Continuity Conditions on Sub-interfaces

.....98

4.3.5: Enforcing the Zero Divergence Condition on the Centre of Interaction Region.....100

4.3.6: Modified Continuity Equations for Non-matching Cells.....104

4.4: Discussion of Monotonicity and Stability of extended EMPFA.....107

4.4.1: M-matrix Condition of extended EMPFA for Spatially Constant Permeability Tensors on Parallelogram Grid.....109

4.5: Numerical Experiments on Convergence and Monotonicity of extended EMPFA.....128

4.6: Robustness of extended EMPFA for Non-matching Cells.....141

Chapter 5: Modelling and Quantification of Structural Uncertainties for Nonintersecting Geological Structures……..……148

5.1: Modelling the Uncertainty of Top and Bottom Reservoir Horizons.....150

5.1.1: Case Description.....150

5.1.2: History Matching of Horizon Parameters.....152

5.1.3: Quantifying the Uncertainties of Reservoir Horizons.....162

5.2: Modelling the Uncertainty of Faults.....167

5.2.1: Case Description.....168

5.2.2: History Matching of Fault Geometrical Properties.....168

5.2.2.1: Multi-layer Model.....169

5.2.2.2: Single-layer Model.....169

5.2.3: Quantifying the Uncertainties of Fault.....180

5.3: Modelling the Uncertainty of Pinchouts.....186

5.3.1: Case Description.....188

5.3.2: History Matching of Pinchout Geometry.....189

5.3.3: Quantifying the Uncertainties of Pinchout.....198

5.4 Comparative Study of Improvement in Reservoir Forecasting With Different Gridding and Flux Approximation Approaches.....205

Chapter 6: Modelling and Quantification of Structural Uncertainties for Multiple Intersecting Geological Structures……..…..208

6.1: Simultaneous Quantification of the Uncertainties of Reservoir Layer Boundaries and Faults.....210

6.1.1 Case Description.....210

6.1.1.1 Parameterisation of Boundaries of Reservoir Layers....212

6.1.2 History Matching of the Geometry of Layer Boundaries and Faults 215

6.1.3 Quantifying the Uncertainties of Faults and Layer Boundaries.....222

6.2 Simultaneous Quantification of the Uncertainties of Pinchouts and Faults.....228

6.2.1 Case Description.....228

6.2.2 History matching of Pinchout and Fault Geometrical Specifications.....229

6.2.3 Quantifying the Convolved Structural Uncertainties of Faults and Pinchouts.....233

Chapter 7: Conclusions and Future Works 241

7.1 Key Findings.....242

7.1.1 Performance of Hybrid Cartesian Cut Cell/EMPFA Approach...242

7.1.2 Concluding Remarks about the Uncertainties of Large Scale Structures.....245

7.2 Future Work.....249

References **251**

Appendix A: Flow Simulation in SUQIB Code and Used Physical Properties 280

A.1 Temporal and Spatial Discretisation.....281

A.2 Coupling Scheme.....283

A.3 Physical properties used in simulator.....286

A.3.1 Relative Permeability.....286

A.3.2 Viscosity.....287

A.3.3 PVT Data.....287

List of Nomenclatures

$\overline{\mathbf{A}}$.....Discretized Matrix Format of Operator $\left[-\nabla.\left(\mathbf{K}\nabla\bullet\right)\right]$

a_i.....Coefficients of Mapping of 1st Cartesian Coordinate x into 1st Coordinate of Reference Space ξ

AMR.....Adaptive Mesh Refinement

$\overline{\mathbf{B}}$.....Discretized Matrix Format of Source/Sink Term in Conservation Equation

BB.....Bottom-Bottom Immersed Boundary-Cell Intersection Flag

b_i.....Coefficients of Mapping of 2nd Cartesian Coordinate y into 2nd Coordinate of Reference Space η

BLtoRR.....Bottom-Left to Right-Right Immersed Boundary-Cell Intersection Flag

bMF.....Reshaped Cell Type of Merged Active Cell Above the Boundary

bNMF.....Reshaped Cell Type of Non-Merged Active Cell Above the Boundary

BtoR.....Bottom to Right Immersed Boundary-Cell Intersection Flag

BtoT.....Bottom to Top Immersed Boundary-Cell Intersection Flag

BTtoRR..... Bottom-Top to Right-Right Immersed Boundary-Cell Intersection Flag

CCC.....Cartesian Cut Cell Method

CDF.....Cumulative Density Function

CPG.....Corner Point Geometry

CVFE.....Control Volume Finite Element Method

DoF.....Degree of Freedom for Central Node of an Interaction Region

DoF^C.....Number of Cells Sharing the Central Node of an Interaction Region

EEMPFA.....Extended Enriched Multipoint Flux Approximation

e_i^{NNC}.....Any Interface Constituting a Non-Neighbour Connection

EMPFA.....Enriched Multipoint Flux Approximation

f.....Vector of Fluxes Passing Through the Semi-interfaces of an Interaction Region

$\hat{f}_{\mathrm{O}}^{i}$.....Specific Flux Entering the Central Node of an Interaction Region

FPS.....Full Pressure Support Scheme

GeoStruct.....Base Class for Geological Structures

GFM.....Ghost Fluid Method

H.M.....History Matched Model

hH..... Height of Pinchout Head Point with Respect to the Datum (*ft*)

IBM.....Immersed Boundary Method

IIM.....Immersed Interface Method

J.....Jacobian Matrix of Space Transformation

K.....Permeability Tensor

K_h.....Horizontal Permeability (*Darcy*)

K_{hv}.....Cross Term of Permeability Tensor (*Darcy*)

k_{ri}.....Relative Permeability of *ith* Flowing Phase

K_v.....Vertical Permeability (*Darcy*)

L_2^{ep}.....Squared Norm of Errors for Pressure

$(L_2^{ep})^{GS}$.....Squared Norm of Errors for Pressure in the Vicinity of Geological Structure

L_2^{ev}.....Squared Norm of Errors for Velocity

$(L_2^{ev})^{GS}$.....Squared Norm of Errors for Velocity in the Vicinity of Geological Structure

L_{∞}^{ep} .....Infinity Norm of Errors for Pressure

$(L_{\infty}^{ep})^{GS}$ .....Infinity Norm of Errors for Pressure in the Vicinity of Geological Structure

L_{∞}^{ev} .....Infinity Norm of Errors for Velocity

$(L_{\infty}^{ev})^{GS}$ .....Infinity Norm of Errors for Velocity in the Vicinity of Geological Structure

lHA.....Opening Angle of Pinchout Lower Triangle at Head Point (*Degrees*)

LL.....Left-Left Immersed Boundary-Cell Intersection Flag

LLRR.....Left-Left to Right-Right Immersed Boundary-Cell Intersection Flag

LLtoBR.....Left-Left to Bottom-Right Immersed Boundary-Cell Intersection Flag

LLtoBT.....Left-Left to Bottom-Top Immersed Boundary-Cell Intersection Flag

LLtoRR.....Corner to Corner Immersed Boundary-Cell Intersection Flag

LLtoTR.....Left-Left to Top-Right Immersed Boundary-Cell Intersection Flag

lTA.....Opening Angle of Pinchout Lower Triangle at Tail Point (*Degrees*)

LtoB.....Left to Bottom Immersed Boundary-Cell Intersection Flag

LtoBtoR.....Left to Top to Right Immersed Boundary-Cell Intersection Flag

LtoR.....Left to Right Immersed Boundary-Cell Intersection Flag

LtoR.....Left to Right Immersed Boundary-Cell Intersection Flag

LtoT.....Left to Top Immersed Boundary-Cell Intersection Flag

LtoTtoR.....Left to Top to Right Immersed Boundary-Cell Intersection Flag

M.....Misfit Function

M.L.....Model with Maximum Likelihood and Lowest Misfit

McMC.....Monte-Carlo Markov Chain Method

NA.....Neighbourhood Algorithm

NAB.....Neighbourhood Algorithm-Bayes

Nar. Idx.....Narrowing Index of Posterior Credible Interval

n_{iter}.....Number of Iterations of NA

n_r.....Number of Models Re-Sampled at each Iteration of NA

n_s.....Number of Models Sampled at each Iteration of NA

n_{si}.....Number of Initial Model Sampled at First Iteration of NA

NTG.....Net to Gross Ratio

NTPFA.....Non-linear Two-Point Flux Approximation

nX, N_x, n_x.....Number of Cell Divisions in x direction

nY, N_y, n_y.....Number of Cell Divisions in y direction

$\mathbf{n}^{\eta}$.....Normal Vector on a Semi-interface with Constant ξ

$\mathbf{n}^{\xi}$.....Normal Vector on a Semi-interface with Constant η

$p(m)$.....Prior Probability Distribution

$p(m|O)$.....Posterior Probability Density

$p(O|m)$.....Likelihood of Data

P.H.C......Permeability Heterogeneity Contrast Between Adjacent Layers

p_{acc}.....Acceptance Probability of New Proposed Model in Gibbs Sampler

PDF.....Probability Distribution Function

P_{ij}.....Transition Matrix for Achieving from $X(j)$ to X(i)

PPD.....Posterior Probability Density

q_i^{Obs}.....Observed Production Rate of *ith* Flowing Phase (*STBD*)

q_i^{Sim}.....Simulated Production Rate of *ith* Flowing Phase (*STBD*)

Q^{NNC}.....Space of all Interfaces Connecting Non-Neighbour Cells

$R(x_i)$.....Radius of Prior Confidence Interval of Horizon Height at x_i (*ft*)

rA..... Angle between Pinchout Major Axis and x axis (*Degrees*)

RR.....Right-Right Immersed Boundary-Cell Intersection Flag

S.....Slope of Fault (*ft/ft*)

SCBB.....Set of Cells with Boundary at the Top

SCBB.....Set of Cells with Boundary at the Bottom

SSS.....Structured Stair-Stepped Gridding

STOIIP.....Stock Tank Oil Initially In Place

T.....Throw of Fault (*ft*)

T.C.....Truth Case

$TH_j(x_i)$.....The Thickness of *jth* Reservoir Layer with respect to datum at x_i

$\mathbf{T}_{ij}$.....Piola Transmissibility Tensor for Interface Connecting Cells *i* and *j*

TL..... Horizontal Distance between Head and Tail Points of Pinchout (*ft*)

TLtoRR.....Top-Left to Right-Right Immersed Boundary-Cell Intersection Flag

TM.....Transmissibility Multiplier for Faults

tMF.....Reshaped Cell Type of Merged Active Cell Below the Boundary

tNMF.....Reshaped Cell Type of Non-Merged Active Cell Below the Boundary

TPFA.....Two-Point Flux Approximation

TPS.....Triangular Pressure Support Scheme

TT.....Top-Top Immersed Boundary-Cell Intersection Flag

TtoR.....Top to Right Immersed Boundary-Cell Intersection Flag

U.....First Diagonal Element of Transmissibility Tensor

uHA..... Opening Angle of Pinchout Upper Triangle at Head Point (*Degrees*)

uTA.....Opening Angle of Pinchout Upper Triangle at Tail Point (*Degrees*)

V.....Second Diagonal Element of Transmissibility Tensor

$\mathbf{V}_i$.....Velocity of *ith* Flowing Phase ($bbl/ft^2.Day$)

W.....Off-Diagonal Element of Transmissibility Tensor

WCI.....Width of Posterior Credible Interval

WOPR.....Well Oil Production Rate (*STBD*)

WWIR.....Well Water Injection Rate (*STBD*)

WWPR.....Well Water Production Rate (*STBD*)

$X(j)$.....The *jth* State of a System Stochastically Evolving in Time

xH.....X-coordinate of Pinchout Head Point (*ft*)

X_S.....X-coordinate of Starting Point of Fault (*ft*)

$\left(\tilde{X},\tilde{Y}\right)$.....Main Axes of a Parallelogram Grid

$z(x_i)$, $h(x_i)$.....Height of a Reservoir Horizon with respect to datum at x_i (*ft*)

$\alpha(e_i^{NNC})$, $\beta(e_i^{NNC})$.....Parameters Measuring the Match of Flux Through Faults Computed by EEMPFA to the True Flux

γ.....A Measure of Accuracy of TPFA for Fluxes Through Fault Plane

ε_1, ε_2.....Measures of Strength of Unphysical Solutions of Pressure

$\theta_{\tilde{X}X}$.....Orientation Angle of First Axis of Parallelogram Grid with first Cartesian Coordinate

$\theta_{\tilde{Y}X}$.....Orientation Angle of Second Axis of Parallelogram Grid with first Cartesian Coordinate

$\kappa\,(x_i)$.....The Curvature of a Reservoir Horizon with respect to datum at x_i

λ.....Dimensionless Measure of Cell Skewness and Permeability Anisotropy

$(\mathbf{\Lambda}_\eta^{\,i})_{\mathbf{1}\times 4}$.....Geometry Vectors of a Semi-interface with Constant ξ

$(\mathbf{\Lambda}_\xi^{\,i})_{\mathbf{1}\times 4}$..... Geometry Vectors of a Semi-interface with Constant η

μ_i.....Viscosity of *ith* Flowing Phase (*Centi-Poise*)

ξ,η.....Coordinates of Uniform Reference Space

$\hat{\xi}, \hat{\eta}$ .....Coordinates of Flexible Quadrature Points

$\pi_i(t)$.....The Probability of Chain Being at State $X(j)$

σ.....Standard Deviation of Mismatch between Observed and Simulated Information

σ_i.....Standard Deviation of Mismatch between Observed and Simulated Production Rate of *ith* Flowing Phase

φ.....Porosity

$\mathbf{\Phi}_C$.....Vector of Potentials at Cell Centres of an Interaction Region

Φ_D.....Dimensionless Cell-Wise Flow Potential

$\mathbf{\Phi}_F$.....Vector of Potentials at Mid Faces of an Interaction Region

Φ_i.....Flow Potential of *ith* Flowing Phase (*psia*)

Φ_O.....Flow Potential at Central Node of an Interaction Region

$\mathbf{\Phi}_V$.....Vector of Potentials at Vertices of Sub-volumes of an Interaction Region

$\psi(\Phi_x, \Phi_y)$.....Tangent of Angle between Potential Drop Vector and x Axis

$\mathbf{\Psi}^i_{2\times4}$.....Shape Matrices of Sub-volumes of an Interaction Region

Chapter 1

Introduction

1.1 Geological Structures

In hydrocarbon reservoirs, different geological features with extended planar shapes are encountered which arise from various sources. These planar features belong to different geological classifications such as:

1. Sedimentological features like stratigraphic sequences which are identified with significant surfaces developing along the boundaries of rock layers deposited at different times and are determined with variations in sediment supply the rate of change in accommodation space (Bryant, 1996). Among them sequence boundaries are the product of a fall in sea level that erodes the sub-aerially exposed sediment surface of the earlier sequence or sequences. These boundaries are diachronous (evolutionary), capping the previous high-stand systems tract and eroding the surface of the down-stepping sediments deposited

during accompanying forced regression associated with the sea level fall (Catuneanu, 2002).

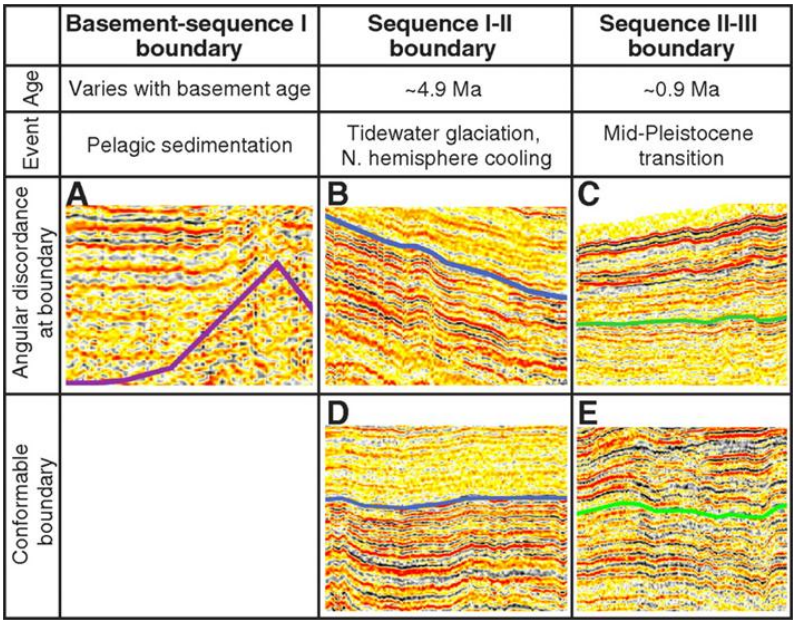

Figure 1.1: Representative facies at sequence boundaries (from Rocee et al., 2011)

2. Unconformities which are buried erosion surfaces separating two rock masses or layers of different ages, indicating that sediments have not been continuously deposited (defined by American Geological Institute, 1962). In general, they describe the surfaces of non-deposition or erosion which represents a break in the rock sedimentary record.

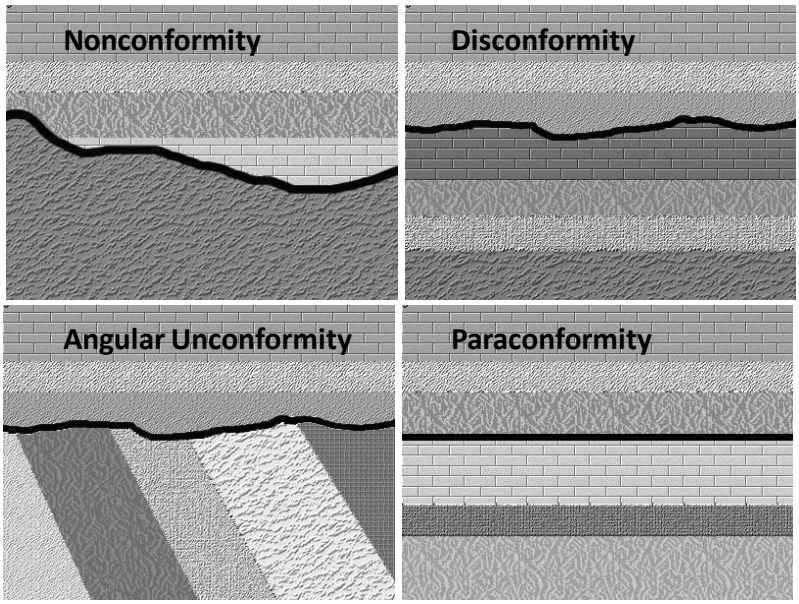

Figure 1.2: Various kinds of unconformities

3. Structural features which are caused by deformation of rock masses or strata as a result of tension or compression stresses imposed on rock masses (Russel, 1955). This stresses are created by tectonic, gravitational, diapiric or compactional processes. Faults and folds are two main large scale structural features mainly associated with magnificent rock volume displacements. They might form favourable geometries for hydrocarbon trapping.

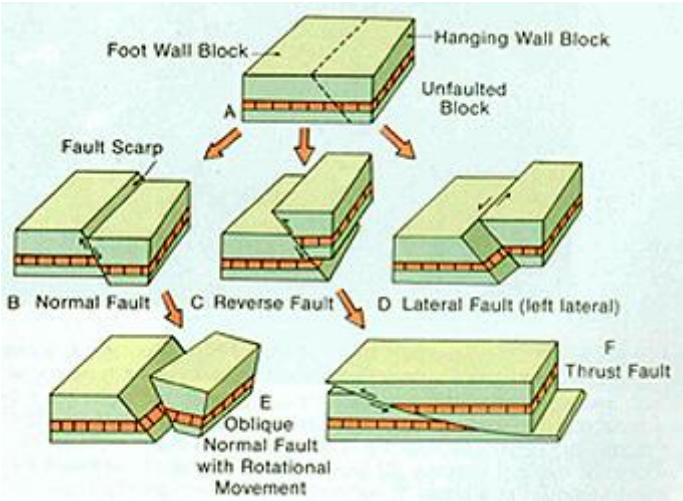

Figure 1.3: Different types of faults due to stresses imposed at variety of directions and strengths on rock body (from American Geological Institute, 1962)

However some features might belong to either of these classes like pinchout which can be due to interrupted deposition (sequence boundaries) or erosion (unconformities). In this thesis we are interested in modelling of those planar features which leave discontinuities into the rock body; either in terms of lithology (unconformities and boundary sequences) or in terms of stratigraphy (faults). For example we will not study micro-structures like fractures, joint or shears. We will use the term “Geological Structures“ with negligence throughout the thesis to describe these features. In hydrocarbon reservoirs geological structures are often recognised as the planes confining different compartments of a reservoir. Petrophysical properties tend to abruptly vary across the geological structures. In this regard, geological structures can be viewed as the reservoir boundaries. One can categorise them into two main families:

1. Internal boundaries such as faults or the boundaries of reservoir layers which separate different reservoir flow units. More gently dipped structures (layers boundaries) determine the depth, thickness and the orientation of each

stratigraphic layer. While faults as the more harshly dipped structures offset reservoir layers and change the stratigraphic connectivity of previously sedimented flow units (Arnold, 2008 and Manzocchi et al., 1999).

2. External boundaries such as reservoir top structure or the water-oil contact surface which control the depth and the vertical extent of the reservoir.

Reservoir performance is strongly influenced by the geometrical and topological specifications of geological structures. As stated by Schaaf et al. [2009], impact of geological structures on reservoir production might be by orders of magnitude bigger than corresponding impact of petrophysical properties. Embedded large-scale discontinuities of rock properties along the planes of geological structures and their complex geometry predominantly govern the reservoir flow behaviour. Thus incorrect determination of their geometry and topology might dramatically reduce the reliability of production forecasts as a result of following disadvantages:

1. Overestimation or underestimation of oil volume originally in place and consequently the production rates.
2. Getting misled in determination of dominant production mechanism of reservoir due to alteration of water-oil and oil-gas contact surfaces
3. Non-trustworthy assessment of gravity force especially in fractured reservoirs where the gravity drainage as an important production mechanism is dependent on reservoir thickness, individual thicknesses of high-permeable and low-permeable layers and their corresponding depths.
4. Deviation from true overall reservoir interconnectivity in vertical and horizontal directions which is strongly influenced by faulting network (Childs et al., 1997 and Knipe, 1997).

1.2 Structural Uncertainties: Sources and Consequences

Seismic surveys are the key tools to determine the location, the size and the shape of geological structures. Seismic waves are sent into the depth of the earth and the reflections coming from different stratigraphic layers are gathered. When a seismic wave encounters a boundary between two layers with different acoustic impedances,

some of the energy in the wave will be reflected at the boundary, while some of the energy will continue through the boundary. The amplitude of the reflected wave is predicted by multiplying the amplitude of the incoming wave by the seismic reflection coefficient, determined by the impedance contrast between the two layers. By observing changes in the strength of reflectors, seismologists can infer changes in the seismic impedances. In turn, they use this information to infer changes in the properties of the rocks at the interface, such as density and elastic modulus. The transverse element of seismic waves (Shear waves) only move through the solids, unlike the longitudinal element (compressional waves) which can be transmitted through both solid and fluid media. This enables the seismic reflection to differentiate between hydrocarbon containing layers (petroleum reservoir, aquifer, and gas cap) and the layers devoid of fluid. Also density contrast among formations containing different saturation distributions of oil, gas and water or enjoying different porosities eventuates in different response times received from different depths of reservoir. This difference yields a powerful tool enabling us to:

1. Determine the reservoir extent and boundaries
2. Make distinction between deposited layers (also potential pinched out layers)
3. Find any interruption of stratigraphic continuity along the bedding layers which is translated as a fault

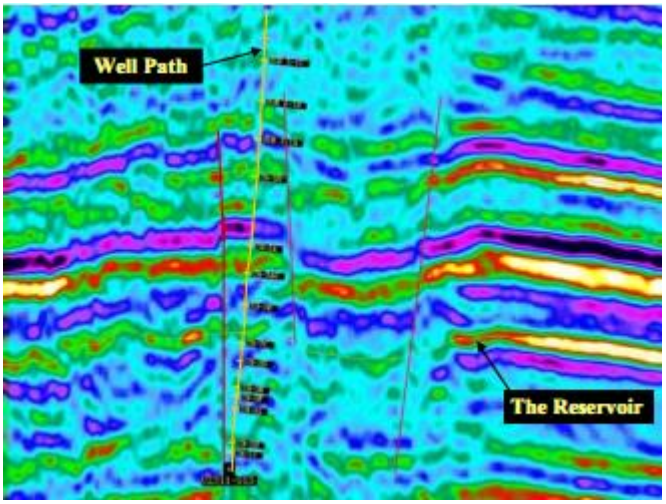

Figure 1.4: A typical seismic cross section (taken from Al Rougha et al., 2004) showing the beddings cut off by three normal faults

If the seismic wave velocity in any rock type is known, then the travel time may be used to estimate the depth to the reflector. Time maps can be converted into depths by means of velocity models per different rock types. Geophysicists use the obtained 3D map to constraint the geometry and location of large scale geological structures. However the predicted reservoir structure is quiet doubtful due to several uncertainties associated with different stages of seismic data processing (Thore et al., 2002 and Røe et al., 2010):

1. Measurement errors in seismic data acquisition due to velocity anomalies, presence of gas cloud, or navigation errors (Downton et al., 2007).
2. Non-uniqueness nature of seismic data migration and time-depth conversion which are both known as inverse problems.
3. Poor seismic resolution due to non-dissociable velocity contrasts in horizontal and vertical directions (Seiler et al., 2010-A).
4. Ambiguity present in interpretation of seismic data made by geophysicists resulting in spread of different possible structural models (Rankey and Mitchel, 2003, Bond et al., 2007 and Baddley et al., 2004).

Uncertain modelling of reservoir structures brings about uncertainties in geometry and topology of geological structures such as top and basin horizon positioning, gross thickness of stratigraphic layers, and fault position and local geometry (Gazet et al., 2009).

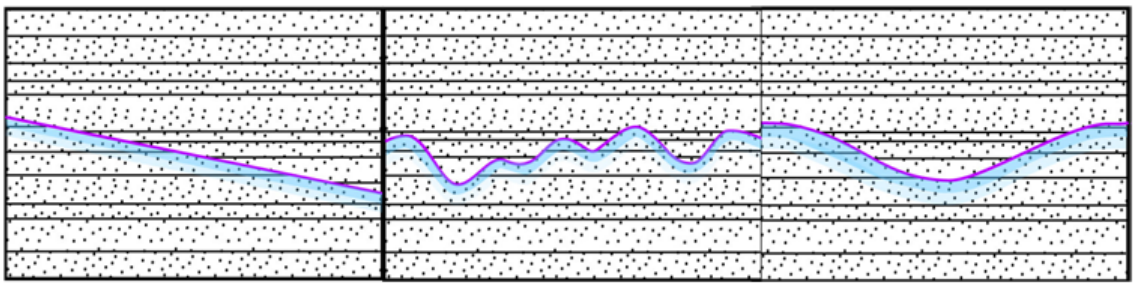

Figure 1.5: Example of uncertainty with geometry of a geological structure; three different realizations from a geological structure (layer-layer boundary) with different degrees of complexity (taken from Lever, 2007)

Reservoir compartmentalisation which is mainly dictated by the structure of the horizons and faults controls the gross reservoir volume and Net To Gross (NTG) ratio (Røe et al., 2010). Even in presence of depth pickings on both sides of a fault, uncertainties reside in the horizon correlation across faults. Although updated structural models for developed fields are usually believed to be more precise; but even these fields are also not immune from uncertainty. Several examples can be found in literature on structural uncertainty which describe the structural uncertainty in mature fields (Dromgoole and Spears, 1997, Williams et al., 2006, Friedel et al., 2009, Salhi et al., 2005). However, strong impression of reservoir volume, connectivity and compartmentalisation from structural uncertainty, makes it as a main contributor to the uncertainty of reservoir production forecasts. Indeed when structural uncertainty is not properly addressed in the framework of uncertainty modelling and quantification, reservoir engineers might fail to design an optimum scenario for reservoir development.

Thus structural uncertainty strongly influences the decisions on reservoir exploration and exploitation. For example to drill wells with improved productivity indices, following points should be taken into account regarding the uncertain geological structures:

1. Wells must be drilled far from the sealing fault, as they restrict the flow towards the well.
2. Wells must be drilled where the high permeable layers have their maximum thickness along the formation.
3. Wells must be drilled where they do not cut through pinched out layers, as pinchouts reduce dramatically the open thickness to the flow along the wellbore.
4. Locations and relative pattern of wells with respect to each other must be designed such that their productivities get optimized regarding the reduced horizontal interconnectivity resulting from the faults offset.
5. In a water flooding program, an optimum placement of injection and production wells is dependent on variation of gross thickness along the formation and individual thicknesses of high and low permeable layers.

In general location and local geometry of geological bodies in large scale determine the production forecast for a given reservoir model. Remembering the reservoir model as one of possible reproductions of real subsurface reservoir, the importance of identifying and constraining the structural uncertainties is clarified.

1.3 Previous Works on Quantification of Structural Uncertainties

Basic idea in conventional approach for uncertainty quantification is varying static properties of reservoir models (like porosity, permeability, transmissibility multipliers) to determine their corresponding uncertainty intervals. As a main drawback, this approach ignores the structural uncertainties of geological objects involved in reservoir models. However significant influence of structural uncertainties on reservoir engineering decisions has raised an increasing demand in industry to account for such uncertainties (Rivenæs et al., 2005). What makes quantification of structural uncertainty less feasible is the deficiency of current tools to conduct automatic history matching and uncertainty quantification workflows capable of updating the structural models. However inflexibility of current geo-modelling softwares does not allow the varying interpretation of reservoir geometry during the history matching process (Irving et al., 2010-B and Seiler et al., 2009). Therefore as a most common practice in works on uncertainty quantification, structural uncertainties have been neglected (Evensen et al., 2007 and Zhang and Oliver, 2009). Works on quantification of structural uncertainties were initiated with more conveniently operational structural parameters like the reservoir depth, layer thickness and aquifer depth. In Palatnik et al. [1994] such structural parameters have been parameterised as region multipliers and a conjugate gradient method has been applied to minimise the objective function in history matching process.

Rivenæs et al. [2005] has considered the fault structural uncertainty by creating stochastic alternative realizations of fault pattern. Structural parameters of each fault pattern realization then were encapsulated and reduced to transmissibility multipliers. Streamline flow simulation then were performed on whole realization dataset and corresponding misfits compared with observed data were ranked to identify best history

matched models. However lack of conducting a direct optimisation loop for history matching is the main deficiency of this method which restricts the quality of matches.

Alternatively in Suzuki and Caers [2008], a large set of prior model realizations of reservoir structure representing the prior structural uncertainty were built and the discrete choice of structural interpretation was considered as one uncertain parameter. A stochastic search algorithm was utilised to tackle obtained discrete parameter space. The employed algorithm was subjected to Hausdorf distance criteria (Cignoni et al., 1998) as a measure of distance from the global minimum of misfit surface in N-dimensional parameter space. Similar to Rivenæs et al. [2005], a good history match is possible when the prior ensemble of structural realizations has been wide enough to cover all inherent structural uncertainties. Indeed this approach is very likely to fail in case of complex reservoir geometry encompassing several uncertain geological structures, as creating a representative ensemble which spans high dimensional uncertain parameter space is very time-consuming and consequently tends to be impractical.

Schaaf et al. [2009] has investigated the influence of uncertainty in reservoir and aquifer depth and thickness on gas storage forecasts. In this work the variation of reservoir and aquifer thickness in history matching workflow has been incorporated with varying volume cells in a one-dimensional reservoir model. However the grid framework itself is not altered during the history matching process. Extension of such approach to two-dimensional or three-dimensional models of oil reservoirs is neither trivial nor functional, because unlike the gas reservoirs, production behaviour in oil reservoirs is strongly impressed by local variation of reservoir or aquifer thickness in two dimensions due to complex phenomena like gravity drainage or gravity segregation.

In another work Schaaf et al. [2009] presented an automatic workflow for simultaneous updating of structural and petrophysical reservoir properties. Studies structural parameters were horizon depths, throw and transmissibility multipliers of fault and facies distribution. Commercial geomodelling software (PETREL 2008) is launched by a software for assisted history matching, such that the simultaneous variation of

structural model and simulation model become possible. However the necessity for rebuilding both geological grid and simulation grid at each step of history matching process is the main drawback, as this would disturb the grid architecture and consequently the equity of simulation errors for all models gets contravened. Slow decrease in objective function and relatively poor data match in this work can be attributed to non-fixed grid state vector during the history matching process. Moreover obtained stochastic geological models were not utilised to quantify structural uncertainties.

Røe et al. [2010] have developed a stochastic geostatistical approach to model the prior geometrical/topological uncertainties of fault surfaces and fault network. Faults are defined as two-dimensional tilted surfaces, where they reside within their corresponding fault uncertainty envelope around the base case (seismic-picked surface). A Gaussian simulated residual is added to base case to simulate the uncertainty envelope, while krigging is applied to condition the fault realization to the well observations. However they have not addressed the complexities with flexible simulation of fault surfaces within a history matching workflow.

Irving et al. [2010-B] have proposed two geologically-based workflow to optimise uncertain structural properties of fault (position, juxtaposition and transmissibility) and depth of reservoir horizons. They have used a kind of fractional experimental design to create a limited ensemble of possible structural models which then used to perform sensitivity analysis and optimisation, therefore no automatic workflow to rebuild grid during optimisation process have been adopted and grid has been deformed manually to adjust to stochastic horizon and fault surfaces. Moreover, variation of fault geometry is represented with altering the across-fault cell connections while grid framework remains unchanged. As a result, geological realism would be less preserved in grid framework.

Seiler et al. [2009] proposed a workflow for assessment of structural uncertainties associated with top and bottom horizons capable of continuously updating the structural model. The production data were sequentially assimilated by mean of an Ensemble

Kalman filter. In another paper (Seiler et al., 2010) their approach were extended to structural uncertainties of faults. They employed an elastic grid approach to conform the grid architecture to evolving geometry of top and basin horizons during the history matching process, in which the corner points of base simulation model were re-adjusted at each step of history matching to honour the renewed geometry of horizon.

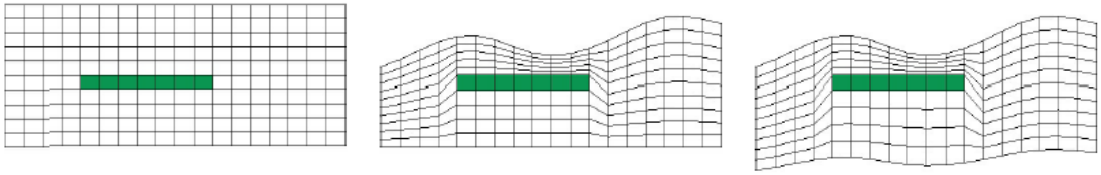

Figure 1.6: The elastic grid approach to fiddle the grid corner points with reforming horizons (from Seiler et al., 2009)

Seiler's approach (schematically shown in figure 1.6) although leaves the same number of cells for all models sampled during history matching process, but the cell deformation would not be restricted just to the neighbourhood of reforming geological structure and the deformation is propagated into the whole grid. Therefore in most parts of discretized region the transmissibility tensor is substantially modified, resulting in different trend of numerical error compared with other models. This infringes a main proposition of history matching which allows comparing goodness of models based on respective discrepancies between simulated and observed data.

1.4 Thesis Statement and Objectives

The significant impact of large scale structural uncertainties on reservoir performance dictates that field development decisions should be built in the light of descriptive reservoir forecasts which take the structural uncertainties into account. Thus it is crucially demanded to create multiple realisations of reservoir geological structures exhibiting good compliance with the observed data. Different nature of structural uncertainties from distributed uncertainties of petrophysical properties calls for totally different parameterisation of history matching process, since unlike the conventional

approaches of history matching, the geometry of structures should be varied in contrast to modification of petrophysical properties within the simulation model.

The need for translation of geometrical variation of structures into the grid structure has turned into the main obstacle against developing competent workflows for assessment of structural uncertainties. A comprehensive workflow for history matching of structures should fulfil two apparently contradictory criteria simultaneously:

- Precise representation of structures geometry on simulation grid to accurately emulate the impact of geometrical configuration on flow
- Not disturbing the gridding pattern within the history matching process to accommodate almost constant simulation error over all models

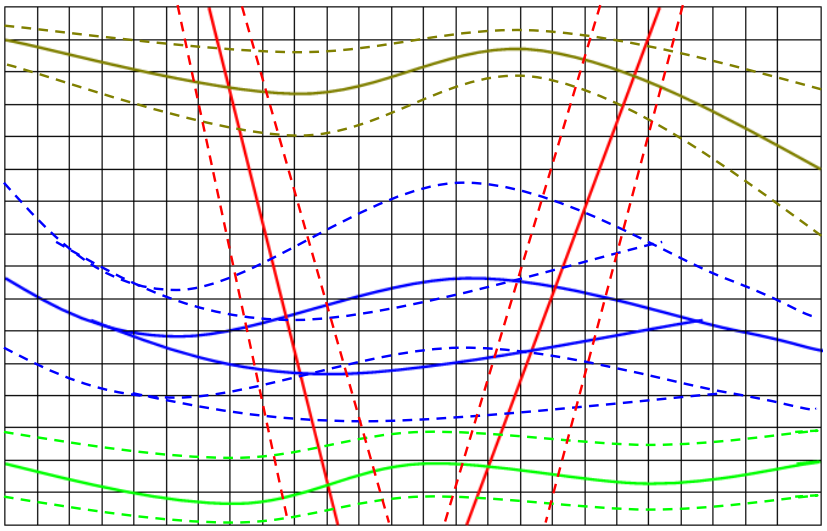

Figure 1.7: Free displacement and deformation of geological structures within their corresponding uncertainty ranges with their bounds shown with dotted lines during the history matching process over a stationary Cartesian grid; the curved green and mustardy green lines are cross sections of top and base horizons of reservoir, blue closed curve is the cross section of a pinchout and tilted nearly vertical lines are vertical cross sections of two faults

This thesis aims toward proposing a robust workflow capable of continual updating of geological structures fulfilling both abovementioned vital criteria. We will link up this workflow to the general framework of uncertainty quantification developed at Heriot-

Watt University in order to constraint the structural uncertainties. The main objectives of thesis are expressed as:

- Developing a powerful algorithm inspired by "Cartesian Cut Cell Method" (Causon et al., 2000, 2001 and Yang et al., 1997, 2000) for rendering the variation of geological structures into a fixed Cartesian grid with very limited and localised cell reshaping
- Adopting and invigorating suitable schemes from the class of "Locally Conservative Flux Approximation Methods" (extended EMPFA) to circumvent the numerical deficiencies emerging in the vicinity of complex reservoir boundaries
- Validate and justify the feasibility and performance of proposed "Hybrid Cartesian Cut Cell/extended EMPFA" for history matching of reservoir models consisting of single or multiple geological structures
- Justify the benefits of proposed workflow for constraining the uncertainties of reservoir reserve and recovery
- Compare the uncertainties arising from different types of structures and incorporate their respective influences on reservoir performance in posterior inferences

1.5 Thesis Outline

Chapter 2 reviews the general concepts and different techniques used for history matching and uncertainty quantification. Specifically the working mechanisms of Neighborhood Algorithm (for history matching) and Neighborhood Algorithm-Bayes (for uncertainty quantification) are explained.

Chapter 3 is dedicated to describe the general algorithm inspired by "Cartesian Cut Cell Method" for importing the free deformation and movement of different geological structures with different geometrical complexity into the stationary Cartesian grid.

Chapter 4 discuses the motivations of using extended EMPFA and the mathematics behind it. Moreover the consistency, stability and accuracy of proposed scheme for the problems offering typical structural complexity are demonstrated.

In chapter 5, using the proposed “Hybrid Cartesian Cut Cell/EMPFA” several synthetic models with non-intersecting structures (reservoir top and bottom structures, faults, pinchout) are history matched and their posterior uncertainty intervals are determined. Different impacts of geological structures with different geometries on reservoir flow and uncertainty are discussed.

In chapter 6, the use of proposed workflow is extended to models enjoying multiple intersecting structures. The influences of convolved sources of structural uncertainty on recovery forecast will be analyzed with reservoir engineering knowledge and testified with posterior inference.

In chapter 7, the summary of research undertaken including the key conclusion is presented. Also some promising ideas of research are recommended for the future work.

In Appendix A, some information about the written flow code was presented which include the matrix solver, temporal discretisation, coupling scheme and so on. Moreover the fluid properties as well as capillary and relative permeability curves used in the simulation exercises are provided.

Chapter 2

An Overview of History Matching and Uncertainty Quantification

Reservoir engineers take decisions about the optimised plans of field development. Thus prediction of the reservoir performance under different scenarios of field development is desired. To accomplish this aim, governing mathematical equations of mass conservation are to be solved numerically on reservoir models as translations of reservoir rock and fluid data onto the numerical grid. Petrophysical properties are distributed throughout the reservoir by interpolating the data sampled at sparse well locations. Also the geometry of different compartments building the petroleum reservoir is determined with interpretation of seismic data and subjected to restricted precision due to poor resolutions and/or noisy signals. However the reservoir model can be tuned by manipulating the petrophysical or structural property distributions in a way that they reproduce the observed production data. Described *history matching* process might come up with multiple models mimicking the production history but not necessarily

giving the similar forecast of reservoir future. In this regard, lack of information on spatial distribution of rock properties and geometry of involved geological structures makes it necessary to introduce the role of *uncertainty* in the reservoir management problems.

In this chapter we will review various approaches for history matching and uncertainty quantification. Also the general framework for uncertainty quantification based on Bayesian statistics is introduced.

2.1 History Matching

Aim of history matching process is to achieve a reasonable match between simulation output and the observed data. During this process, dynamic information representing the field performance is utilised to update the reservoir simulation model. This information may include production rates data, well pressure measurements, tracer data, time-lapse seismic data and other information sources. In general history matching is conducted in order to improve the robustness and functionality of the reservoir model for future predictions. In this regard, history matching helps to decision making about the optimised scenarios of field development.

Works on history matching were started with manual approaches in which the input parameters of reservoir model were manually readjusted in order to obtain similar outcomes from reservoir model to observed data. Although such an approach involves trial-and-errors, but reservoir engineering and geological judgments and reservoir-specific experiences accelerates the process. However the growing use of optimisation tools has facilitated the history matching process in recent decades. Automatic or assisted approach for history matching reduces the manual work done by reservoir engineers to obtain a consistent simulation model with reservoir performance data. In this approach, uncertain reservoir parameters are determined, then the problem of calibrating reservoir model with observation data is reduced to an optimisation problem with respect to uncertain parameters in which the discrepancy between observation data and simulation outcomes is to be minimised. A measurement of discrepancy between

observed data and simulation outcome is defined by a standard weighted summation of least squares, when we assume the Gaussian statistics for the measurement and simulation errors (Tarantola, 1987, Christie et al., 2005).

$$M = \sum_{i=0}^{N} \frac{\left(Obs - Sim\right)_i^2}{2\sigma^2} \tag{2.1}$$

In Eq. 2.1, *Obs* and *Sim* are referred to as the observed and simulated values of production data (e.g. oil production rates, water cuts, bottom hole pressures, and so on), also σ represents the standard deviation of errors, where a Gaussian probability distribution is proposed for measurement errors of observed data and simulation error is assumed to be zero. It is worth mentioning that term $\left(Obs - Sim\right)$ can be expressed as the difference between simulation error and measurement error. So at negligible values of simulation error, σ is almost identical to standard deviation for discrepancy term $\left(Obs - Sim\right)$. For most reservoir engineering purposes, measurement errors at each time step are assumed to be independent and a constant value is assigned to σ. In this way each step of history matching process (as an "inverse" problem) is itself a "forward" problem where the set of updated reservoir parameters are feed into the simulator and observable quantities like production rates and well pressures are computed for calculating the misfit.

2.1.1 Literature Review of Automatic History Matching

Gradient-based methods were the initial optimisation tools employed for the adjustment of reservoir models during history matching processes (Slater et al., 1970, Thomas et al., 1971, Chen et al., 1973 and Anterion et al., 1989). All these methods are inspired from the original idea of Newton-Raphson method originally designed for finding successively better approximations of roots of a single-variable real-valued function. These methods require calculating the derivatives of objective function (Misfit function for history matching applications) with respect to uncertain reservoir parameters called as the sensitivity coefficients or the gradients. Starting from an initial guess of uncertain parameters, sensitivity coefficients will then be used to calculate new set of uncertain parameters within their initial allowed intervals leading into smaller misfit values. Different variations of such an approach have been used in petroleum industry for

history matching, e.g. Gauss-Newton least-square procedure (Thomas et al., 1970, Watson et al., 1986), optimal control theory (Chen et al., 1973), Adjoint method (Li et al., 2001), and so forth.

The main drawbacks of Gradient-based methods in terms of difficulty in implementation and quality of results can be summarised as:

1. Need for individual computation of sensitivity coefficients for each parameter at each iteration and at each time step (Bissel et al., 1994).
2. Potential entrapment in local minima rather than achieving global minima (Gomez et al., 2001).
3. Tendency to return single history-matched model as the final result.

Minimisation of misfit function has many local or global solutions, thus the history matching problem can be considered as an "ill-posed" problem. Therefore the single history-matched reservoir model obtained from *Gradient-based methods* is only one of the possible reservoir models reproducing the observed data. Remembering the fact that history-matched model will be used for forecasts of reservoir performance, the importance of multiple history-matched models would be clarified. Figure 2.1 shows the uncertainty associated with oil recovery prediction when several models have been found which honour the observations.

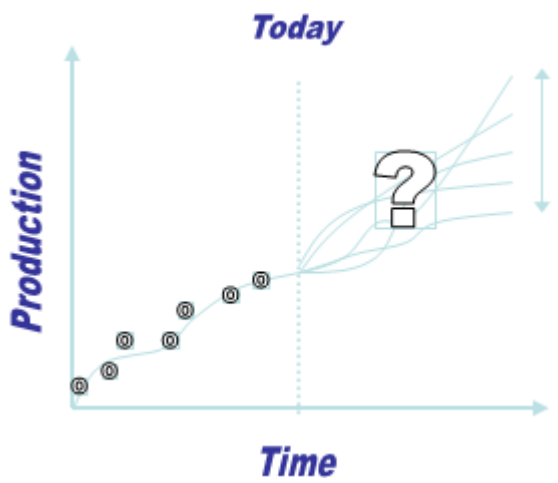

Figure 2.1: Multiple forecasts for multiple solutions to history matching problem

In the early 90's, the importance of generating multiple history matched models had been widely clarified and the research were focused on optimisation methods capable of finding multiple solutions. Stochastic methods are capable of finding multiple minima (Holger et al., 2004); therefore realistic prediction of future reservoir performance becomes possible.

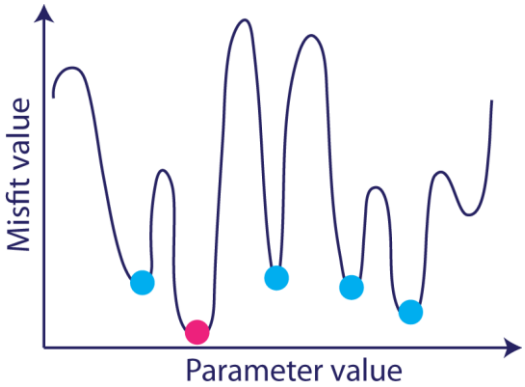

Figure 2.2: Global minimum (pink) and multiple local minima (blue) for a misfit function

In stochastic optimisation methods, the parameter space is randomly explored, introducing such randomness into the search process:

1. Accelerates the progress in minimising the misfit function (Holger et al., 2004).
2. Abates the sensitivity of the method to the modelling errors (Spall et al., 2003).
3. Enables the method to escape the local minima and increases the possibility of finding the global minima (Holger et al., 2004).

Tuning runtime parameters of stochastic methods gives the flexibility to make a balance between the exploration of search space and the exploitation of better solutions. An optimal search is achieved when the different areas in the parameter space are properly searched, such that as much as possible local minima are found. In this way, a reliable quantification of uncertainties associated with forecasts is assured. However when a faster reduction of misfit value is desired, previously visited areas in search space are refined successively to get better solutions; In this case search is exploitation-dominated.

In petroleum industry, among different stochastic methods, there has been much more interest in evolutionary population-based algorithms. Such algorithms are inspired from real population-based systems in nature (Ant colony, Social behaviour of a flock of birds and so on) and their runtime parameters emulate the multiple intelligent individual agents of their fundamental real systems. In these algorithms a population of solutions is generated at each step of optimisation and then the fitness of each member of population is evaluated and ranked. Thereafter multiple intelligent individuals utilize the interactions among members (solutions for the current step) to update the solution for the next step. Improvement of the quality of solutions in this way can give (at least theoretically) any possible search sequences (Koppen, 2004). It means that the search within the parameter space would be effectively navigated such that algorithm is capable of simultaneously refining different already spanned regions (which might be far away from each other) for finding better solutions and approaching the global minimum out of several local minima.

Some of stochastic methods applied in history matching problems are as followings:

1. Genetic Algorithm: Romero et al. [2000] and Erbas et al. [2007]
2. Evolutionary Search Strategies: Schulze-Riegert et al. [2001] and Selberg et al. [2007]
3. Simulated Annealing: Ouenes et al. [1993] and Portella et al. [1999]
4. Particle Swarm Optimisation: Banks et al. [2007] and Lazinica [2009]
5. Scatter Search: Sousa et al. [2006]
6. Chaotic Optimisation: Mantica et al. [2002]
7. Ensemble Kalman Filters: Evensen [2003] , Nævdal [2002] and Bianco et al. [2007]

In this thesis, we will employ Neighbourhood Algorithm (NA) for the history matching of uncertain geological structures. So in the next section, we will explain the working mechanisms of the method and some of its applications in history matching.

2.1.2 Neighbourhood Algorithm

The Neighbourhood Algorithm (NA) has been originally by Sambridge [1999-A] to solve a seismic waveform inversion problem. NA is categorised as a stochastic method searching for models with good match to the data. In this algorithm a random set of models is generated and then objective function is computed for all models to evaluate and rank them. Then the search space will be geometrically represented in term of Voronoi diagram (Okabe et al., 1992). This diagram divides the finite-dimensional search space into separate cells which are the nearest neighbourhood region of each of initial models. Thus starting from randomly generating n_{si} models, search space will be decomposed into n_{si} cells around n_{si} initial points, such that the interfaces of each cell are the equidistant lines drawn between each pair of initial neighbour points.

Then n_r best models based on ranking of lowest misfits are chosen and n_s new models are generated by a random walk search in the Voronoi cells of models selected. Thus at each iteration, n_s / n_r new individual models are generated at each cell. After re-evaluation of objective functionsa for n_s new models, the geometry of the old Voronoi diagram is updated. The procedure will be iterated until a predetermined stopping condition such as maximum number of iterations is satisfied.

Behaviour of NA in terms of exploration/exploitation in the search space is determined by manipulating the tuning parameters (n_{iter} , n_s and n_r). Sambridge [1999-A] stated that amount of exploration and exploitation is affected by the n_s/n_r ratio rather than the individual values of these two tuning parameters. He recommends a reasonable good solution would be obtained when n_s is selected about the number of model parameters and number of re-sampled models (n_r) is between 2 and ($n_r/2$). According to Elabed [2003] higher values of n_s/n_r ratio results in faster convergence of algorithm to good-fitting regions, while at lower n_s/n_r ratios NA is more explorative. Moreover size of initial population (n_{iter}) affects the quality of results especially in high-dimensional search spaces, as higher n_{iter} provides more information from explored search space and leads the algorithm towards more diverse solutions throughout the search space (Erbas, 2007). Potential entrapment of NA in local minima has been reported by Elabed [2003] for cases that first best models are in a restricted small region of search space. In such cases, next iterations of NA just results in more refinement of that region, while the rest

of search space is left unexplored. In figure 2.3, the general procedure of neighbourhood algorithm has been schematically represented.

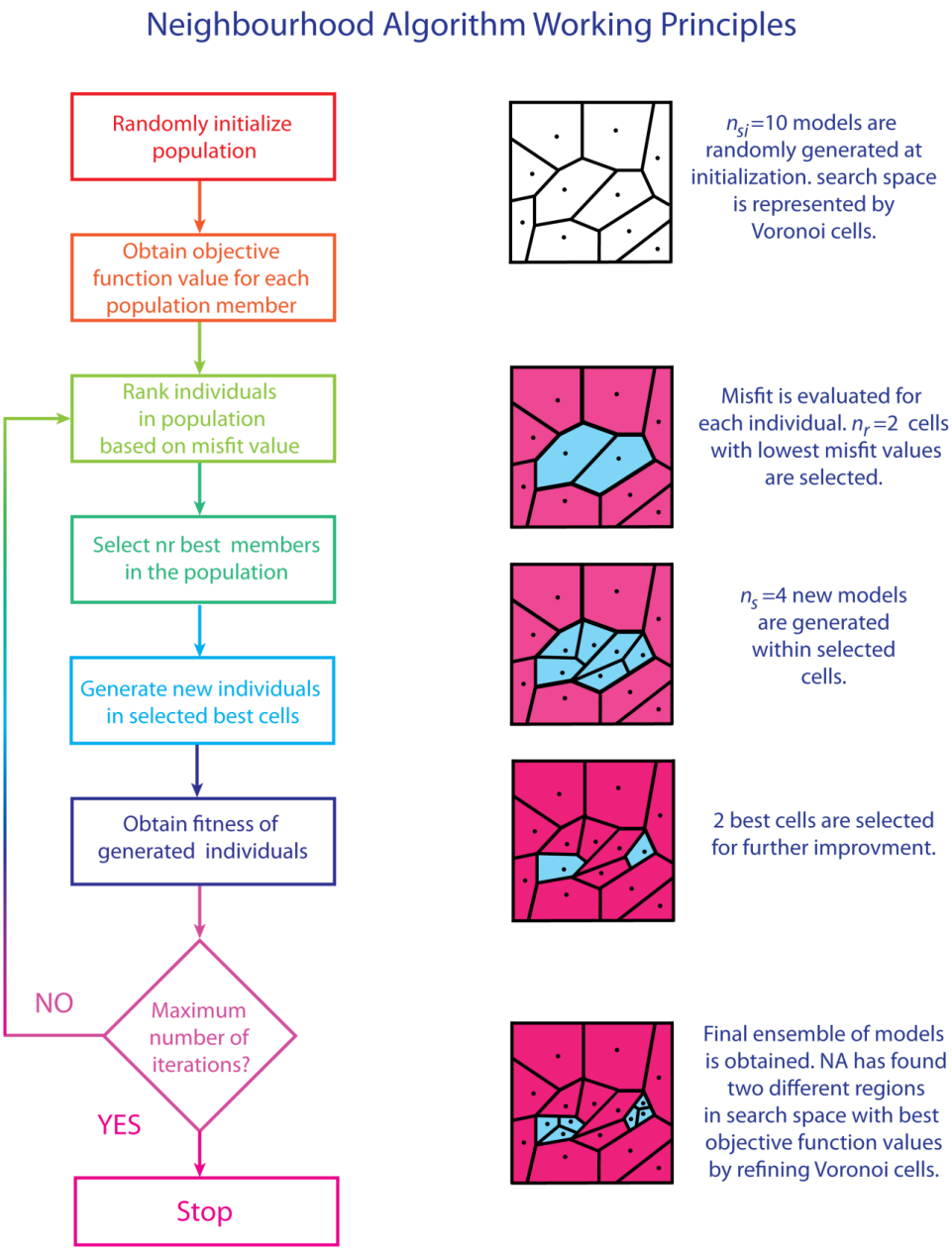

Figure 2.3: General working flowchart of Neighbourhood Algorithm (from Hajizadeh, 2011)

Despite many efforts to generalize suggestions for selecting tuning parameters of NA, it seems that this decision is principally governed by the physics of the problem in terms of distribution of local minima throughout the parameter space and the convolved impacts of matching parameters on simulated solutions. There have been reports using

the minimum possible value (n_s/n_r = 1) by Beghein et al. et al. [2002, 2004] to higher values (n_s/n_r =4 or 5) by Kennett [2006]. Therefore in this thesis, suitable values of NA tuning parameters will be selected according to type of problem and the desired quality of result for each specific problem. A problem in which the solution is materially less sensitive to some of matching parameters in contrast with rest of them, should be conducted with more explorative modes ($n_s/n_r \rightarrow 1$) to properly span the parameter space for as much as good solutions (local/global minima). This would enhance the assessment and quantification of inherent uncertainties.

NA has been applied to various ranges of problems, especially to the problems in the field of seismology. Several researchers have employed NA for different inversion problems in seismic (Kennett [2006], Jansky et al. [2007], Cerv et al. [2007], Yao et al., 2008).Also several applications of neighbourhood algorithm in petroleum engineering can be seen in the literature. As a pioneering works, Christie et al. [2002] has used Neighbourhood Algorithm to obtain multiple history-matched models in the Teal South reservoir. Also history matching of both real (Nicotra et al., 2005 and Valjak, 2008) and synthetic (Subbey et al., 2003) reservoirs has been performed by means of neighbourhood algorithm. Stephen and MacBeth [2006] and Stephen et al. [2007] have applied NA for simultaneous history matching of production and 4-D seismic data. Arnold [2009] has used the NA as the choice of sampling algorithm in a geologically-parameterised history matching framework, where the fault parameters or channel parameters are history matched.

As mentioned by Hajizadeh [2011], NA has been mainly applied in low dimensional optimization problems with less than 25 unknown parameters. In this thesis we aim to investigate the structural uncertainties for small 2D models with limited number of geological structures. So considering the simplicity of tuning the NA and its robustness for more exploratory modes (compared with many other stochastic methods), we will use it relevantly for structural history matching.

2.2 Uncertainty in Reservoir: Sources and Quantification

Prediction of reservoir performance is associated with uncertainties arising from the lack of accurate and reliable knowledge about the reservoir rock and fluid properties (Gavalas et al., 1976). Large financial investments required for field development plans have made it necessary to decide based on accurate quantification of these uncertainties. Uncertainties impacts the decisions about the infill drilling, water flooding scenarios, enhanced oil recovery plans and consequently the design of well surface injection or production facilities (Birchenko et al., 2008).

Randomness, fuzziness and incompleteness of reservoir data bring about the uncertainties in petroleum reservoirs (Blockley et al., 2000). Randomness is referred to as the lack of data which leaves some reservoir data patterns hidden underground (especially for geological structures) and reduces the clarity and visibility of those patterns. This would prevent from fitting a certain statistical model to the reservoir data. Measurement errors or non-comprehensive reservoir parameterisation might induce an inaccurate (fuzzy) expression of reservoir data or fuzziness. Most common type of uncertainties occurring in petroleum reservoirs is the incompleteness uncertainty. Incomplete and interrupted rate and pressure measurements especially in the early stages of reservoir production reduce the certainty and reliability of history-matched reservoir models (Caumon et al., 2004). However the deficiencies of current technologies to acquire more representative information from reservoir system prevents us from setting up a more precise reservoir model and result in non-reliable predictions of reservoir performance.

The sources of errors contributing to uncertainty in reservoir engineering can be categorised in two main groups:

1. Data measurement inaccuracies: Low accuracy of measurement tools or the operator errors in recording and interpreting the data constitute most usual errors in both direct and indirect measurement of reservoir static or dynamic information (Iwegbu et al., 2007). However each type of data measurements has its own specific errors:
    a. Direct measurements of reservoir static properties (porosity and permeability) from a very small core are poor representatives of

underground reality. Because initial and boundary condition imposed on a core sample during the laboratory measurement might be different from reservoir conditions. Moreover exposition of core to different pressures when it is carried from reservoir to laboratory alters its pore pressure and consequently yields wrong measurement of rock properties. Elkins [1972] and Chappell et al. [2007] have discussed the uncertainties in determination of initial oil in place (Stock Tank Oil Initially In Place or briefly STOIIP) and prediction of reservoir recovery arising from imperfect measurement of porosity and permeability.

b. Intrinsic limitations of any indirect data measurement methods (e.g. well logging for porosity or saturation, well testing for permeability, seismic surveys for reservoir structure) might eventuate in significant uncertainties. Small penetration depths for well logging leave a porosity or saturation value coming from a limited area around the well. Also structural uncertainties resulting from poor quality of seismic data belong to this category.

2. Simulation errors: Incorrect input data, inadequate representation of physics of reservoir flow and imprecise computational approximations employed in numerical methods are the main factors leaving erroneous modelling of reservoir flow (Christie et al., 2005).
    a. Interpolations made to produce maps of rock properties throughout the reservoir from limited and sparse measured data remain uncertainties in geological model which are exacerbated when transferred to the simulation model.
    b. Imperfect translation of inherent physics of flow into the mathematical equations, unknown details of sub-grid heterogeneity and reduced information due to upscaling induce the physics errors.
    c. Solution errors are developed as a result of following grounds:
        i. Simplifying assumptions for solving reservoir mathematical equations.
        ii. Round-off errors due to limitation of computer memories for decimal digits.
        iii. Numerical dispersion due to discretization of mathematical operators on reservoir simulation cells.

2.2.1 Methods for Uncertainty Quantification

The most common definition of uncertainty quantification is to determine state of uncertain processed information quantitatively by means of assigning a probability distribution for describing that information. Such an approach suits well to problems that have been stochastically modelled which is the case for most geological uncertainties. However structural uncertainties related to fault or the top structures have been also tackled with scenario-based approach. Samson et al. [1996] has used this approach to investigate the impact of different scenarios for seismic interpretation of top structure and water-oil contact on gross-rock volume estimates.

The main goal in probabilistic methods for uncertainty quantification is the calculate forecast uncertainty based on a posterior probability distribution of reservoir models. Such a probability distribution is assigned to the ensemble of models generated during the history matching process based on a posterior inference. According to Erbas [2007] classification of uncertainty quantification methods, three groups can be recognised regarding how they process the history matching result to determine the posterior probability distribution:

1. Methods using the single best model with lowest misfit value: Linearization about the maximum posteriori (LMAP) (Oliver, 1996)
2. Methods using a subset of history matched models: the randomized maximum likelihood (RML) method (Oliver et al., 1996)
3. Methods using a the whole ensemble of models: Markov chain Monte Carlo (McMC) method (Behrenbruch et al., 1985)

Bayes theorem, named after Thomas Bayes, is a formal way to update our beliefs about the state of a system in terms of probabilities, when we are provided with information (Christie et al., 2005 and Sivia, 1996). When applied for uncertainty quantification purposes on continuous problems, Bayes theorem is written as:

$$p(m \mid O) = \frac{p(O \mid m)\, p(m)}{\int_M p(O \mid m)\, p(m) dm} \qquad (2.2).$$

where *M* is the space of reservoir models, *m* is a vector of model parameters (an arbitrary model from space *M*), *O* is a vector of the observed data (including the dynamic reservoir information), *p(m)* is the prior probability distribution and *p(O|m)* is the likelihood of the data defined as a measure of the quality of the fit of model (*m*) predictions to the observed data (*O*). Finally *p(m|O)* expresses the posterior probability density (PPD) representing our updated knowledge about the model (*m*) in the light of observations (*O*).

In this thesis we will employ the Bayesian framework (developed by the uncertainty quantification group at Heriot-Watt university) to quantify the structural uncertainties. It is a systematic procedure to update current knowledge of a system based on newly obtained data (Christie et al., 2005). In a Bayesian inference, the Bayes theorem is used to perform inferences about the value of some parameter of interest based on the prior information and new observed information.

The model likelihood is maximised when the difference between the simulation results and observations (or the misfit value) gets minimised, thus a direct relation between likelihood function and the misfit value is expected. Likelihood of a model can be interpreted as the probability that true value of reservoir observation is equal to simulation outcomes based on proposed reservoir model. Commonly with the assumption of normal (Gaussian) distribution of measurement errors around zero with a variance σ^2 at any given time-step (*t*), the log of likelihood is taken proportional to the negative of misfit value ($M \propto -\log(p(O|m))$). In effect measurement errors are supposed to stay independent at different time steps and consequently the likelihood of the model is obtained from the product of the probabilities of individual measurements at all time-steps of available data points (*N*). So one would end up with:

$$p(O|m) = \left(\frac{1}{\sigma\sqrt{2\pi}}\right)^N \prod_{t=1}^{N} \exp\left\{-\frac{1}{2}\frac{(Obs - Sim)_t^2}{\sigma^2}\right\} \qquad (2.3).$$

Eq. 2.3 is written for single observation parameter measurement on a single well. However it can be extended to be utilised for problem with multiple flowing data types

(like production and injection rates of flowing phases, bottomhole pressures, gas oil ratio and water cuts) measured on multiple wells (Barker et al., 2001).

$$p(O \mid m) = \prod_{i=1}^{N_w} \prod_{j=1}^{N_p} \left(\frac{1}{\sigma_{ij}\sqrt{2\pi}}\right)^{N_t} \prod_{k=1}^{N_t} \exp\left\{ \omega_{ijk} \left[-\frac{1}{2} \frac{(Obs_{ij} - Sim_{ij})_k^2}{\sigma_{ij}^2} \right] \right\} \tag{2.4}$$

in which N_w is the number of wells with subscript i running over wells, N_p is the number of production data types with subscript j running over them and N_t is the respective number of production data report times with subscript k runs over time-steps. Observed data (Obs_{ijk}) and simulated ones (Sim_{ijk}) for each of the parameters (j) have been reported at time steps k with a standard deviation of σ_{ij}. ω_{ijk} denotes the extra weighting factor for each parameter at each time step reported at each well. These weights reflect the importance of some of data types at specific time steps (Hajizadeh, 2011).

Results from a posterior inference often are expressed as the Bayesian credible intervals (Erbas, 2007). Such intervals predict that the true values of the parameters (true model) have a particular probability of lying in the credible interval given the data actually obtained. Therefore a narrower credible interval is equivalent to the more confidence in history-matched reservoir model and less uncertainty associated with them. To determine these intervals, Cumulative Posterior Distribution (CDF) is needed from posterior which can be calculated by summation of PPDs arranged in an ascending order (Christie et al., 2005). In this thesis credible interval is reported as the interval of parameters corresponding to 10% to 90% CDF values ([p10,p90]). However based on the mean, mode, variance or any other statistical measures from posterior probabilities, conclusion about posterior beliefs can be drawn.

In this thesis we will use Neighbourhood Bayes Algorithm or briefly saying NAB (developed by Sambridge, 1999-B) to build an approximation for the real posterior probability distribution. In the next section we will explain the working mechanism of NAB. In figure 2.4 the general workflow used in this thesis for history matching and uncertainty quantification of geological structures has been depicted.

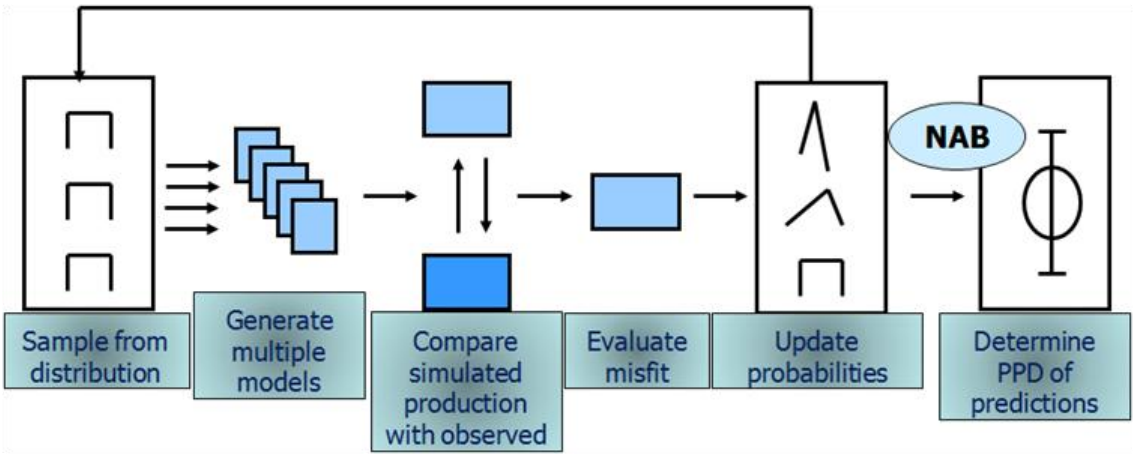

Figure 2.4: Complete history matching and uncertainty quantification framework (Sivia, 1996, Christie et al., 2005), it is statistically a consistent way to make inference about a given ensemble of models generated within history matching process. This allows for forecasting the reservoir performance with reduced uncertainty.

2.2.2 Neighbourhood Bayes Algorithm for Posterior Inference

Neighbourhood Bayes Algorithm belongs to the general class of Markov chain Monte Carlo (McMC) techniques (Gilks et al., 1994) generally proposed for sampling from probability distributions. Posterior inference can be directly made based on what have been sampled by these techniques from posterior probabilities. To perform this technique, a sequence of random states of a system stochastically evolving in time ($X(0)$, $X(1)$, ... ,$X(n)$) (called Markov Chain) is constructed by proposing that probability distribution for next state ($X(n)$) is totally determined by probability distribution of current state ($X(n\text{-}1)$) (Bonet-Cunha et al., 1998). Starting from an initial non-stationary state, the Markov chain is then expanded by let the system to move from state $X(i)$ to new state $X(j)$ based on a joint probability distribution called transition matrix P_{ij} which expresses the probability of achieving the state $X(j)$ at a single step from the state i. Denoting $\pi_i(t)$ as the probability of the chain being at state $X(i)$ at time t, probability of updating the chain state at time t+1 to $X(j)$ (joint probability) is obtained from $\sum_i \pi_i(t) P_{ij}$.

The state of the Markov chain after a large number of steps is then used as a sample of the desired distribution (commonly known as the equilibrium distribution). The quality of the sampling improves as a function of the number of steps and the probability is almost independent of initial state after a large number of steps. Then the equilibrium probability distribution is specified by the visiting frequency of states over the long chain (Gamerman, 1997). To extract proposed samples from distributions like posterior distribution, Markov chain should lead into a stationary state coinciding with the target distribution. Sampling is usually performed randomly which is preferable over expensive direct samplings. A random walk propagates in a Brownian manner and is not necessarily conducted in a straight direction. The simplest random walk algorithm used for sampling in McMC methods is the *Metropolis–Hastings algorithm* (named after Metropolis et al., 1953). Metropolis-Hastings Algorithm moves the system state from $\boldsymbol{\theta}^{t}$ to $\boldsymbol{\theta}^{t+1}$ in a Brownian manner based on an acceptance probability which is obtained from the individual probabilities of current and proposed next states and transition matrix P_{ij}. If acceptance probability is larger than a tolerance, then system state is updated to $\boldsymbol{\theta}^{t+1}$, otherwise current state is retained. When the joint distributions (i.e. transition matrices) are not known explicitly, a special case of Metropolis-Hastings Algorithm (Gibbs sampler explained by Casella et al., 1992) is used which employs conditional probabilities. The Gibbs sampling algorithm generates an instance from the distribution of each variable in turn, conditioned to the current values of the other variables. Gibbs sampler yields a sequence of samples forming a Markov chain which its stationary distribution is the demanded joint distribution (Gelman et al., 1995). Gibbs sampling is especially suitable to sample the posterior distribution of a Bayesian framework which are typically indicated as an ensemble of conditional distributions.

Applying a straightforward McMC technique for predicting the posterior probabilities of reservoir model, it is required to run reservoir models for a giant number of possible states within the prior range and then evaluate the likelihoods from mismatch with the observations. Obviously this is very time-consuming to simulate all the required models. NAB (Sambridge, 1999-B) has been designed to resolve this kind of problem in different areas of science and engineering using the Bayesian statistics. An already ensemble of models created by a stochastic sampling algorithm is imported into the NAB routine and the inference is performed from information from whole ensemble. As

an important advantage, NAB avoids any forward running of reservoir simulator for all the models generated by the sampling algorithm or each model resampled.

NAB uses a Gibbs sampler to build an approximation of real posterior probability distribution (PPD). The previously explored multidimensional search space is represented with Voronoi cells. NAB proposes an already determined PPD for each model is constant over the Voronoi cell which encompasses that model. Then NAB interpolates PPD of unknown points in the search space.

NAB requires conditional probability distribution function (PDF) ($\pi(\theta_i \mid \theta_{-i})$) is determined for full parameter range. The probability of current state being at θ_i along the ith parameter axis conditioned to fixed values of other parameters is expressed by $\pi(\theta_i \mid \theta_{-i})$ NAB finds the intersections of each parameter axis with lines drawing from centres of Voronoi cells and attributes a constant PDF to each segment confined within two successive intersections which is specified from product of the PPD value for Voronoi cell by the width of the segment.

An arbitrary point from input ensemble ($\boldsymbol{\theta}^0 = (\theta_1^0, \theta_2^0, ..., \theta_n^0)$) is chosen as the start point of NAB and then Gibbs sampler performs random walks along each parameter axis in multi-dimensional parameter space. Random deviations from the PPD constructed over each parameter axis are followed by determining the acceptance probability of proposed point:

$$p_{acc} \propto \frac{\pi(\theta_i^p \mid \theta_{-i})}{\pi(\theta_i^{\max} \mid \theta_{-i})} \qquad (2.5).$$

in which $\pi(\theta_i^{\max} \mid \theta_{-i})$ gives the maximum PDF along the selected axis. If the step is rejected, then the process is repeated until completely cycling through each parameter axis. A new state vector is generated when the cycling through all parameter axes is carried out once. Updating the state vector $\boldsymbol{\theta}^t$ to $\boldsymbol{\theta}^{t+1}$ is continued until meeting convergence criteria. After the parameter space has been satisfactorily spanned by many independent random walks starting from different location in input ensemble, true

posterior distribution can be approximated with the obtained conditional. In figure 2.5, the working mechanism of Gibbs sampler for NAB has been schematically shown for a two dimensional parameter space.

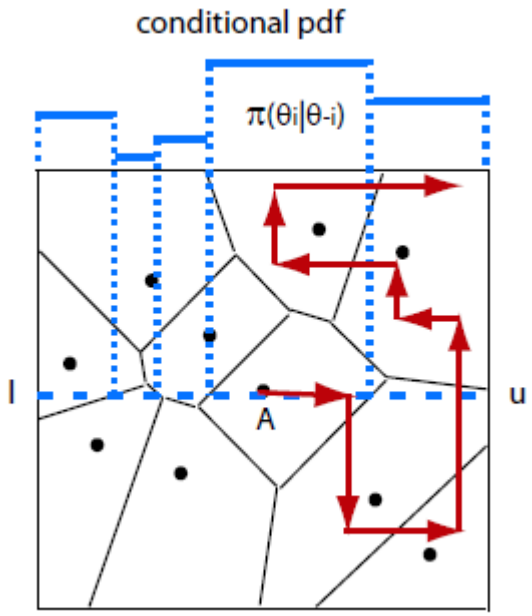

Figure 2.5: Algorithm of Gibbs sampler used in NAB (from Erbas, 2007)

To make Bayesian appraisal about the future uncertainty associated with reservoir performance, NAB constructs a resampled ensemble smaller from the input ensemble. Then the posterior probability *p(m|O)* is approximated from the visiting frequency of resampled models. Then the inference is carried out by running forecast simulations over the resampled ensemble resulting in determination of bounds of Bayesian credible interval for the recovery prediction.

Erbas [2007] has investigated the relation between resolution of input ensemble and the performance of NAB to narrow down the uncertainty. She has concluded that the ideal input ensemble of NAB is generated by a sampling algorithm balanced between exploring and refining the misfit surface.

Chapter 3

Cartesian Cut Cell Method

This chapter describes how an adapted form of *Cartesian Cut Cell Method* is applied to reconstruct new models during the process of history matching. At each step of history matching process new geometrical specifications are assigned for geological structures. The reformed boundaries of the new structures should be mapped into the grid framework in order to build a new model. Cartesian Cut Cell Method translates the complex geometry of the renewed reservoir boundaries into the grid while it assures not distorting Cartesian grids away from reservoir boundaries (faults, pinchouts, layer boundaries, reservoir top and base structures).

SUQIB (the code for Structural Uncertainty Quantification assisted by an Immersed Boundary approach) is a C++ code that we have developed for tackling the problem of structural uncertainty in two-dimensional models. This code is capable of handling multiple uncertain structures with demanded degree of complexity. SUQIB modifies the

grid framework at each step of history matching by means of Cartesian Cut Cell Method to account for the updated geometry of geological structures. It employs the Enriched Multipoint Flux Approximation to compute the flux terms in flow equation especially for degenerated cells left after cutting the *grid* with new geological surfaces. We will explain the procedure of Cartesian Cut Cell based on the workflow of SUQIB and its classes and routines.

3.1 Introduction to the Family of Immersed Boundary Methods (IBM)

As discussed in Chapter 1, assessment of structural uncertainties requires continuous updating of geometry of embedded geological objects during the history matching process. Such a successive variation raises the need for regridding at each step of history matching. Obviously unstructured gridding or corner point grid as a standard method in petroleum engineering for representation of geological structures (Ponting, 1989) can provide body-fitted grids conforming to the renewed surfaces of uncertain structures. This leads into models having different gridding patterns with different trends of numerical errors and violates the main proposition for history matching which assumes numerical errors for different models are approximately similar. Thus the misfits calculated for variable models are not anymore comparable. However high computational expense imposed by regridding at each step is another disadvantage. On the other hand Cartesian grids preserve the trend numerical error constant over all models, whilst it cannot conformally follow the complex geometry of uncertain structures and leaves inaccurate approximations of flow variables in the vicinity of the uncertain structures.

Thus it is desired to modify Cartesian gridding such that no general regridding is needed, but more accurate flow approximation is made with introducing corrector-modifier terms in flux equations. This is the main idea behind the *Immersed Boundary Method* developed by Peskin [1972, 1977, 1981, 1982] to study the flow patterns around the heart valves. In computational fluid dynamics, there has been always an interest in developing numerical methods that compute flow fields with complex stationary and/or moving immersed boundaries on fixed Cartesian grids. The transparent preference of these methods over the conventional body-conformal

approaches is the invariant computational grid regardless of the geometric complexity of the immersed boundaries. In this way the complex geometry of boundaries is decoupled from its mapping onto the computational grid.

The novel technique employed by Peskin turned out to a very helpful method for the problems of fluid-solid interactions which numerous different variants of it have been developed in last 40 years. In this method solutions of a variable coefficient elliptic equation (Poisson Equation) are sought:

$$\nabla.\left(\beta\left(\vec{x}\right)\nabla P\left(\vec{x}\right)\right) = f\left(\vec{x}\right) \quad x \in \Omega \qquad (3.1),$$

where the domain Ω has been divided into two disjoint sub-domains Ω^{+} and Ω^{-} by an embedded boundary Γ. Poisson equation describes the flow in many biological systems with fluid-solid interaction. In the original work by Peskin [1972], Immersed Boundary Method was applied for blood flow in an artificial heart with blood-valve common surface. Coefficient β jumps across the embedded boundary resulting in discontinuity of the flow variable P and the term $\beta\nabla P$ along the embedded boundary. Embedded boundary is moving in time and its geometry is deformed while Cartesian grid on the background is stationary. The tension imposed on the fluid due to deformation of Γ is expressed with singular stresses $\int P\left(\vec{x},t\right)\delta\left(\vec{x}-X\left(\vec{x},t\right)\right)d\vec{x}$, where $X\left(\vec{x},t\right)$ represents the trend of embedded boundary. Peskin [1977, 1981] has employed discretized forms of mentioned singular stresses at certain points along the embedded boundary to distribute the discontinuity over the a buffer layer of cells in the vicinity of Γ. However this approach leaves a first-order precision, as the discretized delta functions smear out the discontinuity across the boundary into a thickness of order of mesh-width.

Lai and Peskin [2000] and Li and Lai et al. [2001] have developed formally second order accurate variants of IBM with reduced numerical dispersion for simulating the flow around a solid embedded object. These methods fail to achieve a second order accuracy when a varying non-smooth delta function is used to translate the discontinuity into the cells. Cortez et al. [2000] have formulated higher order approximation of boundary forces. The generalized IBM developed by Tornberg et al. [2003-A, 2003-B,

2004] minimizes the distribution of singular forces over the computational grid and leads into higher order accurate approximation of pressure. In general despite the simple implementation of IBM and its capability to complex geometries, its main drawback is its limitation on order of precision. However increasing the resolution of grid in the vicinity of embedded boundary can improve the accuracy of results. This is what has been investigated by Roma et al. [1999] where IBM has been coupled with *Adaptive Mesh Refinement*.

Different versions of Peskin basic approach have been applied to simulate a wide variety of problems in fluid mechanics and biology. Some examples are heat transfer problems over the heterogeneous media, interface diffusion or the complex aerodynamic flow predictions. The continuity equation (mass conservation equation) for fluid flow in porous media is written as:

$$\nabla.\left(-\mathbf{K}\left(\vec{x}\right)\nabla\Phi\left(\vec{x}\right)\right)=Q\left(\vec{x}\right) \qquad (3.2),$$

where $\mathbf{K}\left(\vec{x}\right)$ stands for permeability tensor, $\Phi\left(\vec{x}\right)$ is the flow potential (summation of hydraulic pressure and gravity heads) and $Q\left(\vec{x}\right)$ refers to as the fluid source/sink terms over the unit volume. Considering the analogy of this equation with Poisson Equation (Eq. 3.1), flow in porous media lies in this category of problems and geological structures with irregular geometries can be regarded as the embedded boundaries. Although they do not deform with time, but their variation during the history matching process sparks the innovative idea of *Quantification of Structural Uncertainty Assisted by Immersed Boundary Methods*.

A significant advance in the class of IBM was made by LeVeque et al. [1994] who developed *Immersed Interface Method* (IIM) in which the discontinuities in the solution and normal gradient across the interface are explicitly incorporated into the finite difference scheme. In this method the standard 5-point stencil of finite difference in two dimensions is converted to a 6-point stencil leading into a sparse but not positive definite. Thus for cells adjacent to the immersed boundary one can write:

$$\nabla.\left(\beta\left(\vec{x}\right)\nabla P\left(\vec{x}\right)\right)_{i,j} = \sum_{k=1}^{6} m_k P_k \quad k \equiv (I, J) \in \{i \pm 1, j \pm 1\} \qquad (3.3).$$

The multipliers m_k are obtained after writing down the Taylor expansion of jump conditions across the interface on closest point of boundary to the cell (i, j). So m_k multipliers translate the jump condition across the interface and relative configuration of cell (i, j) and interface into the flow equations. IIM has been applied for several moving interface/free boundary problems like works done by Hou et al. [1997] on Hele-Shaw flow, Li et al. [1999-A] on Stephan flow and crystal growth, Li et al. [1999-B] on electro-migration voiding.

The Ghost Fluid Method (GFM) developed by Fedkiew et al. [1999-A, 1999-B] has been proposed based on the similar philosophy to IIM. But it results in symmetric positive definite systems of discretized equations.

Sharp Interface Cartesian Method was first introduced by Udaykumar et al. [1999, 2001] to model the viscous incompressible flow around embedded solid objects with complex geometries. Unlike the already explained method, a finite volume discretization can be implemented in this method as well as finite difference method. However the sharpness of immersed interface is preserved by reshaping the control volumes through which interfaces passes. Different application of this method can be found in the literature for fluid-solid interaction and solidification problems (Udaykumar et al., 2002, 2003, Marrela et al., 2005, Liu et al., 2005). However the communication between the moving boundary and the flow solver is usually accomplished directly by modifying the computational stencil near the immersed boundary.

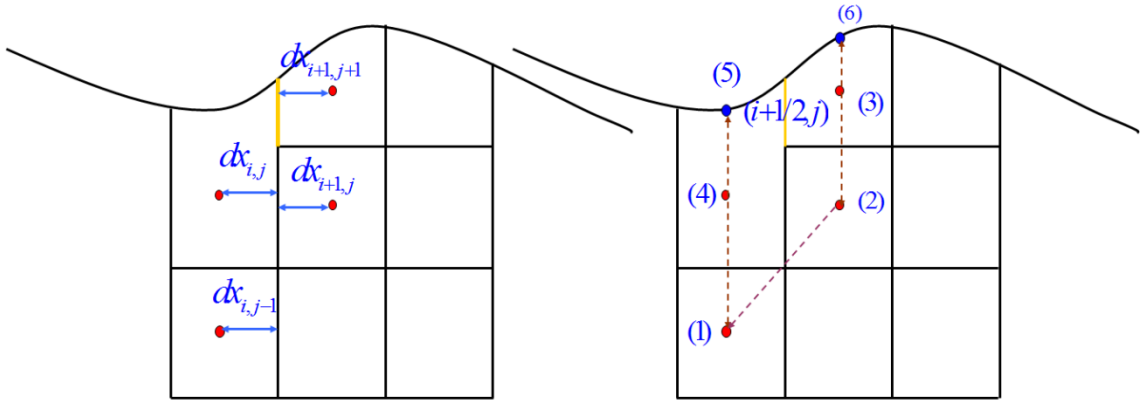

Figure 3.1: Left: Calculation of pressure gradient for an interface in the vicinity of immersed interface, Right: 6 point stencil used to determine the unknown parameters of polynomial, the yellow coloured interface is the target interface for calculating the pressure gradient and the area bounded between dotted lines and curved boundary is the area at which the pressure is described with a quadratic-linear polynomial.

For example the pressure gradient across the interface between cells (3) and (4) in figure 3.1 is calculated with a polynomial linear respect to *x* and quadratic with respect to *y*.

$$P = c_1 xy^2 + c_2 y^2 + c_3 xy + c_4 y + c_5 x + c_6 \tag{3.4}$$

To obtain the unknown coefficients a 6-points stencil is formed around target face comprising of 4 cell centres in the bulk and 2 points on the boundary. Eq. 3.4 should be satisfied for the pressures at cell centres. Also polynomial is obliged to satisfy the jump conditions of pressure or its gradient for two points on the boundary, thus the impacts of discontinuity and complex geometry of immersed interface are reflected in flow equations. This method leaves a linear combination of pressures at 4 cell centres included in the stencil for the normal pressure gradient ($\left(\frac{\partial P}{\partial x}\right)_Y = \sum_{j=1}^{4} \tau_x^j P_j$).

Although sharp interface Cartesian method is implemented based on the finite volume scheme and assures the mass conservation unlike other variant of IBM family, but it is not suitable for porous media flow, because:

1. Conductivity coefficient β (analogue to permeability) is assumed to be continuous everywhere except across the immersed boundary. So this method

does not suggest how the local variation of β can be incorporated in discretizing the flow equation. While in porous media, pressure field is convolved with the permeability field.

2. In our knowledge, none of variants of sharp interface Cartesian method address the problem of multiple intersecting boundaries.

However the basic idea of reshaping the cells affected by immersed boundary in Sharp Interface Cartesian Method had been borrowed from the *Cartesian Cut Cell Methods*. This method was initially utilised in the aerospace community to create the boundary-fitted grids for multi-component incompressible flow problems. Wedan et al. [1983], Barber [1992], De Zeeuw et al. [1993] and Berger et al. [1995] have developed adaptive Cartesian grid capable of tracking rapid-deforming boundaries. Cartesian Cut Cell Method has been applied by Causon et al. [2000, 2001] and Yang et al. [1997, 2000] for modelling the shallow water flows. This method avoids step-wise representation of irregular boundaries unlike the conventional Cartesian grid, as it deforms the cells intersected by boundaries when the boundary is not aligned with grid-lines. Portions of those cells located outside the immersed boundary (within the solid phase) will be discarded. It means that they will be deleted from the computational grid on which a flow equation is discretized. Remaining part of cut cell is retained if its centroid falls outside the boundary; otherwise it is merged to one of its adjacent cells having:

1) Lowest volume among all active cells in the neighbourhood
2) Largest normal area on common face

The first condition should be satisfied to avoid numerical instabilities due to large volume contrast between neighbour cells and the second one assures the flow connectivity. One should make a compromise between these two criteria.

Complex geometries of moving boundaries are accommodated by updating the local cut cell information on a stationary Cartesian grid. So without any need for general regridding, immersed boundaries are reproduced conformally in Cartesian grid with boundary-fitted cells. Such a combination of Cartesian cell in the bulk of fluid and

boundary-fitted irregular cell adjacent to immersed boundary is much less likely to produce non-physical solution than unstructured body-fitted grid. As the corresponding solution matrix is sparser than the matrix for fully unstructured grid.

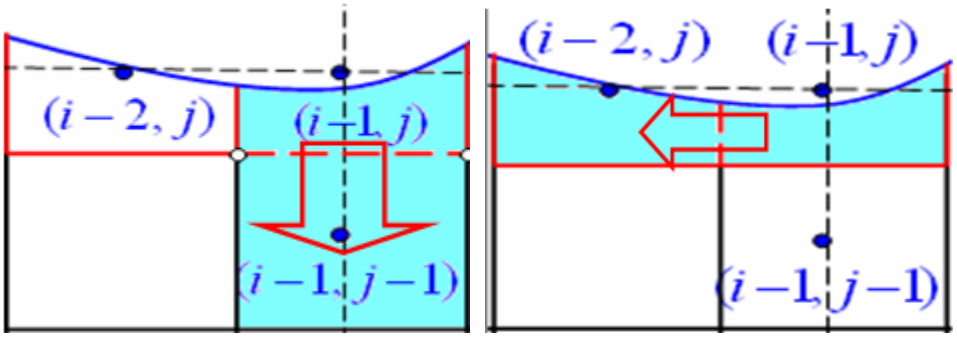

Figure 3.2: Left: Merging of partially fluid cell based on criteria of largest normal volume, Right: Merging based on criteria of lowest volume, the cells at the end of red arrows are the host cells which absorb a partially fluid cell.

Cartesian Cut Cell method creates grids with less sensitivity to high petro-physical heterogeneity and permeability anisotropy in terms of producing non-physical solution compared with unstructured body-fitted grid. As the later frequently fails in avoiding excessively skewed or stretched cells. As shown by Coirier and Powell [1993] results obtained from Cartesian Cut Method are remarkably as accurate as solution obtained from high-resolution Cartesian grids. Ji et al. [2006, 2008, 2010] have developed a hybrid Cut Cell/AMR method for elliptic equation with variable coefficient and embedded boundaries. They have used marker points to track non-smooth boundaries with a cubic splin. Also Adaptive Mesh Refinement is applied on cut cells to increase the solution accuracy and reduce the occurrences of degenerated partial volumes. Similar approach had been already implemented by Aftosmis et al. [1997, 1999] for modelling the aerodynamic flows around complex geometries.

The general procedure for adapting the Cartesian Cut Cell Method to geological structures will be explained in next section.

3.2 General Workflow for Reshaping Ill Cells

The main pre-processing procedure at each step of history matching process is to generate a grid conforming to the reservoir boundaries. In SUQIB code "***IllCells***" is a class in which *Cartesian Cut Cell Method* has been implemented and it is the program responsible for the pre-processing stage. General algorithm for reshaping ill cells is explained based on the methods of "***IllCells***" class. "***IllCells***" class gets pure Cartesian grid as the inputs and returns ensemble of new conformed cells.

3.2.1 The Interacting Data Structures

"***IllCells***" class interacts with three main data structures: the grid, the interfaces and the reservoir boundaries.

3.2.1.1 The Grid

At all steps of history matching process, grid is initially structured such that the number of (rectangular) cells in **X** and **Y** directions and cells spacing in both directions remains constant. Grid divisions in both directions are uniform for all cells. It is presumed that ratio of axial to vertical extensions for each cell is around ten which accords to average cell aspect ratio in commercial reservoir simulators. When grid is initialized, each cell is stored in terms of an array containing X and Y coordinates of 4 corner points. Sequence of cells is numbered staring from lower most left cell, running right till the end of row and then continuing from most left cell in upper row. Also for each cell, directional indices (***i,j***) are set to determine directional numbering in **X** and **Y** directions.

3.2.1.2 The Interfaces

In two-dimensional sense, each interface is a segment which is shared by borders of two adjacent cells. Thus each interface is stored in terms of two pairs: one pair of starting and end points of the segment and another pair of indices of two interconnecting cells. Horizontal and vertical interfaces are stored in two different data structures named as ***"HInterfaces"*** and ***"VInterfaces"*** classes respectively. When grid is initialized with **nX** and **nY** divisions in **X** and **Y** directions, constructors of ***"HInterfaces"*** and

"VInterfaces" classes receive cells specification from the grid and assign (**nX*** (**nY+1)**) and ((**nX+1)*nY)** interfaces to each class respectively. A pointer to each interface is stored in the array of connections for both cells which share this interface. So after initialization each cell does share two horizontal and two vertical interfaces with the neighbour cells.

3.2.1.3 The Reservoir Boundaries

In two-dimensional sense, a reservoir boundary can be represented as smooth open curves, unless for pinchouts where the boundaries of this structure create a closed curve. Two general types of reservoir boundaries can be distinguished in terms of their effect on the reservoir compartmentalisation:

1) *Nearly Horizontal Boundaries*: which are recognised with the abrupt variation of media (rock and fluid) properties in vertical direction, thus they truncate the reservoir into compartments mainly extended in horizontal direction. The boundaries of reservoir stratigraphic layers and pinchouts belong to this group of boundaries. As cells in reservoir models are principally elongated in horizontal direction, the horizontal dimensions are shrunk noticeably within the visual grid representation, as a result nearly horizontal boundaries might be depicted sharply dipped and seem considerably deviated from horizontal trend.

2) *Nearly Vertical Boundaries*: which constitute reservoir compartments separated from one another in horizontal direction. Faults are best instances of this type through which sharp changes of rock properties may or may not appear.

Trend of boundary curve can be given as an array of points along with an equation to interpolate the boundary trend between these points. Although in SUQIB code different classes were implemented for faults, boundaries of reservoir layer and pinchouts, but they are all inherited from the same base class ***"GeoStruct"*** and benefit from similar methods for determining position of arbitrary points with respect to them.

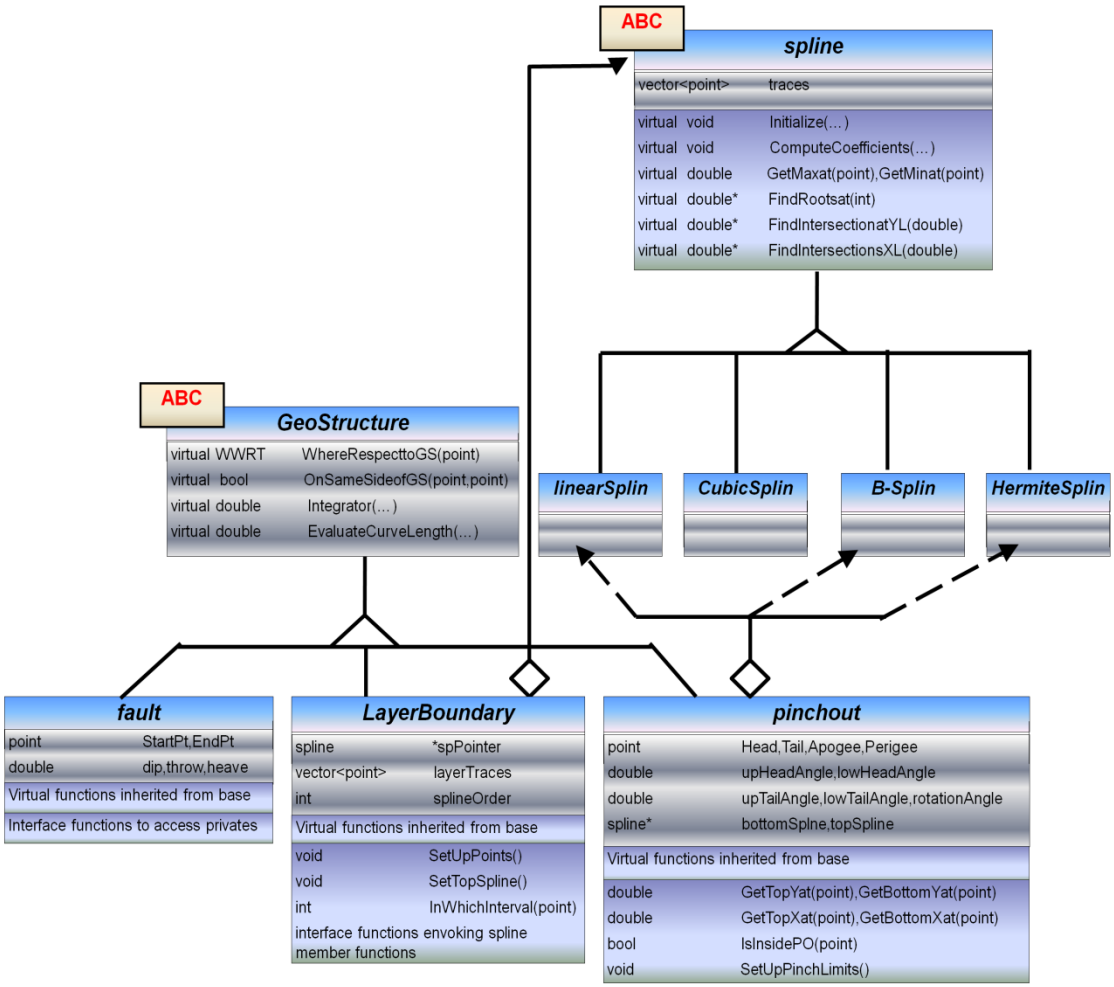

Figure 3.3: UML flowchart for "***GeoStruct***" class and its derived classes (ABC stands for abstracts only classes which no object can be instantiated from their base class.)

3.2.2 Finding Cells Defected by Imposition of Reservoir Boundaries

In a new step of history matching process, one has to update local cut cell information according to newly imposed reservoir boundary on stationary Cartesian background. To achieve this goal, "***IllCells***" class uses the information in 3 main involved data structures to answer these questions about each cell:

1) *Is boundary cutting through this cell?*

2) *If so, how cell is split on two sides of boundary?*

The main information which provides the answers to first question are intersection points of interfaces. ***"InitializeDefectedMap"*** is a method employed by "***IllCells***" class to intersect horizontal and vertical interfaces versus reservoir boundaries. Indices of

both cells which share the same intersected interface is stored in an array which collects the ill cells (defected cells).

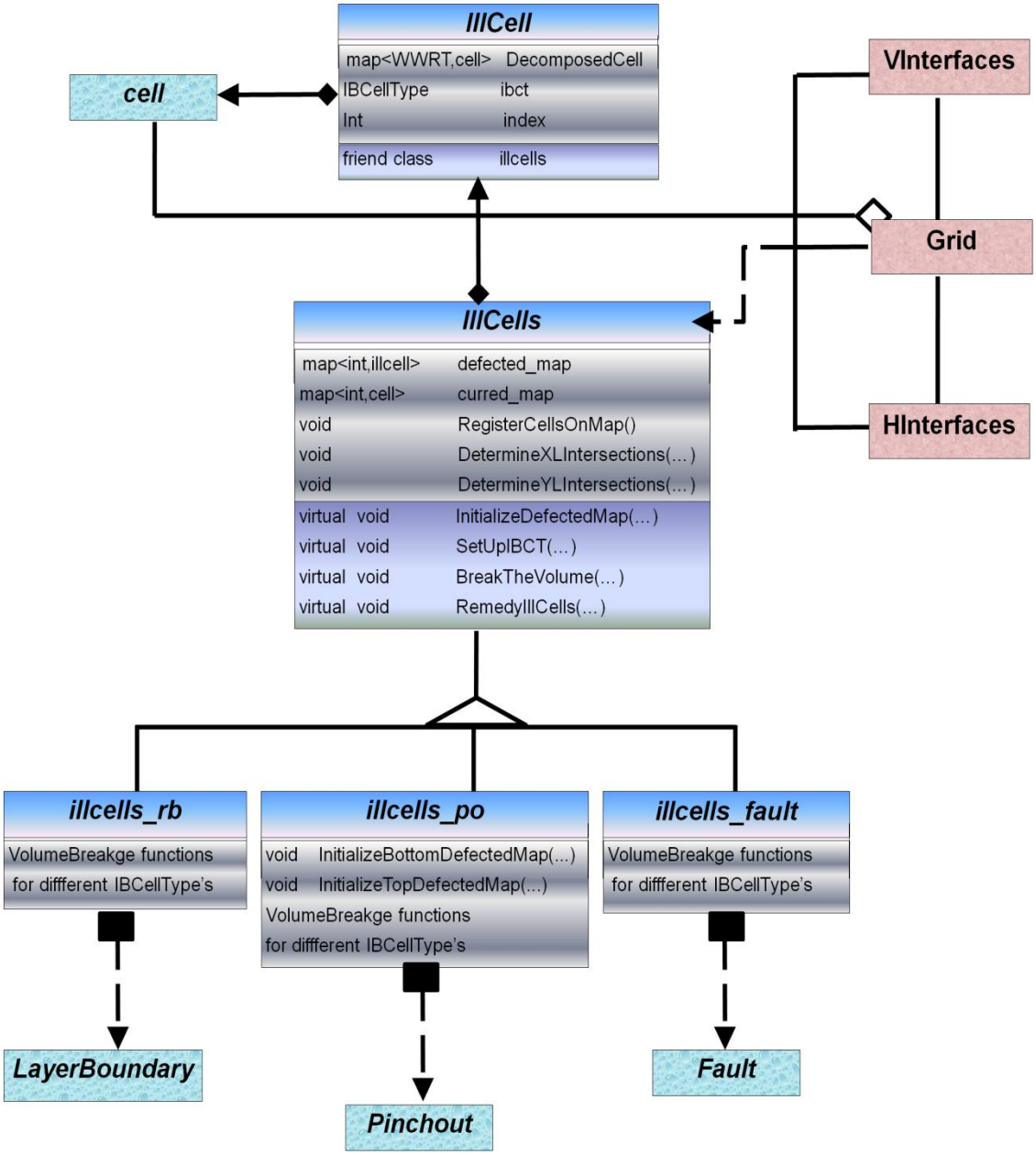

Figure 3.4: UML flowchart for "***Illcells***" class and its derived classes

3.2.3 Determining the Relative Cut Cell/Boundary Configuration

To answer the second question, each defected cell is assigned a flag reflecting the relative position of boundary with respect to cell interfaces. For example when

boundary is entering the cell from left interface and exiting from upper interface, a ***"LtoT"*** flag is assigned to this cell. Table 3.1 shows sketches for different possible cell/boundary geometrical configuration and corresponding flags. ***"SetUpIBCType"*** is the name of the method implemented in ***"Illcells"*** to give each ill cell relevant flag based on the intersection points of cell interfaces.

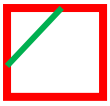	***LtoT***		***BtoT***		***TT***	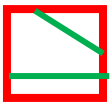	***TLtoRR***
	BtoR	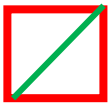	***LLtoRR***	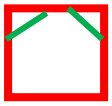	***LtoTtoR***	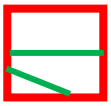	***LLtoBR***
	TtoR	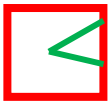	***RR***		***LtoBtoR***	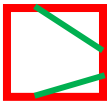	***BTtoRR***
	LtoB	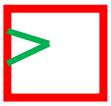	***LL***	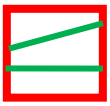	***LLRR***	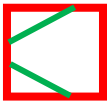	***LLtoBT***
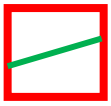	***LtoR***	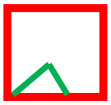	***BB***	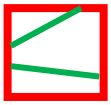	***LLtoTR***	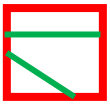	***LLtoBR***

Table 3.1: IB-cell flags assigned for possible boundary-cell geometrical configurations

3.2.4 Splitting the Cells Volume

Each of ill cells will be decomposed into sub-cells which lie completely on one side of boundary only. ***"BreakTheVolume"*** is the method invoked by "***IllCells"*** class to decompose ill cells. Each sub-cell is assigned a flag (named sub-cell/boundary flag) determining position of sub-cell with respect to boundary. Based on the type of reservoir boundaries, three main categories are distinguished in terms of splitting the ill cells. In figures 3.5, 3.6, 3.7 typical sub-cells remaining after cell decomposition for each category has been sketched:

1) For boundaries mapped as nearly vertical open curves:

Cells truncated by trend of fault structures are split into two sub-cells with ***"Left"*** and ***"Right"*** sub-cell/boundary flags respectively.

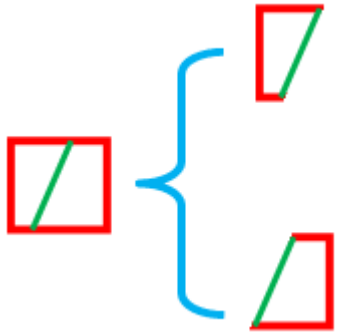

Figure 3.5: Cells cut through by a nearly vertical boundary

2) For boundaries mapped as nearly horizontal open curves

Cells truncated by boundaries of reservoir layers are split into two sub-cells with ***"Above"*** and ***"Below"*** sub-cell/boundary flags respectively.

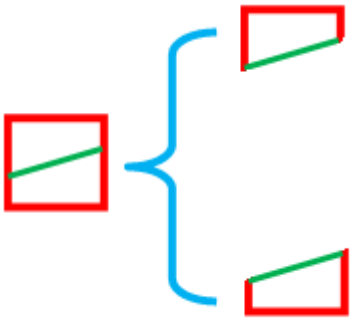

Figure 3.6: Cells cut through by a nearly horizontal boundary with open curve

3) For boundaries mapped as nearly horizontal closed curves

Cells truncated by only one of branches (upper or lower) of closed curve representing pinchout boundaries, are treated in a similar way as cells in category 2. But the others are decomposed into three sub-cells with ***"Above", "Inside"*** and ***"Below"*** sub-cell/boundary flags respectively.

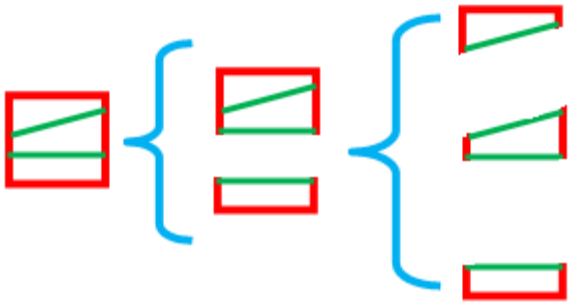

Figure 3.7: Cells cut through by a nearly horizontal boundary with closed curves

Intersection points of cells interfaces and the local geometry of reservoir boundaries are the information used to determine the corner points of sub-cells and recalculating their corresponding volumes. Splitting an ill cell into two sub-cells can be algorithmically expressed as following:

a) Order corner points of ill cell anti-clockwisely starting from lowest most left point.

b) Consider two sub-cells, name them ***"Left"*** and ***"Right"*** for nearly vertical boundaries and ***"Below"*** and ***"Above"*** for nearly horizontal boundaries.

c) Loop over array of corner points of ill cell:

   1) Store n^{th} element of corner points array in ***"Left"*** or ***"Below"*** sub-cell.

   2) Before incrementing index of corner points array, check if any of intersection points lies on the interface passing through current corner point and the next one?

   3) Increment array index by one. If answer of step 2) was correct, assign first intersection point to both sub-cells. Then go to step 4), otherwise repeat step 1) until condition in step 2) is fulfilled.

   4) Store current element of corner points array in ***"Right"*** or ***"Above"*** sub-cell.

5) Check if another intersection point lies on the interface passing through current corner point and the next one.

6) Increment array index by one. If answer of step 5) was correct, assign second intersection point to both sub-cells. Then go to step 7), otherwise repeat step 4) until condition in step 5) is met.

7) Store remaining corner points in ***"Left"*** or ***"Below"*** sub-cell.

d) Use triangulation for dividing sub-cells into triangles and calculate their volume.

Similar procedure is utilised to split ill cells into three sub-cells. Except that algorithm described above is applied in two stages. First stage is the splitting the ill cell respect to lower branch of boundary into "***Below"*** and ***"Above"*** sub-cells and at second stage ***"Above"*** sub-cell is decomposed along the upper branch of boundary to create sub-cells flagged as ***"Inside"*** and ***"Above".***

3.2.5 Creating New Cells

"RemedyIllCells" is the method employed by "***IllCells"*** class to create reshaped cells following reservoir boundaries. Subject to local orientation of boundary, ***"RemedyIllCells"*** treats ill cells in two different ways:

1) For an ill cell whose at least one of its vertical and one of its horizontal interfaces are intersected, there exist two ill cells in their immediate proximity where one of directional indices (***i*** or ***j***) are incremented or decremented by one. Among these two ill cells, one mainly lying on the other side of boundary is picked and sub-cells emerging from two neighbour ill cells with the same sub-cell/boundary flags are to be integrated with each other. Each reshaped cell will inherit the directional indices from the ill cell giving its larger sub-cell to the reshaped cell.

2) For an ill cell whose just horizontal interfaces or vertical interfaces are intersected, cells in its vicinity with the same directional index in the direction normal to intersected interfaces (***j*** for horizontal interfaces and ***i*** for

vertical interfaces) are not ill. Larger sub-cell of ill cell is retained with the same directional indices as initial ill cell and smaller one is merged into the neighbour cell on the same side of boundary.

To fuse two sub-cells or a sub-cell and a cell into a unified cell, following procedure is applied (throughout the procedure, we use the term “element” to mention any member of corner points array of any cell, also term “summation cell” means the final cell created after joining two or more sub-cell together, term “breakage” refers to as any point along the common face between neighbour sub-cells at which the slope changes, by “match”, we mean the existence of any mutual element of corner points arrays of two sub-cells):

1) Arrange corner points of both sub-cells in trigonometric direction.
2) Loop over corner points of sub-cell 1.
    a. For each element, loop over corner points of the sub-cell 2.
    b. Compare that element with corner points of sub-cell 2 one by one.
    c. If found any matches, store mutual point in an array called common face and break inner loop.
    d. If didn’t find any matches, store the point in the corner points array of summation cell.
3) Loop over corner points of sub-cell 2.
    a. Compare each element with the points of common face. If it didn’t match any of them, store it in the corner points array of summation cell.
4) Assess if there is any breakage in the boundary at one of the points of common face.
    a. Loop over corner points of sub-cell 1.
        i. Loop over corner points of sub-cell 2.

1. If current corner points of sub-cell 1 and sub-cell 2 are not on the common face:

    a. Check if both of corner points in trigonometric order are after or before first point of common face.

    b. If the answer to above question is yes, Calculate slope of lines passing through each of current corner points and first point of common face.

    c. If calculated slopes are not equal, add first point of common face to the corner points array of summation cell.

    d. Repeat steps a. to c. for the second point of common face.

5) Rearrange corner points of summation cell in anticlockwise order.

Figure 3.8 demonstrates an example of merging two sub-cells when the boundary is discontinuous at one of their common corner points. Unlike most works on Cartesian Cut Cell method (Popinet et al., 2003, McCorquodale et al., 2001, Ji et al., 2008), the geometric fidelity of reshaped cells to very irregular boundaries is assured by avoiding the linear interpolation between the first and last intersection point. Instead the geometry of boundary is tracked locally to ascertain conservative cell reshaping.

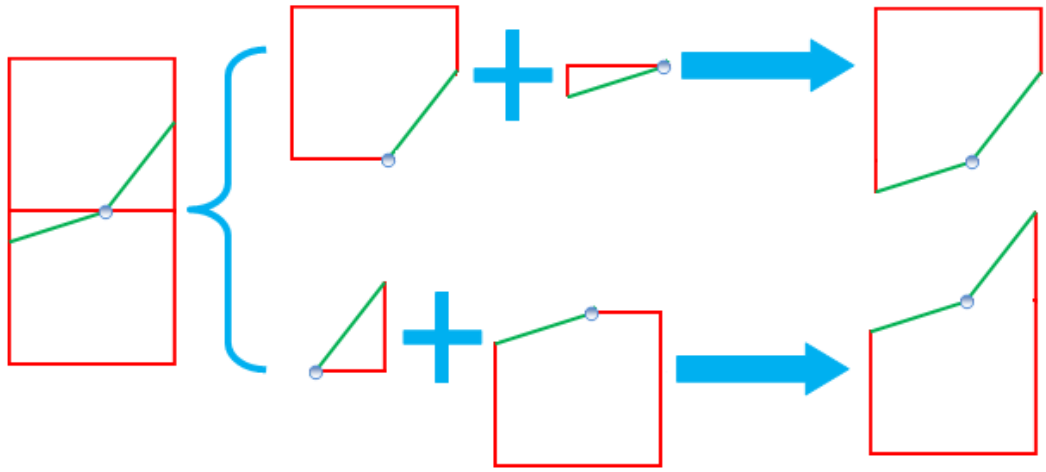

Figure 3.8: Preservation of boundary breakage after cell reshaping

Figures 3.9, 3.10 and 3.11 demonstrate schematically how new cells are created after applying "***RemedyIllCells***" method for ill cells truncated by nearly horizontal open boundaries, nearly vertical boundaries and nearly horizontal closed boundaries.

Two cases shown in the left side of figure 3.9 show a horizontal interface shared by two adjacent ill cells is intersected by the boundary. Therefore ***"Above"*** sub-cells from two ill cells are blended form a cell replacing ill cell in the upper row. Similarly reshaped cell in the lower row is obtained from merging "***Below***" sub-cells together. For other cases horizontal interfaces of an ill cell are not intersected, thus smaller sub-cell is merged into an adjacent perfect cell in the same column located in same side of boundary as the smaller sub-cell. For example if smaller sub-cell is above the boundary, it will be merged into the cell from upper row, accordingly larger sub-cell ("***Below***" sub-cell) will substitute the initial ill cell in the grid framework.

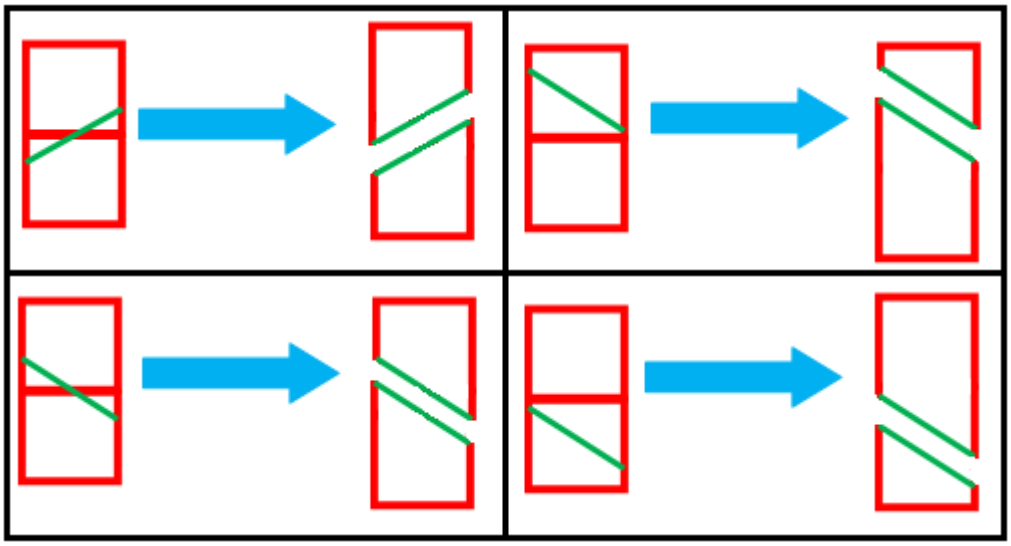

Figure 3.9: Remedied cells emerging after cutting the cells by a nearly horizontal open boundary

In first two cases of figure 3.10, two adjacent ill cells are cut through by the boundary at one of their vertical interfaces. Therefore both reshaped cells are obtained from blending two connected sub-cells lying on the same side of boundary. In two last cases of this figure 3.vertical interfaces of an ill cell are not intersected, thus depending on the sub-cell/boundary flag of smaller sub-cell, it will be merged into a perfect cell on the left or right side of ill cell. Treatment of ill cells intersected with two branches of a closed nearly horizontal boundary (shown in figure 3.11) is a kind of generalisation of treatment of ill cells cut by an open nearly horizontal boundary. Cell on the side of intersected horizontal interface (either at upper or lower column or both) exchanges its smaller sub-cell with the sub-cell of target cell located in the same geological layer (the same sub-cell/boundary flag). While the Cell on the side of non-intersected horizontal interface (either at upper or lower column or both) receives the adjacent sub-cell of target cell which is in trapezoidal shape. Depending on IB-cell flag, any combination of these two cases might occur. In all cases, the middle sub-cell of ill cell (with sub-cell/boundary flag "***Inside***") is retained and replaces the initial target cell.

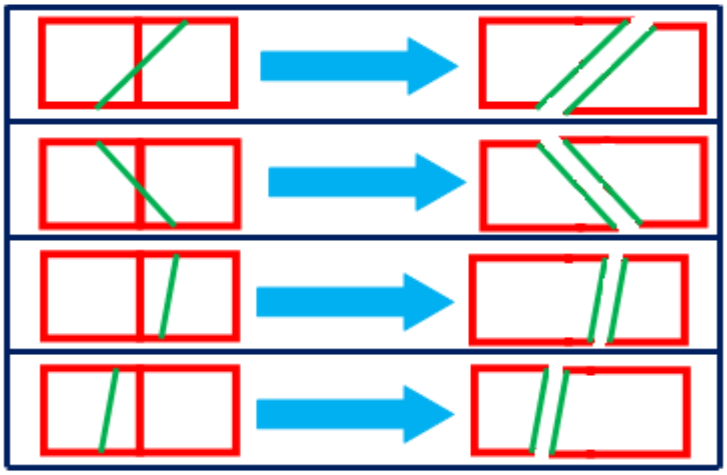

Figure 3.10: Remedied cells emerging after cutting the cells by a nearly vertical boundary

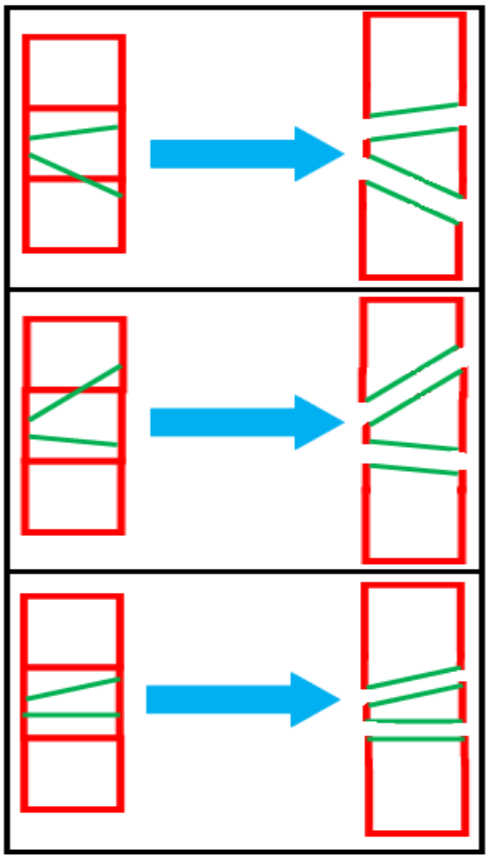

Figure 3.11: Remedied cells emerging from cells cut by a nearly horizontal closed boundary

To pictorially demonstrate the effects and the implications of Cartesian Cut Cell method for most complex cases occurring at the edges of a nearly horizontal closed boundary,

we investigate two cases with IB-cell flags of ***BB*** and ***RR***. The effects on neighbouring cells would be exhibited within the final reshaped grid shown in figures 3.12 and 3.13.

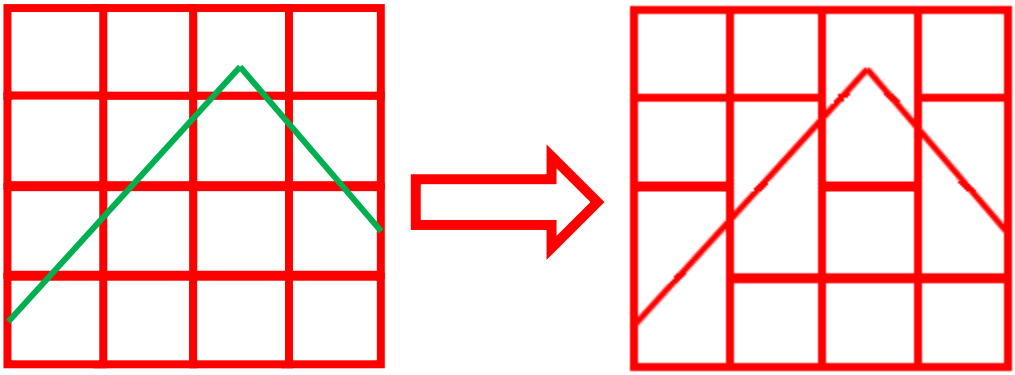

Figure 3.12: Reshaped cells by Cartesian Cut Cell method for IB-cell flag of ***BB***, trend of a nearly horizontal boundary is shown with green colour imposed on red gridlines.

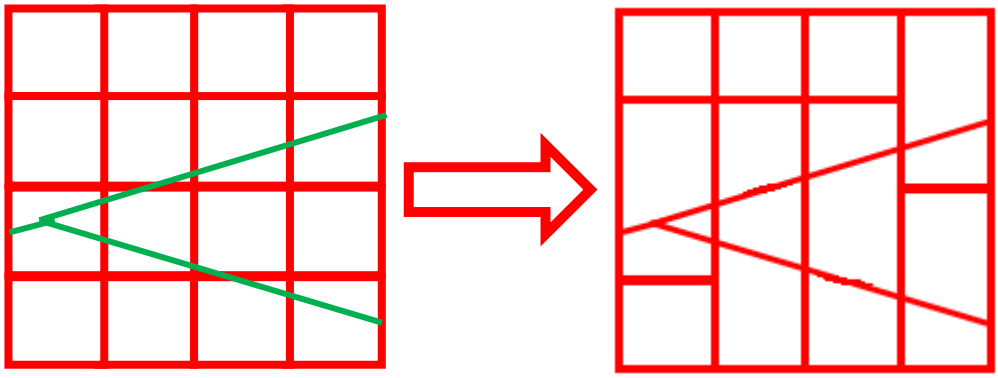

Figure 3.13: Reshaped cells by Cartesian Cut Cell method for IB-cell flag of ***RR***, trend of a nearly horizontal boundary is shown with green colour imposed on red gridlines.

3.3 Treating Multiple Intersecting Boundaries

Several boundaries might coexist in a reservoir model. As long as these boundaries are not intersected, general algorithm explained in section 2 is followed to create a reshaped grid framework honouring the geometry of reservoir boundaries. However special treatments are required to handle models with multiple intersecting boundaries. This happens when a nearly vertical boundary like fault is present along with nearly horizontal boundaries like pinchouts or reservoir layers. In such models first all nearly

horizontal boundaries are imposed into the Cartesian grid and then grid is truncated by the trend of the fault structure. Those cells which remained unchanged after imposition of nearly horizontal boundaries are mannered according to the algorithm illustrated for cutting cells with nearly vertical boundaries. As explained in section 3.2, cells cut by the fault are reshaped using neighbour cells located in the same row. But due to local geometry of nearly horizontal boundaries, connections of cells conforming to these boundaries need to be redefined, which might result in connections between cells from two different rows. Cells on both sides of such connections are called *non-matching cells*. With the values expected for the slope of nearly horizontal boundaries and the aspect ratio of the cell, maximum difference between indices of non-matching cells in vertical direction is one. To distinguish between cells reshaped after imposition of nearly horizontal boundaries, each of them is given a flag called *reshaped cell type*. This flag determines:

1) *Either this cell is a non-merged portion of an ill cell or it has created from merging portions from two neighbour cells?*

2) *Where is the position of boundary relative to the cell which has been aligned with that boundary? Either is it below the cell or above the cell?*

Figure 3.14 shows typical sketches for *non-matching cells* and flags assigned to them according to their type. Collection of three cells (two non-matching cells along with the third non-merged virginal cell connected to both of them) is called *"set of cells with boundary at the bottom"* (***SCBB***) whenever the lower borders of non-matching cells coincides with a reservoir boundary. In contrary *"set of cells with boundary at the top"* (***SCBT***) refers to as a collection of three cells overlapping a reservoir boundary at upper boundary of two non-matching cells. Moreover figure 3.14 represents the different types of reshaped cells with blue colour. ***"bNMF"*** and ***"bMF"*** are the types for cells above the boundary, first one for non-merged cells and second one for merged cells. Besides ***"tNMF"*** and ***"tMF"*** are the types for cells below the boundary, first one for non-merged cells and second one for merged cells.

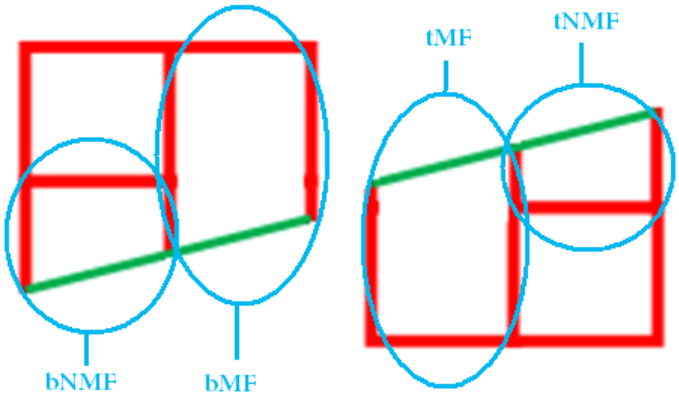

Figure 3.14: Different types of non-matching cells, Left: ***"SCBB"*** and Right: ***"SCBT"***

Modified reshaping algorithm for cutting cells with faults has been implemented in class ***"Illcells_fault"*** which is a derived class from ***"Illcells"***. It does have homonymous methods to be applied in a stepwise manner to form boundary adjusted cells.

3.3.1 Determining the Relative Fault-Cell Geometrical Configuration

Cells whose already been reshaped in order to conform to the boundaries of reservoir layers or pinchouts, have at least one of their horizontal interfaces replaced with an oblique segment from nearly horizontal boundaries. Also for merged non-matching cells (e.g. those flagged as ***"bMF"*** or ***"tMF"*** in figure 3.14) both or one of their vertical interfaces is extended by merging with interface in the same line belonging to cells from upper or lower row. Therefor in order to obtain local orientation of a nearly vertical boundary cutting through the cell, one has to consider following points:

a) Intersection points of the already imposed boundaries with faults are determined. Local geometry of the boundaries at each reshaped cell and the type of that cell determine intersections at horizontal or nearly horizontal interfaces.

b) Intersection points of vertical interfaces with fault trend are calculated. Left and right interfaces of reshaped cells located in the same row are serached for possible intersection points. Moreover for merged reshaped cells, extensions of their vertical interfaces to upper or lower rows should be assessed for possible intersection points.

Table 3.2 demonstrates typical sketches of reshaped cells truncated by faults and relevant cell-boundary flag for each case. In table 3.2, red dotted horizontal line shows a horizontal interface shared by two cells which at least one of them is cut by a nearly horizontal boundary. Thus after reshaping two cells and fitting their corner points to the boundary this horizontal interface disappears and a segment of boundary shared by both reshaped cells (coloured with green) turns out to be upper or lower border of reshaped cells. Blue or yellow segment cutting through the reshaped cells represents trend of a fault. Yellow segments for fault trend are observed for merged reshaped cells when the extended part of a vertical interface into upper or lower row is intersected.

Reshaped cell type / *Cell-boundary flag*	**tMF**	**bNMF**	**bMF**	**tNMF**
BtoR	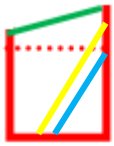	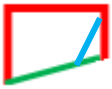	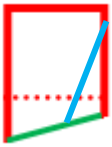	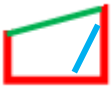
LtoB	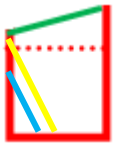	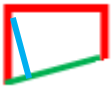	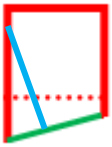	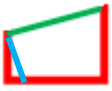
LtoT	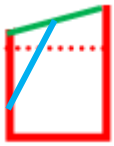	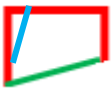	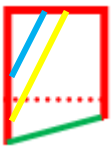	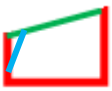
TtoR	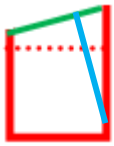	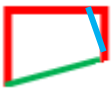	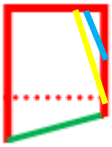	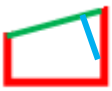
BtoT	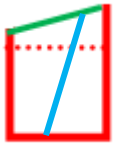		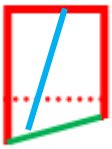	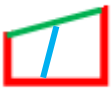

Table 3.2: Cell-boundary flags assigned to cells reshaped by boundaries of reservoir layers

3.3.2 Splitting the Cells Volume

To decompose degenerate cells with respect to trend of faults crossing them, an algorithm similar to that described in section 2.3 (for reshaping cells cut by non-intersecting boundaries) is employed. Flags assigned to each ill cell (both reshaped cell type and cell/boundary configuration type) determine points at which fault enters or exits the ill cell. These two points along with the corner points of degenerate cell are passed to ***"BreakTheVolume"*** method.

3.3.3 Creating New Cells

For non-intersecting faults, adjacent cut cells located in the same row exchange their smaller portions with each other. When fault cuts cells fitted already to the nearly horizontal boundaries, two different case scenarios are expected:

1) Cut cell and an adjacent cell (either cut or uncut but in the same side of smaller sub-cell of cut cell) have the same reshaped cell type. Therefore cells are reshaped similar to case of non-intersecting cells. Figure 3.15 demonstrates an example of matching reshaped cells adjusted to a nearly horizontal boundary. Two cells in the lower row are both flagged as ***"tMF"*** and cells in the upper row are flagged as ***"bNMF"***. Thus exchanging the sub-cells takes place between cells from the same row.

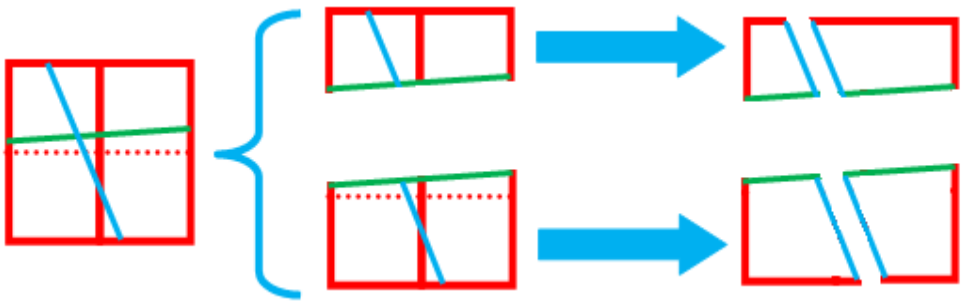

Figure 3.15: Matching reshaped cells cut with fault

2) Cut cell and an adjacent cell (either cut or uncut but in the same side of smaller sub-cell of cut cell) have different reshaped cell types. Merged

reshaped cell has been extended into the lower or upper row. Thereafter in addition to a non-reshaped cell located in the same row, each merged non-matching cell will be connected to a non-merged cell from upper or lower row. For such a set of two non-matching cells and a virginal cell, there exist four cutting states versus fault trend.

a) Both non-matching cells are cut by fault trend but non-reshaped cell remains uncut. The smaller sub-cell of non-merged non-matching cell is amalgamated with the larger sub-cell of merged non-matching cell. Resultant is a cell with two tilted borders coinciding boundary of a reservoir layer and the fault which supplants merged non-matching cell. The interface shared by two non-merged cells is extended to truncate smaller sub-cell of merged cell. For a ***"SCBB"*** (shown in figure 3.16) upper and lower portions of this sub-cell are merged respectively into the virginal cell and the larger sub-cell of non-merged non-matching cell. But for a "***SCBT"*** (shown in figure 3.17) upper and lower portions are absorbed by larger sub-cell of non-merged non-matching cell and the virginal cell respectively. Black dotted arrows show the direction of absorption of smaller sub-cells.

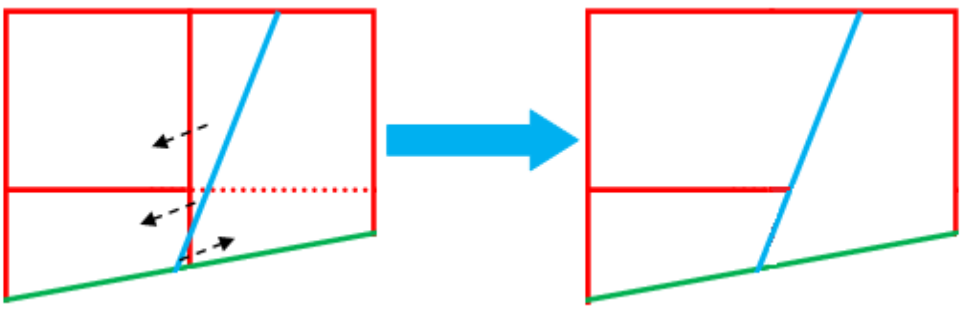

Figure 3.16: Cutting status a: ***SCBB*** (with ***"bNMF"*** & ***"bMF"*** flags)

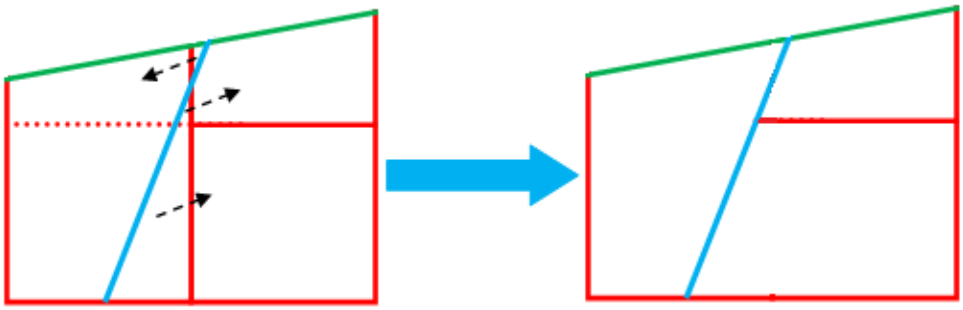

Figure 3.17: Cutting status a: ***SCBT*** (with ***"tNMF"*** & ***"tMF"*** flags)

b) All three cells get cut by the fault trend. It is likely that cell-boundary flag for the non-merged non-matching cell is **"*BtoT*"** and its larger sub-cell isn't in same side as larger sub-cell of merged non-matching cell. Thus it will be substituted by its larger sub-cell. Smaller sub-cells of non-reshaped cell and non-merged non-matching cell will be absorbed by larger sub-cell of merged non-matching cell. Finally larger sub-cell of non-reshaped cell is combined with smaller sub-cell of another non-matching cell to readjust their connection with fault trend.

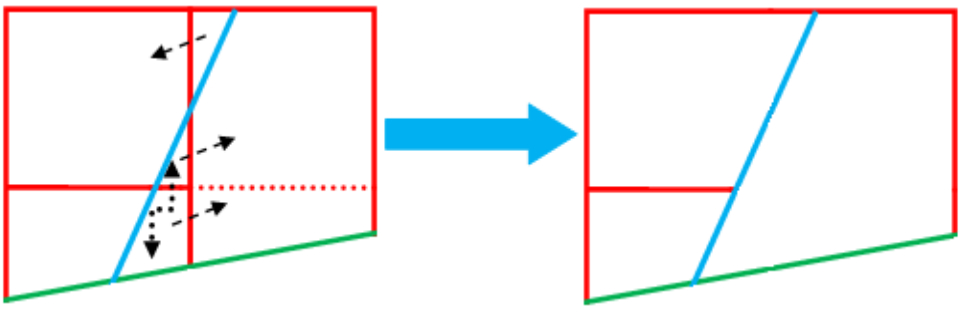

Figure 3.18: Cutting status b: ***SCBB*** (with ***"bNMF"*** and ***"bMF"*** flags)

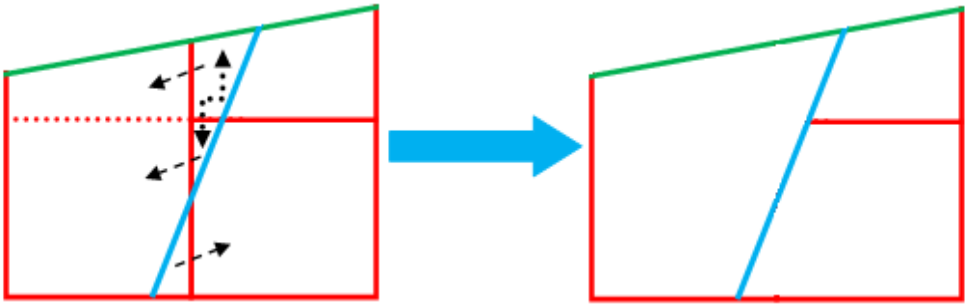

Figure 3.19: Cutting status b: ***SCBT*** (with ***"tNMF"*** and ***"tMF"*** flags)

c) Just merged non-matching cell is cut with fault trend. Thus if its smaller sub-cell is in the same side of fault as two other cells, it will be replaced with its larger sub-cell inheriting both directional indices. But the smaller sub-cell is divided into two portions by extension of interface interconnecting two uncut cells. For a ***"SCBB"*** (shown in figure 3.20) upper and lower portions are merged respectively into the virginal cell and the non-merged non-matching cell. While for a "***SCBT"*** (shown in figure 3.21) they are fused with the non-merged non-matching cell and the virginal cell respectively.

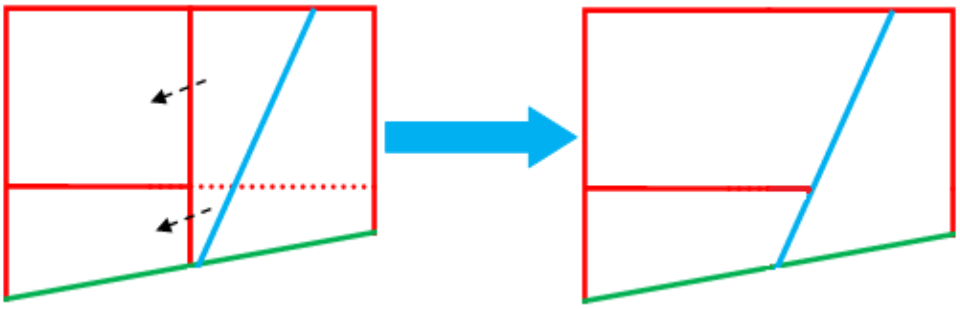

Figure 3.20: Cutting status c: ***SCBB*** (with ***"bNMF"*** and ***"bMF"*** flags)

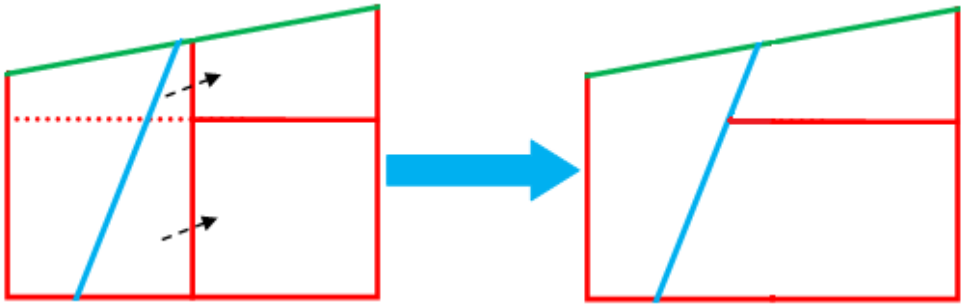

Figure 3.21: Cutting status c: ***SCBT*** (with ***"tNMF"*** and ***"tMF"*** flags)

d) The non-reshaped cell and the non-merged non-matching cell are cut with ***"BtoT"*** flag and the merged non-matching cell remains uncut. Among smaller sub-cells of two cut cells at least one of them is in the same side of fault as uncut cell. Thus uncut cell will absorb interconnected sub-cells from each cut cell. However one of absorbed sub-cells might be larger sub-cell of its parent cut cell, but to preserve cell convexity, direction of merging should be the same for both sub-cells. For a ***"SCBB"*** (shown in figure 3.22) or a ***"SCBT"*** (shown in figure 3.23) larger sub-cell of non-merged non-matching cell is interconnected with uncut cell, so it is merged to uncut cell. The virginal cell and non-merged non-matching cell are accordingly substituted with their retained smaller and larger sub-cells.

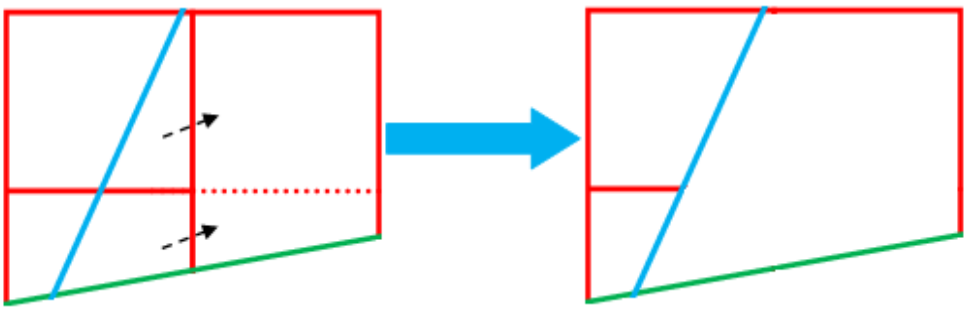

Figure 3.22: Cutting status d: ***SCBB*** (with ***"bNMF"*** & ***"bMF"*** flags)

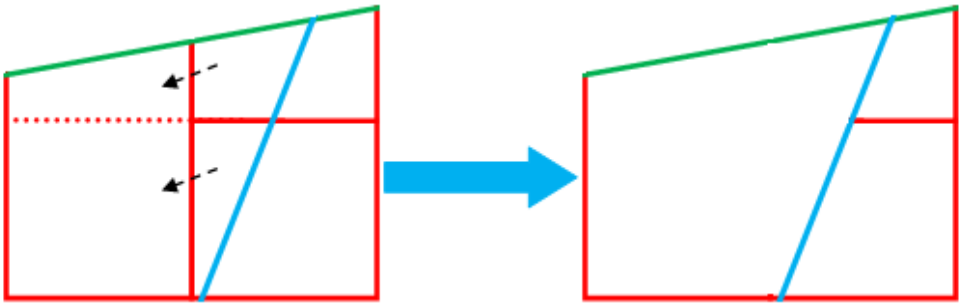

Figure 3.23: Cutting status d: ***SCBT*** (with ***"tNMF"*** & ***"tMF"*** flags)

3.4 Redefining Cell Connections

Readjusting borders of cells with reservoir boundaries causes some of horizontal or vertical interfaces no longer exist but they are replaced with tilted segments of the reservoir boundaries. Moreover conforming the cells to the multiple intersecting horizontal and vertical boundaries might result in connections between cells from different rows. Such connections (called "non-neighbour connections") will appear also when cells on the hanging wall of a fault are displaced upward or downward. Term "non-neighbour connection" signifies connection between cells which do not share any common interface in natural cells ordering based on their directional indices. It means for a cell with directional indices (***i,j***), there are four natural neighbour connections in Cartesian grid framework with four cells which only one of their directional indices differs from (***i,j***) by one. Thus natural neighbours of the cell are cells with directional indices (***i-1,j***) , (***i+1,j***) , (***i,j-1***) , (***i,j+1***) . Any other connection for this cell is regarded as "non-neighbour connection".

To clarify how non-neighbour connections are created, consider a small scale two-dimensional grid shown in figure 3.24 when a curved boundary of reservoir layers and a fault are embedded into the grid:

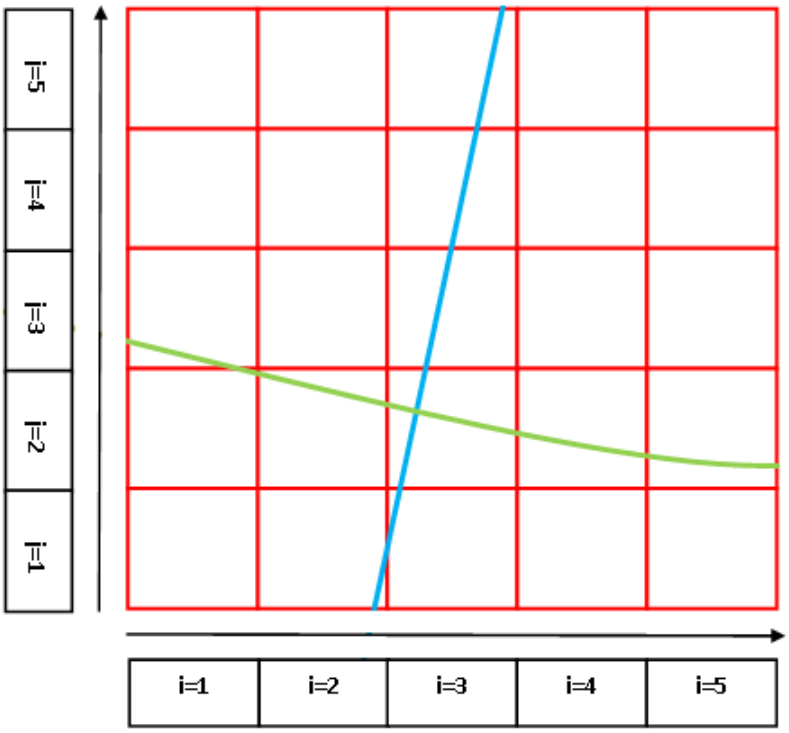

Figure 3.24: Nearly horizontal boundary (coloured green) and nearly vertical boundary (coloured blue) imposed on Cartesian grid background

Figure 3.25 demonstrates three non-neighbour connections have been created after reshaping the grid:

1. “Face 1”: between cells with indices (3,3) and (4,2).
2. “Face 2”: between cells with indices (2,3) and (3,4).
3. “Face 3”: between cells with indices (3,3) and (4,4).

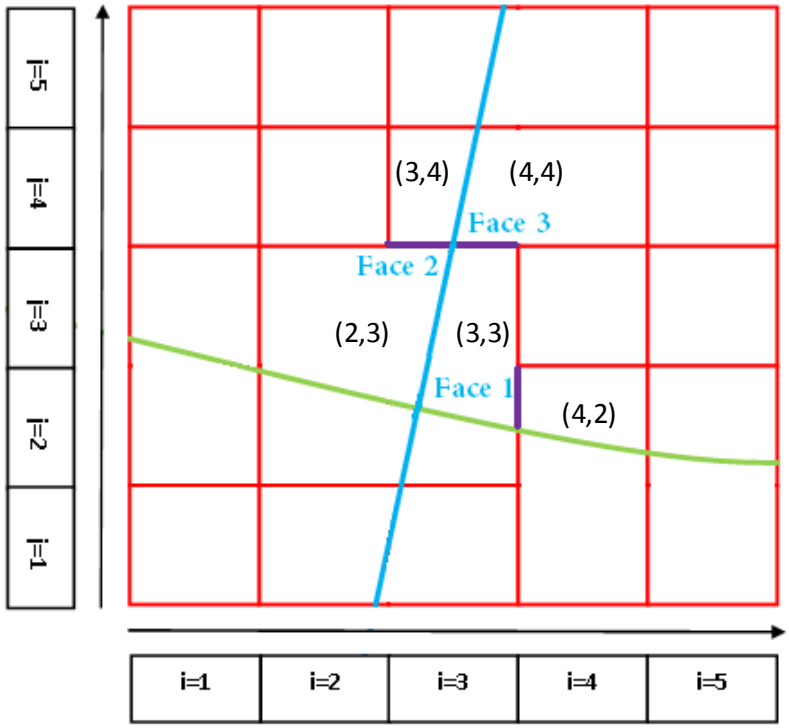

Figure 3.25: Grid reshaped to follow boundaries; Non-neighbour connection (coloured purple)

In figure 3.26 non-neighbour connections coinciding with fault plane have been shown. This kind of connections appears after applying fault throw on cells located in hanging wall of fault. For example cell with directional indices (2,3) is interconnected to cells with indices (4,4) and (4,5).

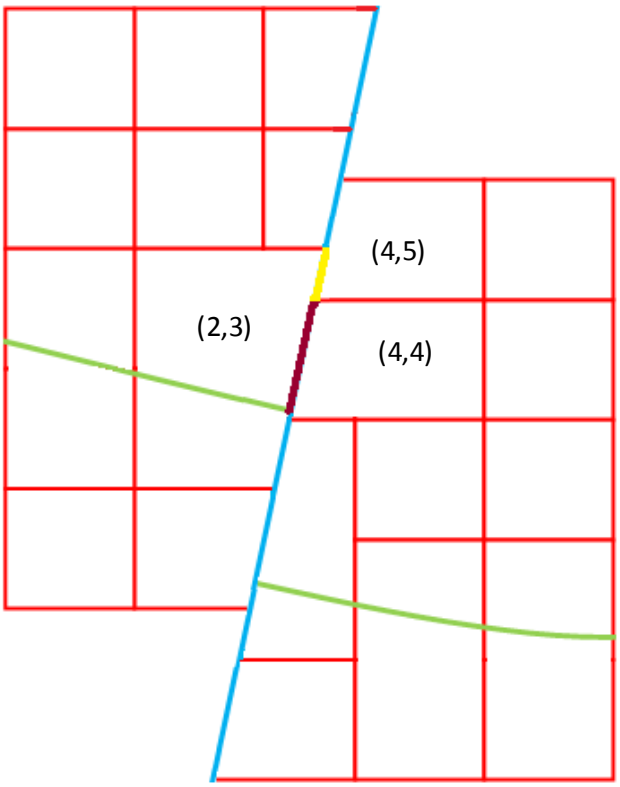

Figure 3.26: Non-neighbour connections due to upward displacement of cell on hanging wall of fault (coloured yellow and brown)

The redefined cell connections constitute a set of interfaces (e.g. tilted interfaces or non-neighbour connections) developed into a buffer layer of cells around the boundaries, this calls for multipoint methods of flux approximation. In chapter 4, we will investigate more in detail the special constraints which motivate for switching from two-point schemes to multipoint schemes for such interfaces.

A new data structure called ***"TInterfaces"*** is introduced to represent tilted interfaces between cells fitted to the reservoir boundaries. ***"FindNeighbours"*** is a method in ***"grid"*** class which modifies cells connections. Implemented procedure in this method is as followings:

1) For each cell, define two Boolean flags:

    a. ***"IsBoundaryInNeighbourhood"*** flag: It is true if and only if the cell or any of its natural neighbours have been reshaped.

b. ***"IsIncludedInIrregularMap"*** flag: It is true if and only if the value of ***"IsBoundaryInNeighbourhood"*** flag for the cell or any of its natural neighbours is true.

2) Connections of cells with false "***IsIncludedInIrregularMap"*** flag remain unchanged.

3) Loop over cells with true "***IsIncludedInIrregularMap"*** flag:

   a. Define a data structure called ***"CellVertices"***. Each element of this data structure should store a pair of a corner point (key value) and an array containing indices of the cells sharing that corner point (mapped value).

   b. Loop over corner points of each cell. If that corner point has not been already allocated to ***"CellVertices"***, insert a new element. Otherwise add the total index of the cell (***i+nX*j***) to the array of cells sharing that corner point for the already inserted element.

4) Loop again over cells with true "***IsIncludedInIrregularMap"*** flag:

   a. Define a data structure called ***"CellPossibleNeighbours"***. Each element of this data structure should store a pair of total index of a cell (key value) and an array containing indices of the cells sharing at least one common point with that cell (mapped value).

   b. Insert a new element in "***CellPossibleNeighbours"*** with the key value of total index of cell.

   c. Loop over corner points of each cell:

      i. For each corner point, find the element in the ***"CellVertices"*** data structure with the key value matching it. Add non-redundant cell indices stored in mapped value of that element to mapped value of newly inserted element in "***CellPossibleNeighbours".***

5) Rearrange elements of "***CellPossibleNeighbours"*** based on their key values in ascending order.

6) Loop over the elements stored in "***CellPossibleNeighbours".***

a. For the cell with the index equal to the key value of current element (called ***"cell1"***), loop over its corner points.

   i. Make a pair of current corner point and next point in trigonometric order. Initialize an interface called "***face1"*** with the composed pair as its starting and ending points.

   ii. Loop over the cells with indices stored in the mapped value of current element of "***CellPossibleNeighbours"*** (called "possible neighbour cells".

      1. Leave cells with indices less than the key value of current element. As they have been already assessed.

      2. For each cell with indices more than the key value of current element (called ***"cell2"***), loop over its corner points.

         a. Initialize an interface called "***face2"*** with a pair of current corner point and succeeding point in trigonometric order as its ending points.

         b. Initialize an interface called "***face3"***. Check if "***face1"*** and "***face2"*** are coinciding. If the answer is yes, assign "***face3"*** the starting and ending points of overlapping segment. Otherwise flag "***face3"*** as "**NULL".**

         c. If "***face3"*** has not been flagged as **"NULL":**

            i. Assign "***face3"*** a pair of indices of interconnected cells (***"cell1"*** and ***"cell2")***.

            ii. Compute its slope. Depending on the slope store it in the relevant data structure.

            iii. Return pointers to "***face3"*** to be set in interconnected cells.

iv. Initialize an interface called "***face4"*** and allocate it with the remaining segment of "***face1"*** which does not overlap "***face2".***

v. Break the internal loop over corner points of "***cell2"***

3. If "***face4"*** has been flagged as **"NULL"**, break the t the possible neighbour cells. Otherwise set "***face1"*** equal to "***face4"*** and go through internal loop over the corner points of the next possible neighbour cell of "***cell1".*** Repeat until "***face4"*** is given "**NULL"** flag.

b. Continue until all interfaces connecting corner points of "***cell1"*** are determined.

3.5 Application of Cartesian Cut Cell Method for a Complex Set of Intersecting Structures

In this section, we will demonstrate schematically the application of Cartesian Cut Cell method for building a partially modified grid over a reasonably realistic model of intersecting geological structures. It would be shown how the Cartesian Cut Cell method alters the computational grid in the vicinity of the geological structures. Assume that a vertical cross section of seismic picked reservoir boundaries (including reservoir top and base structures, a pinchout and two faults, shown in figure 3.27) has been given and it is desired to impose it on the stationary Cartesian grid in the background and truncate the intersected cells. The reservoir layers are assumed to be gently dipped (creating nearly horizontal boundaries). Although the sharp medium properties variation occurs across the layer or pinchout boundaries, but inside each layer, the petrophysical heterogeneity might still exist. Each layer is distinctive in terms of porosity-permeability relations or the probabilistic specifications of rock property distribution.

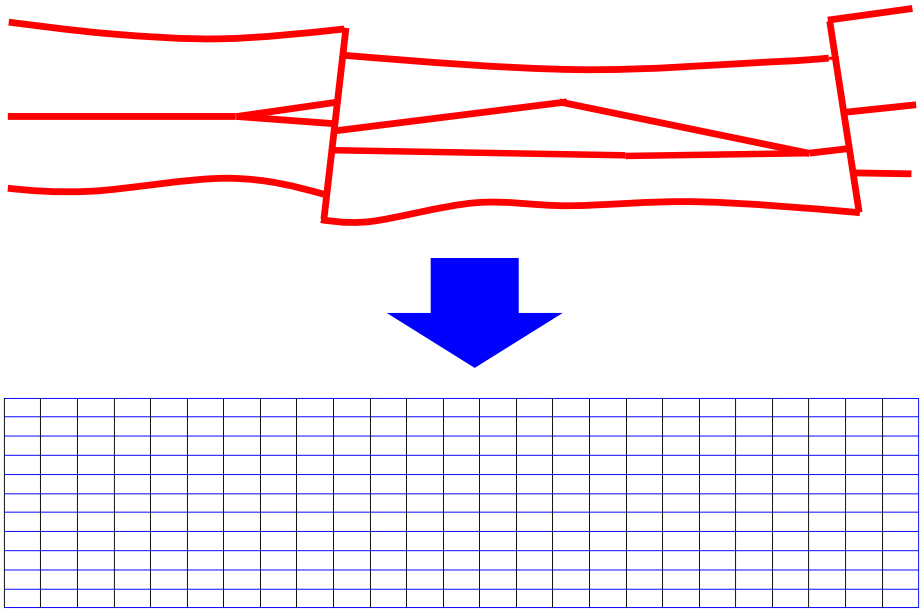

Figure 3.27: Superimposing a renewed geometry of geological structures (shown with red colour) on a pure stationary Cartesian grid in the background

In order to honour the reservoir inherent geology and compartmentalisation, cutting the affected cells out of Cartesian grid should be performed in a step-wise manner complying with the sequence of geological events that created structures. This means that Cartesian grid should be modified in the same time order as geological events and geological structures are overlaid on Cartesian grid according to following order:

1. Sedimentological structures: Sequence boundaries of reservoir layers starting from the most underneath one (oldest one) and moving upward until reaching to any structure created from erosion.

2. Erosional structures: The sequence boundaries of possible pinched out layers.

3. Possible Re-sedimentations: Sequence boundaries of layers deposited over an eroded or interrupted depositional layer.

4. Faulting: The planes of faults extending into previously deposited layers.

As faults are the latest structures to be laid over the grid, we need to return the sketch of geological structures to the state before vertical displacement of stratigraphic layers. In this way the horizontal continuity of reservoir layers before faulting is recovered.

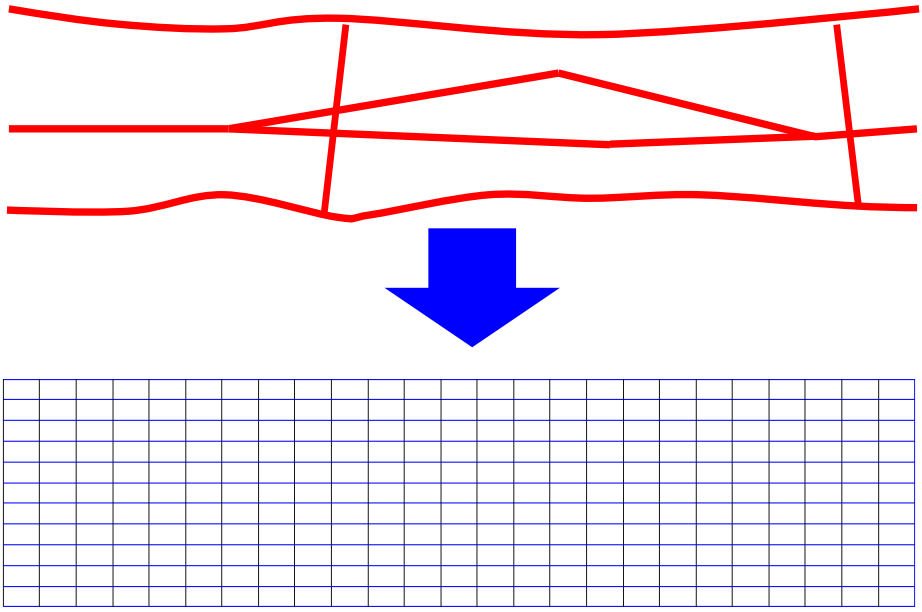

Figure 3.28: Superimposing a renewed geometry of geological structures returned to the state before faulting (shown with red colour) on a pure stationary Cartesian grid in the background

Figures 3.29 to 3.32 show how the grid is truncated through by the reservoir base structure, reservoir top structure, pinchout and zero offset faults respectively. Finally according to figure 3.33, all the corner points of cells inside the blocks over the fault planes are displaced vertically and horizontally over a distance of throw and heave of their corresponding fault. The final stage accommodates for the offset created by faults.

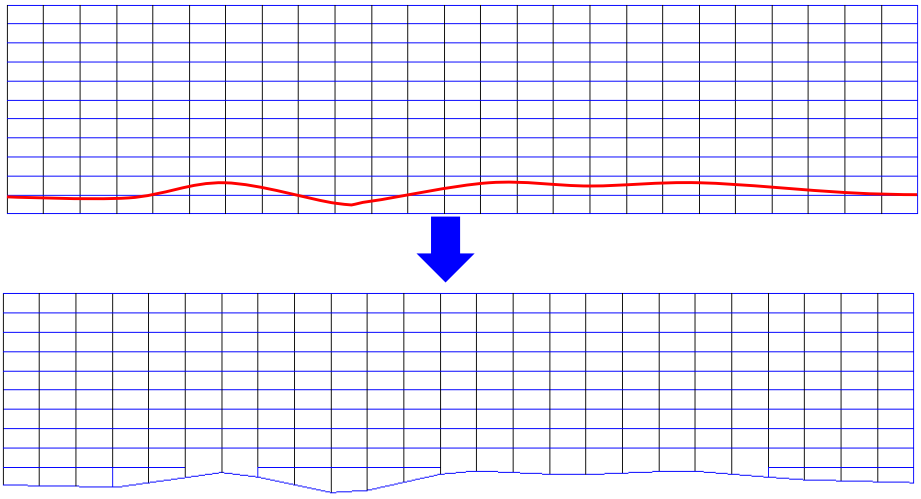

Figure 3.29: Cutting the reservoir bottom structure through the Cartesian grid

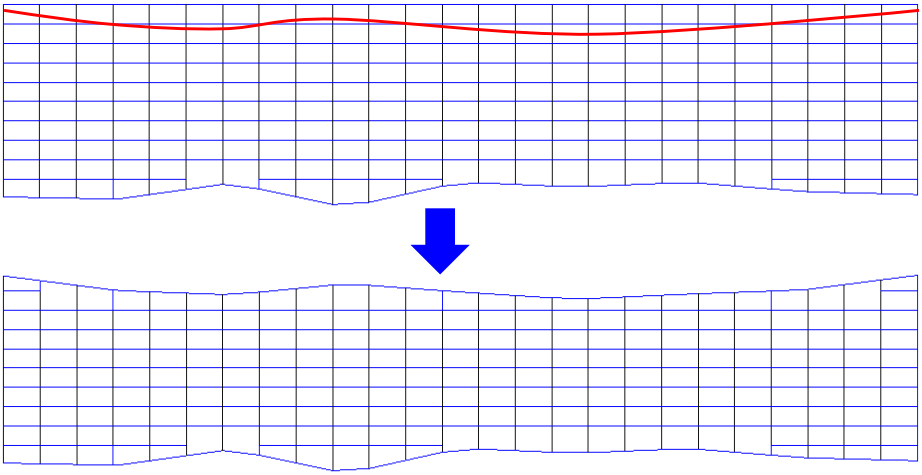

Figure 3.30: Cutting the reservoir top structure through the Cartesian grid

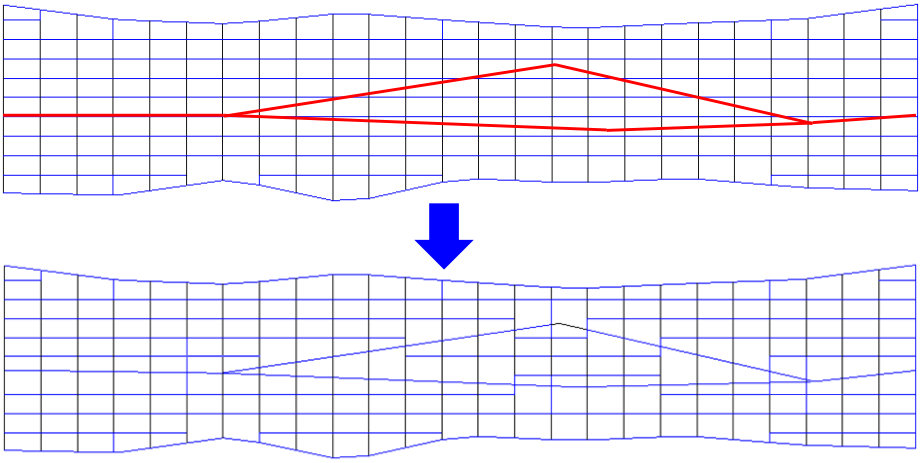

Figure 3.31: Cutting the pinchout through the Cartesian grid

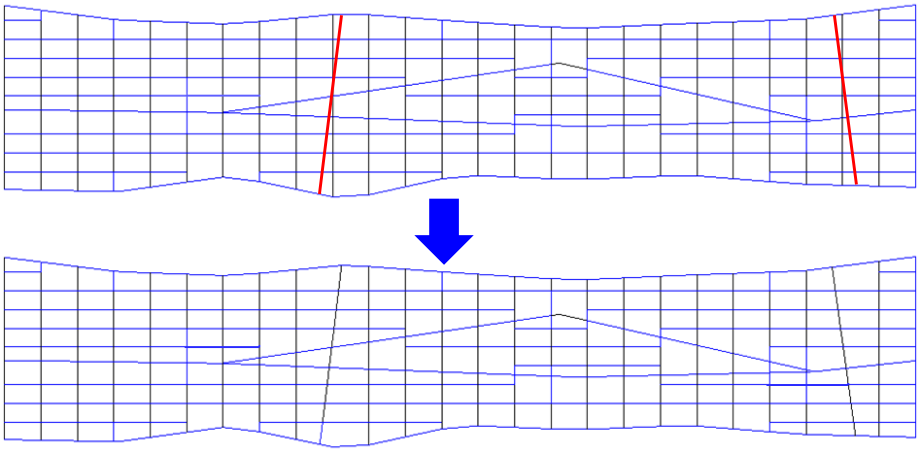

Figure 3.32: Cutting the zero-offset faults through the Cartesian grid

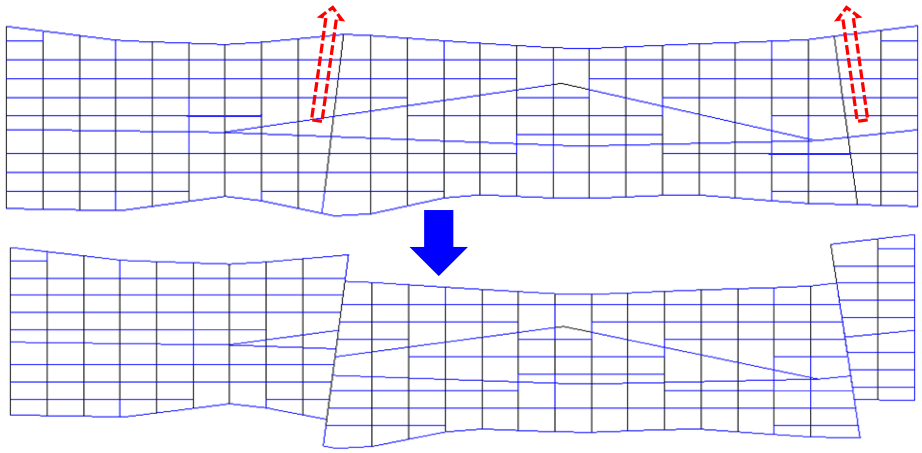

Figure 3.33: Applying the offset of faults on cells located over the fault's planes

The final grid is distinctive in contrast with standard discretisation approaches, as it avoids from stair-stepped geological structures produced by structured Cartesian gridding, while it is free of curved gridlines developed into the body of grid away from boundaries as it is the case in unstructured gridding.

3.6 Priorities of Cartesian Cut Cell Method over Corner Point Grid

This chapter introduced the application of Cartesian Cut Cell method for adaptation of 2D grid architecture to updated surfaces of geological structures during history matching process. However most commonly used method for representation of complex structure in reservoir engineering has been corner point grid. In section 3.1 we rejected the choice of a corner point grid for a history matching process of geological structure. However even for simulation of a model with fixed geological structure, it is expected that Cartesian Cut Cell method results in a more consistent grid honouring the reservoir geology with less numerical complexities. Corner point gridding defines each 3D cell as the volume restricted between four vertical pillars and eight ending points of these pillars. Despite the flexibility of corner point grids, as listed by Aarnes et al. [2008] corner point grid geometry leads to some difficulties. We explain preferences of Cartesian Cut Cell method in terms of avoiding most of such difficulties. However we believe that such improvements are considerable for models of localised gently dipped reservoir layering.

1. In corner point gridding, at each sedimentary bed the vertical divisions of grids get affected by trend of inter-layer boundaries. Therefore each face would be aligned either to the trend of geological structures or to an inflected trend with arbitrary inclination. While in Cartesian Cut Cell approach only those horizontal or vertical faces which are intersected with geological surfaces, are replaced with tilted interfaces conforming the geological surfaces. This leaves most of cells with faces aligned to the planes of Cartesian coordinates. Therefore for most of cells, compact stencils in solution matrix will be obtained. This yields a more well-posed solution matrix with less computational efforts needed and less possibility of non-physical solutions.

2. Corner point cells might have zero volume, especially at partially eroded beds (e.g. pinchout). As a result non-neighbour connections across the overlapped boundaries of eroded beds will be formed. This creates more complex sparsity patterns in solution matrix and reduces its well-posedness. While in Cartesian Cut Cell method no cell is accommodated for the eroded parts of sedimentary beds and non-neighbour connections just occur next to faults.

3. Degenerate cells with triangular or trapezoidal shapes in 2D grid and polyhedral shape in 3D grid may appear in corner point grid geometry. In Cartesian Cut Cell method such cells with high aspect ratios (ratio of largest face length to the length of smallest face) are merged to one of their adjacent cells (in the same geological compartment) in the cost of creating a non-neighbour connection. In this way the dependency of discretisation matrix to cell geometry and its complexity is reduced.

In the next chapter, it will be shown that more monotonic solutions are obtained for a Cartesian grid partially modified to account for introduced structures.

Chapter 4

Extended Enriched Multipoint Flux Approximation Method

This chapter is totally devoted to explain the extended "Enriched Multipoint Flux Approximation Method" (extended EMPFA) for reconstruction of flux over the faces of cells conformed to the surfaces of geological structures. We first review the works done in petroleum industry for solving the mass conservation and Darcy's equations and then introduce in details the extended EMPFA technique.

The main specific goals of this chapter are as followings:

1. To clarify the motivation for use of a multipoint flux approximation method for quadrilateral cells of irregular shape.

2. To specify the preference of extended EMPFA method over the conventional MPFA methods in the vicinity of faults and pinchouts or for local grid refinement.
3. To testify the improvement of extended EMPFA by using a double-family quadrature in terms of increased flexibility to yield resolved monotonic solutions per optimised quadrature values.
4. To demonstrate the convergence and consistency of developed flux approximation scheme over models of geological structures.

4.1 The Motivation for Using Multipoint Schemes to Approximate the Flux

The fluid flow in porous media is modelled with Darcy's law ($\mathbf{V} = -(1/\mu)\mathbf{K}\nabla\Phi$). Throughout this chapter, any bold symbol refers to as a vector, a tensor or a matrix. In Darcy's law the volumetric velocity vector ($\mathbf{V}$) is proportionated to the negative normal gradient of potential ($-\nabla\Phi$). The proportionality factor ($(1/\mu)\mathbf{K}$) expresses the media flow conductivity and it is directly related to the rock permeability ($\mathbf{K}$) divided by the fluid viscosity. Rock permeability in general is a tensor, in which the diagonal elements define the tendency of rock matrix to conduct the fluid in the same direction as the direction of potential drop. On the other hand, off-diagonal terms represent the flow conductivities of rock matrix in a direction other than the direction of potential drop.

$$\mathbf{K} = \begin{bmatrix} K_{xx} & K_{xy} \\ K_{yx} & K_{yy} \end{bmatrix} \tag{4.1}$$

Letting C_i and C_j as two adjacent cells of general geometry and F_{ij} as their common interface, the fluid flux passing through F_{ij} (denoted by f_{ij}) is calculated from integration of Darcy velocity over common interface.

$$f_{ij} = -\frac{1}{\mu} \int_{s \in F_{ij}} \mathbf{n}_{ij}^{T} \bullet \mathbf{K}\nabla\Phi ds \tag{4.2}$$

In which $\mathbf{n}_{ij}$ is the unit normal flux on F_{ij}. The resultant depends mainly on the geometry of common interface. A simple commonly-used equation for one-dimensional problems resembling the original Darcy's law is written as:

$$\mathbf{f}_{ij} = \frac{1}{\mu}\left|F_{ij}\right|\bar{K}\left(\Phi_{C_i} - \Phi_{C_j}\right) \quad (4.3).$$

In which $\bar{K}$ is a kind of harmonic average of permeabilities at cells sharing interface F_{ij} obtained as:

$$\bar{K} = \frac{K_i K_j \left(L_1 + L_2\right)}{L_1 K_i + L_2 K_j} \quad (4.4).$$

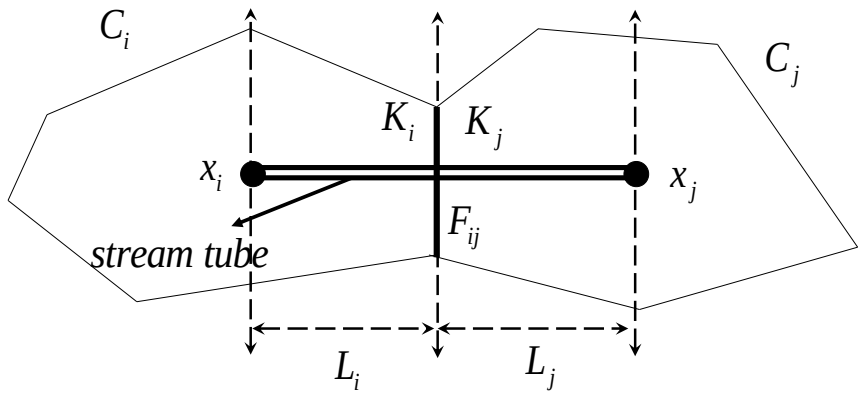

Figure 4.1: One dimensional transmissibility estimation applicable for stream tube between cell centres perpendicular to the interface

Term $\left|F_{ij}\right|\bar{K}$ is usually called the two point transmissibility and is represented with t_{ij}. For problems of higher dimensions, letting $\mathbf{K}_i$ and $\mathbf{K}_j$ as the permeability tensors in cells C_i and C_j, the following criteria must be met to express f_{ij} by a similar equation to Eq. 4.3.

- The segment $\left(x_i, x_j\right)$ connecting the centres of adjacent cells is orthogonal to the common interface F_{ij}.
- At least one of eigen-vectors of both $\mathbf{K}_i$ and $\mathbf{K}_j$ is in the same direction.
- The segment $\left(x_i, x_j\right)$ is parallel to the predominant common eigen-direction of tensors $\mathbf{K}_i$ and $\mathbf{K}_j$ (the direction of one of common eigen-vectors making a closer angle with the interface F_{ij}.

With these conditions, by letting K_i^h and K_j^h as the eigen-values of $\mathbf{K}_i$ and $\mathbf{K}_j$ corresponding to their common eigen-direction, Eq. 4.4 can be used to calculate the average permeability across F_{ij}. The eigen-vectors of permeability tensor at each point are called the principal directions of permeability. Also original full tensor can be mapped into a diagonal tensor at a certain rotation angle of original coordinate. If everywhere inside the discretized region, each of principal directions of permeability tensor are perpendicular to one of axes of coordinates on gridlines, then the grid is called **K**-orthogonal (Heinemann et al., 1991), in effect the flux through all interfaces can be obtained with the simple two point flux approximation (TPFA) method.

In petroleum industry, corner point gridding or unstructured gridding (PEBI grids) are used to create cells aligned to geological surfaces to accurately represent their geometrical features. Therefore **K**-orthogonality condition is very likely to be violated over most cells and general integrated flux over interfaces (Eq. 4.2) no more diminishes to TPFA scheme. Using Gauss divergence theorem surface integral in Eq. 4.2 is converted to a volume integral over all cells sharing at least one vertex with F_{ij}. Letting $N(i,j)$ as the set of all cells C_k involved in the volume integration, multipoint flux approximation method is inspired by generalizing the two point equation of flux approximation as:

$$f_{ij} = \frac{1}{\mu} \sum_{k \in N(i,j)} t_{ij}{}^{k} \Phi_{C_k} \qquad (4.5).$$

For general non **K**-orthogonal and curvilinear grid, there has been an interest to express the Darcy's law in a dimensionless uniform space with coordinates (ξ, η). In the new space, the flux is obtained from:

$$f_{ij} = -\frac{1}{\mu} \int_{\Gamma \in F_{ij}} \left(\mathbf{T}_{ij} \nabla \Phi(\xi, \eta) \right) \bullet \mathbf{d\Gamma} \qquad (4.6),$$

in which:

- $\nabla\Phi_{\xi,\eta}$ is the potential gradient in dimensionless uniform space given by $\mathbf{J}\nabla\Phi$, and $\mathbf{J}$ is the Jacobian of space transformation ($\mathbf{J} = \frac{\partial(x,y)}{\partial(\xi,\eta)}$).
- $\mathbf{T}_{ij}$ is called transmissibility tensor (general Piola tensor, Edwards and Rogers, 1998-A) for interface between cells C_i and C_j and its elements are given by:

$$\begin{aligned} T_{11} &= (K_{xx}y_\eta^2 + K_{yy}x_\eta^2 - 2K_{xy}x_\eta y_\eta)\big/\det(\mathbf{J}) \\ T_{22} &= (K_{xx}y_\xi^2 + K_{yy}x_\xi^2 - 2K_{xy}x_\xi y_\xi)\big/\det(\mathbf{J}) \\ T_{12} &= (K_{xy}(x_\xi y_\eta + x_\eta y_\xi) - (K_{xx}y_\eta y_\xi + K_{yy}x_\eta x_\xi))\big/\det(\mathbf{J}) \end{aligned} \qquad (4.7).$$

- $\mathbf{d\Gamma} = \begin{bmatrix} d\xi & d\eta \end{bmatrix}^T$ is the tangential vector drawn on an infinitesimal segment of F_{ij}.

As explained in chapter 3, Cartesian Cut Cell method creates cells conformed to the geometrically complex geological structures. The large scale flow behaviour is significantly influenced by geological structures, for example their geometry and location determines the main flow paths and connectivity of different part of reservoir (Holm et al., 2006). Therefore although most Cartesian cells outlying the geological structures remain unchanged, but main concern should be focused on finding a higher precision flux approximation scheme in the vicinity of geological structures.

Cartesian Cut Cell method imposes two main kinds of irregularities on cell geometry, both causing the violation of required criteria for using TPFA scheme:

1. In order to honour the inclined surface of faults and pinchouts or the curved bedding planes, some of cell's interfaces become tilted with spatially varying inclinations. Even though the intact Cartesian cells are **K**-orthogonal, the segment connecting centres of two adjacent cells sharing a tilted interface is not anymore perpendicular interface surface. In figure 4.2, the tilted interfaces substitute a vertical interface (left) and a horizontal interface (right) to conform the adjacent cells to the plane of a fault (left) and to the plane of a stratigraphic layer (right). However for almost vertically-dipped faults or very smoothly-

dipped layers, TPFA still yields a sufficient approximation of flux over the tilted interface (Wu and Parashkevov, 2009).

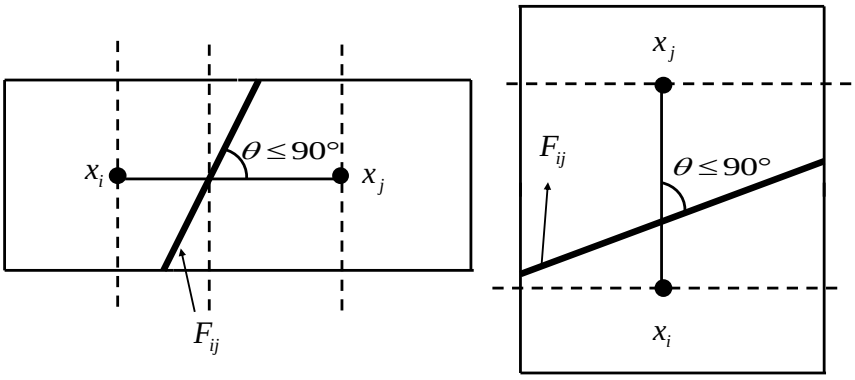

Figure 4.2: Tilted interfaces aligned to the surface of geological structures

2. As discussed in chapter 3, the second kind of the cell degeneracy caused by Cartesian Cut Cell method is the non-neighbour connections. Such connections happen between the cells which naturally do not share any interface based on their logical indices. For such a connection, one of cells (called C_i) shares one of its faces with two cells (called C_j and C_k). Thus the segments connecting the centres of cells involved in non-neighbour connection ((C_i, C_j) and (C_i, C_k)) are inclined and can make various angles other than $0°$ with their corresponding dominant common eigen-direction of permeability ($\mathbf{v}_K{}^1(i,j)$ or $\mathbf{v}_K{}^2(i,j)$).

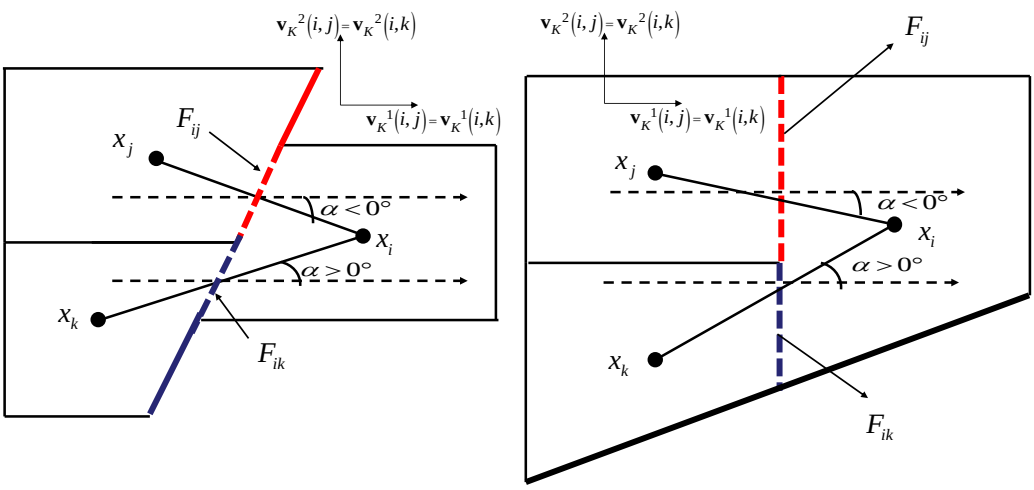

Figure 4.3: Non-neighbour connections occurring in the vicinity of a fault (Left) and a bedding plane (Right), when the Cartesian Cut Cell method reshapes the rectangular cells to conform their faces with the boundaries of geological structures.

For non-neighbour connections displayed in figure 4.3, segments between centres of connected cells are neither perpendicular to their common interface, nor parallel to the predominant common eigen-direction of permeability ($\mathbf{v}_K^{\,1}(i,j)$ or $\mathbf{v}_K^{\,1}(i,k)$).

The effects of deviated non K-orthogonal grids on accuracy of TPFA scheme for flow simulation have been investigated by Wu and Parashkevov [2009]. According to their conclusion, for most practical purposes TPFA leaves a relatively small error in approximation of horizontal flow, while considerable error in vertical flow is obtained. As a common practice in reservoir simulation, faults are represented at angles very close to right angle. However for more acute angles of fault inclinations, it is believed that accuracy of horizontal flux approximation with two-point scheme is considerably reduced as well. This discussion motivates us to employ a suitable multipoint scheme inspired by Eq. 4.5 for approximation of flux. It is worth mentioning that there are some researches (e.g. Chen et al., 2008) on application of TPFA for fine scale heterogeneous models that show TPFA is not good enough particularly in combination with upscaling and it should be extended to non-linear TPFA (NTPFA) which takes into account the main pressure gradient direction for transmissibility calculation. NTPFA has been successfully applied in conjunction with global or local upscaling techniques.

4.2 Literature Review on Class of MPFA Methods and Related Techniques

Extensive research in recent decades has been carried out in order to solve mass conservation equation in porous media for general grid with full permeability tensor. Solving a discretized from of mass conservation equation with a finite volume approach requires determination of continuous mass flux through the interfaces between the control volumes exhibiting strong permeability discontinuities. In this view control volume MPFA method belongs to a broader family of methods called *locally conservative control volume methods* (Klausen and Russell [2004], Edwards and Zheng, 2008). Locally conservative control volume methods have been designed to circumvent the O(1) error imposed by TPFA (the traditional scheme used by most simulators) for general non **K**-orthogonal grids.

Most of pioneering works in the class of locally conservative flux-continuous control volume methods (e.g. Aavatsmark et al., 1994, 1996, 1998-A, 1998-B, Edwards and Rogers, 1994, 1995, 1998, Verma and Aziz, 1997) were introduced for discretization on 2-D quadrilateral grids for anisotropic heterogeneous permeability fields. MPFA can be used for both corner point and cell centred grids, but here we will present our explanations of flux approximation schemes for cell centred grids. MPFA is inspired by generalization of idea behind TPFA which leads into a harmonic average permeability for the interface of two 1-D cells by enforcing potential and flux continuity at interface. MPFA is aimed to make involved potentials at all cells sharing at least one vertex with the target interface in flux term at that interface. In MPFA potential and flux continuity condition are imposed along the sub-interfaces bounded in a volume formed around each cell vertex (O) by connecting the centres of cells (C_i) sharing that vertex and the midpoints of interfaces sharing that vertex (M_i). This volume which is a polygon in 2-D and a polyhedron in 3-D is called *interaction region*. Clearly each cell is divided into as many sub-volumes as the number of its vertices. Dealing with cells of general quadrilateral shape, for matching 2-D grids, each interaction region comprises from four sub-volumes (or sub-cells) inherited from one of involved cells.

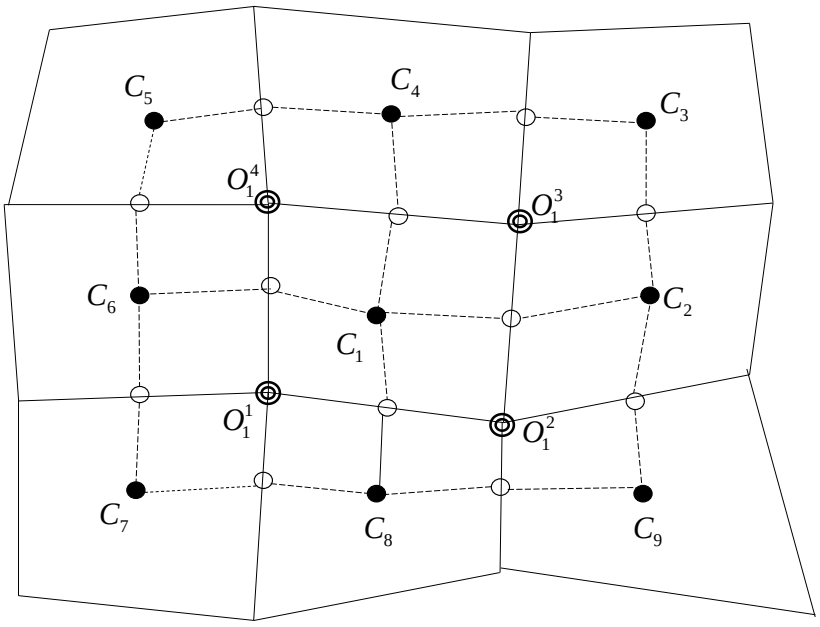

Figure 4.4: MPFA, Four interaction regions built on vertices of cell C_1; dotted lines connect cell centres (shown with filled small circles) to midpoints of corresponding cell interfaces (shown with empty small circles) to create the interaction regions around the cell vertices (shown with two concentred small circles).

MPFA supposes a linear variation of potential at each sub-volume. Each sub-volume potential function is determined with three potential (one potential at corresponding cell centre and two other at starting and ending points of two sub-interfaces). This leaves total of 12 unknown potentials. Imposing potential continuity across the interface midpoints (M_i) reduces the degrees of freedom to 8. By applying flux continuity across sub-interfaces, one can specify the potentials at midpoints of sub-interfaces in terms of potentials at cell centres.

Flux passing through the ith sub-interface evaluated as its facet in k^{th} sub-volume is determined from $f_i^k = -\mathbf{n}_i^k \bullet K^k \nabla \Phi^k$. With a linear potential variation, constant potential gradient at each sub-volume is specified from the potentials at edges of $M_{bi}^i C_k M_i$ in which *bi* depends on the trigonometric order of two sub-interfaces:

$$bi = \begin{cases} i-1 & if \quad (i=k \ \& \ k \neq 1) \\ 0 & if \quad (i=k \ \& \ k=1) \\ i+1 & if \quad (i=k+1 \ \& \ k \neq 4) \\ 1 & if \quad (i=k+1 \ \& \ k=4) \end{cases} \qquad (4.8).$$

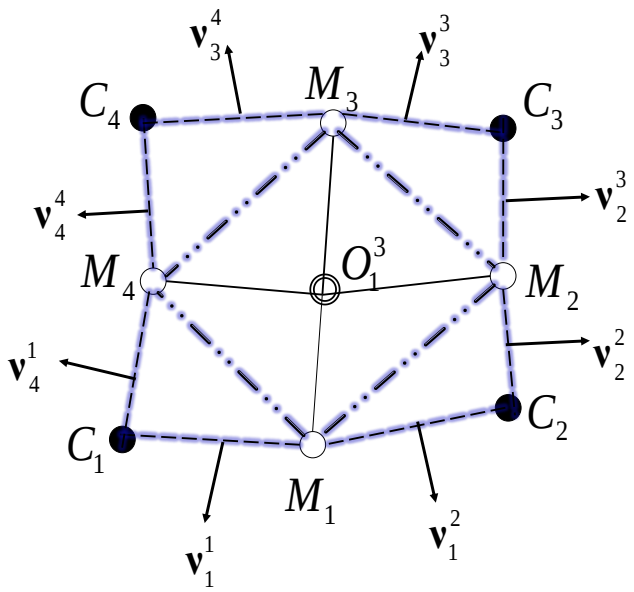

Figure 4.5: Linear variation of potential within the $M_{bi}^i C_k M_i$ triangles (with edges at a cell centre and mid-points of two consecutive cell interfaces) is utilised for potential approximation throughout whole the interaction region.

The vector of potential differences between cell centre (C_k) and each of mid-interfaces (M_{bi}^{i} or M_i) is obtained from $\Delta\Phi^k = \mathbf{X}_k \nabla\Phi^k$, in which:

$$\Delta\Phi^k = \begin{bmatrix}\Phi_{bi} - \Phi_k & \Phi_i - \Phi_k\end{bmatrix}^T \quad (4.9),$$

$$\mathbf{X}_k = \begin{bmatrix} x(M_{bi}) - x(C_k) & y(M_{bi}) - y(C_k) \\ x(M_i) - x(C_k) & y(M_i) - y(C_k) \end{bmatrix} \quad (4.10).$$

This gives the discrete potential gradient in sub-volume k as $\nabla\Phi^k = \mathbf{X}_k^{-1}\Delta\Phi^k$ in which $\mathbf{X}_k^{-1}$ is expressed as following:

$$\mathbf{X}_k^{-1} = \frac{1}{|\mathbf{X}_k|}\begin{bmatrix} y(M_i) - y(C_k) & -(y(M_{bi}) - y(C_k)) \\ -(x(M_i) - x(C_k)) & x(M_{bi}) - x(C_k) \end{bmatrix} \quad (4.11).$$

Vectors $\mathbf{v}_{bi}^k$ and $\mathbf{v}_i^k$ are defined as the normal vectors on segments $C_k M_{bi}$ and $C_k M_i$:

$$\begin{cases} \mathbf{v}_{bi}^k = \begin{bmatrix} y(M_{bi}) - y(C_k) & -(x(M_{bi}) - x(C_k)) \end{bmatrix}^T \\ \mathbf{v}_i^k = \begin{bmatrix} y(M_i) - y(C_k) & -(x(M_i) - x(C_k)) \end{bmatrix}^T \end{cases} \quad (4.12).$$

By this notation $|\mathbf{X}_k|$ is twice of area bounded in triangle $M_{bi}C_kM_i$ and constant potential gradient is given by $\frac{1}{|\mathbf{X}_k|}\begin{bmatrix}\mathbf{v}_{bi}^k & \mathbf{v}_i^k\end{bmatrix}\Delta\Phi^k$. Hence flux at sub-interface OM_i is expressed as $f_i^k = \left(\omega_{ik}^i \Delta\Phi_i^k + \omega_{ik}^{bi}\Delta\Phi_{bi}^k\right)$ in which:

$$\omega_{ik}^{i/bi} = -\frac{\mathbf{n}_i^k \bullet K^k \mathbf{v}_{i/bi}^k}{|\mathbf{X}_k|} \quad (4.13),$$

$$\Delta\Phi_{i/bi}^k = \Phi_{i/bi} - \Phi_k \quad (4.14).$$

Four flux continuity condition on starting and ending points of sub-interfaces writing as $f_i^k = f_i^{N(k)}$ describe the MPFA O-method, in which $N(k)$ stands for the index of sub-volume sharing the ith sub-interface with k^{th} sub-volume. Introducing two vectors of potentials ($\mathbf{\Phi}_C = \left(\Phi_{C_1}, \Phi_{C_2}, \Phi_{C_3}, \Phi_{C_4}\right)^T$ and $\mathbf{\Phi}_F = \left(\Phi_{M_1}, \Phi_{M_2}, \Phi_{M_3}, \Phi_{M_4}\right)^T$) and the vector of fluxes ($\mathbf{f} = \left(f_1, f_2, f_3, f_4\right)^T$), final 4×4 system of equations relating potentials at mid-faces to those as cell centres is expressed as:

$$\mathbf{f} = \mathbf{A}_1\mathbf{\Phi}_C + \mathbf{B}_1\mathbf{\Phi}_F = \mathbf{A}_2\mathbf{\Phi}_C + \mathbf{B}_2\mathbf{\Phi}_F \qquad (4.15).$$

From Eq. 4.15, flux vector would be determined as $\mathbf{f} = \mathbf{T}_{4\times4}\mathbf{\Phi}_C = \left[\mathbf{B_1}(\mathbf{B_1} - \mathbf{B_2})(\mathbf{A_2} - \mathbf{A_1}) + \mathbf{A_1}\right]\mathbf{\Phi}_C$. Described scheme is known as O-method reminding the shape of polygon formed by connecting cell and interface points. For general grids the O-method does not lead into a symmetric discretized operator and hence it is only conditionally convergent [Aavatsmark, 2008, Klausen and Winther, 2006-B). Conditional convergence of O-method has been conjectured by Klausen and Winther [2006-A, 2006-B] and Aavastmark et al. [2007-C]. However according to several numerical convergence tests performed on rather rough grids (e.g. Edwards and Rogers, 1998-A, Eigestad and Klausen, 2005, Pal et al., 2006-A), MPFA O-method (or its variants) shows almost super-linear convergence for the potential and linear convergence for the flux on a variety of grid. In 4.5 we will explain more about the convergence of a numerical scheme. Apart from the classical problem of accuracy and stability (translated in the context of convergence studies), there has been much interest in designing variants of MPFA yielding non-oscillatory solutions. MPFA O-method has been shown to be suffering from spurious oscillations or spurious extrema at boundaries even if scheme converges to the correct solutions (Aavastmark, 2007-A, 2008). For non-linear solutions, monotonicity is not satisfied for whole values of grid aspect ratio and anisotropy ratio. Aavstmark et al. [1996, 1998-A] have developed an equivalent discretization to MPFA O-method in dimensionless uniform space which is useful for studies of monotonicity behaviour. The monotone region is usually specified within a unit square diagram. Vertical and horizontal axes of this diagram are $Min(T_{11},T_{22})/Max(T_{11},T_{22})$ and $|T_{12}|/Max(T_{11},T_{22})$ respectively. To broaden the monotone region, several modifications of MPFA O-method have been presented. Though demonstrated by Edwards and Zheng [2008], lying in monotone region is not enough to get physically meaningful solutions, but M-matrix regions are the only regions where one can claim the solution can be free of spurious oscillations. Firstly M-matrix conditions for general 9-point schemes were introduced by Edwards [1995] and Edwards and Rogers [1998]. The only spatially symmetric scheme was presented in Friis et al. [2008]. Also the source of symmetry has been demonstrated Edwards and Pal [2008].

MPFA L-method developed by Aavatsmark et al. [2006, 2007-B, 2008] uses the same interaction region as O-method, but computation of transmissibilities for each sub-interface is performed individually by applying the continuity conditions within the volume spanning the corresponding sub-interface and one of its neighbour sub-interfaces. This builds a triangular interaction region (shown in figure 4.5) in which potentials and fluxes at starting and ending points of involved sub-interfaces and central point of interaction region are unknown. Interaction region is divided into four triangular sub-volumes by connecting central point, a cell centre and a mid-interface point. Applying the potential and flux continuity conditions across faces between sub-volumes, two desired fluxes are expressed in terms of potentials at three involved cell centres. To select the optimum triangular interaction region (*triangle (1)* or *triangle (2)* shown in figure 4.6), the quantity $S = \left| t_1^1 - t_2^1 \right|$ is compared between two interaction regions. One with smaller S is selected to obtain transmissibilities of sub-interface $O_1^3 M_1$. Satisfaction of this condition leaves more compact approximation of flux which approaches TPFA scheme by minimisation of transmissibility difference between cells sharing the proposed interface. As inspected by Aavatsmark [2007-A] and Aavatsmark et al. [2008], using MPFA L-method, more sparse solution matrix is obtained leading to a broader domain of convergence and monotonicity.

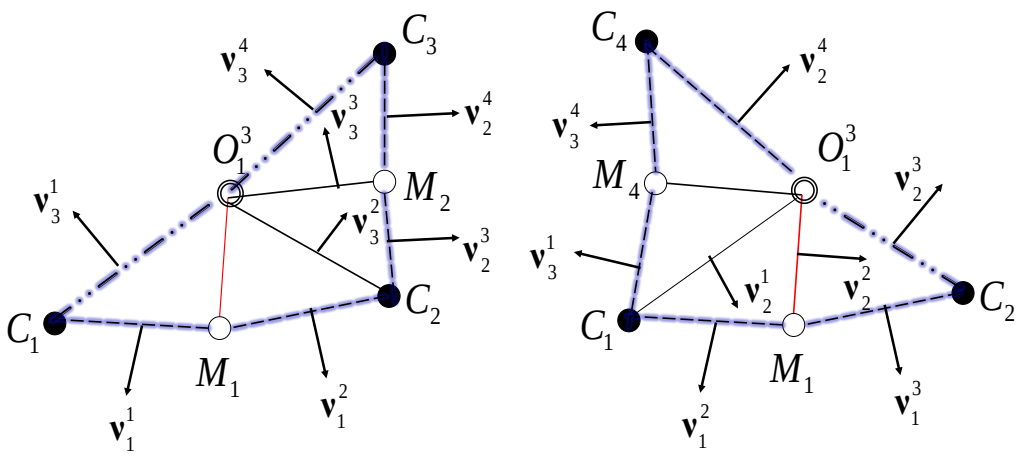

Figure 4.6: Two choices of interaction region built on red sub-interface for MPFA L-method; Left: *Triangle (1)*, Right: *Triangle (2)*

Extension of L-method for local grid refinement has been studied by Aavatsmark [2007-A]. However he has mentioned that 2-D methodology of MPFA L-method cannot be easily implemented for 3-D problems. Moreover choice of triangular interaction regions is not generalised and somewhat ad-hoc (Aavatsmark, 2008). Pal and Edwards [2007, 2011] achieved analogous schemes to MPFA L-method via triangulations favouring permeability anisotropy.

Nordbotten and Eigestad [2005] have developed a MPFA Z-method with a different interaction region to achieve more monotonic results on quadrilateral grids especially on skewed grid with high aspect ratios.

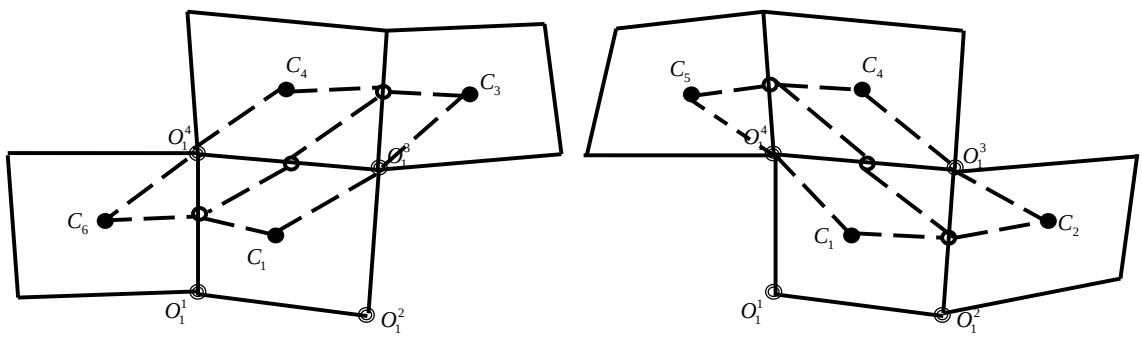

Figure 4.7: Choices of interaction region for Z-method

Interaction region for Z-method comprises of three mid-interfaces, four cell centres and two cell vertices. Therefore 12 equation are needed to find 12 degrees of freedom (two (potential and flux) per each mid-interface and one (potential) per each cell centre or cell vertex). Applying the flux and potential continuity across sub-interfaces and potential continuity on cell vertices leaves only two undetermined degrees of freedom. One can relate potentials at centres of cells completely located inside the interaction region (C_1 and C_4) to the potentials at midpoint of two neighbour interfaces and two cell vertices based on linear variation of potential. This closes the system of equations for desired fluxes. Despite more monotonic results, the extension of this method for 3-D problems and non-matching cells still has remained unanswered.

Edwards and Rogers [1998-A] introduced the quadrature parameterisation for flexibly relocate the flux continuity point on each sub-interface. Full pressure continuity is achieved by introduction of an additional auxiliary interface pressure at the common corner of the connecting sub-cells defining the flux interaction region, leading to full pressure support (FPS). They used the curvilinear coordinate transformation into logical rectangular coordinates within the triangles forming by connecting flux quadrature points and cell centre at corresponding sub-volume. This allows for expressing potential as a linear piecewise function with respect to logical coordinates within each triangle (named triangle pressure support (TPS) in Edwards and Zheng, 2008).

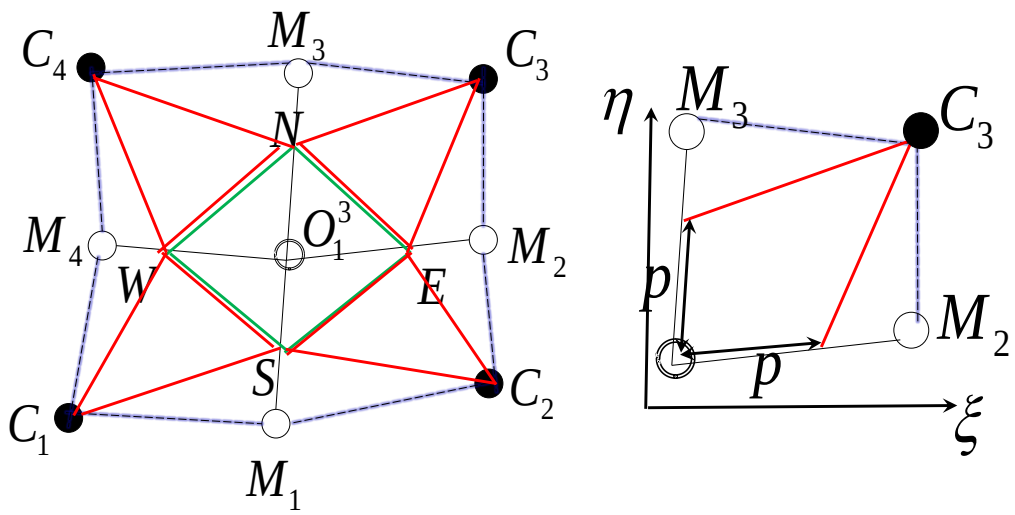

Figure 4.8: Left: Flux continuity points on sub-interfaces (N, S, E, W); Right: Isotropic quadrature parameterisation for triangular flux continuous scheme (TPS)

As Edwards and Rogers [1998-A] have shown with appropriate choose of quadrature ($0 < p < (1/2)$) the monotonicity characterises of discretized system is enhanced. MPFA O-method is regarded as an extreme case of flexible quadrature scheme developed by Edwards and Rogers [1998-A], denoted by MPFA O(0)-method by Nordbotten et al. [2007] in contrary to MPFA O(0.5)-method with wider monotonicity region.

Edwards and Zheng [2008] developed a new family of flux continuous locally conservative schemes motivated by discretization method of Crumpton et al. [1995]

which require full continuity of potential across the interface in contrary with the earlier schemes based on point-wise flux and potential continuity. They compared their earlier flux continuous methods using triangle pressure support (TPS) with the new full pressure support schemes by mapping both formulations onto the more transparent control-volume finite element (CVFE, Edwards, 1995, Cai et al., 1997) in the case of a spatially cell-wise constant tensor. Moreover the full pressure support method (FPS) based on bilinear potential approximation at each sub-volume were introduced in the same paper. TPS were shown to have a reduced CVFE quadrature range and leading to decoupled (strongly oscillatory) solutions for very anisotropic full permeability tensors. While quadrature flexibility of FPS enjoying full CVFE quadrature range allows to minimise the spurious oscillations in discrete potential solution. Single-parameter family of TPS and FPS schemes were extended by Edwards and Zheng [2010] to more robust double-parameter families of flux continuous schemes by allowing use of different quadrature points on individual sub-interfaces. They have shown that full tensor effects with large off-diagonal values can be properly tackled with appropriate choice of quadrature points leading to resolved solutions with minimal oscillations. Also the extension of flux continuous schemes (TPS and FPS) to multi-parameter families of schemes for 3-D problems has been presented by Edwards and Zheng [2011].

Chen et al. [2008] have ascribed the non-physical solutions of MPFA O-method to its non-efficiently accurate approximation of potential gradients (in particular Φ_y) within sub-volumes. The oscillations would be more severe for large grid aspect ratios (large grid divisions in horizontal direction), because a constant linearly interpolated gradient between cell centre and the ending point of one of its surrounding sub-interfaces is second order accurate only along the segment connecting points used in gradient calculation. Propagation of this gradient into the whole sub-volume leads to a poor gradient approximation especially close to other mid-interface when Φ_{xy} is of order or greater than $Max(\Delta x, \Delta y)^{-1}$. To achieve more precise potential gradients, they developed an enriched version of MPFA (EMPFA) which considers the potential at central point of interaction region as another temporary unknown. The potential is interpolated either bilinearly within each sub-volume or linearly within each triangle between central point, cell centre and the ending point of one of its surrounding sub-interfaces. Zero

divergence condition is enforced on central point to give auxiliary equation required for deleting added temporary unknown.

It seems that promoted accuracy of EMPFA obtained by increasing the dividing points and continuity conditions influences both the convergence and monotonicity matters. Higher convergence rates for potential and flux for EMPFA have been reported by Chen et al. [2008] compared with MPFA O-method. On the other hand, the monotonicity region of EMPFA was shown to be comparable or narrower from that O-method and narrower than that of L-method by Aavatsmark [2008]. However as an important advantage for a highly anisotropic full permeability tensor which lies outside of monotonicity regions of all methods, EMPFA yields much less amplified oscillations. This provides an evidence of robustness of EMPFA to leave more physically meaningful solutions for very wide range of anisotropy and grid aspect ratio. But in further studies performed by Aavatsmark [2008], EMPFA led to strongest boundary unphysical extrema for a model with no-flow boundary conditions among variants of MPFA method. This can be attributed to the fixed continuity points on sub-interfaces (their starting and ending points) and we believe that optimised choice of continuity points along sub-interfaces can reduce boundary extrema. This idea is motivated by minimal oscillations observed in solution of models having no-flow boundary conditions when FPS with anisotropic quadrature points is used (Edwards and Zheng, 2010). In this thesis we will use an extended version of EMPFA by applying flexible continuity points (idea inspired from FPS method).

It is worth pointing out that there are some other schemes from class of locally conservative methods for solving elliptic differential equation of mass conservation in porous media. Mimetic finite difference (MFD) developed by Shashkov and Steinberg [1996] and Hyman and Shashkov [1997] shows promising results for very anisotropic highly heterogeneous media. However undetermined monotonicity condition and the higher computational cost in contrast with MPFA methods (Alpak, 2010) still has remained unresolved. Mixed finite element method (Arbogast et al., 1997, Chou et al., 2001) has been successfully tested on very distorted 2-D grids, but due to additional degree of freedom, it is computationally expensive. Klausen and Russell [2004] have

presented comprehensive study of relationships between some these locally conservative schemes in terms of their common postulating foundations and method of solution.

4.3 Extended EMPFA for General 2-D Quadrilateral Cells

4.3.1 Bilinear Potential Approximation

In general each two-dimensional sub-volume Ω is regarded as the convex area bounded between its vertices. Set of vertices for each sub-volume (*SV*) includes three or four points (A_i) arranged in anti-clockwise order:

$$SV = \bigcup_i A_i,\ SV \in \Omega \qquad (4.16).$$

A sub-volume of quadrilateral shape can be mapped into a square with unit edges called standard reference element. The rule of such a mapping attributes each point inside the quadrilateral (located in (*x*,*y*) plane) with a unique point inside the unit square (located in (ξ,η) plane). It is postulated that:

- Mapping preserves the order of corner points.
- Left most and lowest borders of the mapped unit square coincide with the principal axes of (ξ,η) plane.

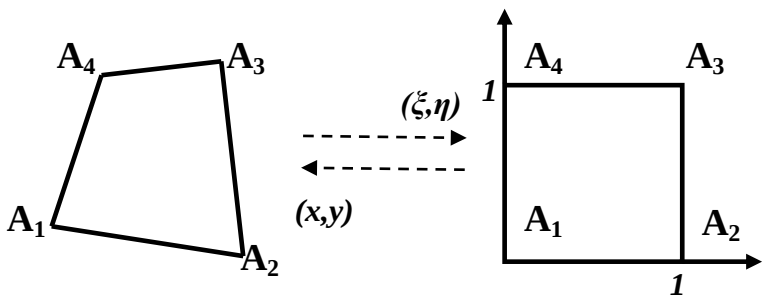

Figure 4.9: Mapping quadrilateral from the computational space into the logical space

Thus:

- $A_1(x_1,y_1)$ is mapped onto $A_1(0,0)$ in (ξ,η) plane.
- $A_2(x_2,y_2)$ is mapped onto $A_2(1,0)$ in (ξ,η) plane.
- $A_3(x_3,y_3)$ is mapped onto $A_3(1,1)$ in (ξ,η) plane.
- $A_4(x_4,y_4)$ is mapped onto $A_4(0,1)$ in (ξ,η) plane.

Bilinear interpolation can be employed to determine a unique point in (x,y) plane corresponding to an arbitrary point (ξ,η) inside the standard reference element.

$$\mathbf{r} = (1-\xi)(1-\eta)\mathbf{r}_1 + \xi(1-\eta)\mathbf{r}_2 + \xi\eta\mathbf{r}_3 + (1-\xi)\eta\mathbf{r}_4 \tag{4.17}$$

Similarly flow potential inside the sub-volume can be obtained from a linear combination of flow potentials at vertices, where the coefficients are bi-linearly related to local parametric coordinates (ξ,η).

$$\Phi = (1-\xi)(1-\eta)\Phi_1 + \xi(1-\eta)\Phi_2 + \xi\eta\Phi_3 + (1-\xi)\eta\Phi_4 \tag{4.18}$$

Rearranging Eq. 4.17 and remembering $\mathbf{r}=(x,y)$, one can find the mapping expression for $\boldsymbol{x}$ and $\boldsymbol{y}$ coordinates.

$$\begin{cases} x = \underset{a_1}{x_1} + \underbrace{(x_2 - x_1)}_{a_2}\xi + \underbrace{(x_4 - x_1)}_{a_3}\eta + \underbrace{(x_1 + x_3 - (x_2 + x_4))}_{a_4}\xi\eta \\ y = \underset{b_1}{y_1} + \underbrace{(y_2 - y_1)}_{b_2}\xi + \underbrace{(y_4 - y_1)}_{b_3}\eta + \underbrace{(y_1 + y_3 - (y_2 + y_4))}_{b_4}\xi\eta \end{cases} \tag{4.19}$$

Eq. 4.19 provides the definitions for the coefficients of bilinear mapping relations for each of computational coordinates:

- $a_i,\ i = 0,1,2,3$ for $\boldsymbol{x}$ coordinate
- $b_i,\ i = 0,1,2,3$ for $\boldsymbol{y}$ coordinate.

4.3.2 Bilinear Approximation of Potential Gradient

It is desired to express potential gradient at any point inside the sub-volume or on its borders as a function of potentials at vertices. Considering Eq. 4.18, directional

derivatives of flow potential in original coordinates (x,y) and logical coordinates (ξ,η) are interrelated through the Jacobian matrix of coordinate transformation ($\nabla\Phi_{(\xi,\eta)} = \mathbf{J}(x,y)\nabla\Phi_{(x,y)}$). Jacobian matrix is expressed as:

$$\mathbf{J}(x,y) = \begin{pmatrix} \dfrac{\partial x}{\partial \xi} & \dfrac{\partial y}{\partial \xi} \\ \dfrac{\partial x}{\partial \eta} & \dfrac{\partial y}{\partial \eta} \end{pmatrix} \qquad (4.20).$$

Thereafter gradient of flow potential in (x,y) coordinates is obtained by:

$$\begin{pmatrix} \dfrac{\partial \Phi}{\partial x} \\ \dfrac{\partial \Phi}{\partial y} \end{pmatrix} = \frac{1}{\det(\mathbf{J})} \begin{pmatrix} \dfrac{\partial y}{\partial \eta} & -\dfrac{\partial y}{\partial \xi} \\ -\dfrac{\partial x}{\partial \eta} & \dfrac{\partial x}{\partial \xi} \end{pmatrix} \begin{pmatrix} \dfrac{\partial \Phi}{\partial \xi} \\ \dfrac{\partial \Phi}{\partial \eta} \end{pmatrix} \qquad (4.21).$$

Directional derivatives of flow potential in (ξ,η) coordinates are computed from Eq. 4.18 and substituted in Eq. 4.21 to end up with Eq. 4.22 which relates potential gradient to the potentials at the sub-volume vertices $\mathbf{\Phi}_V = (\Phi_1, \Phi_2, \Phi_3, \Phi_4)^T$:

$$\begin{pmatrix} \dfrac{\partial \Phi}{\partial x} \\ \dfrac{\partial \Phi}{\partial y} \end{pmatrix} = \frac{1}{\det(\mathbf{J})} \underbrace{\begin{pmatrix} \dfrac{\partial y}{\partial \eta} & -\dfrac{\partial y}{\partial \xi} \\ -\dfrac{\partial x}{\partial \eta} & \dfrac{\partial x}{\partial \xi} \end{pmatrix} \begin{pmatrix} -(1-\eta) & (1-\eta) & \eta & -\eta \\ -(1-\xi) & -\xi & \xi & (1-\xi) \end{pmatrix}}_{\mathbf{\Psi}_{2\times 4}} \underbrace{\begin{pmatrix} \Phi_1 \\ \Phi_2 \\ \Phi_3 \\ \Phi_4 \end{pmatrix}}_{\mathbf{\Phi}_V} \qquad (4.22).$$

For a specific point (ξ,η), matrix $\mathbf{\Psi}_{2\times 4}$ (introduced in Eq. 4.22) is a function of shape of sub-volume only, which shows its deviation from a standard unit square. Recalling bilinear interpolation of x and y from Eq. 4.4, matrix $\mathbf{\Psi}_{2\times 4}$ can be rewritten with a linear dependence on local parametric coordinates (ξ,η):

$$\mathbf{\Psi} = \mathbf{\Psi}^0 + \xi\mathbf{\Psi}^1 + \eta\mathbf{\Psi}^2 \qquad (4.23),$$

in which matrices $\mathbf{\Psi}^i_{2\times 4}$ are defined as:

$$\mathbf{\Psi}^0 = \begin{pmatrix} (b_2 - b_3) & b_3 & 0 & -b_2 \\ -(a_2 - a_3) & -a_3 & 0 & a_2 \end{pmatrix} \qquad (4.24),$$

$$\mathbf{\Psi}^1 = \begin{pmatrix} -(b_2+b_4) & (b_2+b_4) & -b_2 & b_2 \\ (a_2+a_4) & -(a_2+a_4) & a_2 & -a_2 \end{pmatrix} \quad (4.25),$$

$$\mathbf{\Psi}^2 = \begin{pmatrix} (b_3+b_4) & -b_3 & b_3 & -(b_3+b_4) \\ -(a_3+a_4) & a_3 & -a_3 & (a_3+a_4) \end{pmatrix} \quad (4.26).$$

Also determinant of Jacobian matrix is expressed in terms of a_i and b_i coefficients.

$$\det(\mathbf{J}) = \underbrace{(a_2b_3 - b_2a_3)}_{J^0} + \xi\underbrace{(a_2b_4 - b_2a_4)}_{J^1} + \eta\underbrace{(a_4b_3 - b_4a_3)}_{J^2} \quad (4.27)$$

Finally one can come up with Eq. 4.28 for the potential gradient at any point inside the quadrilateral sub-volume:

$$\nabla\mathbf{\Phi} = \frac{\mathbf{\Psi}^0 + \xi\mathbf{\Psi}^1 + \eta\mathbf{\Psi}^2}{J^0 + \xi J^1 + \eta J^2}\mathbf{\Phi}_V \quad (4.28).$$

4.3.3 Flux Reconstruction on Sub-volume Faces

Denoting $\partial\Omega$ as the boundary of sub-volume and Γ as an arbitrary segment on $\partial\Omega$, flux passing through Γ can be computed from Eq. 4.29:

$$f = -\int_\Gamma (\mathbf{K}\nabla\Phi).\mathbf{n}d\Gamma \quad (4.29).$$

In which **n** is the unit normal vector on Γ orienting in outward direction. For a tangential element dΓ on $\partial\Omega$, one can write:

$$\mathbf{n}d\Gamma = \mathbf{n}^\eta d\xi + \mathbf{n}^\xi d\eta \quad (4.30).$$

Where $\mathbf{n}^\eta$ and $\mathbf{n}^\xi$ are the unit normal vectors drawn on segments with constant ξ and η respectively.

$$\mathbf{n}^\eta = \begin{pmatrix} -y_\xi \\ x_\xi \end{pmatrix}^T = \begin{pmatrix} -(b_2+b_4\eta) \\ (a_2+a_4\eta) \end{pmatrix}^T \quad (4.31)$$

$$\mathbf{n}^\xi = \begin{pmatrix} y_\eta \\ -x_\eta \end{pmatrix}^T = \begin{pmatrix} (b_3+b_4\xi) \\ -(a_3+a_4\xi) \end{pmatrix}^T \quad (4.32)$$

Using Eq. 4.28 and Eq. 4.30, the flux passing through segment Γ is expressed as:

$$f = -\left\{ \int_{\Gamma} \frac{1}{J^0 + \xi J^1 + \eta J^2} \left[\mathbf{\Lambda}_\eta d\xi + \mathbf{\Lambda}_\xi d\eta \right] \right\} \mathbf{\Phi}_V \qquad (4.33),$$

where:

$$\left(\mathbf{\Lambda}_\eta \right)_{1\times 4} = \mathbf{\Lambda}_\eta^0 + \xi \mathbf{\Lambda}_\eta^1 + \eta \mathbf{\Lambda}_\eta^2 \qquad (4.34),$$

$$\left(\mathbf{\Lambda}_\xi \right)_{1\times 4} = \mathbf{\Lambda}_\xi^0 + \xi \mathbf{\Lambda}_\xi^1 + \eta \mathbf{\Lambda}_\xi^2 \qquad (4.35),$$

$$\mathbf{\Lambda}_\eta^i = \mathbf{n}^\eta \mathbf{K} \mathbf{\Psi}^i, i = 0,1,2 \qquad (4.36),$$

$$\mathbf{\Lambda}_\xi^i = \mathbf{n}^\xi \mathbf{K} \mathbf{\Psi}^i, i = 0,1,2 \qquad (4.37).$$

$\mathbf{\Lambda}_\eta^i$ and $\mathbf{\Lambda}_\xi^i$ are functions of geometry of sub-volume and the corresponding segment Γ. Figure 4.9 shows that at any faces of standard reference element, one of the logical coordinates (ξ or η)is constant. Thus in Eq. 4.33 integration is only performed on variable local coordinate over the interval [0,1]:

$$f = \begin{cases} -\left[\int_0^1 \frac{\mathbf{\Lambda}_\eta^0 + \xi \mathbf{\Lambda}_\eta^1 + \eta \mathbf{\Lambda}_\eta^2}{J^0 + \xi J^1 + \eta J^2} d\xi \right] \mathbf{\Phi}_V & \eta = \text{constant} \\ -\left[\int_0^1 \frac{\mathbf{\Lambda}_\xi^0 + \xi \mathbf{\Lambda}_\xi^1 + \eta \mathbf{\Lambda}_\xi^2}{J^0 + \xi J^1 + \eta J^2} d\eta \right] \mathbf{\Phi}_V & \xi = \text{constant} \end{cases} \qquad (4.38).$$

Here it is desired to construct the flux on any of OM_i segments shown in figure 4.5 which are the common faces between the sub-volumes. Chen et al. [2008] has proposed to take the integrand in the Eq. 4.38 out of integral and compute it in logical coordinates at the midpoints of interfaces between cells included in the interaction region (M_i). This scheme can be regarded as a particular case of flux continuous FPS scheme developed by Edwards and Zheng [2008, 2010, 2011] which fulfils the full potential continuity along the sub-interfaces. This method picks an arbitrary point on OM_i segment (excluding point O) called quadrature point and then enforces the fluxes coming from both sub-volumes sharing segment OM_i to satisfy mass conservation condition. Such a family of methods can be referred to as the “flexible point-wise EMPFA” schemes.

Table 4.1 shows the fluxes calculated with the flexible point-wise EMPFA scheme, when M_i is the quadrature point. Depending on the position of point M_i in the trigonometric order of corner points of corresponding sub-volume, it is assigned different pairs of local parametric coordinates. Thus fluxes are given for any possible pairs of (ξ,η) for point M_i.

ξ	η	f
0	0	$-\left(\left(\mathbf{\Lambda}_{\xi}^{0}+\mathbf{\Lambda}_{\xi}^{2}\right)/J^{0}\right)\mathbf{\Phi}_{V}$
0	1	$-\left(\left(\mathbf{\Lambda}_{\xi}^{0}+\mathbf{\Lambda}_{\xi}^{2}\right)/\left(J^{0}+J^{2}\right)\right)\mathbf{\Phi}_{V}$
1	0	$-\left(\left(\mathbf{\Lambda}_{\xi}^{0}+\mathbf{\Lambda}_{\xi}^{1}\right)/\left(J^{0}+J^{1}\right)\right)\mathbf{\Phi}_{V}$
1	1	$-\left(\left(\mathbf{\Lambda}_{\xi}^{0}+\mathbf{\Lambda}_{\xi}^{1}+\mathbf{\Lambda}_{\xi}^{2}\right)/\left(J^{0}+J^{1}+J^{2}\right)\right)\mathbf{\Phi}_{V}$
0	0	$-\left(\left(\mathbf{\Lambda}_{\eta}^{0}+\mathbf{\Lambda}_{\eta}^{1}\right)/J^{0}\right)\mathbf{\Phi}_{V}$
1	0	$-\left(\left(\mathbf{\Lambda}_{\eta}^{0}+\mathbf{\Lambda}_{\eta}^{1}\right)/\left(J^{0}+J^{1}\right)\right)\mathbf{\Phi}_{V}$
0	1	$-\left(\left(\mathbf{\Lambda}_{\eta}^{0}+\mathbf{\Lambda}_{\eta}^{2}\right)/J^{0}+J^{2}\right)\mathbf{\Phi}_{V}$
1	1	$-\left(\left(\mathbf{\Lambda}_{\eta}^{0}+\mathbf{\Lambda}_{\eta}^{1}+\mathbf{\Lambda}_{\eta}^{2}\right)/J^{0}+J^{1}+J^{2}\right)\mathbf{\Phi}_{V}$

Table 4.1: Point-wise fluxes calculated at point M_i

Fluxes given in table 4.1 are the special cases of the double family of FPS schemes (Edwards and Zheng, 2008, 2010) with the maximum values of flux quadrature parameters. We denote the coordinates of flexible quadrature points within the logical space with $(\hat{\xi},\hat{\eta})$ to differentiate it from the axes of coordinates in logical space (ξ,η). Flux quadrature parameters can vary from zero to unity and are given their maximum values ($\hat{\xi}=1$ and $\hat{\eta}=1$), when the point-wise EMPFA scheme at point M_i is utilised. Fluxes obtained with FPS scheme for each sub-interface on its both facets inside two sub-volumes are given in table 4.2, in which i_{SI} and i_{SV} respectively stands for sub-interface index and sub-volume index. Figure 4.10 shows the position of flux quadrature parameters on sub-interfaces.

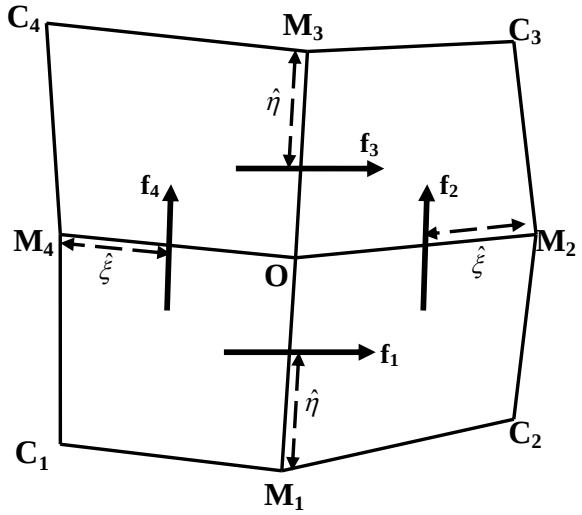

Figure 4.10: Flux quadrature parameters $\left(\hat{\xi},\hat{\eta}\right)$ for FPS scheme

i_{SI}	i_{SV}	F
1	1	$-\left(\left(\mathbf{\Lambda}_\eta^0+\mathbf{\Lambda}_\eta^1+\hat{\eta}\mathbf{\Lambda}_\eta^2\right)/\left(J^0+J^1+\hat{\eta}J^2\right)\right)\mathbf{\Phi}_V$
	2	$-\left(\left(\mathbf{\Lambda}_\eta^0+\hat{\eta}\mathbf{\Lambda}_\eta^2\right)/\left(J^0+\hat{\eta}J^2\right)\right)\mathbf{\Phi}_V$
2	2	$-\left(\left(\mathbf{\Lambda}_\eta^0+\left(1-\hat{\xi}\right)\mathbf{\Lambda}_\eta^1+\mathbf{\Lambda}_\eta^2\right)/\left(J^0+\left(1-\hat{\xi}\right)J^1+J^2\right)\right)\mathbf{\Phi}_V$
	3	$-\left(\left(\mathbf{\Lambda}_\eta^0+\left(1-\hat{\xi}\right)\mathbf{\Lambda}_\eta^1\right)/\left(J^0+\left(1-\hat{\xi}\right)J^1\right)\right)\mathbf{\Phi}_V$
3	3	$-\left(\left(\mathbf{\Lambda}_\eta^0+\left(1-\hat{\eta}\right)\mathbf{\Lambda}_\eta^2\right)/\left(J^0+\left(1-\hat{\eta}\right)J^2\right)\right)\mathbf{\Phi}_V$
	4	$-\left(\left(\mathbf{\Lambda}_\eta^0+\mathbf{\Lambda}_\eta^1+\left(1-\hat{\eta}\right)\mathbf{\Lambda}_\eta^2\right)/\left(J^0+J^1+\left(1-\hat{\eta}\right)J^2\right)\right)\mathbf{\Phi}_V$
4	4	$-\left(\left(\mathbf{\Lambda}_\eta^0+\hat{\xi}\mathbf{\Lambda}_\eta^1\right)/\left(J^0+\hat{\xi}J^1\right)\right)\mathbf{\Phi}_V$
	1	$-\left(\left(\mathbf{\Lambda}_\eta^0+\hat{\xi}\mathbf{\Lambda}_\eta^1+\mathbf{\Lambda}_\eta^2\right)/\left(J^0+\hat{\xi}J^1+J^2\right)\right)\mathbf{\Phi}_V$

Table 4.2: Flexible point-wise fluxes calculated at flux quadrature position points ($\hat{\xi}$ and $\hat{\eta}$)

On the other hand *f* can be obtained from integrating on variable parametric coordinate (ξ or η) over the interval [0,1]. Local mass conservation implies that net flux passing through the common face between two sub-volumes is zero. Equating integrated fluxes from both sides of OM_i segment, "face-wise" family of EMPFA schemes are obtained.

In table 4.3 and table 4.4, formulas for the face-wise fluxes constructed on OM_i segments are given per constant values of ξ and η respectively.

ξ		F
0	$J^2 \neq 0$	$\frac{-1}{J^2}\left(\ln\left(\frac{J^0+J^2}{J^0}\right)\mathbf{\Lambda}_\xi^0+\left(1-\left(\frac{J^0}{J^2}\right)\ln\left(\frac{J^0+J^2}{J^0}\right)\right)\mathbf{\Lambda}_\xi^2\right)\mathbf{\Phi}_V$
	$J^2 = 0$	$-\left(\left(\frac{1}{J^0}\right)\mathbf{\Lambda}_\xi^0+\left(\frac{1}{2J^0}\right)\mathbf{\Lambda}_\xi^2\right)\mathbf{\Phi}_V$
1	$J^2 \neq 0$	$\frac{-1}{J^2}\left(\ln\left(\frac{J^0+J^1+J^2}{J^0+J^1}\right)\left(\mathbf{\Lambda}_\xi^0+\mathbf{\Lambda}_\xi^1\right)+\left(1-\left(\frac{J^0+J^1}{J^2}\right)\ln\left(\frac{J^0+J^1+J^2}{J^0+J^1}\right)\right)\mathbf{\Lambda}_\xi^2\right)\mathbf{\Phi}_V$
	$J^2 = 0$	$-\left(\left(\frac{1}{J^0+J^1}\right)\left(\mathbf{\Lambda}_\xi^0+\mathbf{\Lambda}_\xi^1\right)+\left(\frac{1}{2\left(J^0+J^1\right)}\right)\mathbf{\Lambda}_\xi^2\right)\mathbf{\Phi}_V$

Table 4.3: Face-wise fluxes calculated on OM_i segments with constant ξ

η		f
0	$J^1 \neq 0$	$\frac{-1}{J^1}\left(\ln\left(\frac{J^0+J^1}{J^0}\right)\mathbf{\Lambda}_\eta^0+\left(1-\left(\frac{J^0}{J^1}\right)\ln\left(\frac{J^0+J^1}{J^0}\right)\right)\mathbf{\Lambda}_\eta^1\right)\mathbf{\Phi}_V$
	$J^1 = 0$	$-\left(\left(\frac{1}{J^0}\right)\mathbf{\Lambda}_\eta^0+\left(\frac{1}{2J^0}\right)\mathbf{\Lambda}_\eta^1\right)\mathbf{\Phi}_V$
1	$J^1 \neq 0$	$\frac{-1}{J^1}\left(\ln\left(\frac{J^0+J^1+J^2}{J^0+J^2}\right)\left(\mathbf{\Lambda}_\eta^0+\mathbf{\Lambda}_\eta^2\right)+\left(1-\left(\frac{J^0+J^2}{J^1}\right)\ln\left(\frac{J^0+J^1+J^2}{J^0+J^2}\right)\right)\mathbf{\Lambda}_\eta^1\right)\mathbf{\Phi}_V$
	$J^1 = 0$	$-\left(\left(\frac{1}{J^0+J^2}\right)\left(\mathbf{\Lambda}_\eta^0+\mathbf{\Lambda}_\eta^2\right)+\left(\frac{1}{2\left(J^0+J^2\right)}\right)\mathbf{\Lambda}_\eta^1\right)\mathbf{\Phi}_V$

Table 4.4: Face-wise fluxes calculated on OM_i segments with constant η

4.3.4 Enforcing the Full Flux Continuity Conditions on Sub-interfaces

Each of quadrilateral sub-volumes of interaction region are independently mapped into the standard reference elements. Thereafter each sub-volume has its own local parametric coordinates. Sub-volumes are indexed in the trigonometric order starting from the lowest most left sub-volume. Sub-volume Ω_i will be mapped into a standard reference element in (ξ^i,η^i) plane. Interaction region is built on a node shared by four cells unless for non-matching cells where central node is the common vertex of three cells. We derive the flux continuity equations for interaction regions built on matching cells and later present the modified equations for interaction regions built on non-matching cells.

For each interaction region, degree of freedom (*DoF*) is defined as the number of interfaces converging at its central node. Also number of cells sharing the central node as their common vertex is represented with DoF^C. Indexing of intersecting sub-interfaces follows the trigonometric order starting with sub-interface shared between Ω_1 and Ω_2. Thus each sub-interface Γ_i is defined as the border between two immediate adjacent sub-volumes in their trigonometric order:

$$\Gamma_i = \Omega_i \bigcap \Omega_I \qquad (4.39),$$

where:

$$I = \begin{cases} i+1 & i < DoF^C \\ 0 & i = DoF^C \end{cases} \qquad (4.40).$$

Satisfying mass conservation on each interface immediately implies:

$$\mathbf{f}_{\Gamma_i}\Big|_{\Omega_i} = \mathbf{f}_{\Gamma_i}\Big|_{\Omega_I} \qquad (4.41).$$

Γ_1 is shared by Ω_1 and Ω_2. On both sub-volumes, the value of first local coordinate (ξ^i) is constant over this sub-interface. Table 4.5 shows the corresponding constant values of ξ^i or η^i for the aspect of each sub-interface located in sub-volume Ω_i. Pair of local parametric coordinates for a sub-interface obtained from Table 4.5 is then used to determine the relevant flux term from tables 4.1 or 4.2 (for the flexible point-wise EMPFA scheme) or from tables 4.3 and 4.4 (for the face-wise EMPFA scheme).

i_{SI}	$i_{SV}=i$	ξ^i	η^i
1	1	1	0-1
	2	0	0-1
2	2	0-1	1
	3	0-1	0
3	3	0	0-1
	4	1	0-1
4	4	0-1	0
	0	0-1	1

Table 4.5: Local parametric coordinates for both facets of each sub-interface

We denote $\mathbf{\Phi}_C$ and $\mathbf{\Phi}_F$ as the vector of potentials at cell centres and interfaces respectively. Also Φ_O is denoted as the potential at central point of interaction region. Using these notations and writing down the flux continuity condition for all four sub-interfaces inside the interaction region, one would come up with a system of four equations which relates $\mathbf{\Phi}_C$ to $\mathbf{\Phi}_F$ and Φ_O.

$$\mathbf{A}_1\mathbf{\Phi}_C + \mathbf{B}_1\mathbf{\Phi}_F + \mathbf{L}\Phi_O = \mathbf{A}_2\mathbf{\Phi}_C + \mathbf{B}_2\mathbf{\Phi}_F + \mathbf{R}\Phi_O \tag{4.42}$$

4.3.5 Enforcing the Zero Divergence Condition on the Centre of Interaction Region

$\mathbf{A}_1$, $\mathbf{A}_2$, $\mathbf{B}_1$, $\mathbf{B}_2$ are 4×4 matrices and **L,R** are 4×1 vectors. It is desired to calculate flux as a linear combination of potentials at cell centres only. Thus potentials at interfaces and central point ($\mathbf{\Phi}_F, \Phi_O$) should be expressed in term of potentials at cell centres ($\mathbf{\Phi}_C$). Another equation is needed to eliminate all five temporary unknowns $\left(\Phi_{F_1}, \Phi_{F_2}, \Phi_{F_3}, \Phi_{F_4}, \Phi_O\right)$. Edwards and Zheng [2008, 2010] and et al. [2008] have proposed to obtain the needed auxiliary equation by demanding potential and flux continuity at the centre of interaction region *O*. When point *O* is neither a source nor a sink, differential form of continuity equation is written as:

$$\nabla.\left(-\mathbf{K}\nabla\Phi\right)\Big|_{O} = 0 \qquad (4.43).$$

Based on Gauss divergence theorem, divergence of vector $-\mathbf{K}\nabla\Phi$ at point O can be reinterpreted as the volume density of its normal outward flux at very small control volume surrounding point O. Thus one can write:

$$\lim_{\Omega_O \to O} \frac{\int_{\partial\Omega_O} \left(-\mathbf{K}\nabla\Phi\right).\mathbf{n}d\Gamma}{\Delta V_{\Omega_O}} = 0 \qquad (4.44).$$

Thereafter zero divergence condition can be approximately satisfied over any small control volume surrounding point O. We construct a control volume Ω_O bounded between surfaces connecting starting and ending points of sub-interfaces (M_i). Zero divergence condition on Ω_O would be satisfied on Ω_O when it shrinks to point O.

$$\lim_{\Omega_O \to O} \int_{\partial\Omega_O} \left(-\mathbf{K}\nabla\Phi\right).\mathbf{n}d\Gamma = 0 \qquad (4.45)$$

Ω_O tends to point O when its corner points (D_i) slip along the sub-interfaces from points M_i towards centre of interaction region.

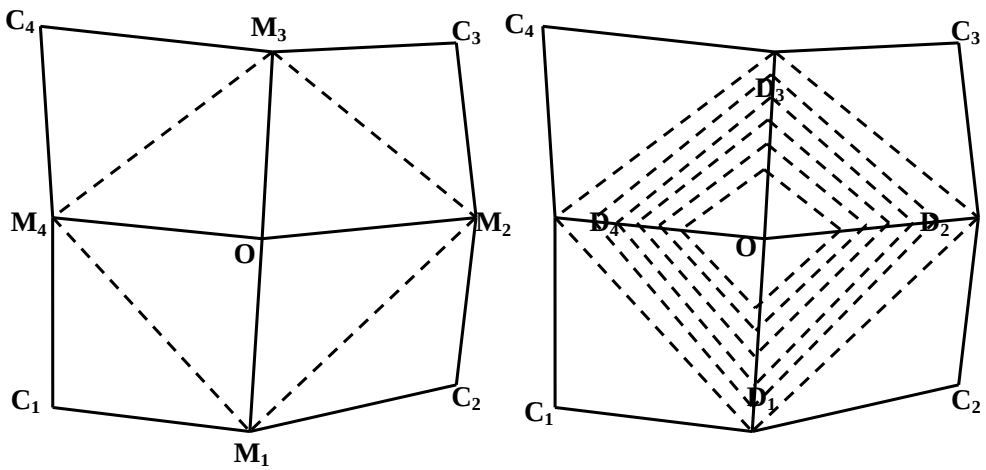

Figure 4.11: Left: Control volume Ω_O surrounding point O shown with dotted line, Right: Ω_O shrinking to point O shown with dotted lines

Eq. 4.45 implies that the net mass flux passing through the borders of Ω_O is zero. Thereafter left hand side of Eq. 4.45 is discretized and reinterpreted as the summation of fluxes at $D_i\, D_{i+1}$ segments.

$$\lim_{\partial\Omega_o \to o} \sum_{\partial\Omega_o} \left(-\mathbf{K}\nabla\Phi\right).\mathbf{n}\Delta\Gamma = \lim_{\partial\Omega_o \to o} \left(\mathbf{f}_{D_1D_2} + \mathbf{f}_{D_2D_3} + \mathbf{f}_{D_3D_4} + \mathbf{f}_{D_4D_0}\right) = 0 \tag{4.46}$$

Segment $D_i\, D_{i+1}$ is inside the $(i+1)^{\text{th}}$ sub-volume and parallel to one of its diagonals. Denoting $\mathbf{\Phi}_V^i = \left(\Phi_1^i, \Phi_2^i, \Phi_3^i, \Phi_4^i\right)^T$ as the potentials at vertices of ith sub-volume, contribution of $(i+1)^{\text{th}}$ sub-volume to the flux at point O can be expressed as the flux passing through $D_i\, D_{i+1}$ when D_i and D_{i+1} approach to each other and to point O.

$$\mathbf{f}_O^{i+1} = \lim_{D_i, D_{i+1} \to O} \mathbf{f}_{D_iD_{i+1}} = -\lim_{D_i, D_{i+1} \to O} \left\{ \int_\Gamma \mathbf{K} \frac{\mathbf{\Psi}}{\det(\mathbf{J})} \cdot \left[\mathbf{n}_\eta d\xi + \mathbf{n}_\xi d\eta\right] \right\}^{i+1} \mathbf{\Phi}_V^{i+1} \tag{4.47}$$

Points D_i are chosen such that at each sub-volume the relative distances of O to D_i and D_{i+1} in logical space are equal. Also points D_i and D_{i+1} approach to O on lines with constant ξ^i or η^i. Therefore the normal vector drawn on segment $D_i\, D_{i+1}$ would comprise both unit normal vectors equally and is located on $\xi^i = \eta^i$ line.

$$\mathbf{f}_O^{i+1} = -\left\{ \mathbf{K}\left(\frac{\mathbf{\Psi}}{\det(\mathbf{J})} \cdot \mathbf{n}_{D_iD_{i+1}} \right) \mathbf{\Phi}_V \right\}_O^{i+1} \underbrace{\lim_{D_i, D_{i+1} \to O} \int_{D_iD_{i+1}} d\xi}_{\varepsilon} \tag{4.48}$$

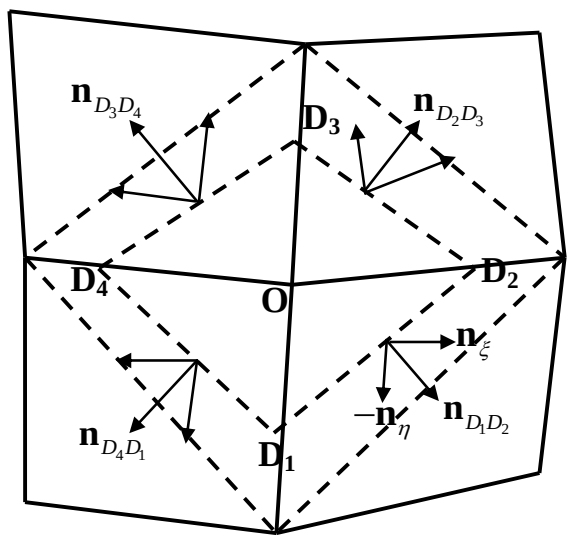

Figure 4.12: Normal outward vector drawn on segment $D_i\, D_{i+1}$

Using Eq. 4.48 flux contributions from all sub-volumes are obtained and put into Eq. 4.46:

$$\lim_{\partial\Omega_o \to o} \sum_{\partial\Omega_o} \left(-\mathbf{K}\nabla\Phi\right).\mathbf{n}\Delta\Gamma = -\varepsilon \sum_{i=1}^{4} \left\{ \mathbf{K}\left(\frac{\mathbf{\Psi}}{\det\left(\mathbf{J}\right)} \cdot \mathbf{n} \right) \mathbf{\Phi}_V \right\}_{\mathrm{O}}^{i} = 0 \qquad (4.49).$$

Term ε approaches zero as Ω_O diminishes to O; but for a very small Ω_O with non-zero volume, ε is not zero. Thus strong zero divergence condition is reduced to an approximate condition which is the fifth equation needed for determining temporary unknown potentials in terms of cell potentials.

$$\sum_{i=1}^{4} \hat{f}_{\mathrm{O}}^{i} = \sum_{i=1}^{4} \left\{ -\mathbf{K}\left(\frac{\mathbf{\Psi}}{\det\left(\mathbf{J}\right)} \cdot \mathbf{n} \right) \mathbf{\Phi}_V \right\}_{\mathrm{O}}^{i} \cong 0 \qquad (4.50)$$

Where $\hat{f}_{\mathrm{O}}^{i}$ is the specific flux entering point O per length of segment $D_{i-1}D_i$. From Figure 4.3 it can be easily recognised that normal vector $\mathbf{n}$ is obtained from vector summation of two unit vectors orienting outward the point O. Each of these unit vectors are either in the same or in the opposite direction of $\left(\mathbf{n}_\eta, \mathbf{n}_\xi\right)$. Equations 4.20, 4.23, 4.31, 4.32 show matrices $\mathbf{\Psi}$, $\mathbf{J}$ and also normal unit vectors $\left(\mathbf{n}_\eta, \mathbf{n}_\xi\right)$ are all dependent on local parametric coordinates at point O. Remembering the trigonometric order of sub-volume vertices, point O gets different pairs of (ξ^i,η^i) at each sub-volume.

i	$\xi_{\mathrm{O}}^{\mathrm{i}}$	$\eta_{\mathrm{O}}^{\mathrm{i}}$	$\mathbf{n}$	$\hat{f}_{\mathrm{O}}^{i}$
1	1	1	$-\left(\mathbf{n}_\xi + \mathbf{n}_\eta\right)$	$-\left(\left(-\mathbf{\Lambda}_\xi^0 - \mathbf{\Lambda}_\xi^1 - \mathbf{\Lambda}_\xi^2 - \mathbf{\Lambda}_\eta^0 - \mathbf{\Lambda}_\eta^1 - \mathbf{\Lambda}_\eta^2\right) / \left(J^0 + J^1 + J^2\right)\right)\mathbf{\Phi}_V$
2	0	1	$\left(\mathbf{n}_\xi - \mathbf{n}_\eta\right)$	$-\left(\left(\mathbf{\Lambda}_\xi^0 + \mathbf{\Lambda}_\xi^2 - \mathbf{\Lambda}_\eta^0 - \mathbf{\Lambda}_\eta^2\right) / \left(J^0 + J^2\right)\right)\mathbf{\Phi}_V$
3	0	0	$\left(\mathbf{n}_\xi + \mathbf{n}_\eta\right)$	$-\left(\left(\mathbf{\Lambda}_\xi^0 + \mathbf{\Lambda}_\eta^0\right) / J^0\right)\mathbf{\Phi}_V$
4	1	0	$-\left(\mathbf{n}_\xi - \mathbf{n}_\eta\right)$	$-\left(\left(-\mathbf{\Lambda}_\xi^0 - \mathbf{\Lambda}_\xi^1 + \mathbf{\Lambda}_\eta^0 + \mathbf{\Lambda}_\eta^1\right) / \left(J^0 + J^1\right)\right)\mathbf{\Phi}_V$

Table 4.6: Local parametric coordinates for centre of interaction region (point O) and corresponding specific fluxes $\hat{f}_{\mathrm{O}}^{i}$

4.3.6 Modified Continuity Equations for Non-matching Cells

Once fitting cut cells to the embedded boundaries, it is very often to come up with non-matching cells. Such cells are also likely to turn up along the fault plane, when cells on fault hanging wall are displaced upward or downward. Interaction regions built on common vertex of non-matching cells comprise sub-volumes from three cells separated with three sub-interfaces. Cells interconnecting through at least one of these interfaces are not natural neighbours based on the numbering of Cartesian cells. Figure 4.13 shows a typical case of non-matching cells. However there are more complex configurations of non-matching cells like non-neighbour connections over the fault plane or the adjacency of a large cell on one of its facets to several smaller cells (case in Local Grid Refinement). Such cases can be conveniently treated via the general procedure explained in this section. In all cases, interaction region is formed by connecting the centre of larger cell on one facet to the centres of smaller cells on another facet and then to mid-points of three interfaces shared by these three cells.

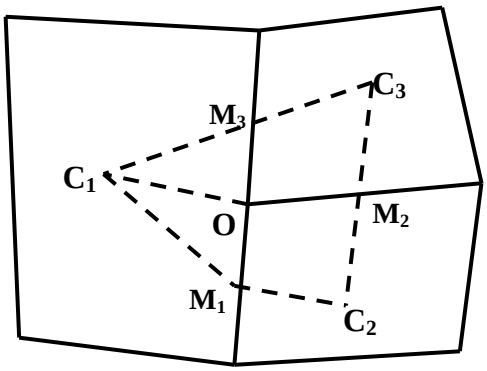

Figure 4.13: Interaction region including non-matching cells shown with dotted lines

Middle points of interfaces of cell 1 shown in figure 4.13 (M_1 and M_3) in most cases are not on the same straight line. In rare cases point O might be a breakage point, but still $\angle M_1OM_3$ is very close to 180°. Thus sub-volume $C_1M_1OM_3$ is a degenerated quadrilateral. It is divided into two triangular sub-volumes along the segment C_1O. Linear approximation of potential is then applied on C_1M_1O and C_1OM_3. Each triangular sub-volume should be mapped into a triangle with unit edges in logical space which is considered as the standard reference element.

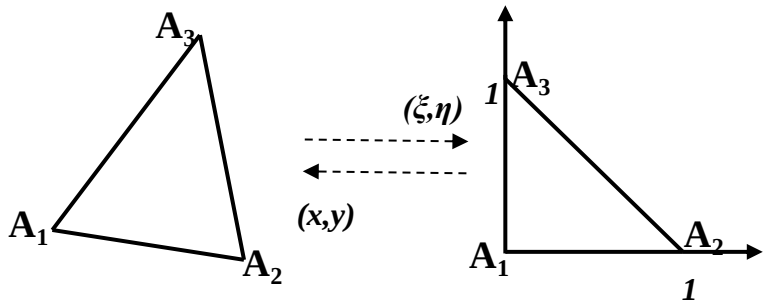

Figure 4.14: Mapping triangle from the computational space into the logical space

Similar assumptions to those proposed for mapping of a quadrilateral would be made. Thus:

- $A_1(x_1,y_1)$ is mapped onto $A_1(0,0)$ in (ξ,η) plane.
- $A_2(x_2,y_2)$ is mapped onto $A_2(1,0)$ in (ξ,η) plane.
- $A_3(x_3,y_3)$ is mapped onto $A_3(0,1)$ in (ξ,η) plane.

Linear expansions of **r** and Φ inside the triangular sub-volume in terms of ξ and η would have the following forms:

$$\mathbf{r} = (1-\xi-\eta)\mathbf{r}_1 + \xi\mathbf{r}_2 + \eta\mathbf{r}_3 \qquad (4.51),$$

$$\Phi = (1-\xi-\eta)\Phi_1 + \xi\Phi_2 + \eta\Phi_3 \qquad (4.52).$$

Eq. 4.51 can be decomposed into two linear interpolations for x and y:

$$\begin{cases} x = \underset{a_1}{x_1} + \underbrace{(x_2 - x_1)}_{a_2}\xi + \underbrace{(x_3 - x_1)}_{a_3}\eta \\ y = \underset{b_1}{y_1} + \underbrace{(y_2 - y_1)}_{b_2}\xi + \underbrace{(y_3 - y_1)}_{b_3}\eta \end{cases} \qquad (4.53).$$

Similar procedure to bilinear potential approximation is followed to produce potential gradient inside the triangle as a linear combination of potentials at vertices.

$$\nabla\mathbf{\Phi} = \frac{\mathbf{\Psi}}{\det(\mathbf{J})}\mathbf{\Phi}_V \qquad (4.54)$$

Where unlike the bilinear potential approximation, matrix $\mathbf{\Psi}$ and Jacobian matrix $\mathbf{J}$ are functions of coefficients of (x,y) linear interpolation and have dependency neither on ξ nor η. In general bilinear interpolation for this case might still work in some cases.

$$\mathbf{\Psi} = \mathbf{\Psi}^0 = \begin{pmatrix} (b_2 - b_3) & b_3 & -b_2 \\ -(a_2 - a_3) & -a_3 & a_2 \end{pmatrix} \tag{4.55}$$

$$\mathbf{J}(x, y) = \begin{pmatrix} \partial x / \partial \xi & \partial y / \partial \xi \\ \partial x / \partial \eta & \partial y / \partial \eta \end{pmatrix} = \begin{pmatrix} a_2 & b_2 \\ a_3 & b_3 \end{pmatrix} \tag{4.56}$$

Depending on trigonometric order of triangle vertices, sun-interfaces (in figure 4.13: segments OM_3 and OM_1) lie on one of two principal axis of logical space or on the hypotenuse of standard reference triangle. Sub-interfaces linear flux then can be expressed as:

$$\mathbf{f} = -\left(\int_0^1 \frac{\mathbf{\Lambda}_\eta^0}{J^0} d\xi + \int_0^1 \frac{\mathbf{\Lambda}_\xi^0}{J^0} d\eta \right) \mathbf{\Phi}_V \tag{4.57}$$

Where $\mathbf{\Lambda}_\eta^0$ and $\mathbf{\Lambda}_\xi^0$ are defined with equations 4.36 and 4.37. One can simply attain Eq. 4.58 flux derived with face-wise EMPFA scheme. Using flexible point-wise EMPFA with quadrature point at ending point of sub-interface (the middle point of primal interface) would lead into the same equations.

$$\mathbf{f} = \begin{cases} \dfrac{-\mathbf{\Lambda}_\eta^0}{J^0} \mathbf{\Phi}_V & \eta = 0 \\ \dfrac{-\mathbf{\Lambda}_\xi^0}{J^0} \mathbf{\Phi}_V & \xi = 0 \\ \dfrac{-\left(\mathbf{\Lambda}_\xi^0 + \mathbf{\Lambda}_\eta^0\right)}{J^0} \mathbf{\Phi}_V & \xi = 1 - \eta \end{cases} \tag{4.58}$$

Once writing down flux continuity condition for three sub-interfaces, one would come up with an equation similar to Eq. 4.20 but with coefficient matrices of different dimensions:

$$\mathbf{A}_1^{3\times3} \mathbf{\Phi}_C^{3\times1} + \mathbf{B}_1^{3\times3} \mathbf{\Phi}_F^{3\times1} + \mathbf{L}^{3\times1} \Phi_O = \mathbf{A}_2^{3\times3} \mathbf{\Phi}_C^{3\times1} + \mathbf{B}_2^{3\times3} \mathbf{\Phi}_F^{3\times1} + \mathbf{R}^{3\times1} \Phi_O \tag{4.59}$$

To eliminate potential at point *O*, again the zero convergence condition is applied on an auxiliary control volume surrounding the centre of interaction region. Figure 4.15 shows how such a control volume can be built for non-matching cells.

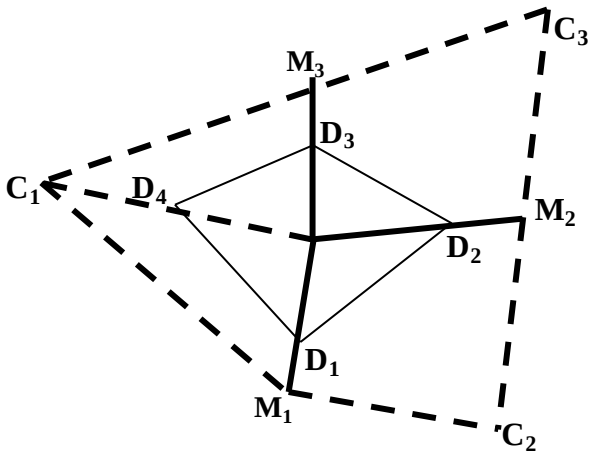

Figure 4.15: Auxiliary $D_1D_2D_3D_4$ control volume used to satisfy zero convergence at *O*

Arbitrary D_i points are selected on OM_i segments such that $|OD_i| = \varepsilon |OM_i|$, except D_4 which is located at distance $\varepsilon |OC_1|$ from the centre of interaction region. Therefore each D_iD_{i+1} segment is parallel to M_iM_{i+1} segment in logical space, where M_4 is replaced with C_1 for non-matching cells. This fact implies that normal vector on segment D_iD_{i+1} would be equated to normal vector on M_iM_{i+1} segment which is a vector combination of unit normal vectors ($\mathbf{n}_\xi$ and $\mathbf{n}_\eta$). Then by letting ε approaches to zero, Eq. 4.50 can be applied as the fifth equation needed. This general procedure can be implemented for full tensor and general geometry problems. However a general FPS scheme for cell-centred triangular grid (with possible non-matching cells) has been developed by Friis and Edwards [2011].

4.4 Discussion of Monotonicity and Stability of extended EMPFA

All the control volume methods explicitly express flux terms of continuity equation in porous media as the linear combination of cell potentials in cell centred grids (or vertex potentials in corner point grids). Equation $-\nabla.(\mathbf{K}\nabla\Phi) = Q$ with non-negative

Dirichlet (or first-type) boundary condition ($\Phi = \Phi_0 \; on \; \partial\Omega$) or Neumann boundary condition ($\nabla\Phi = cte \; on \; \partial\Omega$) is discretized, leading to a system of equation:

$$\bar{\mathbf{A}}\mathbf{\Phi} = \bar{\mathbf{B}} \qquad (4.60),$$

where $\bar{\mathbf{A}}$ and $\bar{\mathbf{B}}$ matrices are the discretized format of operator $\left[-\nabla.\left(\mathbf{K}\nabla\bullet\right)\right]$ and the source term (Q) over the computational grid respectively. As Aavatsmark [2002], Nordbotten [et al 2005, 2007] and Lipnikov et al. [2011] stated, discretized system of equation would satisfy monotonicity condition if and only if the inverse of matrix $\bar{\mathbf{A}}$ has elements all greater than zero. Satisfying $\bar{\mathbf{A}}_{i,j}^{-1} > 0$ would ensure obtaining non-negative potentials if a positive source term and boundary condition has been imposed. Although a positive $\bar{\mathbf{A}}^{-1}$ does not guarantee elimination of all spurious oscillations, but for moderate anisotropic heterogeneous permeability field on grids with small aspect skew, it gives stable potentials. However as Aavatsmark [2002] and Eigestad et al. [2002-A] stated, instability may happen for strong permeability anisotropy and heterogeneity and high grid skewness. A sufficient condition for preventing the spurious extrema presented by Edwards and Rogers [1998], Eigestad et al. [2002-A], Edwards and Zheng [2008] and Lipnikov et al. [2011] is that $\bar{\mathbf{A}}$ is an M-matrix. Positive definite or monotone matrices with non-positive off-diagonal elements are M-matrices. Aavastmark [2002], Nordbotten [et al 2007] have conjectured that M-matrix condition is too restrictive for MPFA O-method and positive off-diagonal elements might be present unless grid is **K**-orthogonal (Heinemann et al., 1991). However whenever $\bar{\mathbf{A}}$ is strictly diagonally dominant for at least one row and $\bar{\mathbf{A}}$ is irreducible, following set of conditions is sufficient for $\bar{\mathbf{A}}$ to be an M-matrix.

$$\begin{cases} \bar{\mathbf{A}}_{i,i} > 0 \;\; \forall i \\ \bar{\mathbf{A}}_{i,j} <= 0 \;\; \forall i, j \;\; j \neq i \\ \sum_i \bar{\mathbf{A}}_{i,j} >= 0 \;\; \forall i \end{cases} \qquad (4.61)$$

According to Edwards and Zheng [2008], local maximum principle (Caffarelli and Carbe, 1995) can be fulfilled with an M-matrix which ensures the stability of solution. Because in absence of source terms ith potential is obtained from

$\left(1/\bar{\mathbf{A}}_{i,i}\right)\sum_{j(i\neq j)}\left(-\bar{\mathbf{A}}_{i,j}\Phi_{i,j}\right)$ which shows $\Phi_{i,i}$ is a weighted average of potentials at adjacent cells. Clearly weights are positive and sum to unity. Thus non-physical solutions are prohibited, because $\Phi_{i,i}$ is bounded between minimum and maximum potential in neighbourhood:

$$\Phi_{\min}^{i,i} \leq \Phi_{i,i} \leq \Phi_{\max}^{i,i} \qquad (4.62).$$

Several schemes were introduced to reduce sensitivity to spurious oscillations where the M-matrix conditions are violated. Among them, flux and matrix splitting scheme introduced by Edwards [1999, 2000, 2001] and Aavatsmark [2002] and developed more by Pal and Edwards [2006-B, 2006-C] were shown to yield stable results for highly anisotropic full permeability tensors. In this method contributions of flux terms related to immediate neighbours are implicitly incorporated into system of equation, while the explicit cross flux terms are inserted in system of equation. As this method creates a similar architecture of solution matrix to that for TPFA, the restrictions on monotonicity are alleviated. Moreover the solution matrix of resulting semi-implicit scheme is sparser and has smaller condition number resulting in higher computational efficiency. Generally flux splitting schemes are more preferable in contrast with grid optimisation techniques (Mlacnik and Durlofsky, 2006) because of imposed maximum principle. In this research we employ flux splitting technique to improve stability and consistency of results for problems suffering restricted M-matrix conditions. More detailed information about flux splitting method is given in Appendix A.

4.4.1 M-matrix Condition of extended EMPFA for Spatially Constant Permeability Tensors on Parallelogram Grid

As the parametric determination of fluxes for varying permeability tensors is tedious, most studies of monotonicity or M-matrix conditions have been limited to spatially constant **K** tensors. Monotonicity is strictly a one-dimensional concept when discussing the numerical solution, so it is not appropriate for analysing the solutions of multi-dimensional problems, as the saddle points might occur. However the only known condition that can ensure a solution consistent with a physical solution that is absent of

spurious oscillations is the M-matrix condition. The crucial conditions for a general single parameter family of MPFA schemes to have M-matrices were first presented in Edwards [1995] and Edwards and Rogers [1998]. While the same single family parameter M-matrix conditions are presented by Nordbotten [et al 2007], the earlier presentations of the conditions are not cited by Nordbotten [et al 2007]. These conditions are derived cell-wise allowing a cell-wise constant variation in the tensor (Edwards, 1995), this is also explained in Edwards and Zheng [2008] in the context of single-parameter family of FPS schemes. More general M-matrix conditions are presented in Edwards and Zheng [2010] for double-parameter family in 2-D and in Edwards and Zheng [2011] for multi-family M-matrix conditions in 3-D. Nordbotten [et al 2007] investigated the solution matrices for general 9-point schemes in homogenous or inhomogeneous media and derived the sufficient criteria of discrete monotonicity. Although apparently these criteria are less restrictive than general M-matrix conditions, but they can only ensure that a positive solution is obtained for a positive $\bar{\mathbf{A}}^{-1}$. Crucially it has not been proven and is generally not known that a scheme with just a monotone matrix will yield a solution free of spurious oscillations; it means that just monotonicity does not yield a local maximum principle as for an M-matrix. However as shown in Edwards and Zheng [2010], the monotone property is enough to prevent fundamental decoupled solution modes occurring, which are an important source of non-physical solutions. Moreover the criteria derived by Nordbotten [et al 2007] are non-linear with respect to off-diagonal elements of $\bar{\mathbf{A}}$. This complicates the monotonicity analysis of MPFA schemes.

In our research, restrictions imposed on M-matrix conditions by grid skewness and non **K**-orthogonality are to some extent mitigated. Because the proposed Cartesian Cut Cell approach would remove the necessity to conform the gridding to the geological layering and allows to create a Cartesian grid with axes overlapping with principal axes of permeability. Thus grid can be **K**-orthogonal mostly everywhere and the chance for disposing of non-physical solutions would be considerably increased. Nevertheless this does not apply to upscaled models from very heterogeneous fine scale permeability maps or models with sharply-dipped layers. Moreover in case of non-localised geological layering with too many layers of different orientations, Cartesian Cut Cell approach would leave grid with cells mostly deformed similar to the unstructured

gridding. Thus **K**-orthogonality is not preserved and M-matrix conditions are still restrictive for getting physical solutions.

Consider uniform parallelogram grid, one can recognise that bilinear relation of computational and logical coordinates on each cell's interface vanishes to a linear relation between corresponding coordinates ($x = a_1 + a_2\xi + a_3\eta$ and $y = b_1 + b_2\xi + b_3\eta$). It means that mapping first rescales and normalizes the computational grid, then rotates the principal axes of grid to a rectangular grid and finally translates it such that first point is located on origin of coordinates in logical space. In effect the non-linear couplings of transmissibility term are avoided. Three auxiliary parameters *U*, *V*, *W* are defined as following which recall the elements of transmissibility matrix in uniform reference space (Eq. 4.7):

$$\begin{aligned} U &= \left(b_3^{\,2}K_h + a_3^{\,2}K_v - 2a_3b_3K_{hv}\right)\big/ J^0 \\ V &= \left(a_2^{\,2}K_v + b_2^{\,2}K_h - 2a_2b_2K_{hv}\right)\big/ J^0 \\ W &= \left(K_{hv}(a_2b_3 + a_3b_2) - (a_2a_3K_v + b_2b_3K_h)\right)\big/ J^0 \end{aligned} \qquad (4.63).$$

Then one can express $\mathbf{\Lambda}_\eta^i$ and $\mathbf{\Lambda}_\xi^i$ for $i = 0,1,2$ from Eq. 4.36 and Eq. 4.37 as:

$$\begin{aligned} \mathbf{\Lambda}_\xi^0 &= J^0\begin{bmatrix} U+W & -U & 0 & -W \end{bmatrix} \\ \mathbf{\Lambda}_\xi^1 &= J^0\begin{bmatrix} -W & W & -W & W \end{bmatrix} \\ \mathbf{\Lambda}_\xi^2 &= J^0\begin{bmatrix} -U & U & -U & U \end{bmatrix} \end{aligned} \qquad (4.64).$$

$$\begin{aligned} \mathbf{\Lambda}_\eta^0 &= J^0\begin{bmatrix} V+W & -W & 0 & -V \end{bmatrix} \\ \mathbf{\Lambda}_\eta^1 &= J^0\begin{bmatrix} -V & V & -V & V \end{bmatrix} \\ \mathbf{\Lambda}_\eta^2 &= J^0\begin{bmatrix} -W & W & -W & W \end{bmatrix} \end{aligned} \qquad (4.65).$$

It can be easily shown that for this simple case face-wise EMPFA scheme is equivalent to flexible point-wise EMPFA with quadrature points at the middle of sub-interfaces ($\hat{\xi} = 1/2$ and $\hat{\eta} = 1/2$). Thus we analyse the M-matrix condition for point-wise EMPFA with arbitrary quadrature points. The resulting **A**, **B**, **C**, **D**, **L**, **R** matrices mentioned in Eq. 4.20 are obtained as followings:

$$\mathbf{A}=\begin{bmatrix}(1-\hat{\eta})U & 0 & 0 & 0\\ 0 & \left(1-\hat{\xi}\right)V & 0 & 0\\ 0 & 0 & -\left(1-\hat{\eta}\right)U & 0\\ 0 & 0 & 0 & -(1-\hat{\xi})V\end{bmatrix} \qquad (4.66),$$

$$\mathbf{B}=\begin{bmatrix}-(1-\hat{\eta})U+W & 0 & 0 & \hat{\eta}U\\ \hat{\xi}V & -\left(1-\hat{\xi}\right)V-W & 0 & 0\\ 0 & -\hat{\eta}U & \left(1-\hat{\eta}\right)U-W & 0\\ 0 & 0 & -\hat{\xi}V & (1-\hat{\xi})V+W\end{bmatrix} \qquad (4.67),$$

$$\mathbf{C}=\begin{bmatrix}0 & -(1-\hat{\eta})U & 0 & 0\\ 0 & 0 & -\left(1-\hat{\xi}\right)V & 0\\ 0 & 0 & 0 & \left(1-\hat{\eta}\right)U\\ (1-\hat{\xi})V & 0 & 0 & 0\end{bmatrix} \qquad (4.68),$$

$$\mathbf{D}=\begin{bmatrix}(1-\hat{\eta})U+W & -\hat{\eta}U & 0 & 0\\ 0 & \left(1-\hat{\xi}\right)V-W & -\hat{\xi}V & 0\\ 0 & 0 & -\left(1-\hat{\eta}\right)U-W & \hat{\eta}U\\ \hat{\xi}V & 0 & 0 & -(1-\hat{\xi})V+W\end{bmatrix} \qquad (4.69),$$

$$\mathbf{L}=\begin{bmatrix}-\hat{\eta}U-W & -\hat{\xi}V+W & \hat{\eta}U+W & \hat{\xi}V-W\end{bmatrix} \qquad (4.70),$$

$$\mathbf{R}=\begin{bmatrix}\hat{\eta}U-W & \hat{\xi}V+W & -\hat{\eta}U+W & -\hat{\xi}V-W\end{bmatrix} \qquad (4.71).$$

Writing down the zero convergence condition over the auxiliary control volume would lead to:

$$\Phi_O=\frac{1}{2\left(U+V\right)}\begin{bmatrix}V & U & V & U\end{bmatrix}\mathbf{\Phi}_F \qquad (4.72).$$

By means of Eq. 4.72 dependency of Eq. 4.42 on Φ_O is removed and it is reduced to a similar format as the MPFA O-method. Thus the transmissibility matrix can be computed from $\mathbf{T} = \mathbf{A} + \mathbf{B}(\mathbf{B} - \mathbf{D})^{-1}(\mathbf{C} - \mathbf{A})$ and sub-interfaces fluxes are expressed as:

$$\begin{bmatrix} \mathbf{f_1} \\ \mathbf{f_2} \\ \mathbf{f_3} \\ \mathbf{f_4} \end{bmatrix} = \frac{1}{4} \begin{bmatrix} (2-\hat{\eta})U + W & -(2-\hat{\eta})U + W & -\hat{\eta}U - W & \hat{\eta}U - W \\ \hat{\xi}V + W & (2-\hat{\xi})V - W & -(2-\hat{\xi})V - W & -\hat{\xi}V + W \\ \hat{\eta}U + W & -\hat{\eta}U + W & -(2-\hat{\eta})U - W & (2-\hat{\eta})U - W \\ (2-\hat{\xi})V + W & \hat{\xi}V - W & -\hat{\xi}V - W & -(2-\hat{\xi})V + W \end{bmatrix} \begin{bmatrix} \Phi_{C_1} \\ \Phi_{C_2} \\ \Phi_{C_3} \\ \Phi_{C_4} \end{bmatrix}$$

(4.73).

A whole cell interface consists of two sub-interfaces from two neighbour interaction regions. Thus in order to set up *m*th row of $\bar{\mathbf{A}}$, fluxes over 8 sub-interfaces are obtained from applying EMPFA on 4 interaction regions built on corner points of *m*th cell with directional indices of (*i*,*j*). Assuming n_x and n_y as the number of divisions in *x* and *y* directions, one can set up table 4.7 for the non-zero element of *m*th row of $\bar{\mathbf{A}}$. This table is comparable with tables obtained by Edwards and Zheng [2010] for double-parameter family of FPS schemes.

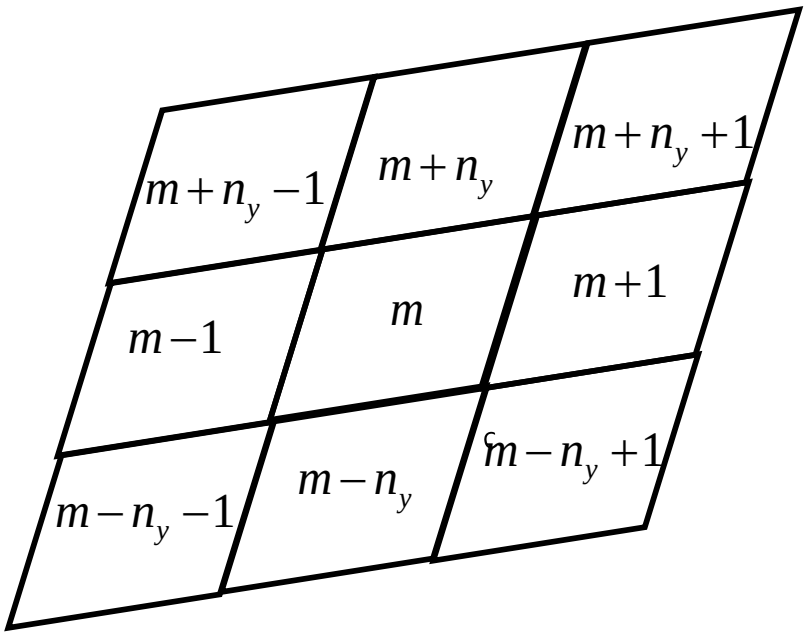

Figure 4.16: Cells in the immediate neighbourhood of *m*th cell contributing to *m*th row of $\bar{\mathbf{A}}$

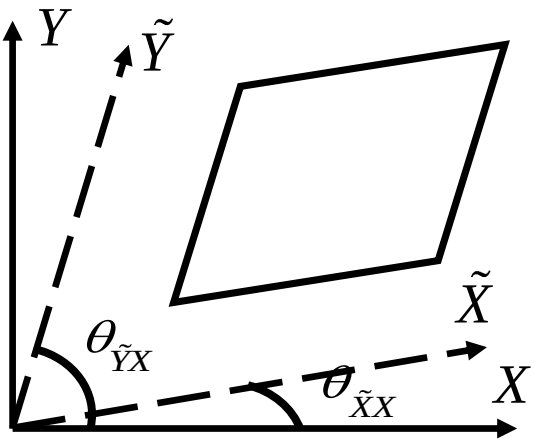

Figure 4.17: Orientation angles of main axes of parallelogram grid $\left(\tilde{X},\tilde{Y}\right)$ with respect to the Cartesian coordinates $\left(X,Y\right)$

Directional indices	Entry of $\bar{\mathbf{A}}$	Point-wise EMPFA
$\left(i-1,j-1\right)$	$\bar{\mathbf{A}}_{m,m-n_x-1}$	$-\frac{1}{4}\left(\hat{\eta}U+\hat{\xi}V\right)-\frac{1}{2}W$
$\left(i,j-1\right)$	$\bar{\mathbf{A}}_{m,m-n_x}$	$-V+\frac{1}{2}\left(\hat{\eta}U+\hat{\xi}V\right)$
$\left(i+1,j-1\right)$	$\bar{\mathbf{A}}_{m,m-n_x+1}$	$-\frac{1}{4}\left(\hat{\eta}U+\hat{\xi}V\right)+\frac{1}{2}W$
$\left(i-1,j\right)$	$\bar{\mathbf{A}}_{m,m-1}$	$-U+\frac{1}{2}\left(\hat{\eta}U+\hat{\xi}V\right)$
$\left(i,j\right)$	$\bar{\mathbf{A}}_{m,m}$	$2\left(U+V\right)-\left(\hat{\eta}U+\hat{\xi}V\right)$
$\left(i+1,j\right)$	$\bar{\mathbf{A}}_{m,m+1}$	$-U+\frac{1}{2}\left(\hat{\eta}U+\hat{\xi}V\right)$
$\left(i-1,j+1\right)$	$\bar{\mathbf{A}}_{m,m+n_x-1}$	$-\frac{1}{4}\left(\hat{\eta}U+\hat{\xi}V\right)+\frac{1}{2}W$
$\left(i,j+1\right)$	$\bar{\mathbf{A}}_{m,m+n_x}$	$-V+\frac{1}{2}\left(\hat{\eta}U+\hat{\xi}V\right)$
$\left(i+1,j+1\right)$	$\bar{\mathbf{A}}_{m,m+n_x+1}$	$-\frac{1}{4}\left(\hat{\eta}U+\hat{\xi}V\right)-\frac{1}{2}W$

Table 4.7: Entries of *m*th row of $\bar{\mathbf{A}}$ with point-wise EMPFA (quadrature points $\left(\hat{\xi},\hat{\eta}\right)$)

These coefficients are in accordance with the formalism of the double family fluxes with Control Volume Finite Element Method (CVFE) developed by Edwards and Zheng [2010]. CVFE methods are presented and developed by Edwards [1995, 1998-B, 2000]. The local CVFE coordinates (ζ, ς) are defined with a bilinear mapping over whole the quadrilateral interaction region.

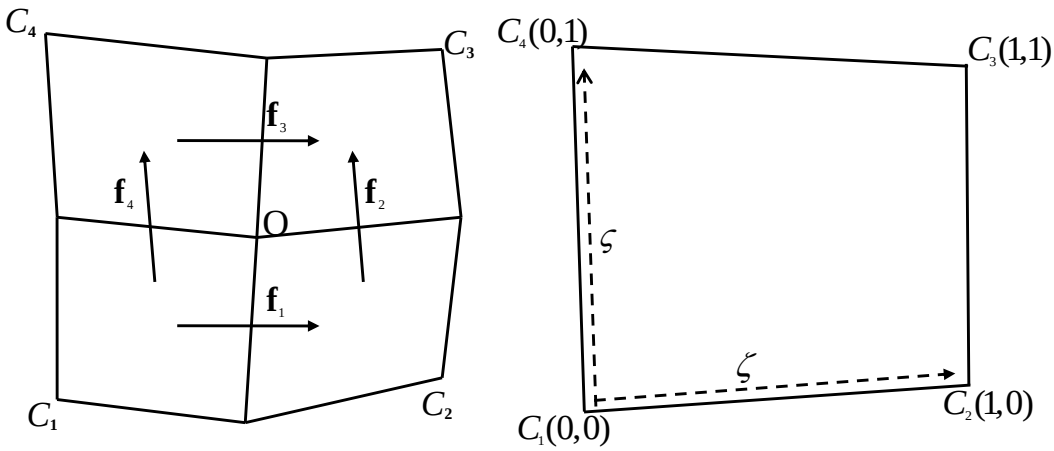

Figure 4.18: Local CVFE coordinates defined on built on four cells sharing vertex *O*

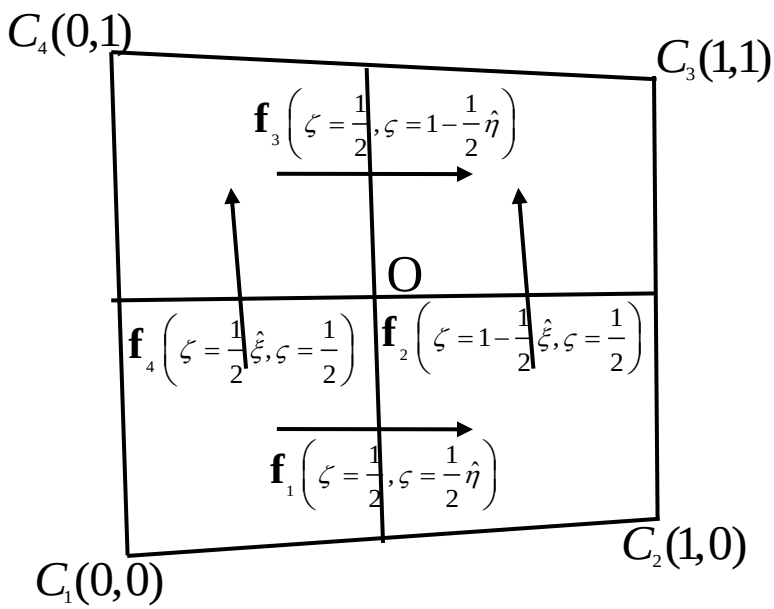

Figure 4.19: Flux quadrature points expressed in terms of local CVFE coordinates

As shown in figure 4.18, in general CVFE cannot cover the possible irregularities of four sub-cells included in the interaction region, when it is used for cell centred grid. However for corner point grid, the primal quadrilateral cell is itself an interaction region which is conformally is mapped into local CVFE coordinates. Edward and Zheng [2008] and Durlofsky [1994] stated that CVFE is locally conservative but does not assure the flux continuity when permeability is discontinuous across the interfaces. So although CVFE is not well-suited for flow modelling in porous media, but for constant permeability fields, but flux continuous schemes can be reformulated in terms of a more transparent nine-point CVFE scheme. Edwards and Zheng [2008, 2010, 2011] have presented single, double and multiple families of CVFE schemes corresponding to isotropic and anisotropic quadrature points respectively. As defined by Edwards and Zheng [2010], anisotropy of quadrature points is recognised with non-equal quadrature points on sun-interfaces involved in interaction region ($\hat{\xi} \neq \hat{\eta}$).

The positive-definiteness of solution matrix ($\bar{\mathbf{A}}$) has been proved by Edwards [1995] for those created with CVFE scheme and by Edwards and Pal [2008] for single-parameter family of MPFA schemes by demonstrating the positivity of corresponding discrete cell energy ($\mathbf{\Phi}^{\mathbf{T}}\bar{\mathbf{A}}\mathbf{\Phi}$) conditioned to a spatially constant elliptic transmissibility tensor ($T_{12}^{\ 2} < T_{11}T_{22}$ or equivalently $W^2 \leq UV$). Also symmetry of solution matrix can be investigated by calculating the corresponding entry of transposed solution matrix ($\bar{\mathbf{A}}_{i,j}^{T} = \bar{\mathbf{A}}_{j,i}$) per each off-diagonal entry of *m*th row of $\bar{\mathbf{A}}$ given in table 4.7. One can diagnose the following set of equalities between four pairs of off-diagonal entries of *m*th row of $\bar{\mathbf{A}}$, this implies the symmetry of solution matrix.

$$\begin{cases} \bar{\mathbf{A}}_{m,m-n_x-1} = \bar{\mathbf{A}}_{m,m+n_x+1} \\ \bar{\mathbf{A}}_{m,m-n_x} = \bar{\mathbf{A}}_{m,m+n_x} \\ \bar{\mathbf{A}}_{m,m-n_x+1} = \bar{\mathbf{A}}_{m,m+n_x-1} \\ \bar{\mathbf{A}}_{m,m-1} = \bar{\mathbf{A}}_{m,m+1} \end{cases} \tag{4.74}$$

In accordance to Edwards and Zheng [2008], flexible point-wise EMPFA scheme results in symmetric positive definite solution matrix for constant tensors. According to

Edwards and Zheng [2010], the non-positivity of off-diagonal entries is assured by holding the following conditions:

$$\begin{cases} \bar{\mathbf{A}}_{m,m-1} = -U + \frac{1}{2}\left(\hat{\eta}U + \hat{\xi}V\right) \le 0 \\ \bar{\mathbf{A}}_{m,m-n_x} = -V + \frac{1}{2}\left(\hat{\eta}U + \hat{\xi}V\right) \le 0 \\ \bar{\mathbf{A}}_{m,m-n_x-1} = -\frac{1}{4}\left(\hat{\eta}U + \hat{\xi}V\right) - \frac{1}{2}W \le 0 \\ \bar{\mathbf{A}}_{m,m-n_x+1} = -\frac{1}{4}\left(\hat{\eta}U + \hat{\xi}V\right) + \frac{1}{2}W \le 0 \end{cases} \quad (4.75).$$

The M-matrix conditions derived in Edwards and Zheng [2010] for the double-parameter family of EMPFA schemes are stated here in Eq. 4.76, where $U = T_{11}, V = T_{22}$, $W = T_{12}$ and $\hat{\xi} = \xi/2$, $\hat{\eta} = \eta/2$.

$$|W| \le \frac{1}{2}\left(\hat{\eta}U + \hat{\xi}V\right) \le Min\left(U,V\right) \quad (4.76)$$

Thus for small or zero off-diagonal coefficient of mapped transmissibility matrix $\left(|W|\right)$, M-matrix condition would be maintained with proper choice of flux quadrature points $\left(\hat{\xi},\hat{\eta}\right)$, such that term $(1/2)\left(\hat{\eta}U + \hat{\xi}V\right)$ satisfies the obtained inequality. For face-wise EMPFA ($\hat{\xi} = 1/2, \hat{\eta} = 1/2$), the M-matrix conditions are expressed as:

$$\begin{aligned} &1)\ \left(Max\left(U,V\right)/Min\left(U,V\right)\right) \le 3 \\ &2)\ |W| \le (1/4)\left(U+V\right) \end{aligned} \quad (4.77).$$

Second condition of Eq. 4.77 is restrictive on off-diagonal elements of mapped transmissibility tensor and it is very likely to be violated in presence of strong permeability anisotropy and large grid aspect ratio, moreover for ratios of maximum to minimum diagonal greater than 3, two matrix coefficients related to immediate neighbours of cell *(i,j)* (both either in vertical direction or horizontal direction depending on maximum diagonal) would be non-negative.

As Edwards and Zheng [2008, 2010, 2011] stated, one essential inequality obtained between the lower and upper bounds of term $(1/2)\left(\hat{\eta}U+\hat{\xi}V\right)$ ($|W|\le Min(U,V)$) ascertains the tensor ellipticity ($W^2\le UV$). This condition is likely to be violated in presence of highly anisotropic permeability fields coupled with high grid aspect ratios. For specific case of uniform rectangular grid the ellipticity condition of transmissibility matrix in logical space reduces to the ellipticity condition of permeability matrix in computational space ($K_{hv}^2\le K_hK_v$). As we discussed in chapter 3, Cartesian Cut Cell approach accommodates a permeability tensor in computational grid with zero or small off-diagonal entries ($K_{hv}\le Min\left(K_h,K_v\right)$) even in the vicinity of complicated cross beddings (curved boundaries of layers, pinched out layers or reservoir top and bottom structures), as it leaves a Cartesian grid with axes of coordinates aligned to the principal axes of permeability tensor. Though for sharply dipped anticline reservoirs with layers oriented with respect to the horizontal axis ($\theta_{\tilde{X}X}>10^{\circ}$), the principal axes of measured permeability tensor are expected to be conforming to the coordinates attached to the layer direction. Consequently off-diagonal elements of rotated permeability matrix in coordinates of Cartesian grid are non-zero. Non-zero cross terms in permeability tensor are retained and might be amplified after upscaling of an anisotropic heterogeneous permeability field (Lee et al., 1998, Wen et al., 2000). As in this thesis we will restrict our modelling to gently dipped bedding layers with orientation angles less than $5°$, the natural coordinate for permeability tensor can be considered the same as that of grid architecture. Therefore the off-diagonal term of permeability tensor can be set zero.

Therefore, the simplified diagonal and off-diagonal terms of mapped transmissibility matrix for the range of problems studied in this thesis, will be expressed as:

$$\begin{aligned} U &= \left(b_3^{\,2}K_h+a_3^{\,2}K_v\right)\big/J^0 \\ V &= \left(a_2^{\,2}K_v+b_2^{\,2}K_h\right)\big/J^0 \\ W &= -\left(a_2a_3K_v+b_2b_3K_h\right)\big/J^0 \end{aligned} \qquad (4.78).$$

The inequality for the upper bound of term $(1/2)\left(\hat{\eta}U+\hat{\xi}V\right)$ is fulfilled if and only if:

$$\begin{cases} \frac{1}{2}\left(\hat{\eta}U+\hat{\xi}V\right)\le U \Rightarrow \frac{\hat{\xi}}{2-\hat{\eta}}\le\frac{U}{V} \;\; if \;\; U=Min\left(U,V\right) \\ \frac{1}{2}\left(\hat{\eta}U+\hat{\xi}V\right)\le V \Rightarrow \frac{\hat{\eta}}{2-\hat{\xi}}\le\frac{V}{U} \;\; if \;\; \mathrm{V}=Min\left(U,V\right) \end{cases} \qquad (4.79).$$

To specify the optimum values of quadrature points, one can set one quadrature parameter and obtain the other one. A simple choice is to let term $\left(1/2\right)\left(\hat{\eta}U+\hat{\xi}V\right)$ tends to its upper limit. So one assign let the quadrature parameter multiplying the minimum diagonal term approaching one and select the other quadrature parameter from the interval allowed by the obtained inequality:

- For $U=Min\left(U,V\right)$, $\hat{\eta}$ approaches to one, while $\hat{\xi}$ varies in the interval $\left[0,\frac{U}{V}\right]$.
- For $V=Min\left(U,V\right)$, $\hat{\xi}$ approaches to one, while $\hat{\eta}$ varies in the interval $\left[0,\frac{V}{U}\right]$.

A specific choice would be obtained by letting the variable quadrature parameter (multiplier of maximum diagonal term) approaching to its allowable upper limit ($Min\left(U,V\right)/Max\left(U,V\right)$). As stated by Edwards and Zheng [2008, 2010], the resulting variable quadrature parameter would approaches zero, when $Min\left(U,V\right)/Max\left(U,V\right)$ decreases in presence of an almost isotropic permeability field ($K_h \cong K_v$) and very large grid aspect ratio ($\left(a_2/b_3\right)>>1$). The coefficients of this scheme (called *H/I-support scheme* in terminology of Edwards and Zheng, 2008, 2010) for both choices of maximum diagonal have been given in table 4.8.

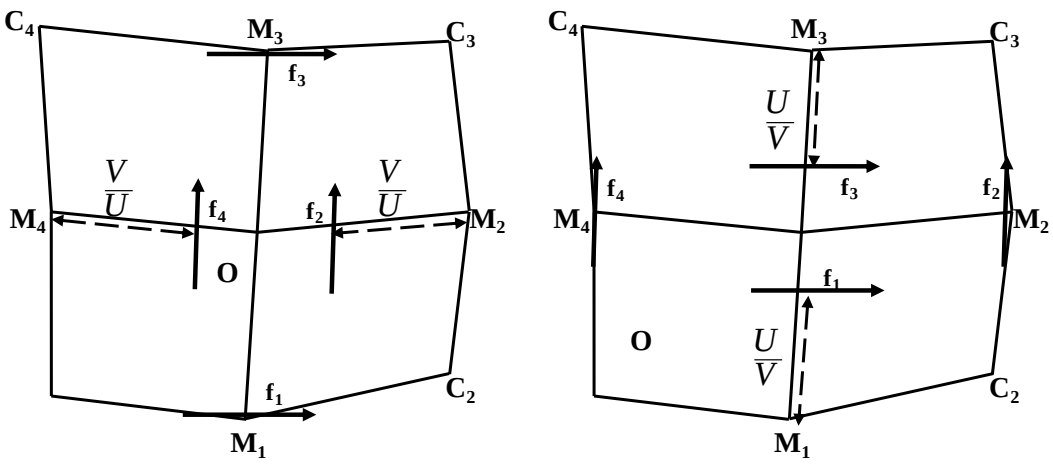

Figure 4.20: Optimum quadrature points, Left: H-support scheme $\left(\hat{\xi} \to 1, \hat{\eta} = (V/U)\right)$ for $V = Min(U,V)$ and Right: I-support scheme $\left(\hat{\xi} = (U/V), \hat{\eta} \to 1\right)$ for $U = Min(U,V)$

Directional indices	H-scheme ($V = Min(U,V)$)	I-scheme($U = Min(U,V)$)
$(i-1, j-1)$	$-\frac{1}{2}V - \frac{1}{2}W$	$-\frac{1}{2}U - \frac{1}{2}W$
$(i, j-1)$	0	$-V + U$
$(i+1, j-1)$	$-\frac{1}{2}V + \frac{1}{2}W$	$-\frac{1}{2}U + \frac{1}{2}W$
$(i-1, j)$	$-U + V$	0
(i, j)	$2U$	$2V$
$(i+1, j)$	$-U + V$	0
$(i-1, j+1)$	$-\frac{1}{2}V + \frac{1}{2}W$	$-\frac{1}{2}U + \frac{1}{2}W$
$(i, j+1)$	0	$-V + U$
$(i+1, j+1)$	$-\frac{1}{2}V - \frac{1}{2}W$	$-\frac{1}{2}U - \frac{1}{2}W$

Table 4.8: Entries of *m*th row of $\bar{\mathbf{A}}$ with H/I-schemes to fulfil M-matrix conditions

Moreover the condition for the lower bound of term $(1/2)\left(\hat{\eta}U+\hat{\xi}V\right)$ would be met by constraining the off-diagonal term to be bounded by the half of minimum diagonal term.

$$|W| \le Min(U,V) \Rightarrow \begin{cases} |W| \le U \\ |W| \le V \end{cases} \tag{4.80}$$

These conditions would reduce to two quadratic inequalities with respect to $x_\eta = a_3$ and $y_\xi = b_2$ as the parameters determining the grid skewness (grid deviation from the state of rectangular Cartesian grid).

$$\begin{aligned} &K_v a_3^2 - a_2 K_v a_3 + (b_3^2 K_h - K_h b_2 b_3) \ge 0 \\ &K_h b_2^2 - b_3 K_h b_2 + (a_2^2 K_v - K_v a_2 a_3) \ge 0 \end{aligned} \tag{4.81}$$

These inequalities would be held for all values of a_3 and b_2, if:

$$\begin{aligned} &\Delta_1' = a_2^2 K_v^2 - 4b_3^2 K_h K_v + 4b_3 b_2 K_v K_h \le 0 \\ &\Delta_2' = b_3^2 K_h^2 - 4a_2^2 K_h K_v + 4a_2 a_3 K_v K_h \le 0 \end{aligned} \tag{4.82}$$

We now define a new parameter $\lambda = (a_2/b_3)^2 (K_v/K_h)$ as a dimensionless measure of grid aspect ratio (a_2/b_3) and anisotropy ratio (K_v/K_h). Criteria in Eq. 4.76 would be met if the following conditions for λ is satisfied:

$$\begin{cases} \lambda \ge \dfrac{1}{4}\left(1-\left(\dfrac{a_3}{a_2}\right)\right)^{-1} \\ \lambda \le 4\left(1-\left(\dfrac{b_2}{b_3}\right)\right) \end{cases} \tag{4.83}$$

$2a_2$ and $2b_3$ express the extension of parallelogram cell in horizontal and vertical directions (X and Y) respectively. So they are attributed to the maximum difference of x-coordinate and y-coordinate along the cell in the respective direction of Cartesian coordinates ($a_2 = x_\xi = x_2 - x_1, b_3 = y_\eta = y_4 - y_1$). On the other hand $2a_3$ and $2b_2$ give respectively the maximum x-coordinate difference of cell in vertical direction ($a_3 = x_\eta = (x_4 - x_1)$) and maximum y-coordinate difference of cell in horizontal direction ($b_2 = y_\xi = (y_2 - y_1)$). Thus ratios (a_3/a_2) and (b_2/b_3) provides measurements of grid

skewness in horizontal and vertical directions respectively. Knowing the variation ranges of $\left(1-\left(a_3/a_2\right)\right)^{-1}$ and $\left(1-\left(b_2/b_3\right)\right)$, one can determine the range allowed for λ such that Eq. 4.76 and consequently M-matrix conditions are satisfied.

In models honouring the geological structures, non-zero b_2 is obtained at cells conforming to the surface of beddings not aligned to the horizontal direction (X). Remembering the maximum value of $\theta_{\tilde{X}X}$ for bedding layers proposed to be modelled in this thesis ($5°$), $|b_2|$ would have a maximum of $\tan(5°)a_2 \cong 0.1a_2$. Also non-zero values of a_3 turn up at cells conforming to surface of non-vertical fault. Faults usually are dipped at small angles with respect to vertical direction. Obviously $|a_3|$ reaches its maximum value of b_3 for the minimum value of fault dip angle which is assumed $45°$.

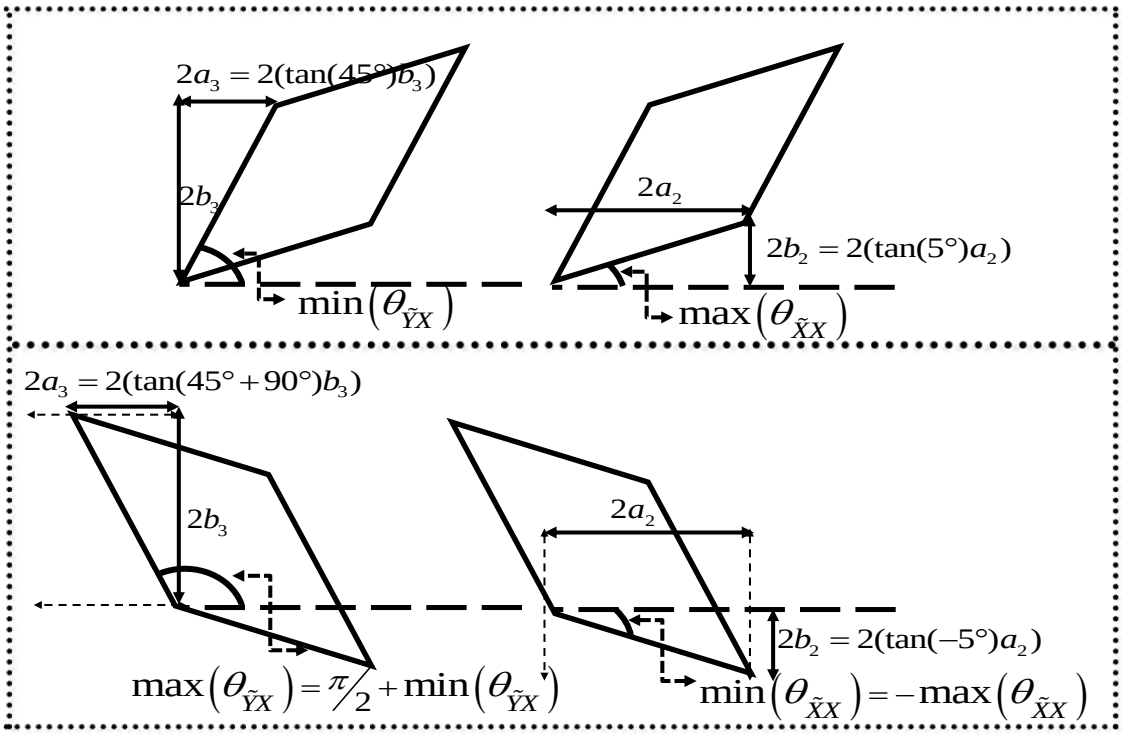

Figure 4.21: Maximum values of a_3 and b_3 corresponding to the minimum fault dip and maximum bedding dip (top picture) and Minimum values of a_3 and b_3 corresponding to the maximum fault dip and minimum bedding dip

From the discussion above, the variation ranges of terms $\left(1-\left(a_3/a_2\right)\right)^{-1}$ and $\left(1-\left(b_2/b_3\right)\right)$ are determined as followings:

$$\begin{cases} \left(1+\left(\dfrac{b_3}{a_2}\right)\right)^{-1} \le \left(1-\left(\dfrac{a_3}{a_2}\right)\right)^{-1} \le \left(1-\left(\dfrac{b_3}{a_2}\right)\right)^{-1} \\ \left(1-0.1\left(\dfrac{a_2}{b_3}\right)\right) \le \left(1-\left(\dfrac{b_2}{b_3}\right)\right) \le \left(1+0.1\left(\dfrac{a_2}{b_3}\right)\right) \end{cases} \quad (4.84).$$

Resulting inequalities removes the dependency of desired M-matrix condition to a_3 and b_2 and reduces it to a relation in terms of anisotropy ratio and cell aspect ratio only. Eventually M-matrix condition of proposed H/I schemes is expressed as:

H/I schemes developed for reservoir models having diagonal permeability tensor would satisfy M-matrix conditions for a parallelogram grid, if:

$$\frac{1}{4}\left(1-\left(\frac{a_2}{b_3}\right)^{-1}\right)^{-1} \le \left(\frac{a_2}{b_3}\right)^2 \frac{K_v}{K_h} \le 4\left(1-0.1\left(\frac{a_2}{b_3}\right)\right) \quad (4.85).$$

The optimum range of cell aspect ratio $\left(a_2/b_3\right)$ fulfilling the M-matrix conditions can be obtained by manual assessment of Eq. 4.85 for different values of cell aspect ratio at a given anisotropy ratio or by simultaneous solving both inequalities. In table 4.9 the allowable ranges of cell aspect ratio for four typical values of anisotropy ratio are given.

$\left(\dfrac{K_h}{K_v}\right)$	$\left(\dfrac{a_2}{b_3}\right)_{\min}^{M-matrix}$	$\left(\dfrac{a_2}{b_3}\right)_{\max}^{M-matrix}$
1	1.21	1.81
10	2.16	4.63
100	5.53	8.28
1000	-	-

Table 4.9: Allowable ranges of grid aspect ratio at different orders of magnitude of anisotropy ratio for H/I scheme

With trial and error, one can determine $\left(K_h/K_v\right) \cong 308$ as the upper limit of anisotropy ratio at which a range of grid aspect ratio fulfilling the M-matrix condition can be found. Though at higher anisotropies, M-matrix range of aspect ratios includes values less than unity which is not applicable, as the reservoir models are extended hundreds or thousands meters in horizontal direction, while usually their vertical extension is less than tens of meters. What makes the aspect ratio larger is the demand for representation of different layers having different rock properties with small grid divisions in vertical direction. Failure to maintain the upper limit of λ prevents from obtaining acceptable aspect ratios for highly anisotropic fields from Eq. 4.85. Accordingly this means that cross term of Piola tensor is not less than minimum diagonal ($|W| > Min(U,V)$).

It can be shown that for a wide range of reservoir simulation problems $Min(U,V) = U$. From Eq. 4.63 (written for non-zero cross permeability) and propositions made for grid skewness, one can show that:

$$\begin{aligned} U^{\max} &= b_3^2 K_h \left(1 + \frac{K_v}{K_h}\cot^2\left(\theta_{\tilde{Y}X}^{\min}\right) + 2\frac{K_{hv}}{K_h}\left|\cot\left(\theta_{\tilde{Y}X}^{\min}\right)\right|\right) \\ V^{\min} &= a_2^2 K_v \left(1 + \frac{K_h}{K_v}\tan^2\left(\theta_{\tilde{X}X}^{\max}\right) - 2\frac{K_{hv}}{K_v}\left|\tan\left(\theta_{\tilde{X}X}^{\max}\right)\right|\right) \end{aligned} \qquad (4.86).$$

Remembering the constraint imposed by tensor ellipticity proposition on upper limit of cross permeability ($|K_{hv}| \le \sqrt{K_h K_v}$), extreme values of diagonal element of mapped transmissibility are expressed as:

$$\begin{aligned} U^{\max} &= b_3^2 K_h \left(1 + \sqrt{\frac{K_v}{K_h}}\left|\cot\left(\theta_{\tilde{Y}X}^{\min}\right)\right|\right)^2 \\ V^{\min} &= a_2^2 K_v \left(1 - \sqrt{\frac{K_h}{K_v}}\left|\tan\left(\theta_{\tilde{X}X}^{\max}\right)\right|\right)^2 \end{aligned} \qquad (4.87).$$

Thus V is the maximum diagonal of mapped transmissibility matrix, if $U^{\max} < V^{\min}$ and hence grid aspect ratio must meet the following condition:

$$\frac{a_2}{b_3} > \frac{\left(\sqrt{\frac{K_h}{K_v}} + \left|\cot\left(\theta_{\tilde{Y}X}^{\min}\right)\right|\right)}{\left|\sqrt{\frac{K_h}{K_v}}\left|\tan\left(\theta_{\tilde{X}X}^{\max}\right)\right| - 1\right|} \qquad (4.88).$$

Away from the root of denominator of Eq. 4.87 (occurring at $\left|\tan\left(\theta_{\tilde{X}X}^{\max}\right)\right| \approx \sqrt{K_v/K_h}$), choosing an adequately large grid aspect ratio (which is common in the reservoir simulation), Eq. 4.87 is satisfied and V becomes the maximum diagonal.

Edwards and Zheng [2008, 2010] have developed *optimal support scheme* applicable to any tensor which leads to an M-matrix for cross term $|W| < Min(U,V)$. Quadrature points are chosen such that absolute value of cross term tends to its upper M-matrix limit ($(1/2)\left(\hat{\eta}U + \hat{\xi}V\right)$). This leads to a 7-point scheme (given in table 4.10) which is either diagonally upward positive-angle support for positive W or diagonally downward negative-angle triangle support for negative W.

Directional indices	$W > 0$	$W < 0$
$(i-1, j-1)$	$-W$	0
$(i, j-1)$	$-V+W$	$-V-W$
$(i+1, j-1)$	0	W
$(i-1, j)$	$-U+W$	$-U-W$
(i, j)	$2(U+V)-2W$	$2(U+V)+2W$
$(i+1, j)$	$-U+W$	$-U-W$
$(i-1, j+1)$	0	W
$(i, j+1)$	$-V+W$	$-V-W$
$(i+1, j+1)$	$-W$	0

Table 4.10: Entries of mth row of $\bar{\mathbf{A}}$ with optimal support scheme

According to tables 4.8 and 4.10, using H/I scheme or optimal support scheme for highly anisotropic non-diagonal tensors ($|W| > Min(U,V) = U$) is likely to yield two positive off-diagonal coefficients depending on the sign of W. A beneficial choice for such tensors is the *extreme anisotropic quadrature scheme* proposed by Edwards and Zheng [2010]. In this approach only the lower limit of M-matrix condition (Eq. 4.76) is supposed to be fulfilled. So quadrature parameters are selected such that term $(1/2)\left(\hat{\eta}U + \hat{\xi}V\right)$ approaches to $(1/2)Max(U,V)$. Quadrature parameter multiplying the maximum diagonal is maximised, while the quadrature multiplying the minimum diagonal is set to zero. Such a scheme results in stencil of coefficients different from that of H/I scheme given in table 4.11. As a preference, unlike the H/I scheme and optimal support scheme, extreme anisotropic quadrature scheme is not dependent on individual diagonal values of mapped transmissibility matrix and is specified only with the maximum diagonal.

The resulting coefficients for all non-immediate neighbours ($(i-1, j-n_x), (i+1, j-n_x)$, $(i-1, j+n_x)$, $(i+1, j+n_x)$) are strictly positive. However for $Max(U,V) > 2Min(U,V)$, a pair of coefficients for immediate neighbours ($(i-1, j)$ & $(i+1, j)$ or $(i, j-n_x)$ & $(i, j+n_x)$) are positive. As expressed by Edwards and Zheng [2008, 2010, 2011], this observation motivates for defining *Quasi M-matrix* (*QM-matrix*) with at maximum two positive off-diagonal elements violating the M-matrix conditions.

Edwards and Zheng [2008, 2010] have applied extreme anisotropic quadrature scheme for several examples of 2-D models having strong anisotropic full permeability tensors and have shown that sharply resolved potential fields with ignorable spurious oscillations can be obtained even beyond the M-matrix condition bounds (for whole ellipticity region) if the solution matrix matches the quasi positive QM-matrix criteria. Thus strong M-matrix conditions for a physical and monotonic solution of elliptic equation of potential in porous media can be mitigated to weaker quasi positive QM-matrix condition which requires:

$$\hat{\xi} = \delta\left(V, Max(U,V)\right)$$
$$\hat{\eta} = \delta\left(U, Max(U,V)\right) \qquad (4.89).$$
$$|W| \le \frac{1}{2} Max(U,V)$$

In which $\delta(\alpha,\beta)$ is the Kronecker delta function returning unity for $\alpha = \beta$ and zero for any other values of α. Such a criterion still preserves the ellipticity condition.

Directional indices	$V = Min(U,V)$	$U = Min(U,V)$
$(i-1, j-1)$	$-\frac{1}{4}U - \frac{1}{2}W$	$-\frac{1}{4}V - \frac{1}{2}W$
$(i, j-1)$	$-V + \frac{1}{2}U$	$-\frac{1}{2}V$
$(i+1, j-1)$	$-\frac{1}{4}U + \frac{1}{2}W$	$-\frac{1}{4}V + \frac{1}{2}W$
$(i-1, j)$	$-\frac{1}{2}U$	$-U + \frac{1}{2}V$
(i, j)	$(U + 2V)$	$(2U + V)$
$(i+1, j)$	$-\frac{1}{2}U$	$-U + \frac{1}{2}V$
$(i-1, j+1)$	$-\frac{1}{4}U + \frac{1}{2}W$	$-\frac{1}{4}V + \frac{1}{2}W$
$(i, j+1)$	$-V + \frac{1}{2}U$	$-\frac{1}{2}V$
$(i+1, j+1)$	$-\frac{1}{4}U - \frac{1}{2}W$	$-\frac{1}{4}V - \frac{1}{2}W$

Table 4.11: Entries of *m*th row of $\bar{\mathbf{A}}$ with extreme anisotropic quadrature scheme

For the reservoir models studied in this thesis with the assumption proposed for maximum grid skewness (figure 4.21) and cross permeability, it can be easily demonstrated that $|W| \le (1/2)Max(U,V) = (1/2)V$. The maximum value of $|W|$ obtained for $a_3 = b_3$ and $b_2 = 0.1a_2$ is $a_2 b_3 (K_v + 0.1K_h)$, while the minimum value of V obtained

for $b_2 = 0$ is $a_2{}^2 K_v$. To satisfy QM-matrix condition, maximum value of $|W|$ should be less than half of minimum value of V. Therefore:

$$\frac{a_2}{b_3} \geq 2\left(1 + 0.1\frac{K_h}{K_v}\right) \qquad (4.90).$$

This condition allows high aspect ratios for any anisotropy ratio. However for any other grid skewness (arbitrary values of $\theta_{\tilde{X}X}^{\max}$ and $\theta_{\tilde{Y}X}^{\min}$), the derivation is completely similar and after a few manipulations we come up with the general form of Eq. 4.90 for more skewed grids ($\theta_{\tilde{Y}X}^{\min} \leq 45°$ and $\theta_{\tilde{X}X}^{\max} \geq 5°$) which is written as:

$$\frac{a_2}{b_3} \geq 2\left(\left|\cot\left(\theta_{\tilde{Y}X}^{\min}\right)\right| + \left|\tan\left(\theta_{\tilde{X}X}^{\max}\right)\right|\frac{K_h}{K_v}\right) \qquad (4.91).$$

This shows that the lower bound of allowable grid aspect ratio is larger for more skewed grids. However QM-matrix condition still allows for high grid aspect ratios.

4.5 Numerical Experiments on Convergence and Monotonicity of extended EMPFA

Convergence of a numerical method implies that the numerical solution approaches to the reference solution as the cell divisions tend to zero. However when an analytical solution is not available as a result of complexity of a PDE or ODE, one can consider the numerical solution for a highly refined model as the exact solution. Thus the error estimates at coarser grids (lower resolutions) can be obtained by computing both square and infinity norms of difference of solution from exact solution over all grids. A convergence study is performed with computing the error norms for coarser grids with successively doubled cell divisions. Then if trend of errors (L_2^{ep} or L_∞^{ep}) is descending for a descending trend of cell divisions (Δx, Δy), then the numerical scheme is convergent and consistent:

$$\lim_{\substack{\Delta x \to \Delta x^{\min} \\ \Delta y \to \Delta y^{\min}}} \frac{L_2^e\left(\Delta x, \Delta y\right)}{\sqrt{\Delta x^2 + \Delta y^2}} = 0 \qquad (4.92).$$

Numerical scheme is said accurate of order *n* and has a convergence rate of *n*, if:

$$\lim_{\substack{\Delta x \to \Delta x^{\min} \\ \Delta y \to \Delta y^{\min}}} L^{e}\left(\Delta x, \Delta y\right) = O\left(Min\left(\Delta x, \Delta y\right)^{n}\right) \tag{4.93}$$

Assuming grid spacing is successively divided by factor $\alpha > 1$ to achieve higher resolutions, convergence rate or the accuracy order can be obtained from:

$$n = \log_{\alpha}\left(\frac{L^{e}\left(\alpha\Delta x, \alpha\Delta y\right)}{L^{e}\left(\Delta x, \Delta y\right)}\right) \tag{4.94}$$

As a common practice error norms are calculated for both potential and normal fluxes which are expressed as:

$$\begin{cases} L_{2}^{ep} = \left(\dfrac{\sum_{i} V_{i}\left(\Phi_{i}^{ex.} - \Phi_{i}\right)^{2}}{\sum_{i} V_{i}}\right)^{1/2} \\ L_{2}^{ev} = \left(\dfrac{\sum_{e\in \mathrm{E}} Q_{e}\left(\dfrac{f_{e}^{ex.} - f_{e}}{|e|}\right)^{2}}{\sum_{e\in \mathrm{E}} Q_{e}}\right)^{1/2} \end{cases} \tag{4.95}$$

In which V_i stands for volume of ith cell, $|e|$ is the normal area of interface e belonging to E (space of interfaces) and Q_e represents the volume associated with interface e (volume of interaction region including interface e for EMPFA and volume encompassed between centres of cells sharing interface e for TPFA). Also infinity norms of errors are defined by $L_{\infty}^{ep} = \underset{i}{Max}\left(\Phi_{i}^{ex.} - \Phi_{i}\right)$ and $L_{\infty}^{ev} = \underset{e}{Max}\left(f_{e}^{ex.} - f_{e}\right)$ for potential and normal velocity respectively.

Initially we perform some simple fundamental convergence tests against the analytical solutions in order to reassure about the trustworthy function of extended EMPFA scheme when the boundaries are translated into the grid using the Cartesian Cut Cell method. The grid types created by Cartesian Cut Cell method are employed to verify the discretisation on grid is correct. The simple 2D model would be a unit square including

a pinchout-like structure with Dirichlet boundary conditions on left and right walls and no flow (Neumann) boundary conditions on top and bottom faces as pictorially demonstrated in figure 4.22. We investigate the 1-phase incompressible flow of oil at steady state conditions with negligible gravity effects. The grid is initially modified from pure Cartesian to conform to the pinchout-like structure.

For the first test we assume the linear potential ($\Phi = ax + by + c$) with a, b, c determined from given boundary conditions, the permeability tensor is assumed constant and diagonal throughout the domain with anisotropy ratio (ratio of horizontal permeability to and vertical permeability) of 100:1. Potential and velocity are calculated over a sequence of four grid resolutions from 64×64 to 8×8 and then compared with analytical solutions to obtain the error. The second order error norms of potential and velocity have been plotted in figure 4.23 exhibiting convergence rates of 1.93 and 1.33 for potential and velocity respectively.

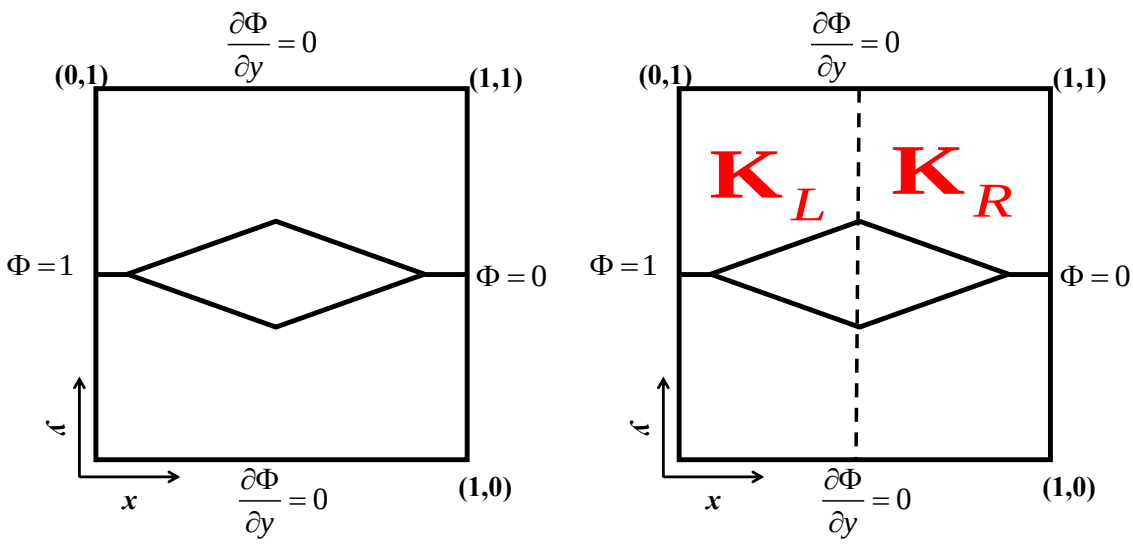

Figure 4.22: Left: Simple 2D model used for convergence tests with analytical solutions, Right: The same model but with permeability discontinuity employed for the third test

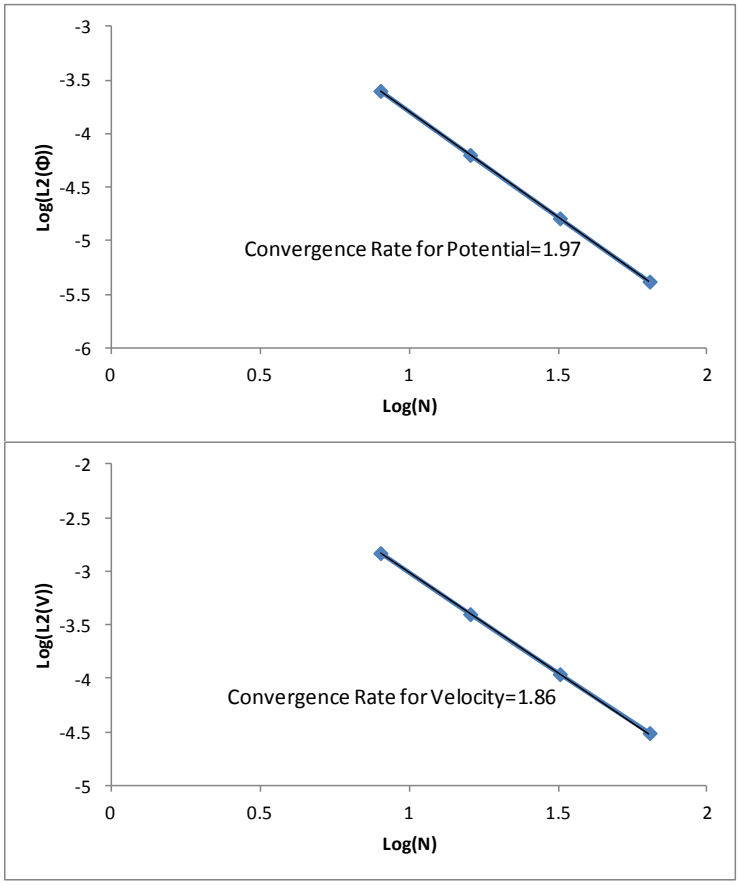

Figure 4.23: Convergence rates of Potential and Velocity for model shown in figure 4.22 with uniform permeability and assumption of linear potential solution

For the second case we keep the same model, but a quadratic solution ($\Phi = ax^2 + by^2 + cx + dy + e$) is assumed for potential, where *a*, *b*, *c*, *d*, *e* are computed from given boundary conditions. The corresponding convergence plots for potential and velocity are plotted in figure 4.24.

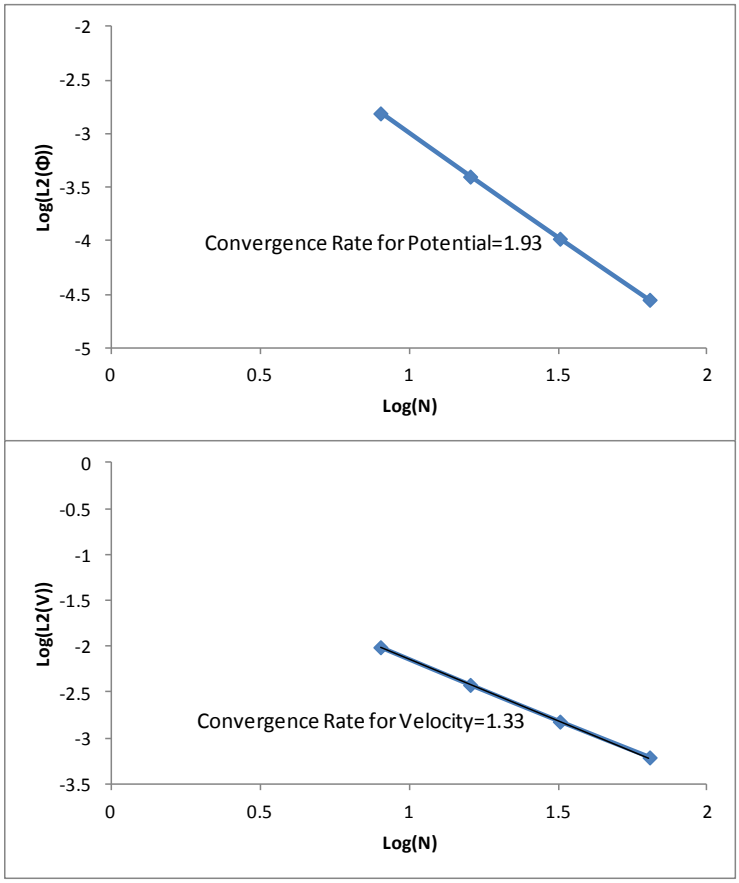

Figure 4.24: Convergence rates of Potential and Velocity for model shown in figure 4.22 with uniform permeability and assumption of quadratic potential solution

As potential and velocity are approximated at higher accuracy by using quadratic solution compared with linear potential, larger error norms and smaller convergence rate are obtained from second test. However still almost second order convergence rate for potential is obtained, while accuracy order for numerical velocity solutions declines to 1.33 indicating a super-linear convergence.

For third test, we embed a permeability discontinuity into the permeability field at centre line *x=1/2* (as shown in figure 4.22-right). For the solution we use the same quadratic solution as one used by Edwards and Rogers [1998]:

$$\Phi = \begin{cases} c_l x^2 + d_l y^2 & x \le 1/2 \\ a_r + b_r x + c_r x^2 + d_r y^2 & x \ge 1/2 \end{cases} \qquad (4.96).$$

Permeability tensor is given by:

$$\mathbf{K} = \begin{cases} \begin{bmatrix} 50 & 0 \\ 0 & 1 \end{bmatrix} & x < 1/2 \\ \begin{bmatrix} 1 & 0 \\ 0 & 10 \end{bmatrix} & x \geq 1/2 \end{cases} \qquad (4.97).$$

With the coefficients computed from the same boundary conditions, quadratic solution is determined and compared at 4 different resolutions with numerical solutions. The resulting convergence plots are depicted in figure 4.25.

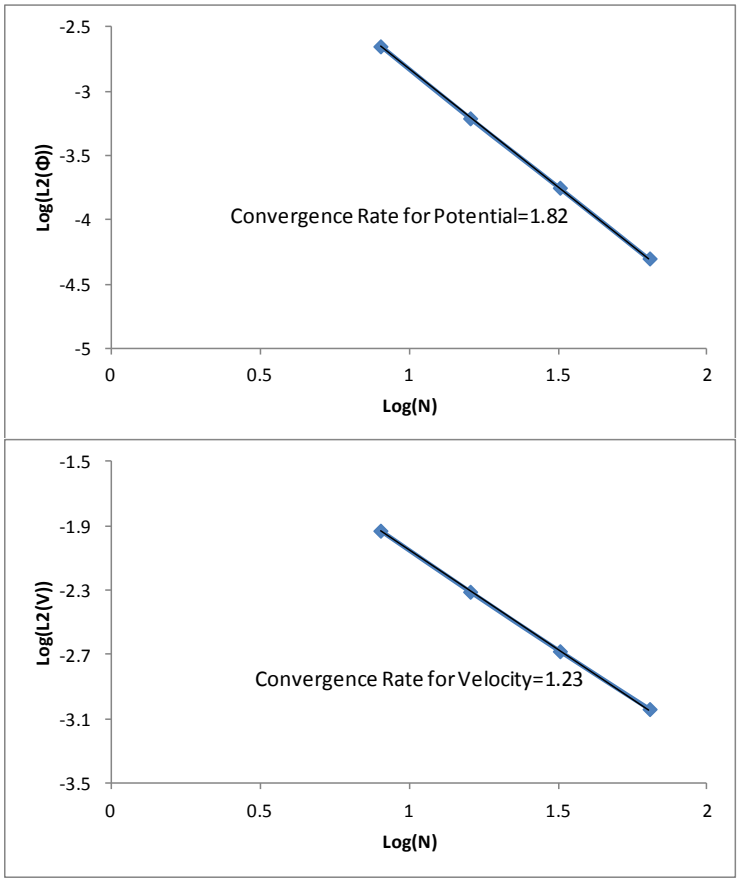

Figure 4.25: Convergence rates of Potential and Velocity for model shown in figure 4.22 with discontinuous permeability and assumption of quadratic potential solution

It seems that discontinuity of permeability results in a bit smaller convergence rates, however almost second order accurate solution of potential and super-linear accuracy of velocity solution guarantees the reliable function of employed gridding/flux approximation technique (Cartesian Cut Cell/extended EMPFA) for discontinuous

permeability fields and non-Cartesian boundaries. So the numerical solution over very refined domains of more complex models can be utilised as an alternative of exact analytical solutions.

Now we want to investigate the convergence of extended EMPFA scheme (applied anisotropic extreme quadrature) for a 2D model including geological features that their structural uncertainties will be studied in next chapters (faults, pinchout and bedding layers). It is a cross section of a reservoir with three stratigraphic layers (middle one is a pinched out layer). Model has been extended 1000 *ft* in horizontal direction and its normal width is 112 *ft*. No-flow boundary condition is imposed and there are two injection and production wells at left and right model extremes with well pressures of 150 *psia* and 50 *psia*. Permeability tensor is diagonal throughout the model with variation shown in table 4.12:

Layer	$K_h\,(Darcys)$	$K_v\,(Darcys)$	$\phi\left(volume/volume\right)$
1	0.1	0.001	0.15
2	0	0	0.02
3	0.4	0.004	0.25

Table 4.12: Rock properties for benchmark model; layers indexed from deepest one

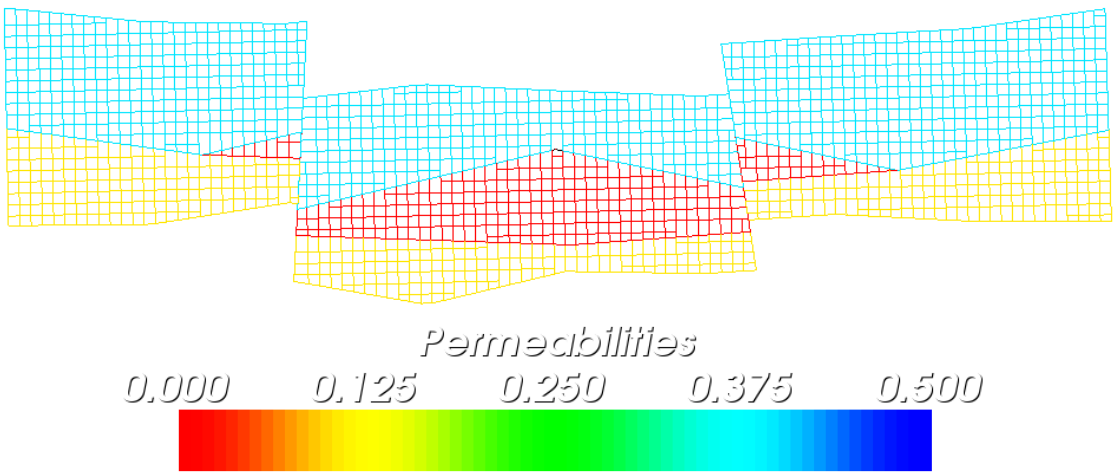

Figure 4.26: Horizontal permeability map overlaid on gridding of benchmark model

In addition to error estimates for whole the model, we calculate the error norms over the cells reshaped by Cartesian Cut Cell Method (to conform to the surfaces of geological structures) and specify the respective error norms with "*GS*" superscript. Numerical solution of a refined model with 1600 divisions in *x* direction and 320 divisions in *y* direction is regarded as the exact solution. The discrete norms of errors calculated at lower resolutions (obtained by successively doubling the grid spacings) have been given in tables 4.13 and 4.14 for potential and velocity respectively. Almost second order convergence rates have been obtained for whole model and for buffer zone around geological structures. This demonstrates the favourable functionality of extended EMPFA to yield solutions over the buffer zone around geological structures with accuracies comparable to those over intact Cartesian cells, while the cells in the buffer zone suffer from skewness, non-neighbour connections and localised large volume contrast (as shown in figure 4.26).

N	N_x	N_y	L_∞^{ep}	L_2^{ep}	$Rate$	$(L_\infty^{ep})^{GS}$	$(L_2^{ep})^{GS}$	$Rate^{GS}$
2000	100	20	7.9344	4.2358		7.9344	6.8319	
8000	200	40	2.1318	1.0536	2.01	2.1318	1.8531	1.88
32000	400	80	0.6253	0.2743	1.95	0.6253	0.5137	1.85
128000	800	160	0.1868	0.0709	1.93	0.1868	0.1530	1.77

Table 4.13: Squared and infinity norms of error for potential along with convergence rates calculated over whole model and cluster of irregular cells individually

N	N_x	N_y	L_∞^{ev}	L_2^{ev}	$Rate$	$(L_\infty^{ev})^{GS}$	$(L_2^{ev})^{GS}$	$Rate^{GS}$
2000	100	20	0.0615	0.0293		0.0615	0.0526	
8000	200	40	0.0334	0.0149	0.97	0.0334	0.0303	0.79
32000	400	80	0.0177	0.0073	1.02	0.0177	0.0162	0.91
128000	800	160	0.0101	0.0038	0.94	0.0101	0.0090	0.84

Table 4.14: Squared and infinity norms of error for velocity along with convergence rates calculated over whole model and cluster of irregular cells individually

Maximum local errors are expected to emerge in the vicinity of geological structures. In accordance with this anticipation, infinity norms of potential and velocity are equal for both whole model and buffer zone. Despite the super-convergence of potential, velocity is only convergent of order one. However convergence rate of velocity over the buffer zone is almost comparable to that for whole model; this indicates extended EMPFA can provide approximation of flux across interfaces in the zone geometrically affected by structures with precisions as good as those for flux obtained by TPFA across unaffected interfaces.

The numerical solution obtained for the coarsest model in the convergence study (depicted in figure 4.27) and one more refined model (depicted in figure 4.28) exhibits a well resolved pressure distribution which is free of any spurious oscillations. Implications of such a solution are more highlighted when we consider no flow boundary conditions imposed along the external boundaries and also on the plane of pinchout; extended EMPFA effectively avoids any unstable extrema. Remembering unfavourable performance of EMPFA against no flow boundary reported by Aavatsmark [2008], this again signifies that using flexible quadrature of FPS scheme can enhance considerably monotonicity behaviour of EMPFA solutions. This guarantees consistent and stable numerical results for the range of 2-D problems proposed to be dealt with in this thesis.

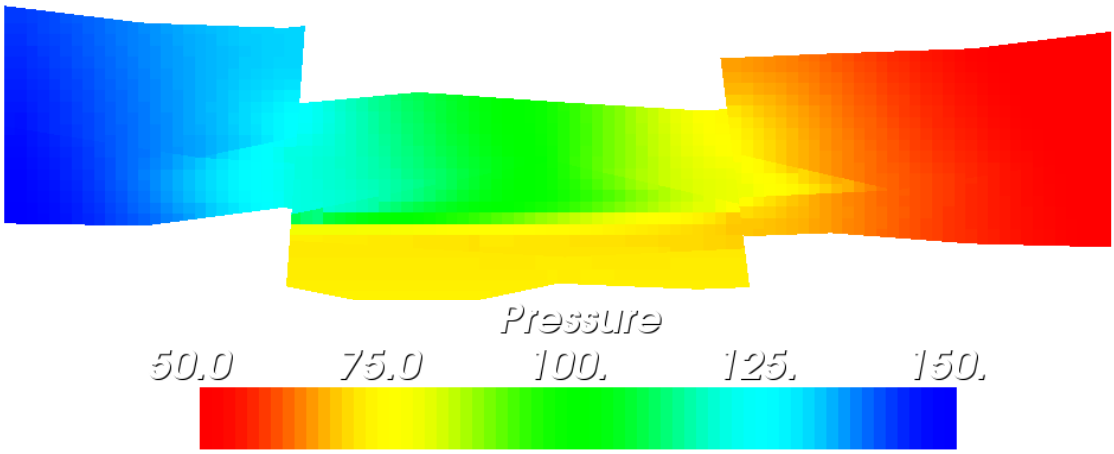

Figure 4.27: Numerical solution of pressure for the lowest resolution examined in convergence study

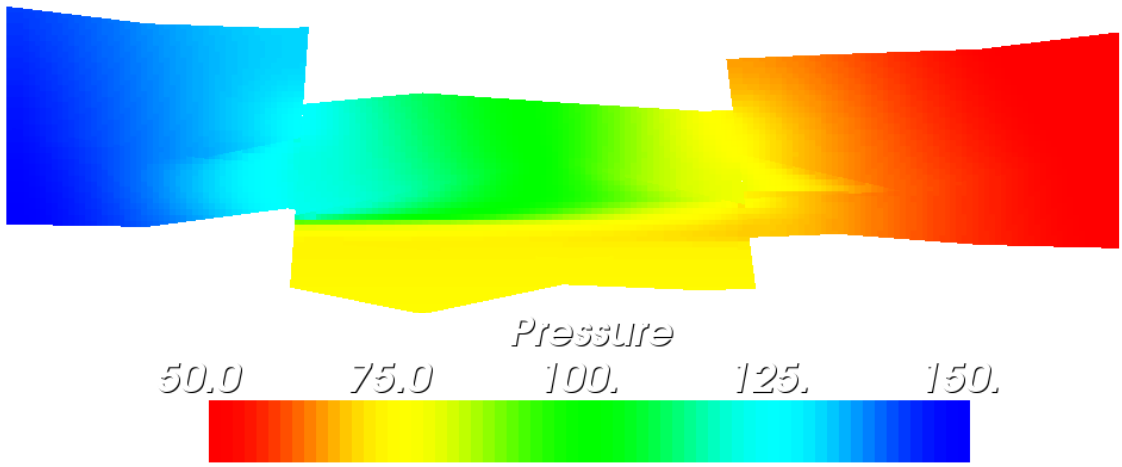

Figure 4.28: Numerical solution of pressure for one further refinement in contrast to coarsest examined model

In order to assure the vigorousness of extended EMPFA to yield minimal oscillatory solutions, we analyse the solutions of benchmark model with different schemes of extended EMPFA and MPFA-O. Nine sets of solutions are obtained for combinations of three typical anisotropy ratios (10,100,1000) and three permeability heterogeneity contrasts (*P.H.C.*) between permeable layers (1,10,100). An ideally monotonic scheme is expected to lead into a potential distribution varying between the potentials imposed at the bottom holes of injection and production wells. So we define a dimensionless cell-wise potential $\Phi_D = \left(\frac{\Phi - \Phi^{prod.}}{\Phi^{inj.} - \Phi^{prod.}} \right)$ which varies in the interval [0,1]. To measure the unphysical solution, we use the quantities proposed by Aavatsmark [2008] which are defined as:

- $\varepsilon_1 = \left(\frac{\Phi_D^{\min}}{\Phi_D^{\max}} \right)$ which determines the amplitude of spurious oscillations and approaches zero for a monotone solution.
- $\varepsilon_2 = \max\left(\max_{\partial\Omega}\left(-\Phi_D\right), \max_{\partial\Omega}\left(\Phi_D - 1\right) \right)$ which determines the strength of unphysical extrema on the boundary of model ($\partial\Omega$).

In tables 4.15 to 4.23, quantities ε_1 and ε_2 obtained by various schemes studied in this chapter have been given for nine specific cases of anisotropy and heterogeneity.

	ε_1	ε_2
MPFA O-Method	-0.021	0.000
Face-wise Extended EMPFA	-0.001	0.009
Optimal Support Scheme	-0.004	0.003
H/I scheme	-0.005	0.007
Anisotropic Quadrature Scheme	-0.001	0.001

Table 4.15: Unphysical solution measuring parameters for $P.H.C.=1$ and $\left(K_h/K_v\right)=10$

	ε_1	ε_2
MPFA O-Method	-0.087	0.003
Face-wise Extended EMPFA	-0.003	0.029
Optimal Support Scheme	-0.011	0.017
H/I scheme	-0.014	0.024
Anisotropic Quadrature Scheme	-0.002	0.004

Table 4.16: Unphysical solution measuring parameters for $P.H.C.=1$ and $\left(K_h/K_v\right)=100$

	ε_1	ε_2
MPFA O-Method	-0.364	0.019
Face-wise Extended EMPFA	-0.017	0.079
Optimal Support Scheme	-0.046	0.066
H/I scheme	-0.059	0.143
Anisotropic Quadrature Scheme	-0.009	0.027

Table 4.17: Unphysical solution measuring parameters for $P.H.C.=1$ and $\left(K_h/K_v\right)=1000$

	ε_1	ε_2
MPFA O-Method	-0.034	0.001
Face-wise Extended EMPFA	-0.002	0.017
Optimal Support Scheme	-0.008	0.005
H/I scheme	-0.007	0.016
Anisotropic Quadrature Scheme	-0.002	0.002

Table 4.18: Unphysical solution measuring parameters for $P.H.C. = 10$ and $\left(K_h / K_v\right) = 10$

	ε_1	ε_2
MPFA O-Method	-0.162	0.006
Face-wise Extended EMPFA	-0.010	0.033
Optimal Support Scheme	-0.031	0.023
H/I scheme	-0.045	0.037
Anisotropic Quadrature Scheme	-0.007	0.005

Table 4.19: Unphysical solution measuring parameters for $P.H.C. = 10$ and $\left(K_h / K_v\right) = 100$

	ε_1	ε_2
MPFA O-Method	-0.383	0.026
Face-wise Extended EMPFA	-0.027	0.117
Optimal Support Scheme	-0.065	0.091
H/I scheme	-0.103	0.148
Anisotropic Quadrature Scheme	-0.018	0.031

Table 4.20: Unphysical solution measuring parameters for $P.H.C. = 10$ and $\left(K_h / K_v\right) = 1000$

	ε_1	ε_2
MPFA O-Method	-0.069	0.004
Face-wise Extended EMPFA	-0.005	0.029
Optimal Support Scheme	-0.021	0.013
H/I scheme	-0.015	0.040
Anisotropic Quadrature Scheme	-0.003	0.006

Table 4.21: Unphysical solution measuring parameters for $P.H.C. = 100$ and $\left(K_h / K_v\right) = 10$

	ε_1	ε_2
MPFA O-Method	-0.231	0.020
Face-wise Extended EMPFA	-0.028	0.118
Optimal Support Scheme	-0.073	0.063
H/I scheme	-0.058	0.157
Anisotropic Quadrature Scheme	-0.019	0.019

Table 4.22: Unphysical solution measuring parameters for $P.H.C. = 100$ and $\left(K_h / K_v\right) = 100$

	ε_1	ε_2
MPFA O-Method	-0.566	0.098
Face-wise Extended EMPFA	-0.085	0.315
Optimal Support Scheme	-0.217	0.140
H/I scheme	-0.306	0.439
Anisotropic Quadrature Scheme	-0.077	0.074

Table 4.23: Unphysical solution measuring parameters for $P.H.C. = 100$ and $\left(K_h / K_v\right) = 1000$

Analysing the information provided by this through study of unphysical solutions leads into the following conclusion:

1. Although unphysical solutions are intensified by increasing both anisotropy and heterogeneity ratios, but the influence of anisotropy augmentation is more severe.
2. In terms of minimal spurious oscillations, the priority of EMPFA schemes with respect to MPFA O-method is obvious, implied by much smaller ε_1. Among different extended EMPFA schemes, face-wise scheme and anisotropic quadrature scheme are more favourable due to remaining consistent at very high anisotropy and heterogeneity with oscillation amplitude less that 8% of true physical solution range.
3. Regarding the matter of boundary extrema, MPFA-O leaves good results for the wide range of anisotropy and heterogeneity, while excluding anisotropic quadrature scheme, extended EMPFA schemes tend to exhibit stronger unphysical extrema on the boundary. However, anisotropic quadrature scheme on the whole provides physical solutions on the boundary comparable to or slightly better than MPFA-method ones.

Our key finding is that anisotropic quadrature scheme is the most optimal method among studied schemes and enjoys the benefits of MPFA O-method and extended EMPFA schemes simultaneously. The result is in accordance with Edwards and Zheng [2010] who showed anisotropic quadrature scheme stays out of strong oscillations in the bulk and unphysical extrema on the boundary for whole the QM-matrix region.

4.6 Robustness of extended EMPFA for Non-matching Cells

Apart from monotonicity and convergence of extended EMPFA, its robustness for handling non-matching cells should be assured. In this regard, several limitations for conventional MPFA methods are well-known; however we will demonstrate that these deficiencies are not inherent to extended EMPFA schemes. As mentioned by Aavatsmark [2007-A], Aavatsmark et al. [2001] and Eigestad et al. [2002-B], MPFA O-method has an unfortunate effect for triangular interaction regions built on non-matching cells when two involved sub-interfaces builds a straight line.

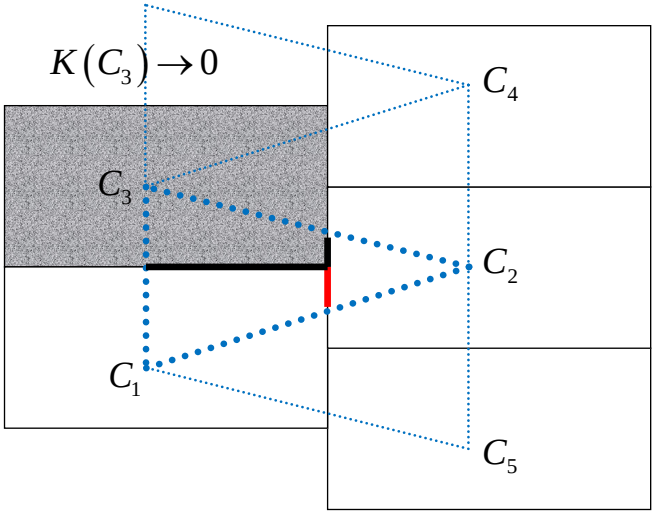

Figure 4.29: Triangular interaction region for non-matching cells

Aavatsmark et al. [2001] showed that if permeability within one of cells contributing to the interaction region (C_3) approaches zero, then MPFA O-method returns very small transmissibility for the interface between permeable cells (C_1 and C_2) in contrast with expected transmissibility (TPFA transmissibility reduced by a factor of relative displacement) . For zero permeability at one of involved cells, predicted transmissibility by MPFA O-method on interface of permeable cells vanishes completely. In general MPFA O-method yields almost identical transmissibilities across two interfaces building a straight line, even the permeability varies between hanging cells (C_1 and C_3) (Aavatsmark, 2007-A). To ensure true representation of reservoir inter-layer connectivity in vertical and horizontal directions, this deficiency should be circumvented. To accomplish this aim, Aavatsmark et al. [2001] and Eigestad et al. [2002-B] have proposed a larger interaction region by inclusion of two more cells (C_4 and C_5) above and below of cell on other side of hanging cells. Such a scheme is not favourable due to reduced sparsity of solution matrix and subsequent elevated problems in terms of convergence and monotonicity. We believe that added degree of freedom and more precise approximation of potential in extended EMPFA can prevent from unfortunate effect over non-matching cells. In this section, we will show that extended EMPFA yields consistent transmissibilities over non-matching cells in the vicinity of faults or pinchouts.

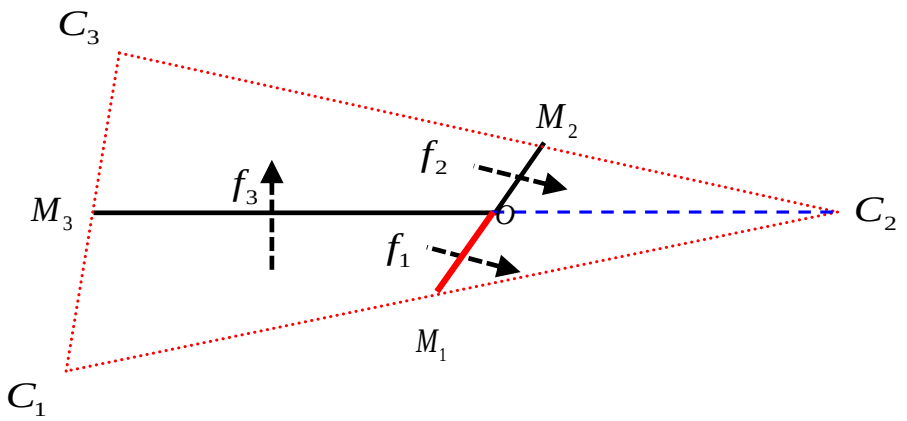

Figure 4.30: Triangular interaction region over non-matching cells; M_1M_2 on the fault plane, dotted arrows shows the fluxes through semi-interfaces

Assuming $\mathbf{K}(C_3)=\mathbf{0}$ in figure 4.29, flux continuity equations along with zero source condition at central point are expressed as:

$$\begin{cases} f_1\left(\Phi_{C_1},\Phi_{M_1},\Phi_O,\Phi_{M_3}\right)=f_1\left(\Phi_{C_2},\Phi_{M_2},\Phi_O\right) \\ f_2\left(\Phi_{C_2},\Phi_{M_2},\Phi_O\right)=0 \\ f_3\left(\Phi_{C_1},\Phi_{M_1},\Phi_O,\Phi_{M_3}\right)=0 \\ \nabla.f_O\left(\Phi_{C_1},\Phi_{C_2},\Phi_{M_1},\Phi_{M_2},\Phi_{M_3},\Phi_O\right)=0 \end{cases} \qquad (4.98).$$

Thus no constraint on flux with respect to potential at impermeable cell is entailed and the flux across the only active interface will be uniquely determined in terms of potentials at centres of two permeable cells ($f_1=t_{11}\Phi_1+t_{12}\Phi_2$). When $t_{11}\cong t_{12}$, extended EMPFA reduces to a TPFA scheme. The generalised TPFA transmissibility between cells *i* and *j* commonly used in commercial reservoir simulators is expressed as:

$$t=\left(\left(K_i\frac{|\mathbf{a}\bullet\mathbf{d}_i|}{|\mathbf{d}_i\bullet\mathbf{d}_i|}\right)^{-1}+\left(K_j\frac{|\mathbf{a}\bullet\mathbf{d}_j|}{|\mathbf{d}_j\bullet\mathbf{d}_j|}\right)^{-1}\right)^{-1} \qquad (4.99),$$

in which $\mathbf{a}$ is the normal areal vector of interface and $\mathbf{d}_i$ is the vector connecting centre of cell i to the centre of cell face which the interface with desired transmissibility belongs to that.

We pay attention that TPFA computes flux across fault plane from $f_e^{TPFA} = \mathbf{v}_x \bullet \mathbf{A}_e^{\mathbf{n}}$ and does not take into account Cartesian velocity in y direction. However as shown for inclined interface in figure 4.30, true normal velocity across fault is obtained by algebraic addition of projected values of Cartesian velocities vectors $(\mathbf{v}_x, \mathbf{v}_y)$ on normal direction to the inclined sub-interface. This leads into the expression:

$$\mathbf{v_n} = -(1/\mu)\left(\cos(\theta) + sign(\theta)\left(\frac{K_v}{K_h}\right)\psi(\Phi_x, \Phi_y)\sin(\theta)\right)K_h\Phi_x \qquad (4.100),$$

in which:

- $sign(\theta)$ is $+1$ for negative fault slopes and -1 for positive fault slopes.
- $\psi(\Phi_x, \Phi_y)$ is the tangent of the angle which potential drop vector $(-\nabla\Phi)$ builds with x direction and equals to ratio (Φ_y/Φ_x).

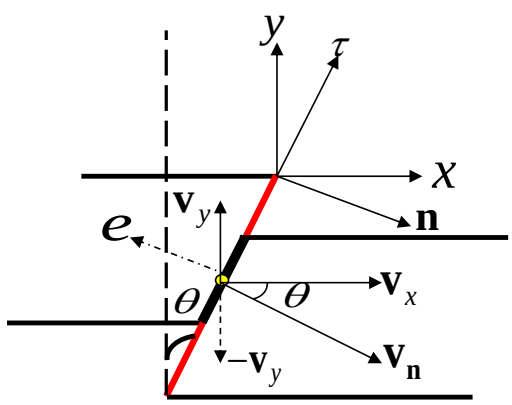

Figure 4.31: Sub-interface not aligned with none of principal directions of **K**-tensor

The term $\gamma = \left(\cos(\theta) + sign(\theta)(K_v/K_h)\psi(\Phi_x, \Phi_y)\sin(\theta)\right)$ giving the ratio of true normal velocity to the velocity in x direction determines how reasonably TPFA approximates the flux across the inclined sub-interface. As long as $\gamma \approx 1$, TPFA transmissibilities remain acceptable. This happens for small θ or in the other word for almost vertically oriented faults. Moreover apart from anisotropy ratio and sign of fault slope, γ is greatly impressed by the preferred direction of potential gradient vector.

Although fluid mainly flows in horizontal direction, but regarding the gravity potential acting in vertical direction and very thin grid vertical divisions compared to horizontal ones, in most cases Φ_y is greater or comparable to Φ_x. However, at high speeds of fluid flow, $\psi\left(\Phi_x,\Phi_y\right)$ is decreased and even drops below unity. For the range of synthetic problems dealt with in this thesis, we found $\psi\left(\Phi_x,\Phi_y\right)$ lies within a narrow interval of $[4,6]$. Variation of γ for typical values of anisotropy ratio and $\psi\left(\Phi_x,\Phi_y\right)$ has been depicted in figure 4.31 over a range of θ covering the maximum fault inclination ($[0°,45°]$).

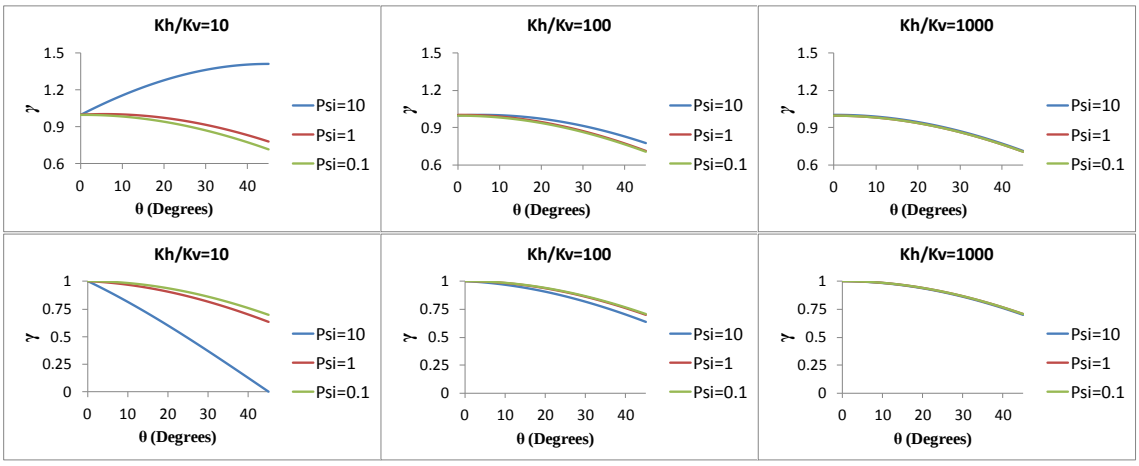

Figure 4.32: Ratio of true normal velocity to horizontal velocity across fault plane; Top: faults with negative slope, Bottom: faults with positive slope

TPFA formulation (Eq. 4.97) calculates the flux over surface normal to line connecting cell centres, thus γ can approximately gives the ratio of true flux to TPFA flux. Therefore extended EMPFA leads to good approximations of $f_e = \mathbf{v_n} \bullet \mathbf{A}_e^{\mathbf{n}}$ on fault plane, if ratio of its calculated flux to f_e^{TPFA} is almost equal to γ. To numerically testify the robustness of extended EMPFA for non-matching cells, we use the benchmark model represented in section 4.5. Within this model we specify all sub-interfaces along the fault planes which are involved in triangular interaction regions with at least one impermeable cell from pinched out layer. We denote Q^{NNC} as the space of all

problematic sub-interfaces ($Q^{NNC} = {}_i\left\{e_i^{NNC}\right\}$). The consistency of fluxes predicted by extended EMPFA over non-neighbour connections is examined by comparison between extended EMPFA and TPFA in terms of transmissibilities computed over all $e_i^{NNC} \in Q^{NNC}$. For each e_i^{NNC}, we define two parameters α and β as:

- $\alpha\left(e_i^{NNC}\right) = \left(\left(t_{11}\Phi_e^+ + t_{12}\Phi_e^-\right)^{e-EMPFA} \Big/ t^{TPFA}\left(\Phi_e^+ - \Phi_e^-\right)\right)\Big|_{e_i^{NNC}}$ which measures how well fluxes computed by extended EMPFA match to the true fluxes.
- $\beta\left(e_i^{NNC}\right) = \left(max\left(t_{11}, t_{12}\right) \big/ min\left(t_{11}, t_{12}\right)\right)\Big|_{e_i^{NNC}}$ which measures how effectively extended EMPFA takes into the account sub-interface inclination and unequal distances of cell centres from sub-interface.

In our benchmark problem, the average value of γ is estimated as:

- For fault with positive slope ($\theta = 25°$): $\bar{\gamma} \approx 0.88$
- For fault with negative slope ($\theta = 30°$): $\bar{\gamma} \approx 0.90$

	Minimum	Average	Maximum
$\alpha\left(e_i^{NNC}\right)$	0.82	0.87	0.94
$\beta\left(e_i^{NNC}\right)$	1.14	1.32	1.61

Table 4.24: Ranges of parameters measuring extended EMPFA robustness over non-neighbour connections in the vicinity of faults

From the information given in table 4.24 for the ranges of parameters α and β, one can draw the following conclusions:

1. Extended EMPFA successfully predicts flux for challenging sub-interfaces aligning to fault plane. Because $\forall\, e_i^{NNC} \in Q^{NNC}$ $\alpha\left(e_i^{NNC}\right) \in \left[0.9\bar{\gamma}, 1.1\bar{\gamma}\right]$ which indicates EMPFA transmissibilities never diminish even in presence of impermeable sub-cell present in interaction regions and calculated flux always remain in a relatively narrow margin about true flux.

2. Vertical permeability is relevantly incorporated into transmissibility calculations over inclined interfaces by extended EMPFA, resulting in smaller flux compared with TPFA ($avg\left(\alpha\left(e_i^{NNC}\right)\right) \approx \bar{\gamma} < 1$) and more reflective translation of fault geometry into the flow simulation even for problematic sub-interfaces.
3. Extended EMPFA provides more accurate approximations of potential gradients for linear or bilinear potential fields in comparison with TPFA. Because it leads to $\beta\left(e_i^{NNC}\right) > 1$ for $e_i^{NNC} \in Q^{NNC}$ which ensures unequal distances of cell centres to the sub-interface is properly translated into the approximated Φ_x. While TPFA leaves equal transmissibilities regardless of the interface inclination or the distance of two cell centres to the interface.

Chapter 5

Modelling and Quantification of Structural Uncertainties for Nonintersecting Geological Structures

Several synthetic models including lone uncertain surfaces will be presented in this chapter. The history matching will be performed on their corresponding structural parameters and the Bayesian inference framework will be employed to determine the updated uncertainty intervals for the geometry of geological structures.

The main specific goals of this chapter are:

1. To justify the feasibility of proposed hybrid Cartesian Cut Cell/extended EMPFA approach for tackling the varying geometry of some characteristic geological structures of different topologies (e.g. gently-dipped versus sharply dipped structures or open versus overlapping structures) during the history matching process.
2. To show the benefits of introduction the reservoir engineering analysis of dependency of flow on structures geometry for following purposes:
    a. To choose an optimised mode of sampling algorithm (Neighbourhood Algorithm) in terms of exploitation or exploration.
    b. To improve the interpretations made based on posterior inference results.
    c. To differentiate among geological structures in terms of impact of their corresponding uncertainties on the static or dynamic reservoir characteristics.

In this chapter, we will perform history matching and uncertainty quantification for three 2-D benchmark model offering the typical single uncertain structures. In figure 5.1, the schematic diagrams of these sample-of-proof models have been shown, where the uncertain structure in each model is marked with red colour.

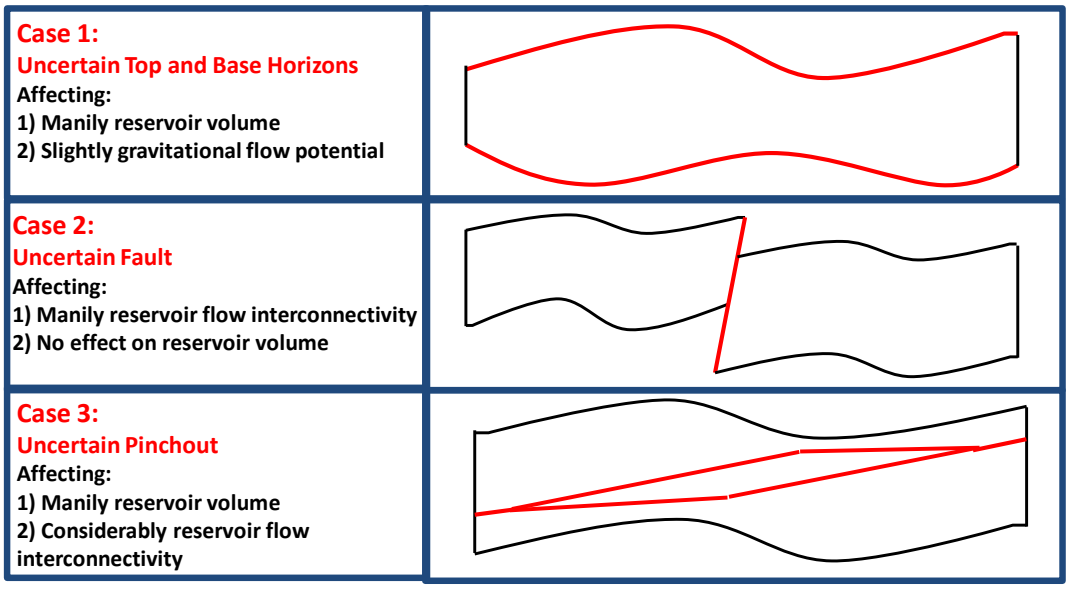

Figure 5.1: Benchmark models of 2-D uncertain structures proposed to be studied in this chapter along with their influences on reservoir state and performance

The relevant details of flow simulator and fluid and rock properties used in the benchmark models studied in this chapter have been provided in Appendix A. The general flowchart we have developed for history matching and quantify the uncertainties of geological structures has been depicted in figure 5.2.

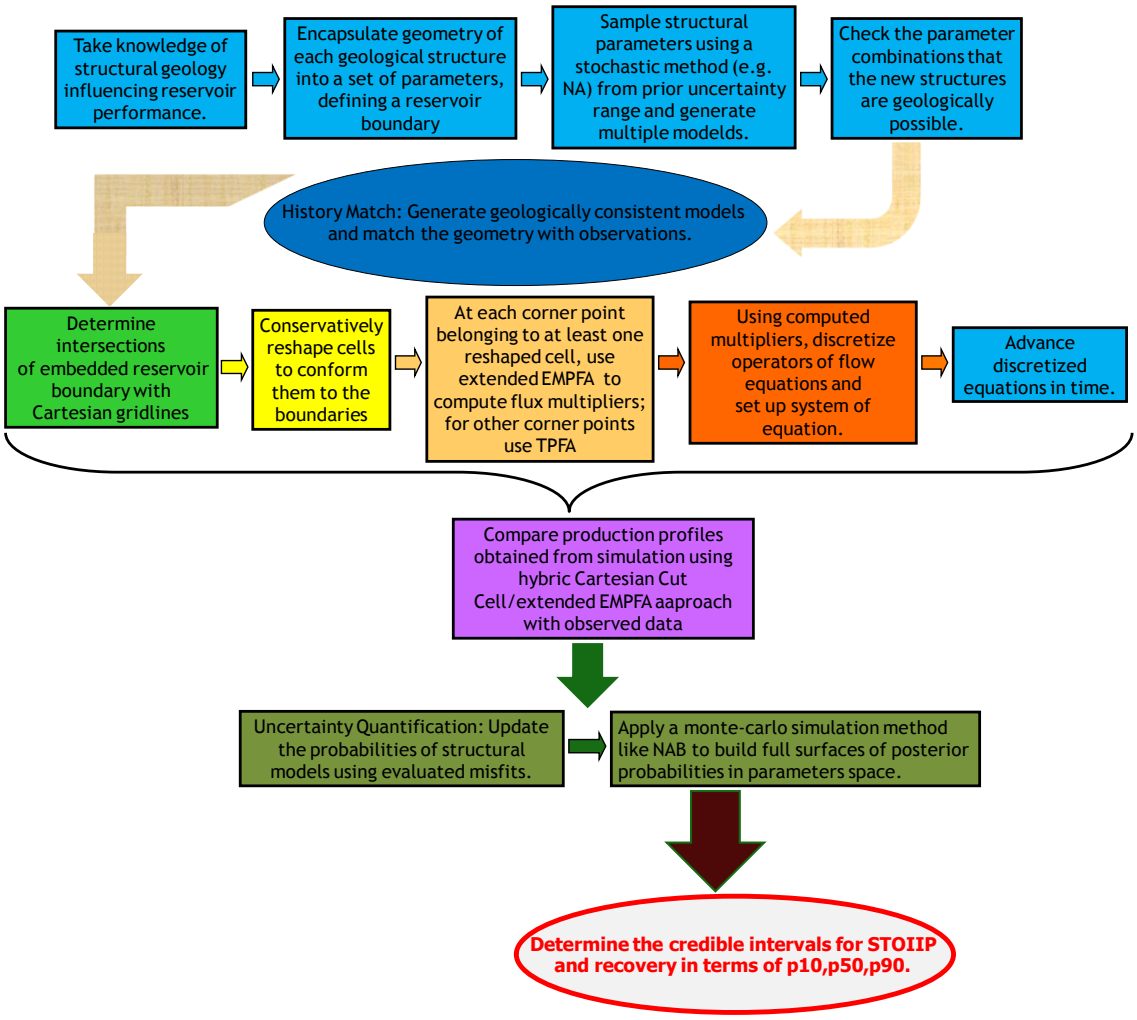

Figure 5.2: The general procedure for history match and uncertainty quantification of geological structures assisted by hybrid Cartesian Cut Cell/extended EMPFA approach

5.1 Modelling the Uncertainty of Top and Bottom Reservoir Horizons

5.1.1 Case Description

Aim is to determine the uncertainty constraints of top and base structures for a two dimensional cross section of a reservoir. It is assumed that the top and the bottom horizons have been already determined from converting the significant horizons distinguished in seismic time map into the depths. Although the reference model of reservoir is the most likely one obtained from seismic, but due to the uncertainties associated with seismic data acquisition, interpretation and time-depth conversion, the curvature and the depth of model horizons are questionable. Reservoir thickness is assumed to vary along the model extension. There is only one oil-bearing layer bounded between top and base structures and no aquifer or gas cap is in contact with oil layer. Model has been extended 1000 *ft* in horizontal direction and its normal width is 112 *ft*. It has been discretized into a 100×20×1 grid, so it is merely a two dimensional model.

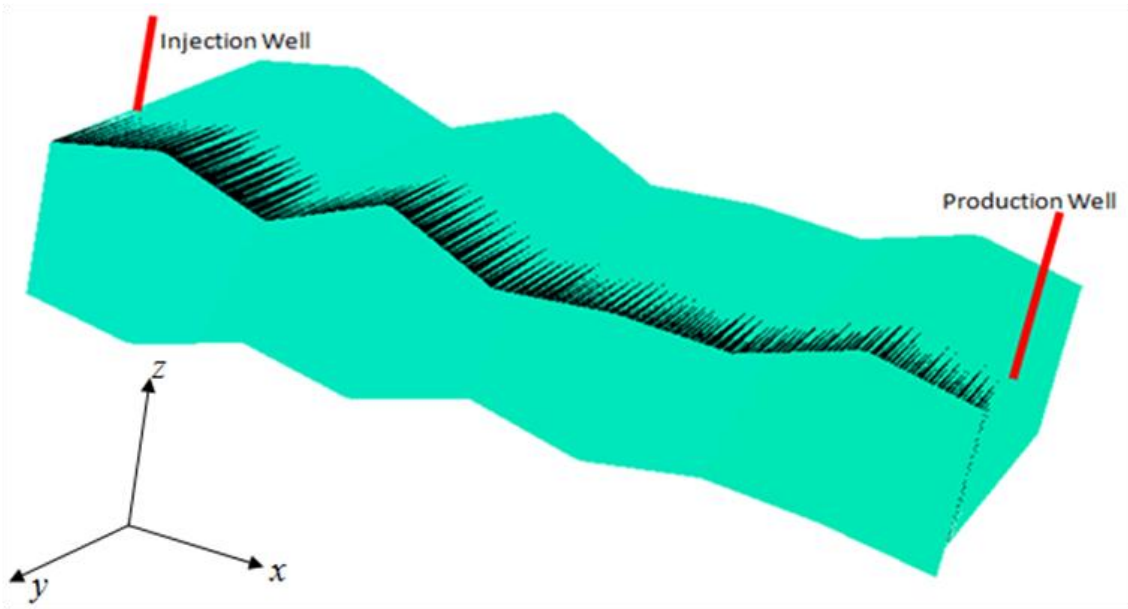

Figure 5.3: Initial uniform pressure of 100 *psia* over the reference model

Reservoir is assumed to have uniform connate water saturation of 0.10 and uniform initial reservoir pressure is 100 *psia*. Two injection and production wells have been drilled in left and right extremes of model respectively. No flow condition is enforced on all boundaries of reference model. Porosity is assumed to be uniform and constant throughout the reservoir with value and 0.20. Also horizontal and vertical permeabilities are uniform and equal to 0.20 *Darcy*s and 0.04 *Darcy*s respectively.

We assume depths of model measured at the bottom of injection and production wells are 199.83 *ft* and 199.17 *ft* respectively. Assuming the depth of 200 *ft* as the datum, top and base horizons can be determined in terms of their height with respect to the datum. Thus each realization of any reservoir horizons (including top and bottom structures and boundaries of reservoir layers) is created by assigning height values to arbitrary points along the model extension. Interpolating between points with given heights should be done conditioned to depths measured at wells to build a horizon realization.

$$Horizon\ realisation \equiv \left\{z\left(x_1\right), z\left(x_2\right), ..., z\left(x_{n-1}\right), z\left(x_n\right)\right\} \middle| \left\{z\left(Inj_i\right), z\left(\mathrm{Pr}od_i\right)\right\} \tag{5.1}$$

5.1.2 History Matching of Horizon Parameters

There is no observed data for this synthetic model, thus we propose two arbitrary sets of heights for the top and base horizons as the truth case. Considering the uncertainties of seismic horizon picking, truth case cannot be attained. It can be assumed that the discrepancy between true horizon and seismic picked horizon is given by stochastic perturbations imposed on each horizon height.

$$reference\ horizon \equiv true\ horizon \oplus random\ perturbation \tag{5.2}$$

Denoting $z^{true}\left(x_i\right)$ as the true horizon height, $z^{ref}\left(x_i\right)$ as the height of reference horizon and $e\left(x_i\right)$ as random perturbation or noise all evaluated at x_i, one may write:

$$z^{ref}\left(x_i\right) = z^{true}\left(x_i\right) + e\left(x_i\right) \tag{5.3}$$

Due to multiple interacting sources of error in seismic and restricted knowledge about them, a margin of error might be assigned to seismic picked horizons. Hopefully true heights would lie in this prior confidence interval with radius of $R\left(x_i\right)$ around seismic picked height.

$$z^{true}\left(x_i\right) \in \left[z^{ref}\left(x_i\right) - R\left(x_i\right), z^{ref}\left(x_i\right) + R\left(x_i\right)\right] \tag{5.4}$$

A constant radius of 2.0 is assigned for the confidence interval of each height for both top and base horizons. In figures 5.4 and 5.5 the prior confidence intervals for base and top horizons along with true and seismic picked horizons has been depicted.

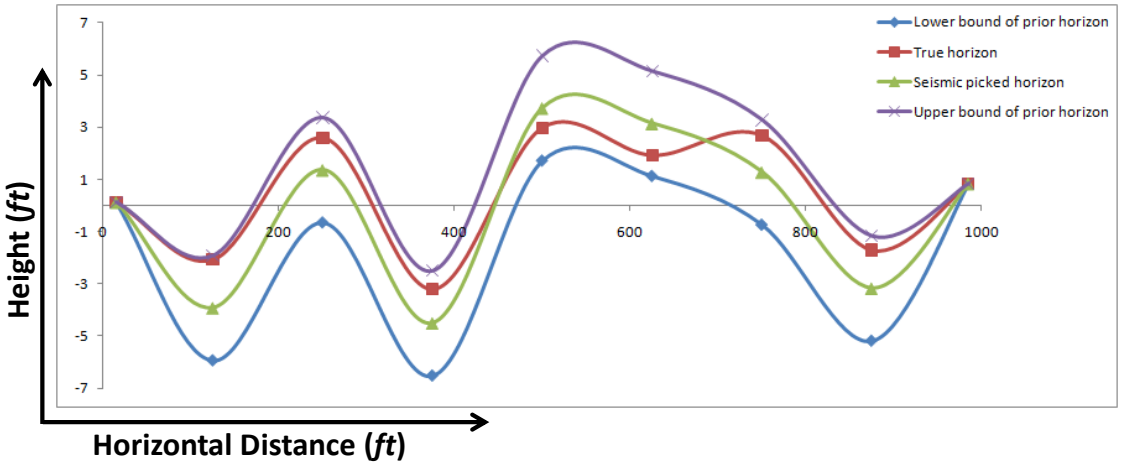

Figure 5.4: Prior range for the base horizon

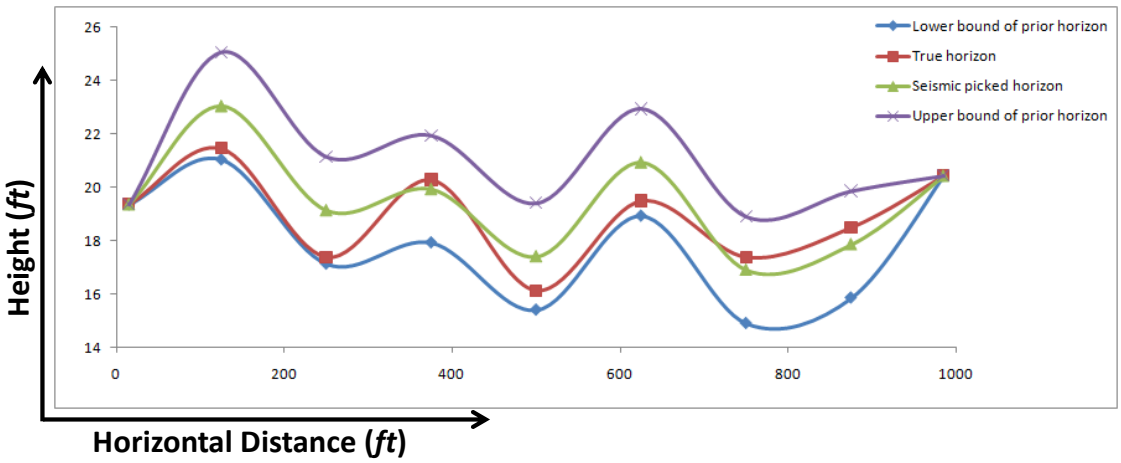

Figure 5.5: Prior range for the top horizon

Table 5.1 gives the height perturbations at 7 locations along the horizontal extension of model for base and top horizons. Zero perturbation is assigned at $x_0 = 15\,ft$ and $x_8 = 985\,ft$ to obey the depths of top and base horizons picked at wells. Reference model has 39302 *STB* of Stack Tank Oil Initially In Place (STOIIP) which shows

following seismic picked horizons results in overestimating of STOIIP by 7% compared with true model with STOIIP of 36826 *STB*.

$x_i(ft)$	15	125	250	375	500	625	750	875	985
$e^{basin}(x_i)(ft)$	0	-1.85	-1.29	0.71	-1.35	1.02	-1.39	-1.45	0
$e^{top}(x_i)(ft)$	0	1.59	1.76	-0.34	1.28	1.44	-0.47	-0.63	0

Table 5.1: Stochastic perturbations imposed on heights of base and top reservoir horizons

Production profiles provided by running in-house simulator (SUQIB) for the model with true horizons are considered as the observed data to be matched. It resembles a real field case where field observations are used to history match the reservoir horizons. Clearly prior confidence interval should be wide enough to ensure history matching leads into finding the true horizons. Letting upper bound of prior top horizon and lower bound of prior base horizon would give the maximum model thickness and consequently maximum oil in place. Accordingly minimum model thickness is obtained letting lower bound of prior top horizon and upper bound of prior base horizon.

Production well is opened to flow at time $t = 0$ *Days* with bottom hole pressure set at 50 *psia*, while water is injected steadily with well injection pressure of 150 *psia*. Production histories of water and oil phases for true horizons have been depicted in figures 5.6 and 5.7, where the gap between production profiles corresponding to the models with maximum and minimum thicknesses from prior uncertainty range clearly delineates the prior unconstrained uncertainties with the recovery forecasts.

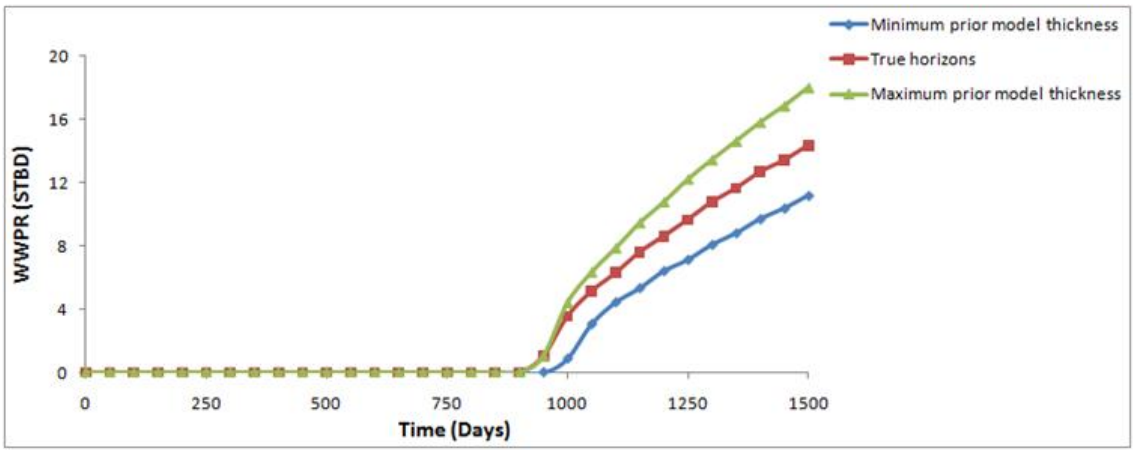

Figure 5.6: Variation of water production profile in prior range for top and base horizons

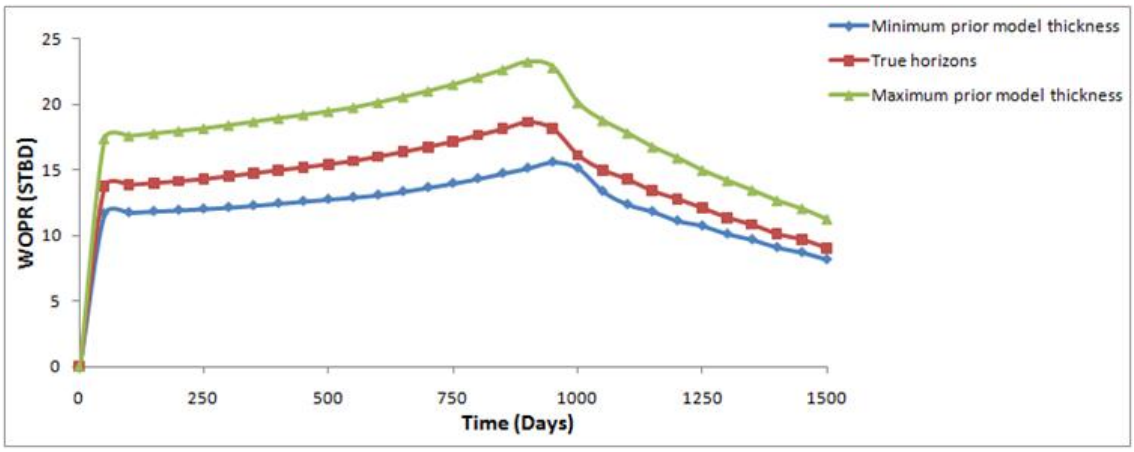

Figure 5.7: Variation of oil production profile in prior range for top and base horizons

Heights sampled through the prior range of horizons with any optimisation technique (Neighbourhood Algorithm here) are passed to SUQIB which updates model horizons and run the simulation. Objective is to minimise the following misfit function which is a normalised measure of difference between observed and simulated production data:

$$M = \sum_{n=1}^{N} \left(\frac{\left(q_O^{obs}(t_i) - q_O^{sim}(t_i)\right)^2}{2\sigma_O^2} + \frac{\left(q_W^{obs}(t_i) - q_W^{sim}(t_i)\right)^2}{2\sigma_W^2} \right) \qquad (5.5),$$

where the standard deviation values for oil and water rates (σ_O and σ_W) are set to 1 *STBD* which is approximately *5%* of average oil and water production rates. The

Optimization method employed here is Neighbourhood Algorithm (NA) (Sambridge, 1999-A) with the input parameters given in table 5.2.

n_{s_i}	n_s	n_r	Iterations	Total Simulations
100	14	2	115	1700

Table 5.2: NA input parameters for history matching of top and bottom horizons

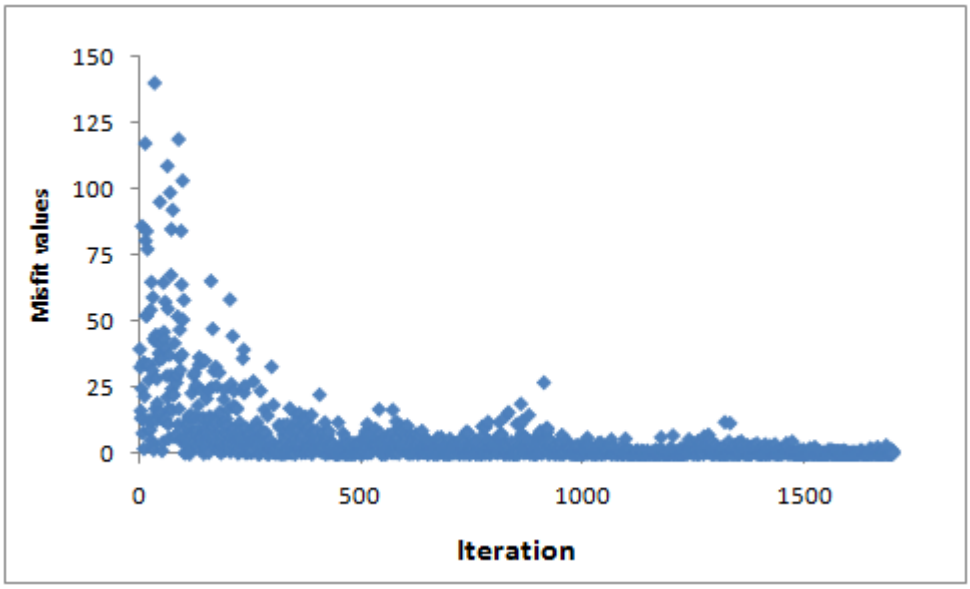

Figure 5.8: Convergence of NA in history matching of top and base horizons

As shown in figure 5.8, misfit value approaches zero. Lowest misfit of 0.024 is obtained after 1650 simulations. History matched top and base horizons have been depicted along with true horizons in figure 5.9. Model with the lowest misfit have STOIIP of 36899 *STB* which is in a very good agreement with true model with 36826 *STB* oil originally in place. Also trends of true horizons are intimately followed by the best model except far away from wells in the middle of axial interval where the curvature of horizon does have the least effect on simulated potential field and consequently on production. Observed spurious uplifting at $x \in [500\ ft, 750\ ft]$ has almost the same dimensions for both top and base horizons, thus it does have a negligible impact on STOIIP.

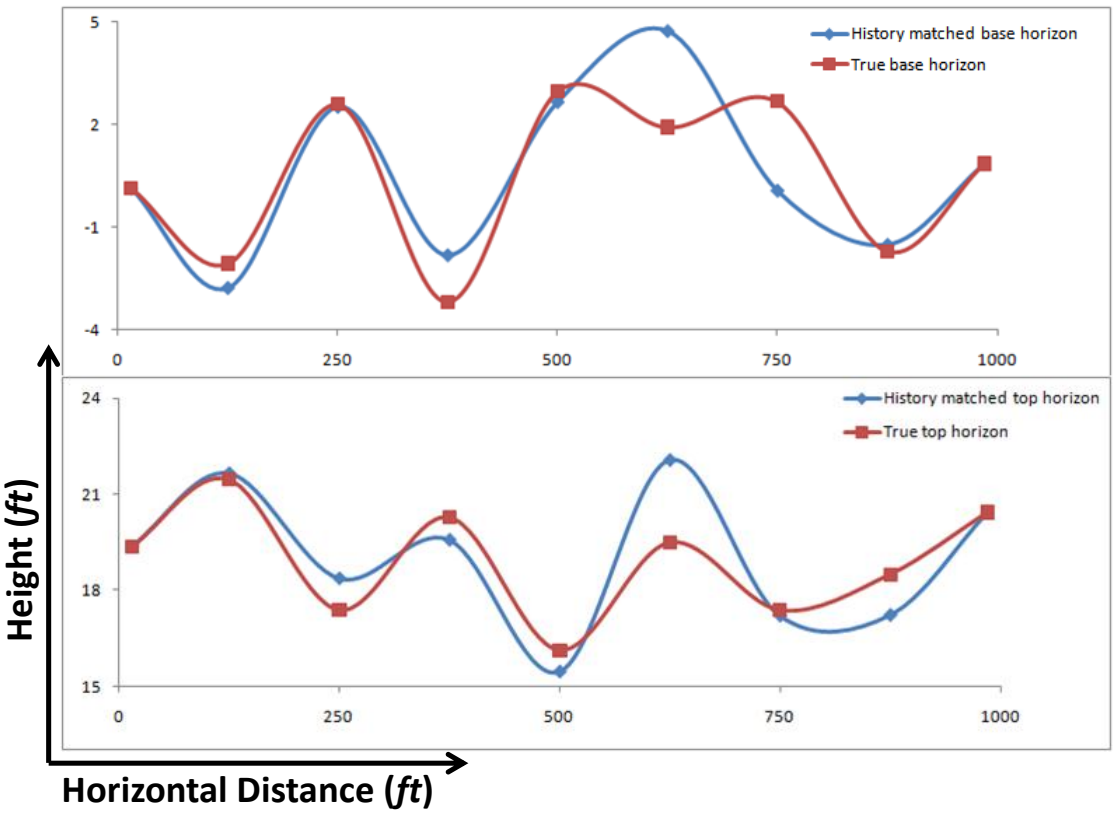

Figure 5.9: Best model compared with true model, top: Base horizon, bottom: Top horizon

Also spatial variation of layer thickness along the horizontal axis has been displayed for both history matched model and truth case in figure 5.10. The average thickness value is almost the same for both models (18.49 *ft* for history matched model and 18.47 *ft* for truth case). However the highest discrepancies between layer thicknesses happen after the spurious uplifting at $x \in [750\ ft, 875\ ft]$, where the fluctuating thickness of truth case is not well reproduced with the averaged thickness trend of history matched model.

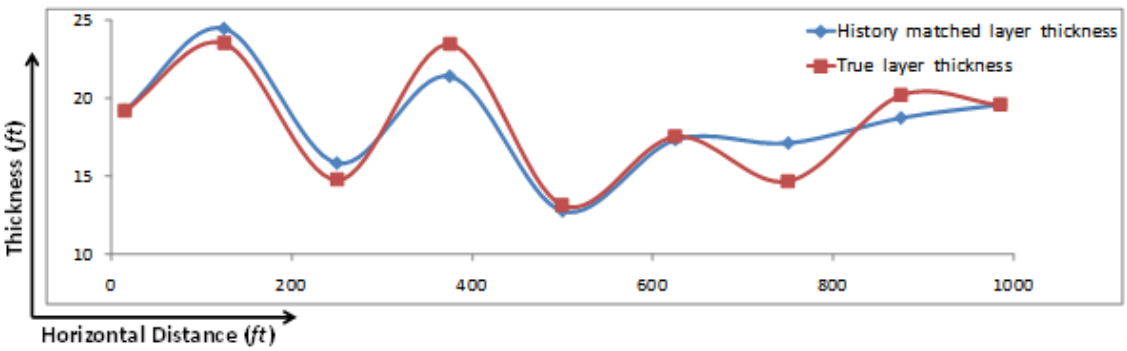

Figure 5.10: Best model compared with true model in terms of layer thickness

We can examine the quality of history matched models in terms of curvature of horizons trend. The curvatures of each horizon trends can be calculated from:

$$\kappa(x_i) = \frac{z''(x_i)}{\left(1 + z'(x_i)^2\right)^{3/2}} \qquad (5.6).$$

The curvatures have been compared between truth case and the history matched model for the base horizon in table 5.3 and for the top horizon in table 5.4. The relative errors of curvature are also given in these tables which are calculated as:

$$rel.\ err.\ (\kappa)(\%) = \left| \frac{\kappa^{T.C.} - \kappa^{H.M.}}{\kappa^{T.C.}} \right| \times 100 \qquad (5.7).$$

$x_i(ft)$	125	250	375	500	625	750	875
$\kappa(x_i)_{top}^{T.C.} \times 10^3$	-0.9906	1.2449	-1.3114	1.2975	-0.9937	0.5697	0.0941
$\kappa(x_i)_{top}^{H.M.} \times 10^3$	-0.8559	0.9443	-1.1921	1.7736	-1.7683	0.8783	0.1363
$rel.\ err.\ (\kappa)(\%)$	13.5	24.1	9.1	36.6	77.9	54.2	44.9

Table 5.3: Spatial variation of curvatures for top horizon along the horizontal direction compared between true and history-matched models

$x_i(ft)$	125	250	375	500	625	750	875
$\kappa(x_i)_{basin}^{T.C.} \times 10^3$	1.2053	-1.7855	1.9320	-1.3600	0.7430	-0.9258	0.9913
$\kappa(x_i)_{basin}^{H.M.} \times 10^3$	1.2976	-1.5842	1.3432	-0.4067	-0.6376	0.3714	0.3351
$rel.\ err.\ (\kappa)(\%)$	7.6	11.3	30.5	80.1	185.8	140.1	66.2

Table 5.4: Spatial variation of curvatures for base horizon along the horizontal direction compared between true and history-matched models

As expected, the maximum relative error for both horizons occurs at the point of spurious uprising ($x = 625\ ft$). The problem is more severe for base horizon as the history matched model gives curvatures with directions opposite of true ones around the spurious uprising point ($x \in (500\ ft, 875\ ft)$). Also comparatively smaller errors close to the injection and production wells are observed. This implies that the potential field and consequently flow behaviour are more influenced by the curvature of horizons in the vicinity of sources or sinks. However moving away from left extreme (injection well) the relative errors for both horizons are increased which indicates the reduced sensitivity of water front advancement to the horizons curvatures. In general the effective gravitational force imposed on water front is influenced in the first place by the layer thickness and secondarily by the local curvatures of top and base horizons. The production profiles are strongly dependent on the sweep efficiency of water front; thus the closer the points to the injection well the more the contribution of their corresponding curvatures to the production profiles. This explains the better history-matched curvatures close to the injection well in contrast with production well. Generally one might conclude that volume bounded between top and base horizons influences dominantly the production, while curvatures predicted for horizons are plausible just near wells. Also history matched model is likely to yield a flattened spatial variation of thickness in case of reaching local minima.

Convergence regions of uncertain heights have been depicted individually for base and top horizon in figure 5.11 and 12 respectively. Red dotted horizontal line shows centre of convergence region, while true heights have been marked with black dotted arrows.

Less discrepancy between true and NA-converged heights for both horizons is observed near to the left extreme, where the injection well is drilled. Effective thickness of oil bearing formation near to injection well dominantly controls the displacement efficiency of water injection. Because remembering water is injected at a constant pressure, volumetric injection rate and gravity segregation effects are mainly determined by the depths of top and base horizons. A weaker concordance between true and NA-

converged heights is distinguished near to the right extreme (around the production well). Although it is expected to achieve true heights around the production well (where the simulated data are extracted from), but spurious uplifting occurred for the fifth height on both horizons influences trend of NA-converged height for sixth and seventh heights and make them displace a bit upward.

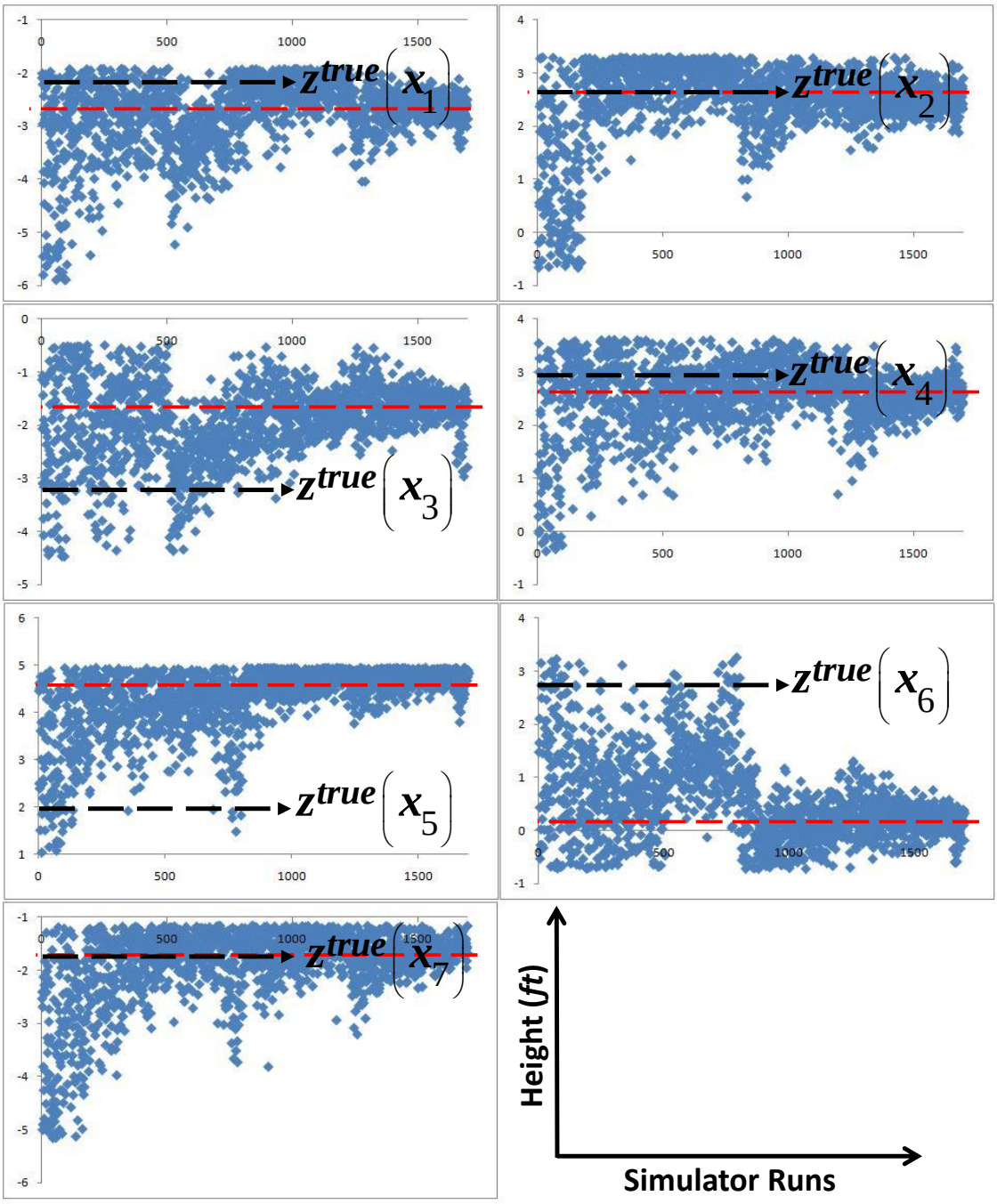

Figure 5.11: Convergence of NA for heights of the base horizon (shown with red colour) in contrast with true heights (shown with block dotted arrows)

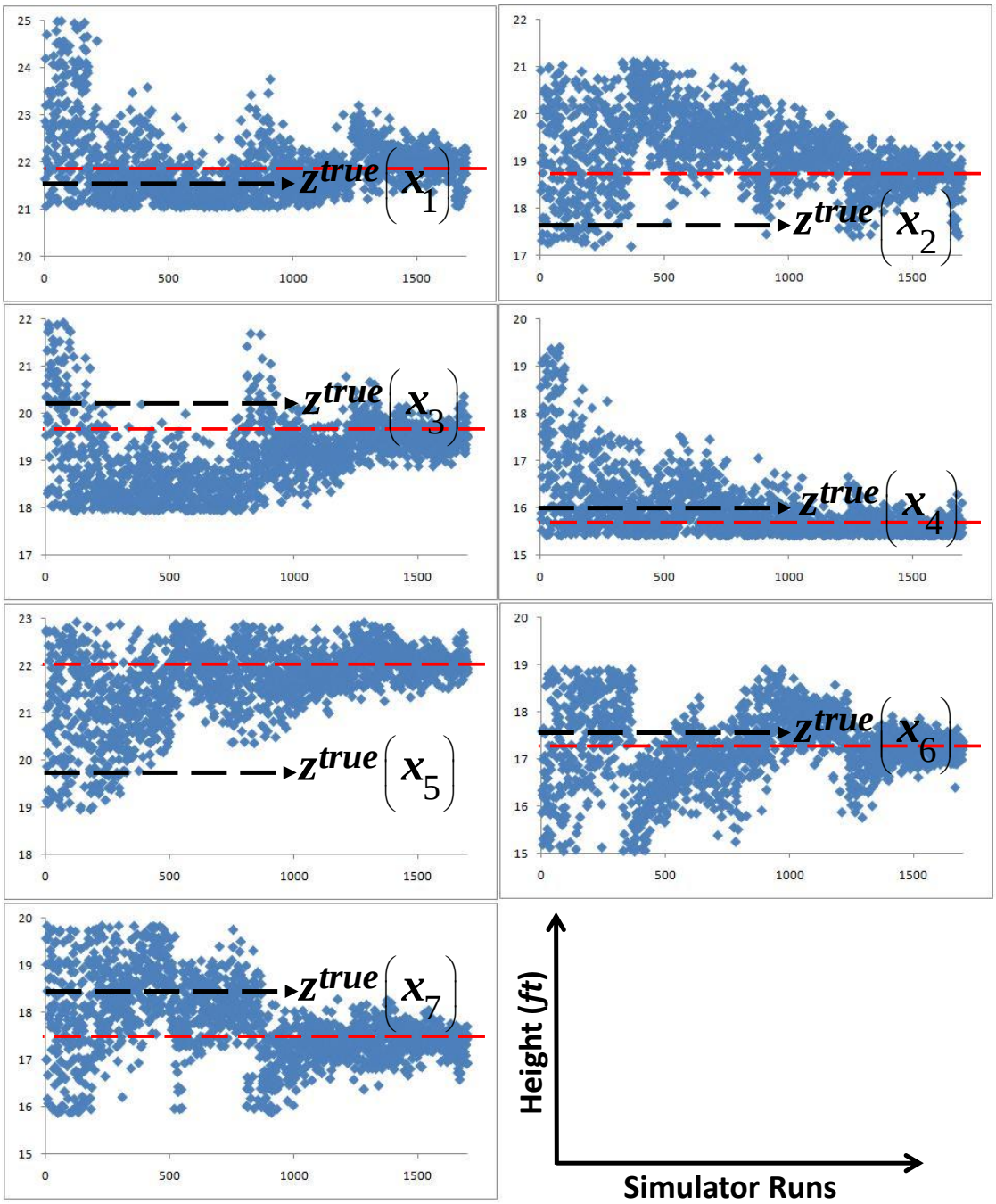

Figure 5.12: Convergence of NA for heights of the top horizon (shown with red colour) in contrast with true heights (shown with black dotted arrows)

Remembering the ratio (n_r/n_s) of $(1/7)$, the neighbourhood algorithm has been run in a more exploitative mode, rather than explorative with a faster convergence. Thus it is very probable that NA gets stuck and converges to local minima especially where the effect geometry of horizons is less significantly seen on production data. We believe this is what happens for the fifth height where spurious uprising turns up.

5.1.3 Quantifying the Uncertainties of Reservoir Horizons

History matching with NA leaves an ensemble of models with horizon heights sampled through the prior confidence interval. In general any kind of probability distribution can be assigned for the prior confidence interval honouring the nature and the sources of uncertainties with horizon heights. In this synthetic problem, a uniform probability is proposed over the prior range**.** To update our beliefs about obtained set of models, it is desired to assign revised probability weights to different models with low misfit based on the likelihood of models obtained from their misfit values ($L(m|O)=e^{-M}$). As discussed in Chapter 2, Bayes rule is a powerful tool which relates posterior probability distribution (PPD) to prior information and likelihood estimation of models:

$$p(m|O)=\frac{L(m|O)\,p(m)}{\int_M L(m|O)\,p(m)\,dm} \qquad (5.8).$$

NA-Bayes library written by Sambridge [1999-B] receives set of sampled models with their corresponding misfits and returns posterior probability densities (PPD) for each model. Obtained incremental probabilities can be converted to cumulative probabilities (CDF). This allows doing posterior inference on the ensemble of models provided by history matching.

Cumulative posterior probabilities are used to determine credible intervals for each parameter; interpolating CDF gives us values corresponding to 10%, 50% and 90% probability for each parameter which are referred to as p10, p50, p90 respectively. p10, p50, p90 obtained for all parameters are gathered and used to construct base and top reservoir horizons. Model built with p10s is most pessimistic model and one built with p90s is most optimistic reservoir model. It is believed that the models built with p10, p50, p90 heights can schematically represent the bounds of updated credible interval for each horizon.

In figures 5.13 and 5.14, p10, p50, p90 for the heights of base and top horizons have been plotted against the axial position (x). For both horizons, truth case (coloured with purple) is well captured within the credible interval, although it varies alternatively between upper and lower bounds. Width of posterior interval defined by $|p90 - p10|$ for each height has been depicted in figure 5.15 which has a plateau of 2.0 for more than half of model extension. Another plateau of almost 2.5 is observed around the fifth point. This indicates spurious results due to local minima might end up with higher uncertainty after posterior inference.

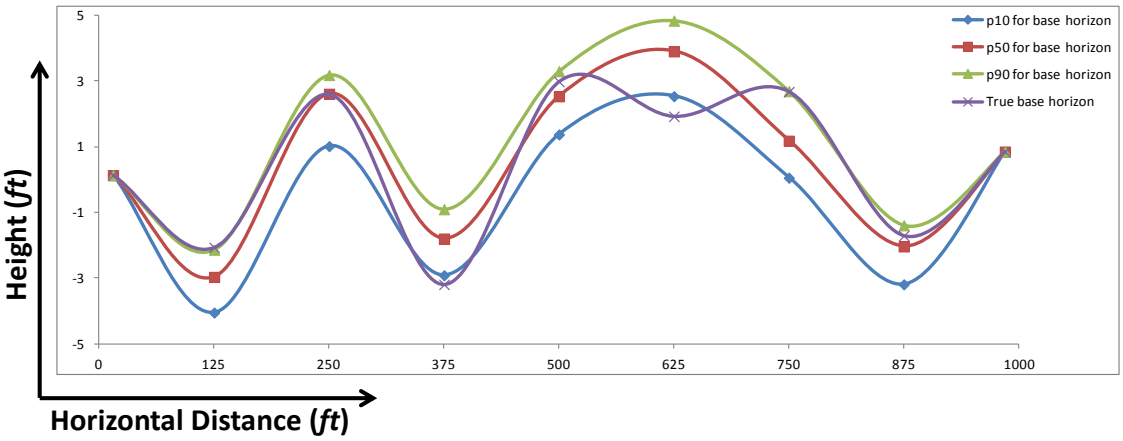

Figure 5.13: Posterior credible interval for base horizon compared with truth case

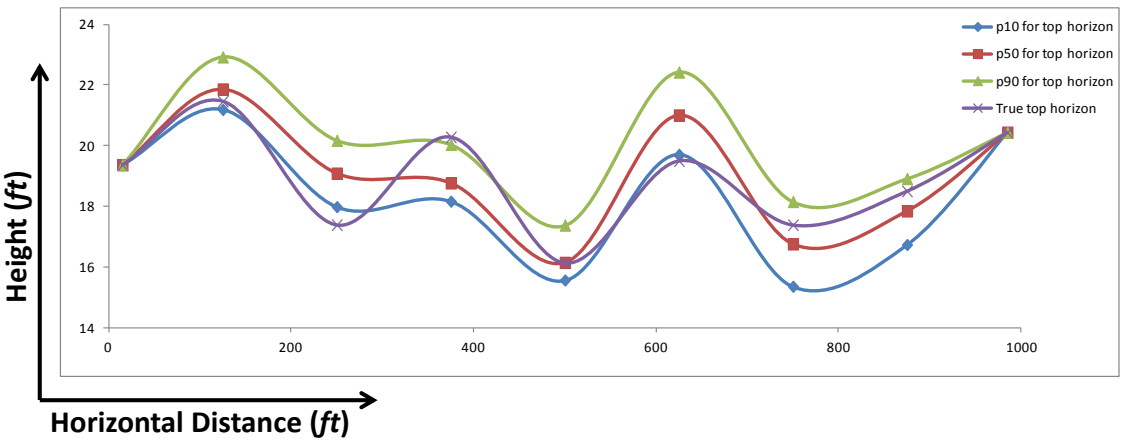

Figure 5.14: Posterior credible interval for the top horizon compared with truth case

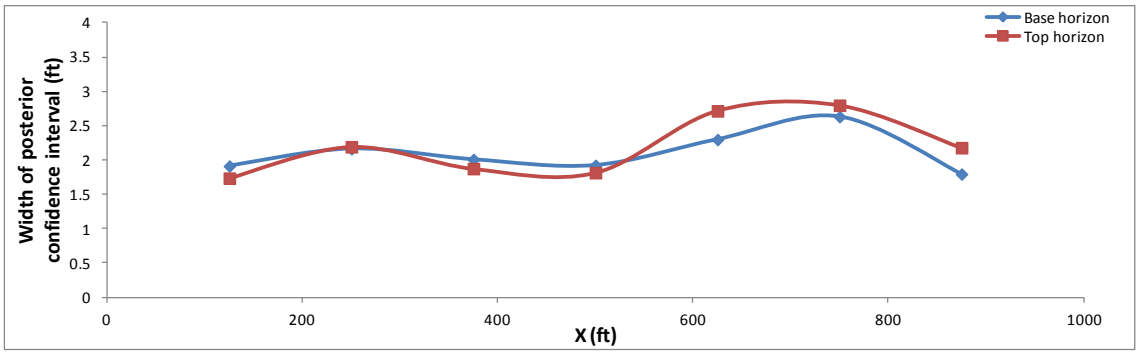

Figure 5.15: Difference between bounds of credible interval for base and base horizons

However remembering the width of prior confidence interval which is 4.0 for all heights, posterior interference leaves an uncertainty range narrowed down by 47.5% and 45.5% for the base and top horizons respectively compared with prior ranges. Clearly less uncertainty is anticipated when NA is run on a more explorative mode. Variation of heights of top and base horizons would immediately alter size of reservoir, so one can investigate uncertainty with oil volume by plotting CDFs versus STOIIP for respective model. This has been depicted in figure 5.16, in which the effect of posterior inference on reducing uncertainty of STOIIP is apparent. The wide prior range of STOIIP between the models with minimum and maximum thickness has been updated to a marginal range of [*35708 STB, 39762 STB*].

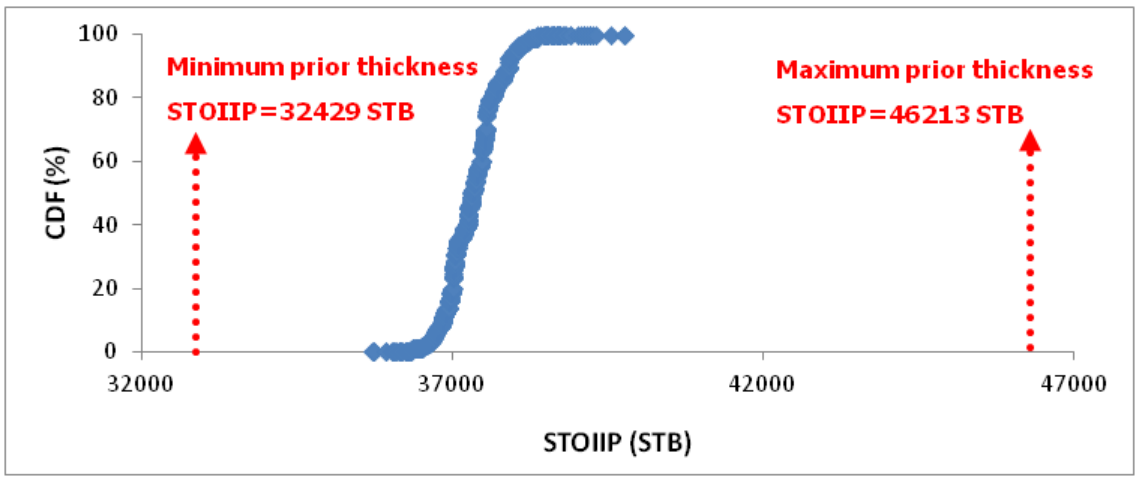

Figure 5.16: Posterior cumulative probability distribution on prior range of STOIIP

As shown in figure 5.17, STOIIP of Truth Case (T.C.) (36826 *STB*) lies between bounds of updated credible interval $[p10 = 36796\ STB,\ p90 = 37904\ STB]$, while STOIIP for reference model (with seismic picked horizons) falls outside the credible interval.

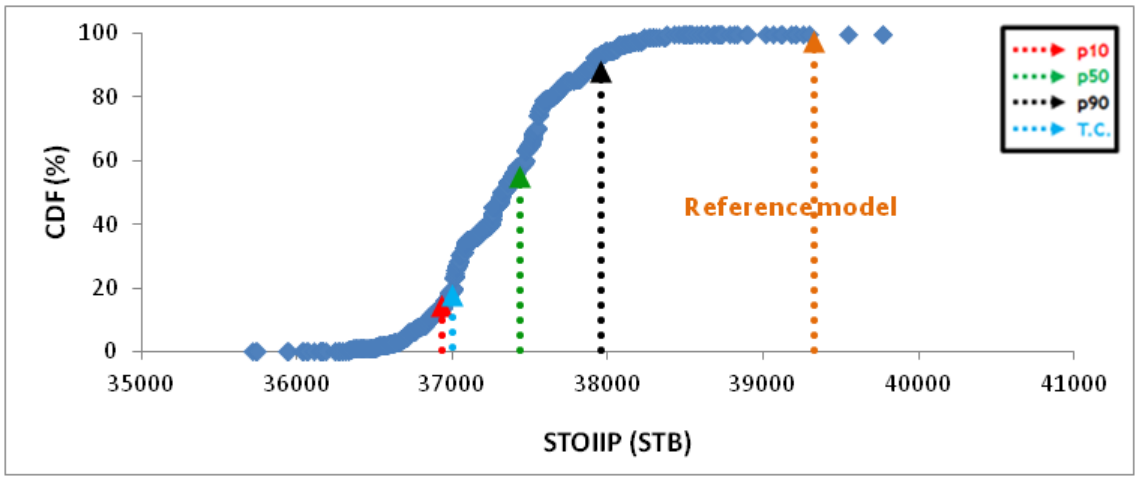

Figure 5.17: Posterior CDF on posterior credible interval of STOIIP

Water and oil production profiles were depicted in figures 5.18 and 5.19 for models built with extreme values of posterior credible interval (p10, p90) along with the true model. Comparing with figures 5.6 and 5.7 (WWPR and WOPR for prior range) clarifies the considerable contribution of Bayesian inference to diminish variability of production profiles caused by structural uncertainties of horizons.

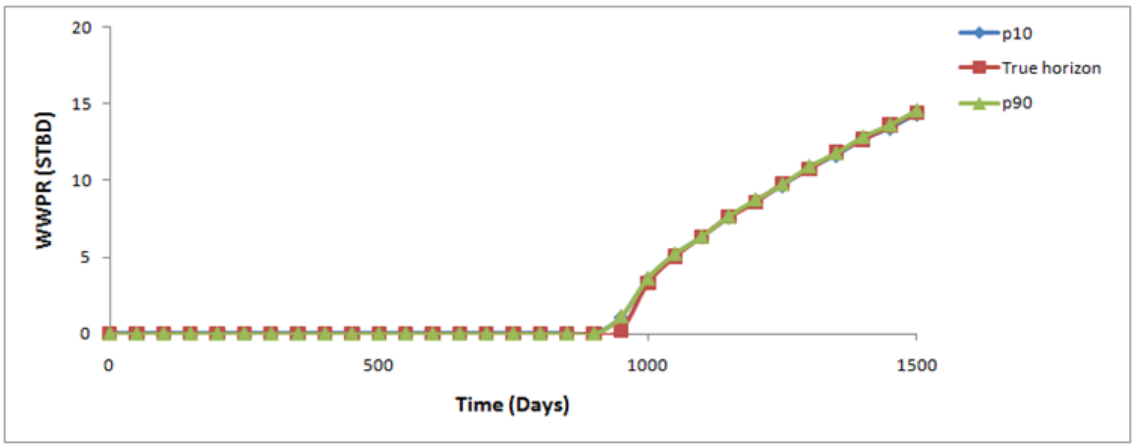

Figure 5.18: Water production for the updated credible interval

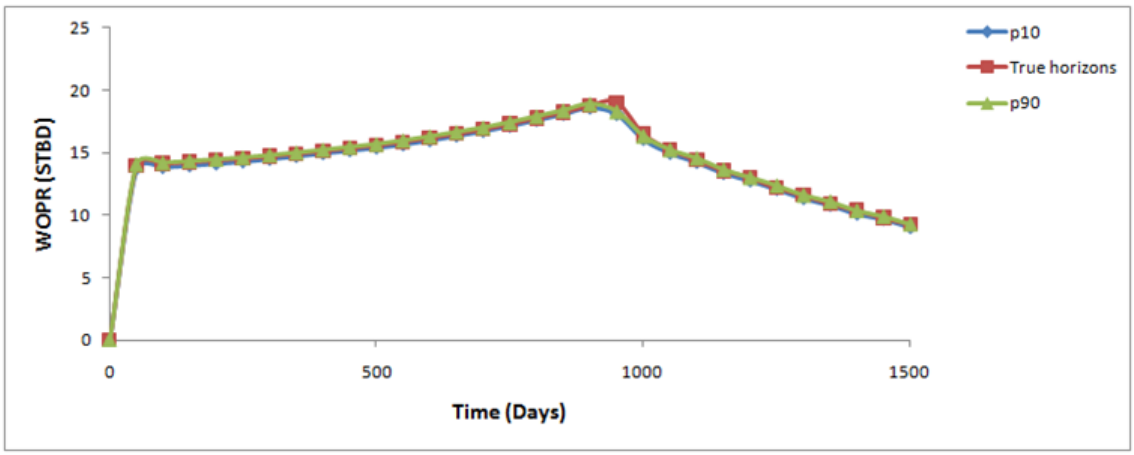

Figure 5.19: Oil production for the updated credible interval

In order to compare the STOIIP uncertainty reduction values for different exploration/exploitation modes of NA, we perform the history matching and uncertainty quantification for different values of (n_r/n_s) and for each ratio, calculate the narrowing index of STOIIP uncertainty interval as defined by Eq. 5.9:

$$narrowing\ index = Nar.\ Idx. = \left(1 - \left|\frac{p90 - p10}{Max - Min}\right|\right) \times 100 \qquad (5.9).$$

The results of this compartive study given in table 5.5.

(n_r/n_s)	$Nar.\ Idx.\ (\%)$
(*1/1*)	6.60
(*1/3*)	6.92
(*1/5*)	7.11
(*1/7*)	7.23
(*1/9*)	7.49
(*1/11*)	6.53

Table 5.5: Variation of narrowing index of STOIIP credible interval against exploration/exploitation modes of NA

Results clearly imply that smaller values of (n_r/n_s) ratio (more exploititive NA modes) leads into more enhancement in STOIIP prediction, as NA would refine the sampling through regions with very good fit into the production data and creates a more compact ensemble which is less scattered throughout the parameter space and consequently a narrower credible interval for STOIIP is obtained. However it seems that for (n_r/n_s) ratios less that (*1/10*), the parameter space is not properly explored by algorithm and some good fitting regions around the truth case are not revisited, as a result narrowing indices would decline by decreasing (n_r/n_s) ratio under (*1/10*).

5.2 Modelling the Uncertainty of Faults

Faults are considered as the planar discontinuities across the volume of rock that significantly displace the stratigraphic layers. By definition, two sides of a normal fault are called hanging wall and foot wall; hanging wall belongs to block occurring above the fault plane and foot wall belongs to block located above the fault plane (Bordie et al., 2007). During the faulting process, some pieces of rocks from either hanging wall or foot wall are broken, crushed and dragged alongside the fault plane (Sperrevik et al., 2002). Resulting material (fault gauge) is spread over the fault surface and accommodates for a flow sealing effect along the fault plane. In addition sub-scale fractures normal to the faulting plane are developed into the hanging and foot walls. Thus fault in reality is not a plane, but has a thickness varying along the fault surface. These fractures and non-uniform distribution of fault gauge over fault surface allows for cross flow leakage through the fault opening.

As stated by Knipe [1997] and Manzocchi et al. [1999], in general flow in reservoir simulation is influenced by faults in two ways:

1. Fault displacements juxtapose different stratigraphic layers of likely high permeability discrepancy. Therefore the horizontal reservoir interconnectivity is altered by fault throw. Moreover fault inclination allows for an increased effect of gravity force on flow especially in the vicinity of fault plane. As a result, fault

inclination can have a positive or negative impact on the reservoir vertical interconnectivity depending on the inclination angle.

2. The altered transmissibility across the fault plane due to the fault gauge and related fractures in faulted zone causes that fault acts as barrier or conduit for fluid flow. Thus the main flow paths throughout the porous rock are impressed by faulting pattern and geometry.

In reservoir simulation the alteration of transmissibility across the fault plane and the possibility of cross leakage is represented with transmissibility multipliers defined for both sides of fault and for both direction ($TM_{x/y}^{+/-}$) which correct the fluxes at each face coinciding with the fault plane ($f_{x/y}^{+/-}\Big|^{fault} = TM_{x/y}^{+/-} * f_{x/y}^{+/-}$). As a common practice in order to history-match the faults, only the fault transmissibility multipliers are varied and its geometry remains fixed. In this thesis we are focused on structural uncertainties, thus transmissibility multipliers are kept constant and history matching is carried out to find optimised models of fault geometry. Obviously simultaneous variation of fault geometry and transmissibility multipliers makes it much harder to isolate the special flow effects imposed by fault geometry and consequently leaves less constrained geometrical uncertainties of fault.

5.2.1 Case Description

Model is a two dimensional cross section of a reservoir with a single fault cutting through the oil bearing formation. Model dimensions are 1000 *ft* length by 20 *ft* height by 112 *ft* width which has been discretized into a $100 \times 20 \times 1$ grid. Similar to model described in Case 1, model does not include any aquifer or gas cap. Initial reservoir pressure is uniform and equal to 100 *psia*.

5.2.2 History Matching of Fault Geometrical Properties

The reference model contains a normal fault which divides the reservoir into two blocks, one on the hanging wall of fault on its left side and one on the foot wall of fault

on its right side. Fault surface is assumed to be determined from the considerable discontinuity appearing in seismic time maps. Considering faults as the geological objects extended mainly in vertical direction, poor vertical resolution of seismic and the noisy nature of seismic data makes geometrical properties of seismic picked fault uncertain. Prior uncertainties for each geometrical property of fault (position, dip and displacement) can be represented with prior confidence intervals. Width of prior confidence intervals are determined from the width of zone within the fault trend can be reasonably picked (Irving, 2010-B).

Here in order to investigate the effect of fault uncertainty on flow inter-connectivity two single layer and multi layer model with similar dimensions and true fault geometry.

5.2.2.1 Multi-layer Model

Model contains six layers of alternating high and low permeabilities. In table 5.6, permeabilities and porosities for each layer has been given where the layers are indexed upward starting from the deepest layer.

Layer	$K_h\left(Darcys\right)$	$K_v\left(Darcys\right)$	$\phi\left(volume/volume\right)$
1	0.3	0.06	0.25
2	0.05	0.01	0.10
3	0.5	0.1	0.25
4	0.05	0.01	0.10
5	0.8	0.16	0.25
6	0.05	0.01	0.10

Table 5.6: Rock properties for multi-layer model containing fault

5.2.2.2 Single-layer Model

Oil bearing formation consists of a single layer of uniform porosity 0.20. Horizontal and vertical permeabilities are uniform and equal to 0.20 *Darcy*s and 0.04 *Darcy*s respectively.

Production data are employed to enhance our knowledge about the fault geometry and narrow down the range of structural uncertainties for fault. Simulated production profiles obtained from running simulation on truth case are considered as the observed data. In our knowledge no other methodology can simultaneously update all the geometrical properties of fault (position, dip, throw) during history matching. Fault in the truth case has the following set of geometrical specifications:

X-coordinate of fault entrance point (*ft*)	780
Fault slope (*ft/ft*)	2.0
Fault throw (*ft*)	4.65

Table 5.7: Fault geometrical specifications for truth case

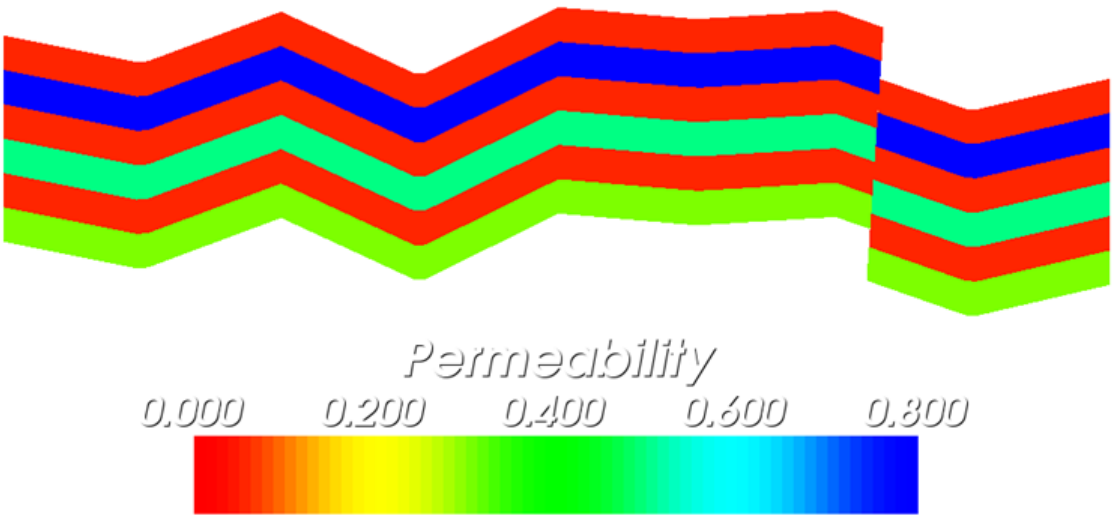

Figure 5.20: Permeability map for multilayer faulted model

Transmissibility multipliers (given in table 5.8) which determine the degree of fault interconnectivity are assumed to be constant over the fault surface on both walls and in both vertical and horizontal directions.

TM_x^-	0.8
TM_x^+	0.8
TM_y^-	0.8
TM_y^+	0.8

Table 5.8: Directional transmissibility multipliers on both sides of fault

The prior uncertainty ranges for geometrical fault specification are listed in table 5.9:

X-coordinate of fault entrance point (*ft*)	350-950
Fault slope (*ft/ft*)	1.25-6.25
Fault throw (*ft*)	-2.0-8.0

Table 5.9: Prior guess of uncertainty ranges for each fault geometrical parameter

Injection well and production well start to flow at time $t = 0\ Days$ with bottom hole pressures set at 150 *psia* and 50 *psia* respectively. Oil and water production histories for both multi-layer and single layer models with true fault geometry have been depicted in figures 5.21 and 5.22. Because of complexity of relation between geometrical fault specifications and resulting potential field, unlike the uncertain horizons, it is not straightforward to determine variation range of production due to structural fault uncertainties. But faults with geometrical specifications picked at extremes of prior uncertainty ranges can be used to rebuild models offering the maximum fault geometrical uncertainties. Production profiles obtained from these models have been plotted in figures 5.23 and 5.24 for multi-layer model and in figures 5.25 and 5.26 for single layer model.

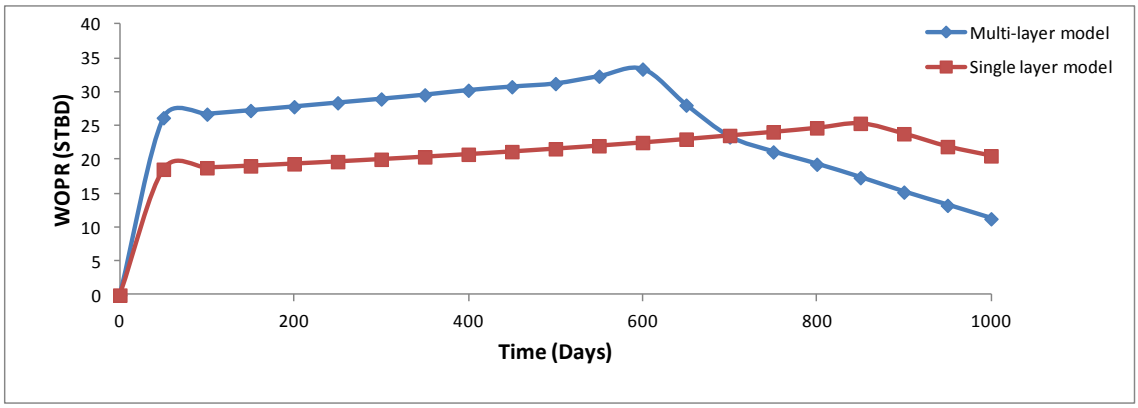

Figure 5.21: WOPR for truth cases of faulted models

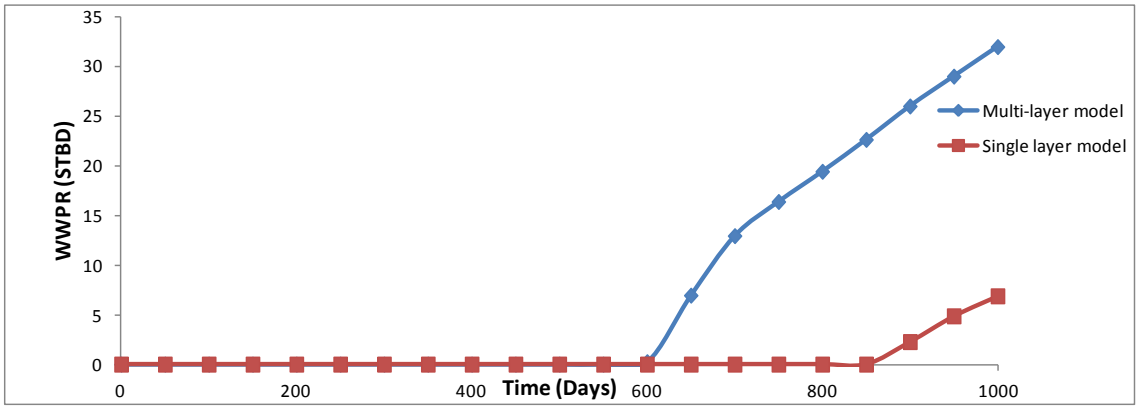

Figure 5.22: WWPR for truth cases of faulted models

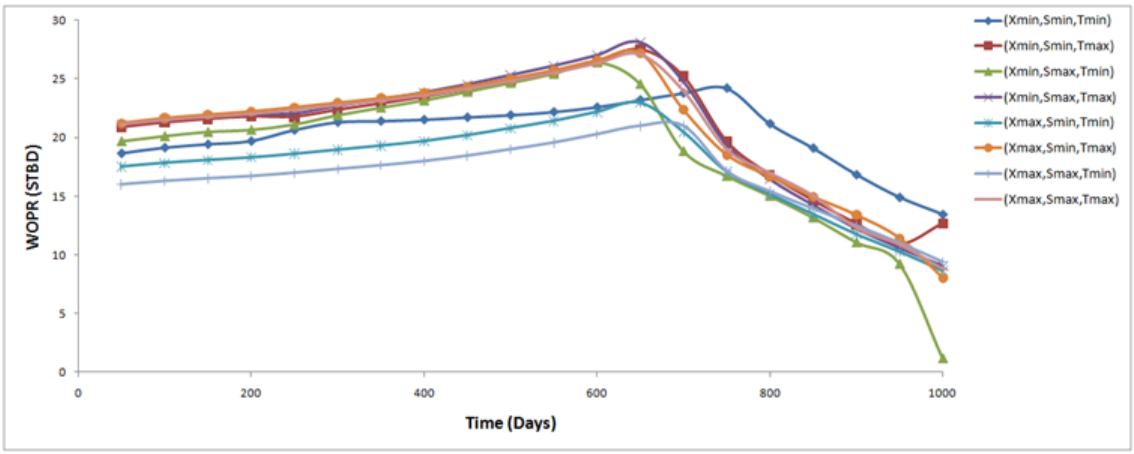

Figure 5.23: Prior uncertainties of oil production for multi-layer faulted model

Predicted production profiles on prior ensemble of fault uncertainties are much more spread for multi-layered model compared with single layer model. This indicates stronger influence of fault displacement and deformation on potential field and consequently flow behaviour in multi-layered model than single layer model.

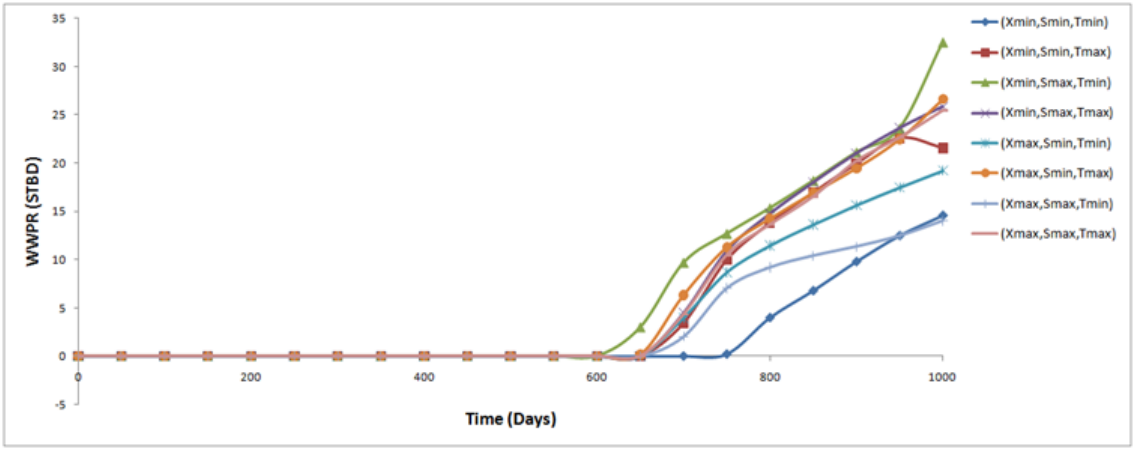

Figure 5.24: Prior uncertainties of water production for multi-layer faulted model

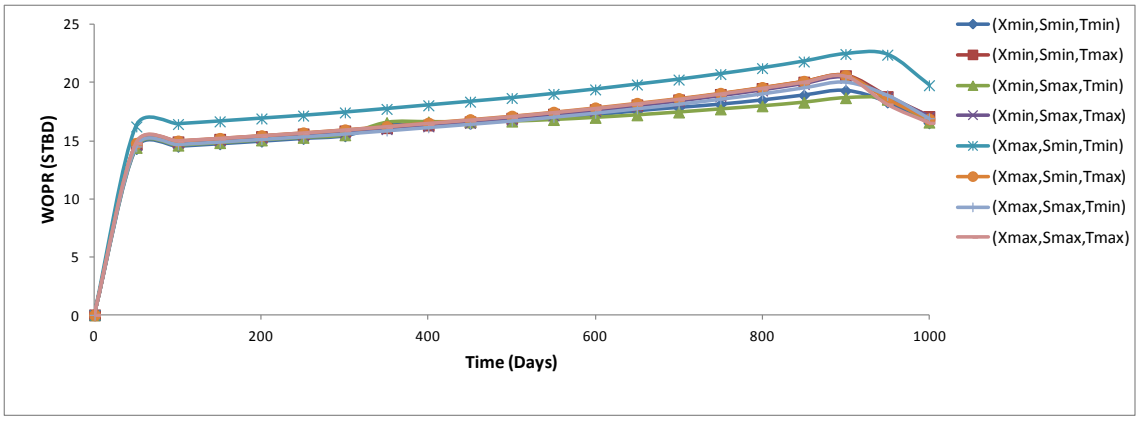

Figure 5.25: Prior uncertainties of oil production for single-layer faulted model

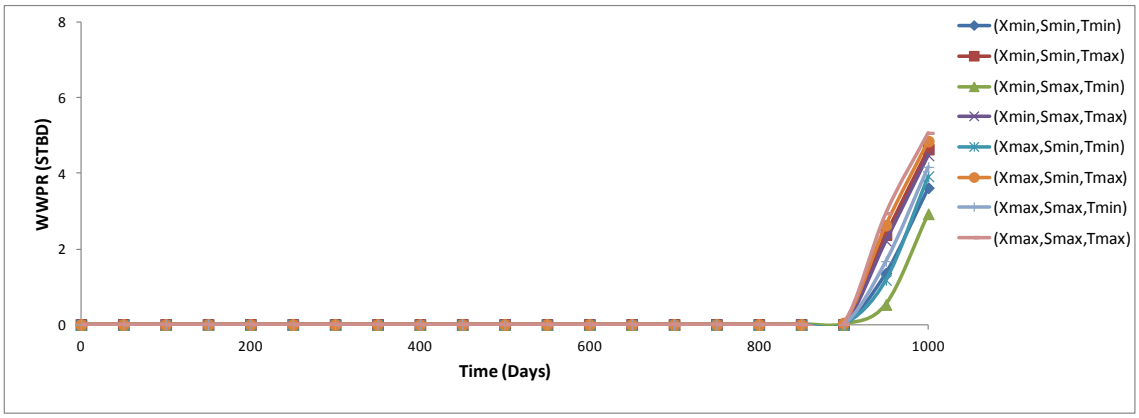

Figure 5.26: Prior uncertainties of water production for single-layer faulted model

Fault throw at its maximum value on the prior range, provides the main contribution to the impact of fault geometry on potential and flow field. Thus as shown in figures 5.23 and 5.24, production profiles predicted for maximum throw (T_{max}) are overlapping regardless of fault location and fault dip varying between extremes of prior ranges. Though as fault throw decreases, production profiles become more sensitive to fault location and dip and the bandwidth of production uncertainty increases. Value of fault throw controls the effective flow conductivity across the fault, as its variation changes the interconnected layers and the surface of each layer-layer interconnection. Also the height difference between two blocks on fault foot and hanging wall sides affects the vertical sweep efficiency of water injection. The higher the block on the hanging wall side, the more gravity potential is maintained for both phases and consequently oil is produced at a higher rate (and water breaks through earlier). Moreover larger fault throw eventuates in less possibility of gravity segregation when displacing phase (water) enters the block on foot wall side. This explains higher production sensitivity to fault throw in multi-layered model.

On the other hand at a constant fault throw, fault location dominantly influences the production. The closer the fault to the right extreme (X_{max}), a longer distance in axial direction should be traversed by water front before entering the block on foot wall side, thus more gravity segregation takes place in left block leading to more deviation from piston-like displacement and a reduced oil production rate. Obviously if parameter

space is explored enough, a narrower posterior uncertainty range is expected for fault throw in contrast with fault location and dip.

It is demanded to match the geometry of fault to the production profiles obtained from simulation on truth cases of both models subject to minimisation of misfit function defined in Eq. 5.5. Input parameters for NA employed for history matching are given in table 5.10:

n_{s_i}	n_s	n_r	Iterations	Total Simulations
300	6	3	120	1020

Table 5.10: NA input parameters for history matching of fault geometry

Misfit values for both faulted models have been plotted in figure 5.27 versus simulations performed on models built with NA optimised fault geometries. Average misfit value is 15.73 when NA optimises multi-layer model which is much higher than corresponding value of 0.034 for single layer model. Moreover late NA convergence to misfits less than unity for multi-layer model contrary to early convergence for single layer model signifies the substantial dependency of production on fault geometry in layered models.

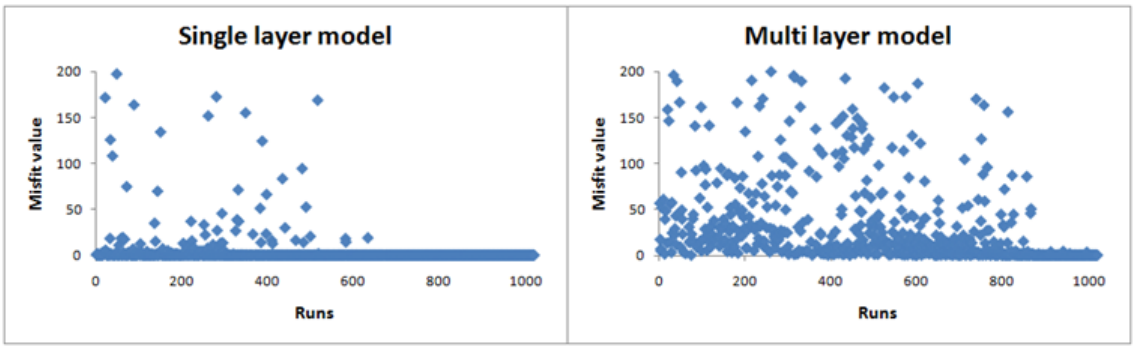

Figure 5.27: NA convergence for history matching on both faulted models

Lowest misfits of 0.019 and 0.003 are obtained after 1009 and 881 runs for multi layer and single layer models respectively. Best NA optimised models were depicted along with the truth cases of multi-layer and single layer models in figures 5.28 and 5.29.

For multi-layer model, history matched values of fault location and fault throw are almost identical to true values. While a significant difference is observed between history matched and true values of fault dip which manifests the fault dip as the parameter with the least influence on production. For single layer case, fault location and throw values obtained for model with lowest misfit are close to the true values, but not as close as multi-layer case.

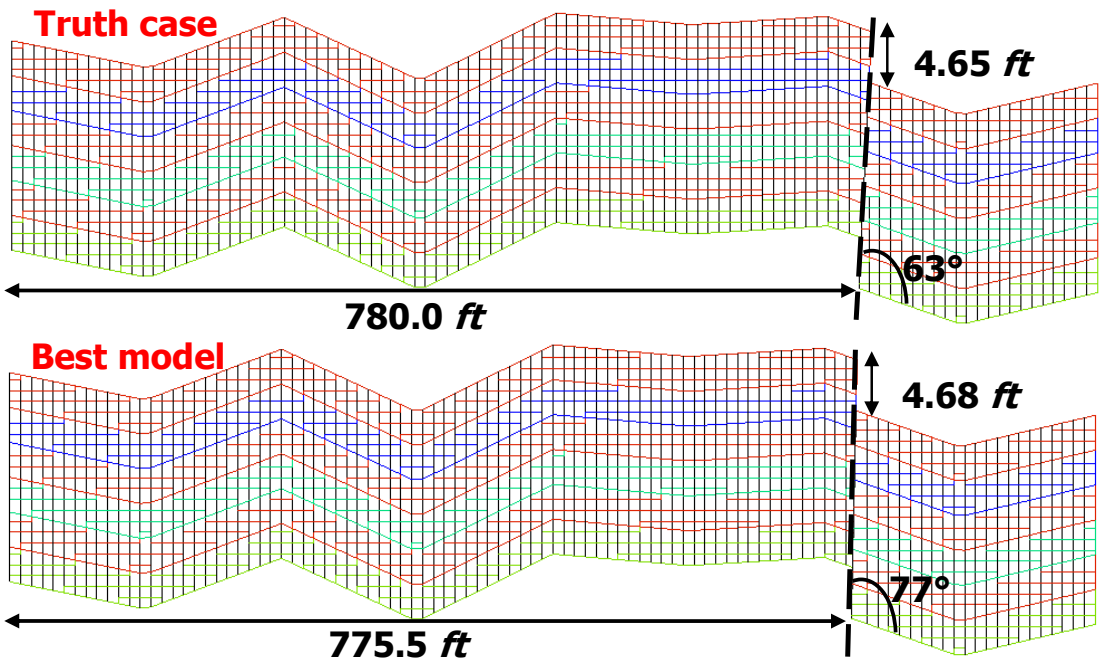

Figure 5.28: Maximum likelihood model compared with truth case for multi-layer model

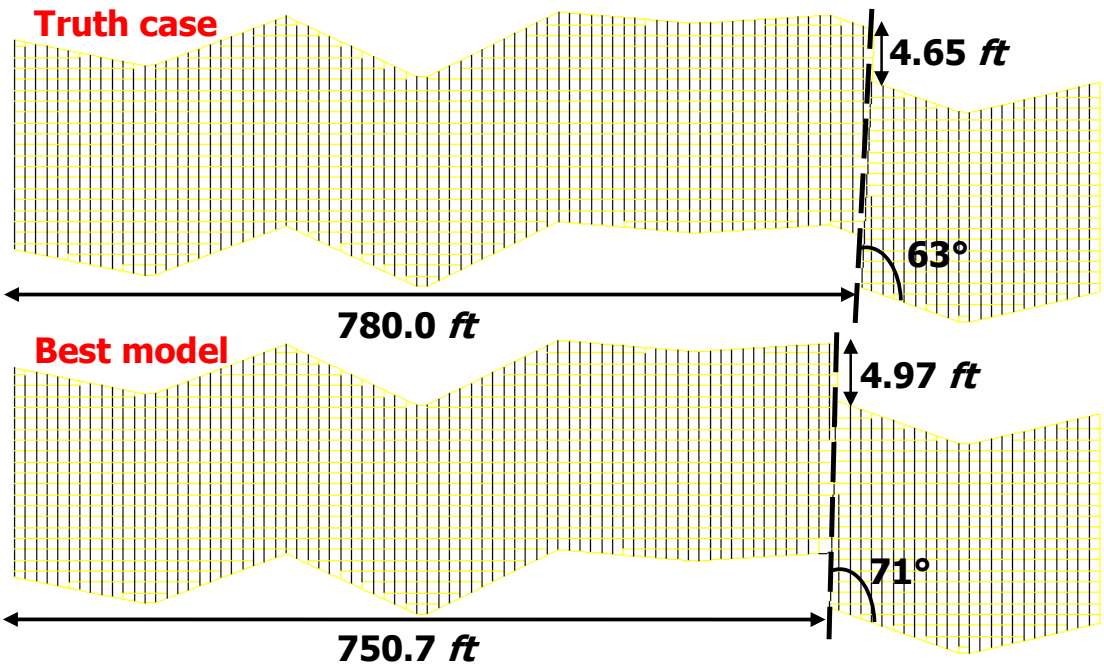

Figure 5.29: Maximum likelihood model compared with truth case for single layer model

For both faulted models, history matched fault slope is considerably far from the true value. As shown in figure 5.30, less fault slope ensues into a larger vertical component of flux vector across the fault surface which enhances the vertical sweep efficiency and increases the production rate. Therefore the production discrepancy resulted from a fault with larger throw compared with truth case (history matched models) can be mitigated by increasing the fault slope such that the same gravity potential is exerted across the fault plane. However augmented impact of increased fault throw on production behaviour in multi layer model should be compensated with a larger fault slope. Thus history matching leaves a larger fault slope in multi layer model in contrast with single layer model.

Indeed the gravity force imposed on the fault plane is much less influenced by fault slope compared with fault throw. Therefore in best history-matched models, fault throw with negligible difference from truth case is accompanied with fault slope with large discrepancy from the true slope. From this discussion fault dip is regarded as the most difficult fault geometrical parameter to be history matched.

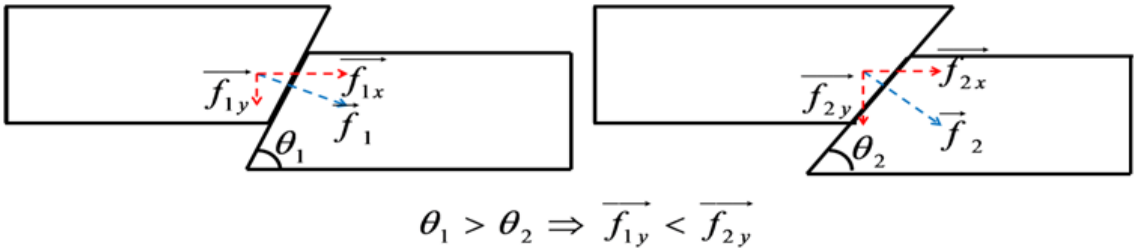

Figure 5.30: Increased vertical flux across fault plane due to reduced fault dip

NA sampling histories for individual fault geometrical parameters have been depicted in figures 5.31, 5.32, 5.33. Centre of NA convergence intervals and the true parameters were displayed with red dotted straight line and the block dotted arrow respectively. For multi-layer model, NA convergence intervals become as narrow as ones for single layer model after much more simulator runs. This confirms the conclusion drawn by the sensitivity analysis of fault geometry. The volume and the complexity of the impact of fault geometry on the flow behaviour are amplified by imposing more heterogeneity. Thus it is more likely for NA to get stuck in local minima in the multi-layer model. Yellow dotted line in figure 5.31 shows occurrence of a local minima for fault throw (the most influential fault parameter).

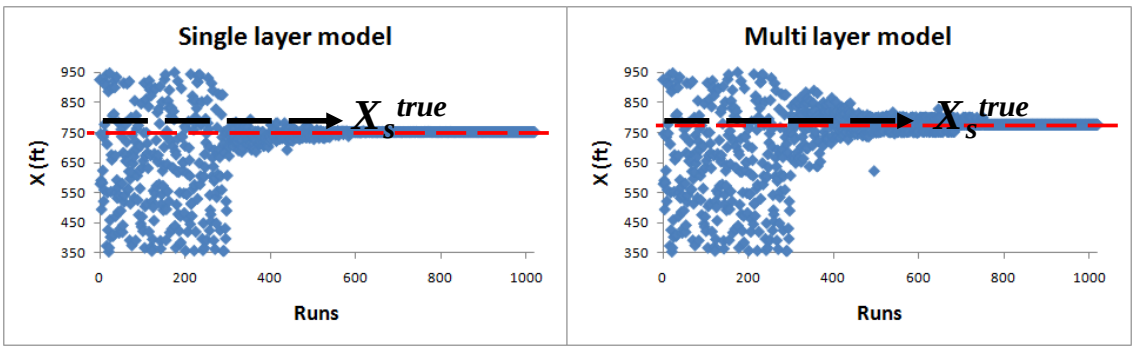

Figure 5.31: History matching trail over both faulted models for fault location

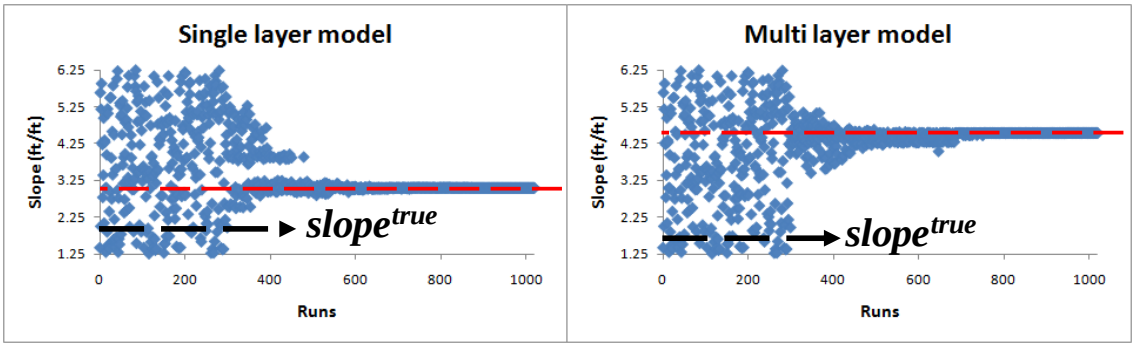

Figure 5.32: History matching trail over both faulted models for fault dip

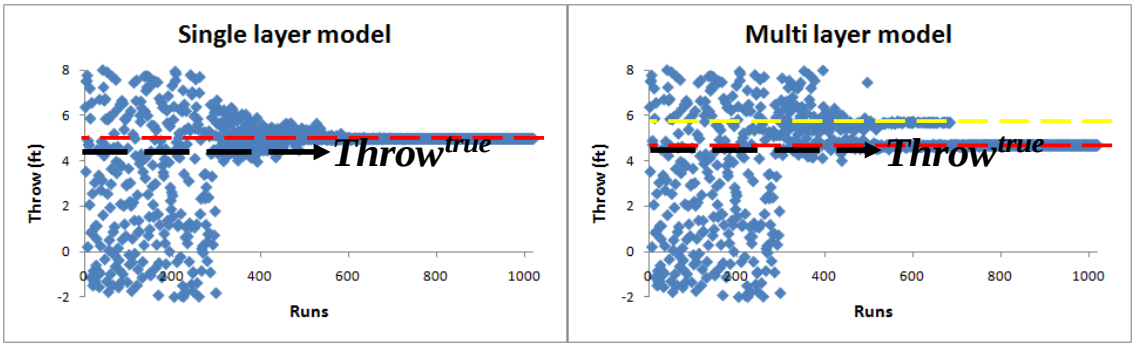

Figure 5.33: History matching trail over both faulted models for fault displacement

Cross sections of misfit surfaces for both faulted models were plotted in figure 5.33 against fault throw. Several local minima are observed for multi-layer model, while single layer model has a much simpler misfit surface with a unique global minimum about 4.97. This reveals that true reservoir vertical and horizontal interconnectivities for multi-layer model are likely to be reproduced by several juxtaposition statuses of bedding layers from different depths. However the stochastic nature of employed optimisation algorithm (NA) and a balanced explorative-exploitative mode of NA ($(n_r / n_s) = 1/2$) ensures to achieve a good sampling and relief from local minima.

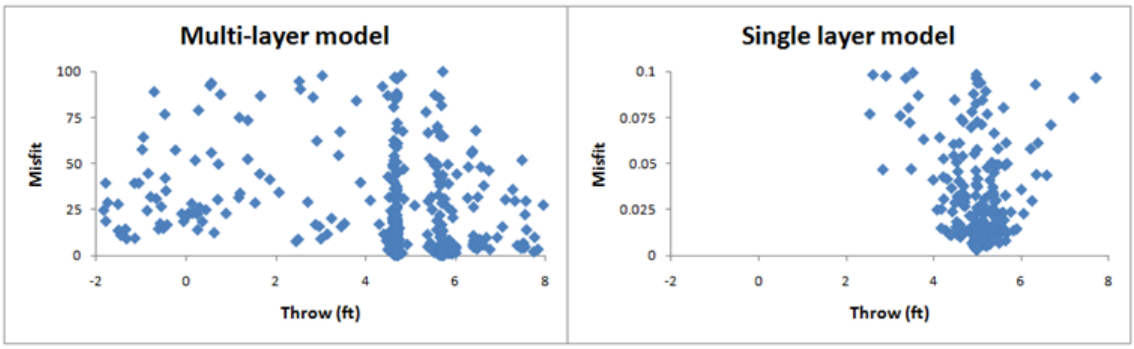

Figure 5.34: Misfit surface for faulted models showing local minima for multi-layered model

5.2.3 Quantifying the Uncertainties of Fault

Ensemble of models sampled through the space of fault parameters is utilised by NAB routine to reconstruct the posterior probability densities. Thereafter posterior Bayesian inference determines the interpolated p10 and p90 values as the bounds of credible intervals and p50 as the median for each fault geometrical parameter.

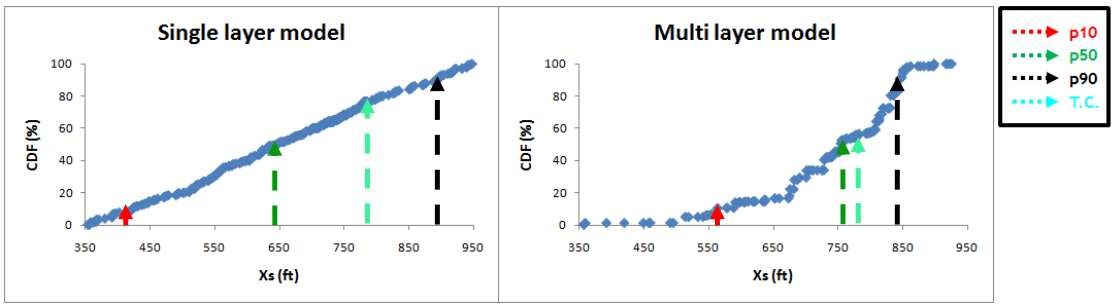

Figure 5.35: CDF for fault location used to determine bounds of posterior credible interval

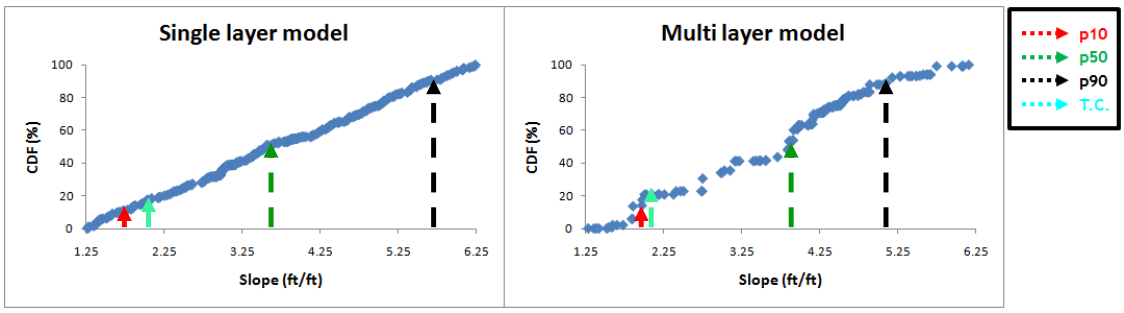

Figure 5.36: CDF for fault slope used to determine bounds of posterior credible interval

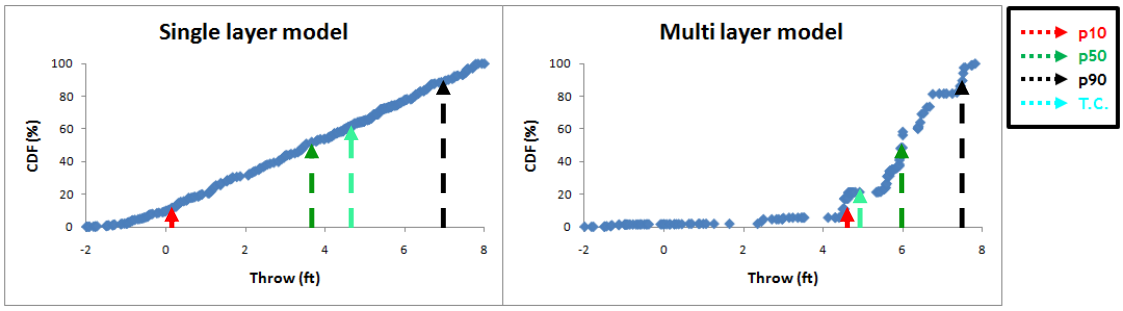

Figure 5.37: CDF for fault throw used to determine bounds of posterior credible interval

Credible intervals for individual parameters have been displayed on CDF plots for both reference faulted models in figures 5.35, 5.36 and 5.37. True fault geometrical parameters for both models lie within the credible interval.

		p10	p50	p90	Mean	T.C.
Single layer Model	X_s (*ft*)	423.1	647.1	893.8	653.0	780.0
	Slope (*ft/ft*)	1.64	3.55	5.63	3.70	2.00
	Throw (*ft*)	0.01	3.50	7.07	3.55	4.65
Multi layer Model	X_s (*ft*)	562.8	754.1	844.5	741.4	780.0
	Slope (*ft/ft*)	1.85	3.85	5.13	3.60	2.00
	Throw (*ft*)	4.48	5.99	7.49	5.86	780.0

Table 5.11: Bounds of posterior credible interval, median and mean vs. true values

CDF varies relatively linearly with respect to geometrical parameters in single layer model, indicating incremental probabilities (PPDs) have been distributed almost equally around the middle point of prior confidence interval with a relatively large standard deviation. This is also evidenced by the fact that mean and p50 values calculated for each parameter are closefitting to the middle point of corresponding prior range. While for multi-layer model, CDF have a completely non-linear behaviour over the prior range of fault parameters, such that the main bulk of CDF values lies to the right of middle point, specifically for the fault throw and location. Also noticing small CDF over the left half-range (values less than middle point of prior confidence interval), more probable data in the posterior are frequently concentrated around the mean value in right

half-range. As a result smaller standard deviations and narrower credible intervals are attained for multi-layer model compared with single layer model. Narrowing index defined by the percentage of contraction of uncertainty range after posterior inference along with corresponding values of standard deviation have been given per each parameter for both faulted models in table 5.12.

Model	Single layer Model			Multi layer Model		
Parameters	X_s	Slope	Throw	X_s	Slope	Throw
Narr. Idx. (%)	21.55	20.20	29.40	53.05	34.40	69.90
Std. Dev.	164.5	1.44	2.59	105.1	1.19	1.47

Table 5.12: Percentage of uncertainty reduction per each parameter for faulted models

The maximum shrinkage of prior uncertainty range occurs for the fault throw in multi layer model emphasising predominant role of height offset imposed by fault on production in multi layer model. In accordance with the sensitivity analysis performed on fault parameters, updated credible intervals are broader in single layer model.

For both faulted models, negative fault throws have been deleted from the posterior credible interval. It is due to completely different flow behaviour for the negative throws. At negative throws, gravitational force opposes the flow potential for both phases when they enter from left downthrown block to the right block, while at positive throws the flowing potential is supported by gravity force across the fault plane. Accordingly considerably smaller production rates are expected for negative throws.

In order to schematically represent the variation of fault geometry within the posterior credible interval, one can rebuild models combining the p10, p50 and p90 values of fault parameters. The extreme geometrical uncertainties can be seen for two faults one built with p10 values and another built with p90 values. Figures 38 and 39 show the

representational comparison between the truth case and the models obtained from combinations of values on the bounds of credible intervals.

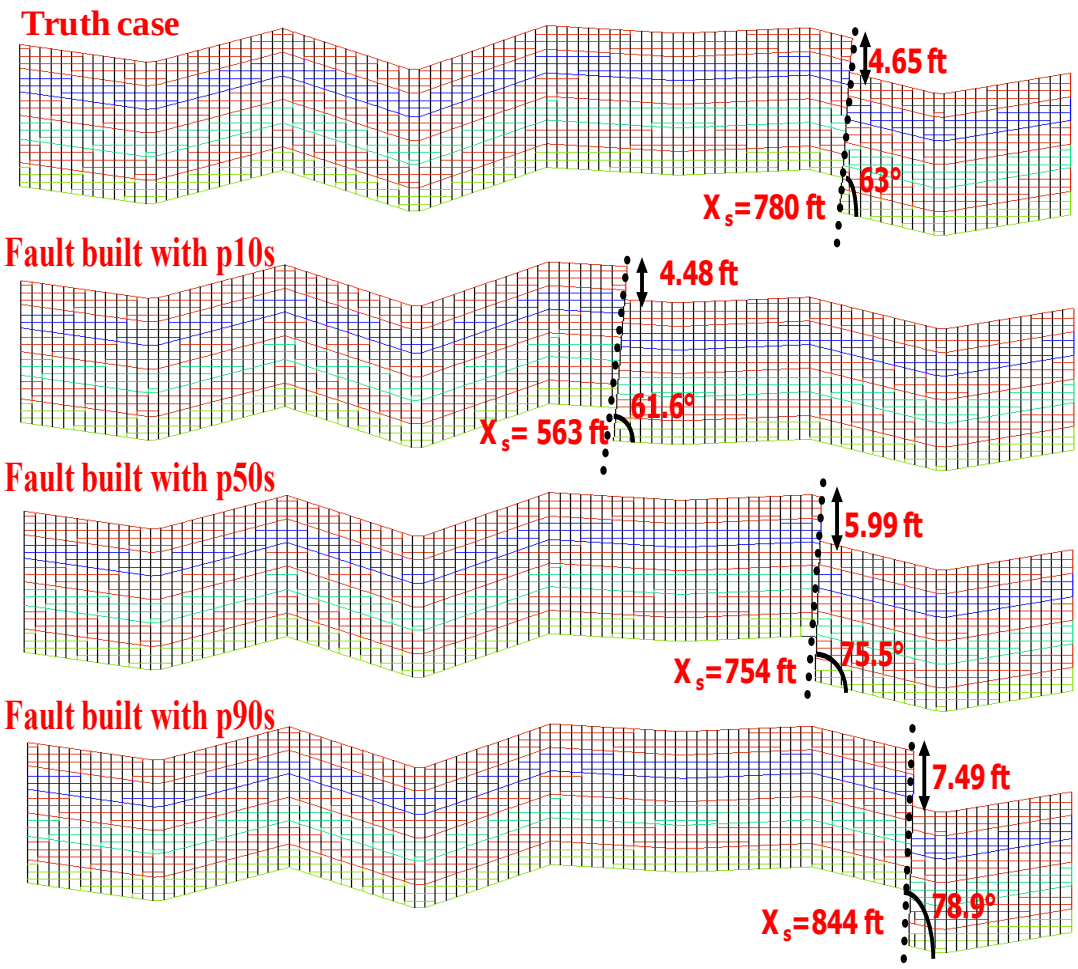

Figure 5.38: Truth case vs. models with extreme posterior structural uncertainties for multi layer model

The proficiency of posterior inference can be testified with re-evaluating the variation range of predicted productions over updated uncertainty ranges. Combining fault parameters arbitrary picked from the bounds of corresponding credible intervals (p10 or p90) would end up with 8 models offering the maximum posterior uncertainties. The narrower the range of production profiles for such a set of models implies the more confined the posterior uncertainties after posterior inference.

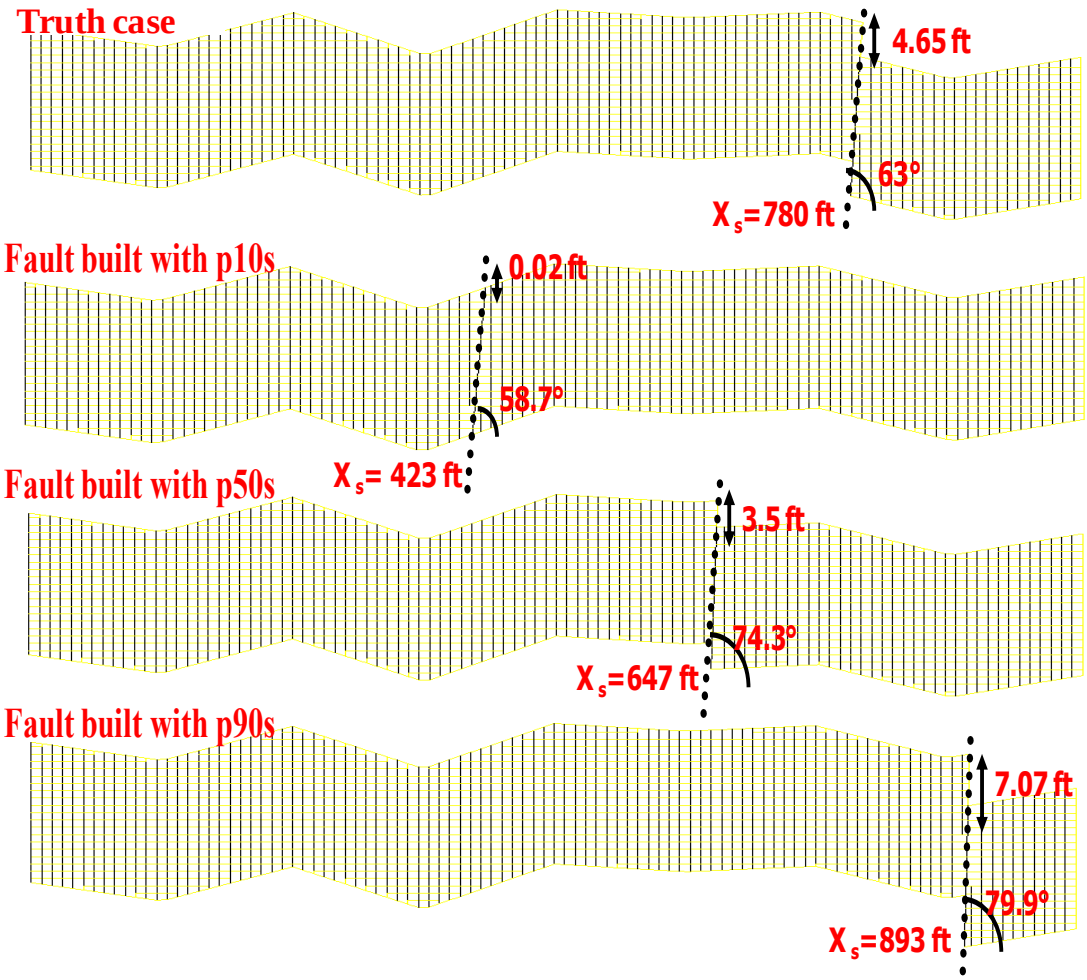

Figure 5.39: Truth case vs. models with extreme posterior structural uncertainties for single layer model

Updated range of uncertainties of oil and water production has been depicted in figures 5.40 and 5.41 for multi layer model and in figures 5.42 and 5.43 for single layer model. Even for the multi-layer model with diverse production profiles at prior, almost coinciding production profiles are obtained for the representative ensemble of extreme posterior uncertainties which confirms the functionality of Bayesian inference for constraining large scale uncertainties like fault.

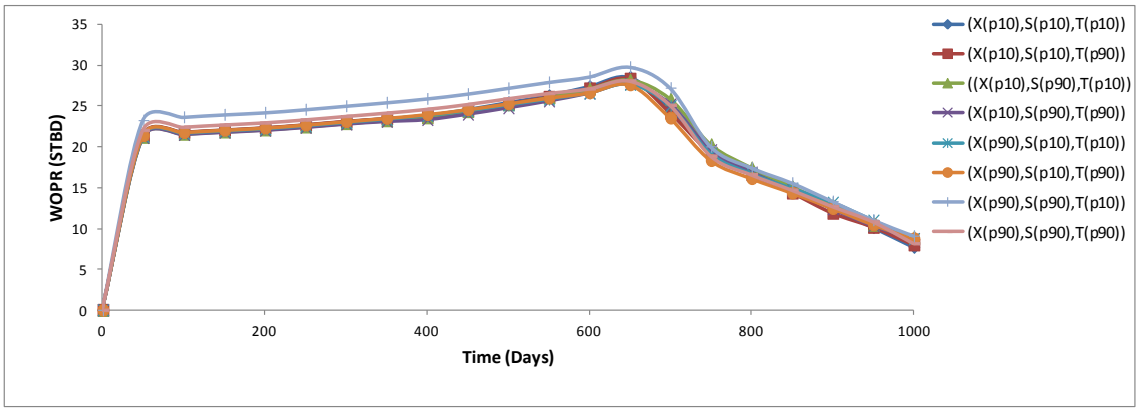

Figure 5.40: Posterior uncertainties of oil production for multi-layer faulted model

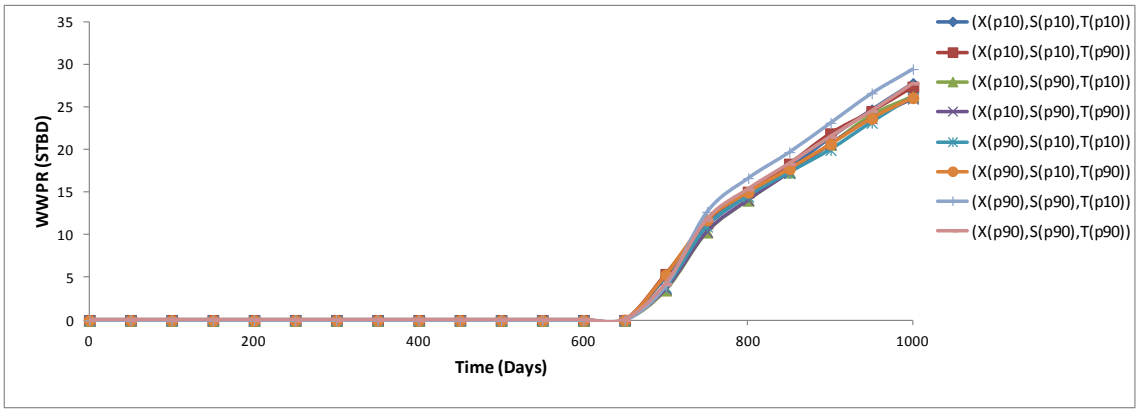

Figure 5.41: Posterior uncertainties of water production for multi-layer faulted model

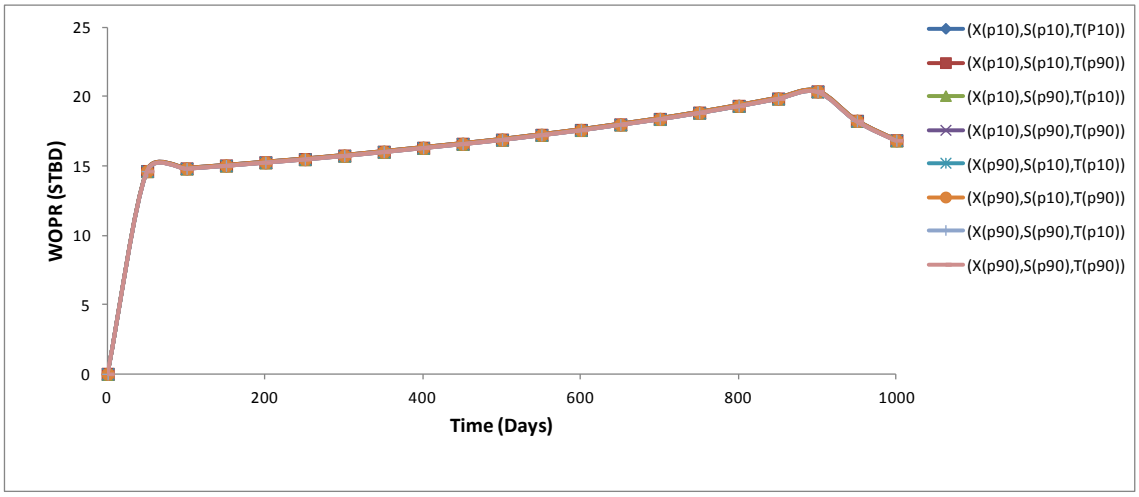

Figure 5.42: Posterior uncertainties of oil production for single-layer faulted model

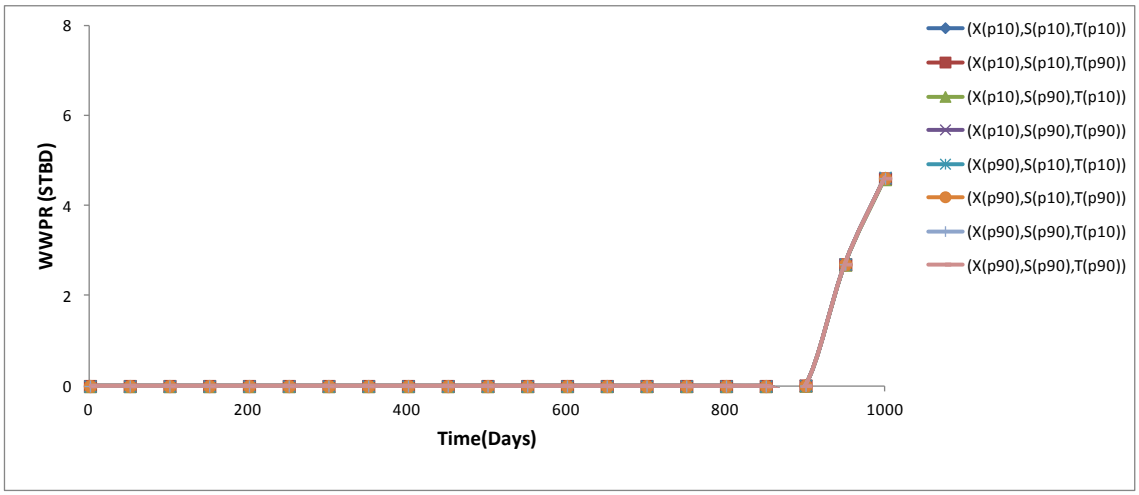

Figure 5.43: Posterior uncertainties of water production for single-layer faulted model

5.3 Modelling the Uncertainty of Pinchouts

According to geological definition, pinchouts are recognised with reduction in bed thickness resulting from down-lapping or on-lapping stratigraphic sequences. Thus it can be considered as an incomplete layer which is terminated with thinning or tapering out (pinching out) against adjacent geological formations. Depending on the nature of layers confining the pinched out layer, pinchout can act as a flow barrier or creates a favourable geometry for a reservoir trap. Here we consider impermeable pinched out layers encompassed with permeable oil bearing formations. Figure 5.44 shows typical instances of pinchouts.

Figure 5.44: Left: on-lapping stratigraphic layers, Right: down-lapping stratigraphic layers (taken from Temistochles Rojas, 2010)

Pinchout geometry can be described with an elongated eclipse with high contrast between major and minor diameters. Therefore it is a rational approximation to represent the pinchout with two almost degenerate triangles with equal bases located one on another upside down. Angles at vertices of bases are very small, such that pinchout has been extended along the over-lapping bases of two triangles termed as the transverse or the major axis of pinchout. As figure 5.45 shows a pinchout can be uniquely specified with (x,z) coordinates of 4 points:

- Head point: the point on transverse axis with smallest x coordinates
- Tail point: the point on the transverse axis with largest x coordinates
- Apogee point: Obtuse-angled vertex of upper triangle
- Perigee point: Obtuse-angled vertex of lower triangle

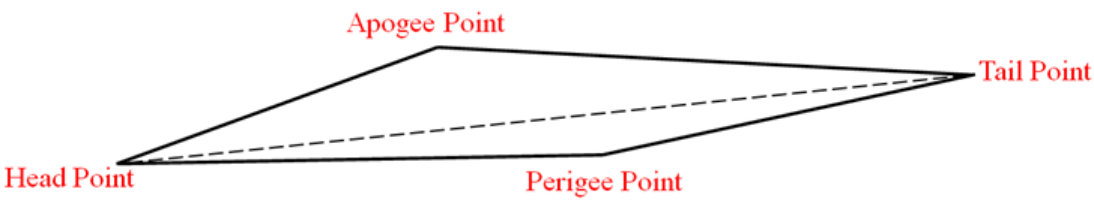

Figure 5.45: Typical pinchout geometry determined with its 4 vertices

Therefore 8 parameters (x and z coordinates of vertices) can define the pinchout. During history matching of a pinchout, optimisation algorithm picks values from the prior range of each parameter. In case of any interference between the prior ranges of coordinates of a pair of pinchout vertices, it is likely to come up with non-meaningful pinchouts. For example for prior ranges of [100,500] and [400,800] for x coordinate of pinchout head and tail points respectively, optimisation algorithm might pick 480 and 450 for x coordinate of head and tail, obviously a pinchout with head point preceded by tail point is not feasible. Thus to remove correlations resulting from such interferences, x and z coordinates of pinchout vertices are re-encapsulated to come up with a new pinchout parameterisation as represented in figure 5.46:

- xH: x coordinate of pinchout head point from the coordinates origin
- hH: Height of pinchout head point with respect to the datum

- rA: Angle between pinchout major axis and *x* axis
- TL: Horizontal distance between head and tail points of pinchout
- uHA: Opening angle of upper triangle at head point
- lHA: Opening angle of lower triangle at head point
- uTA: Opening angle of upper triangle at tail point
- lTA: Opening angle of lower triangle at tail point

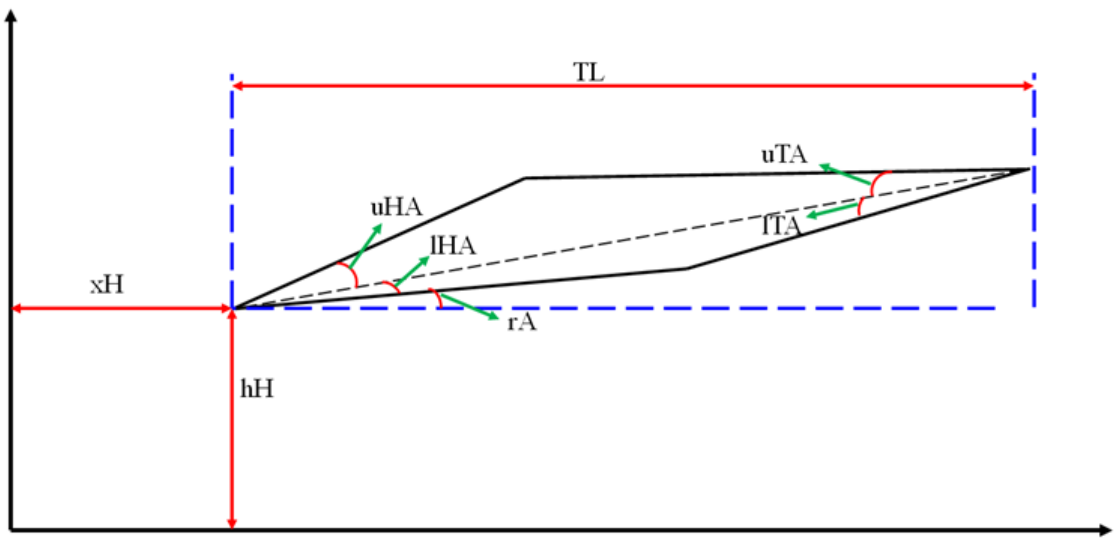

Figure 5.46: Pinchout parameterisation with head point coordinates, total length and 5 angles

5.3.1 Case Description

Model is a two dimensional cross section of a reservoir with three stratigraphic layers. Model dimensions are 1000 *ft* length by 20 *ft* height by 112 *ft* width which has been discretized into a $100\times20\times1$ Cartesian grid. Heights of reservoir top and base horizons are given in table 5.13. Initial grid would be extended upward and downward and then using Cartesian Cut Cell method it is reformed to accommodate top and base horizons. Similar to model described in Cases 1 and 2, model does not include any aquifer or gas cap. Initial reservoir pressure and initial connate water saturation are uniform and equal to 100 *psia* and 0.1 respectively.

$x_i(ft)$	15	125	250	375	500	625	750	875	985
$h^{basin}(x_i)(ft)$	-1.13	-5.97	-3.31	-6.05	-2.07	-0.82	-1.67	-4.70	-1.84
$h^{top}(x_i)(ft)$	20.36	22.45	24.98	21.47	20.14	23.09	19.89	20.65	22.43

Table 5.13: Heights of top and base horizons for pinched out model

5.3.2 History Matching of Pinchout Geometry

The pinched out model contains three layers of different petrophysical properties as given in table 5.14. The second layer is a pinched out layer, such that at injection and production wells drilled at left and right extremes of model just two stratigraphic layers are detected. Its negligible permeability causes it has a sealing effect against the flow.

Layer	$K_h(Darcys)$	$K_v(Darcys)$	$\phi\left({volume}/{volume}\right)$
1	0.15	0.03	0.15
2	0.00000002	0.000000004	0.02
3	0.25	0.05	0.25

Table 5.14: Rock properties for layers of the model containing pinchout

Uncertainty with the pinchout geometry comes from the similar sources to those of the top and base reservoir horizons, as the upper and lower branches of pinchout are recognised within a margin of error from the visible boundaries in seismic time map.

Here a pinchout with the geometrical specifications given in table 5.15 is considered as the truth case. The prior range of uncertainties per each parameter has been provided in this table as well. Top and bottom branches of pinchout get confluent together away from the pinchout body and overlap with the boundary of layers confining the pinchout subjected to the depths picked at wells.

Pinchout parameters	Truth case	Prior range
xH (*ft*)	180.0	50-250
hH (*ft*)	6.5	5.5-8.5
rA (°)	0.15	-0.25-0.25
TL (*ft*)	500.0	300-700
uHA (°)	1.15	0.6-1.6
lHA (°)	0.35	0.0-0.6
uTA (°)	1.10	0.6-1.6
lTA (°)	0.40	0.0-0.6

Table 5.15: Truth case and prior uncertainty ranges for pinchout geometrical parameters

Obtained production data after running the simulator on truth case are employed as the observed data. History matching is then conducted to find an optimised geometry of pinchout which reproduces the most fitting production profiles to the observed data. Similar to cases 1 and 2 injection well and production well are opened to flow at time $t = 0$ *Days* with bottom hole pressures set at 150 *psia* and 50 *psia* respectively and the production history is recorded for 1500 *Days*. Oil and water production histories for the true pinchout geometry have been depicted in figure 5.48.

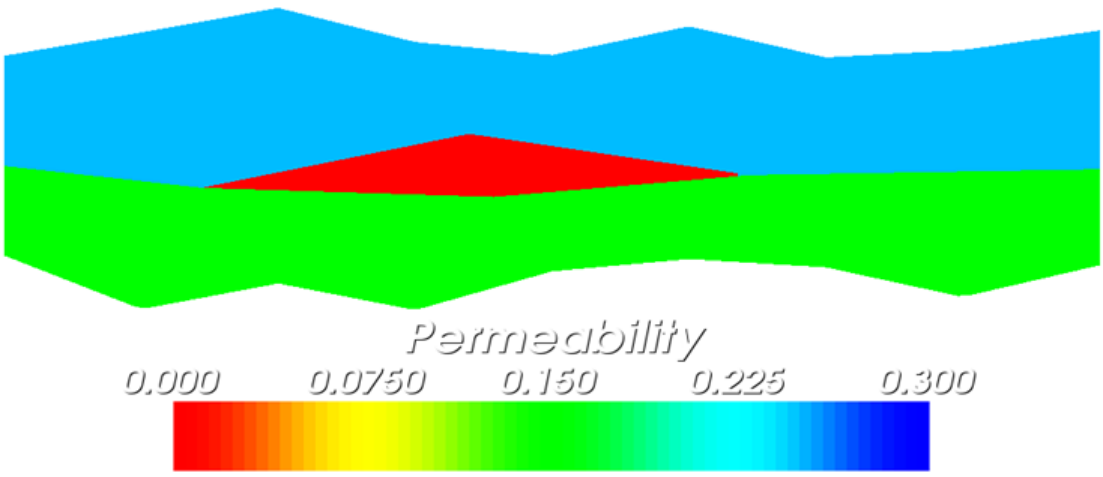

Figure 5.47: Permeability map for the truth case of model containing pinchout

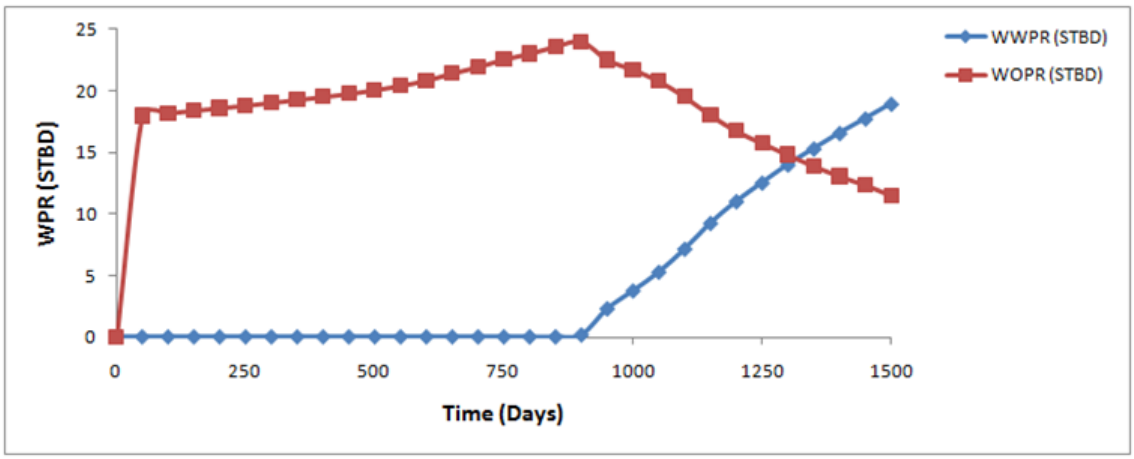

Figure 5.48: Production history for the true pinched out model

To determine the impact of prior pinchout uncertainties on production behaviour, one has to set up an ensemble of priorly probable models. Production profiles obtained from such an ensemble can represent satisfactorily the prior uncertainties with prediction of production history, if the variation of geometrical parameters in the ensemble covers properly the corresponding prior ranges. Here all parameters affecting the size of pinchout (uHA, lHA, uTA, lHA, TL) are encapsulated into one parameter termed as pinchout size (S). Thus the prior representative ensemble is created with 16 pinchouts with parameters picked at the extremes of prior ranges for each of 4 parameters (S, X(xH), H(hH), R(rA)). Oil and water production profiles for this ensemble are shown in figures 5.49 and 5.50 respectively in which “m” and “M” stand for the minimum and maximum of relevant prior range (e.g. Xm=50 *ft* , XM=250 *ft*).

Remembering studied pinchout as a low-porosity impermeable layer, the minimum pinchout size would be corresponding to maximum volume of oil in place. Because as pinchout shrinks, boundaries of two more high-porosity permeable layer extends. Consequently maximum oil production and earliest water breakthrough are attained for the minimum pinchout size. Also production behaviour at minimum pinchout size (Sm) is not noticeably influenced by other parameters, as almost similar production profiles are obtained for different combinations of head point location and rotation angle alternating between the extremes of relevant prior ranges.

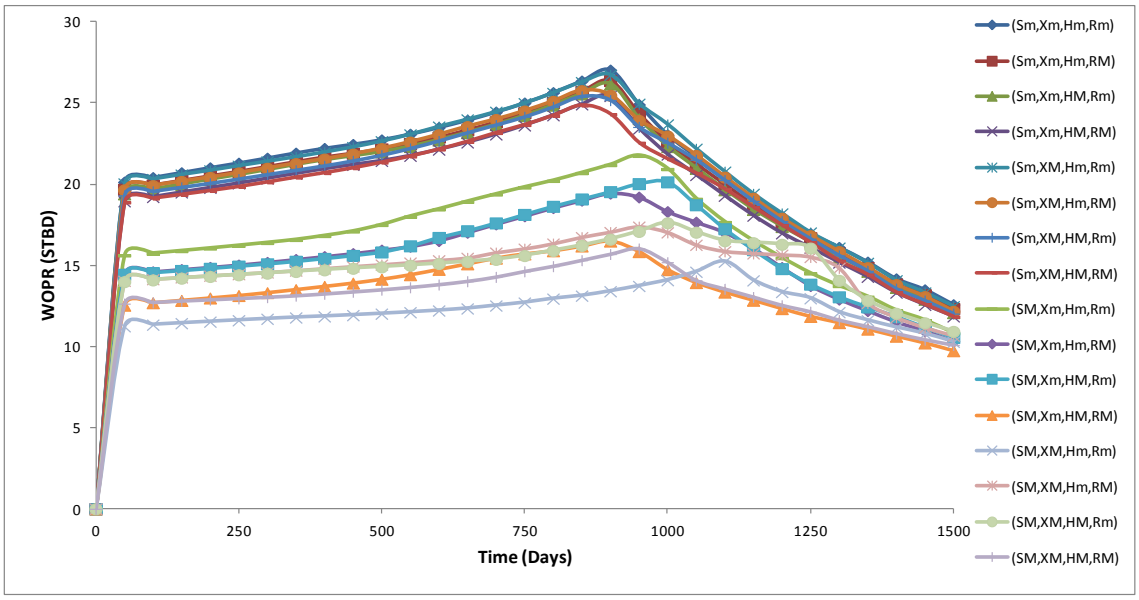

Figure 5.49: Prior uncertainties of oil production for pinched out model

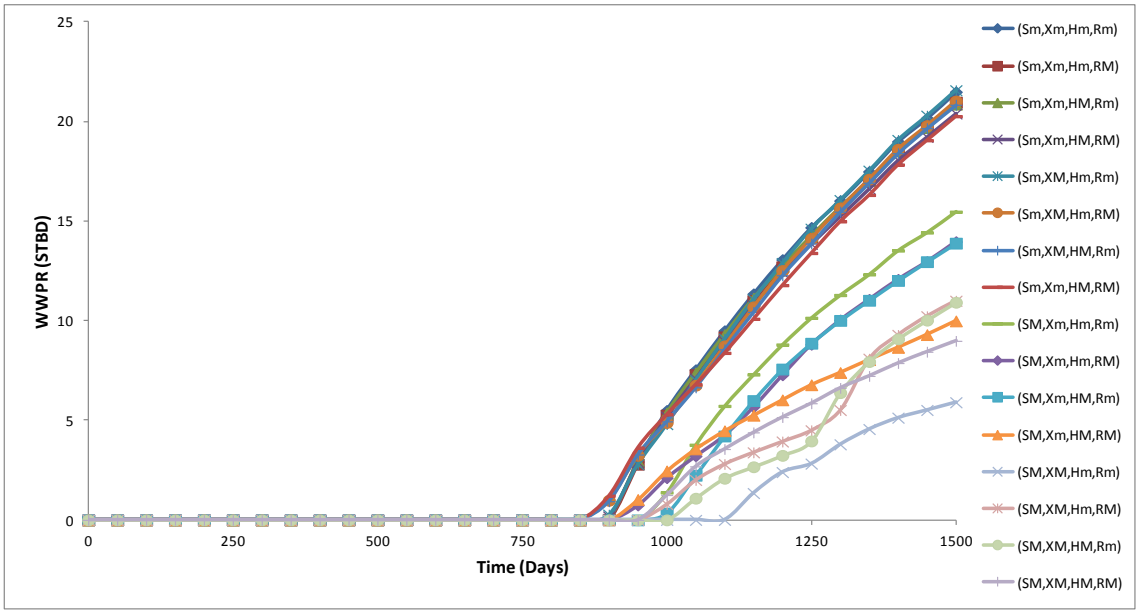

Figure 5.50: Prior uncertainties of water production for pinched out model

On the other hand for the maximum pinchout size (corresponding to the minimum priorly probable STOIIP) production profiles are very diverse. This indicates the elevated dependency of flow behaviour on head point location and rotation angle with enlarging the pinchout (increasing the interior angles and total length). Among them a large discrepancy is observed between two pinchouts having the minimum head point

height and minimum rotation angle. Closer one to the injection well (xH_{min}=50 ft) results in highest production rates and third earliest water breakthrough among pinchouts of maximum size, whilst one with maximum distance from injection well (xH_{max}=250 ft) ends up the lowest production rates and latest water breakthrough. Impermeable pinchout enforces the water front to decompose into two semi-fronts moving above and below the pinchout. We define two “water semi-fronts" as the moving fronts of fluid got separated from each other at head point of a pinchout and stay unconnected along the impermeable body till the tail point point. However pinchout as a flow barrier prevents gravity from re-unifying semi-fronts until the tail point and would enhance sweep efficiency in upper layer. The longer the distance that water front has to traverse before reaching pinchout, the more gravity segregation occurs and consequently water front deviates more its piston-like shape, Thereafter the semi-front formed in upper layer would be thinner in contrast with pinchout closer to the injection well, so more porous more permeable upper layer is not properly swept and smaller displacement efficiency and production rates are achieved. Also as shown in figure 5.51, faster advancement of water semi-front in upper layer and earlier breakthrough is expected for the closer pinchout to the injection well.

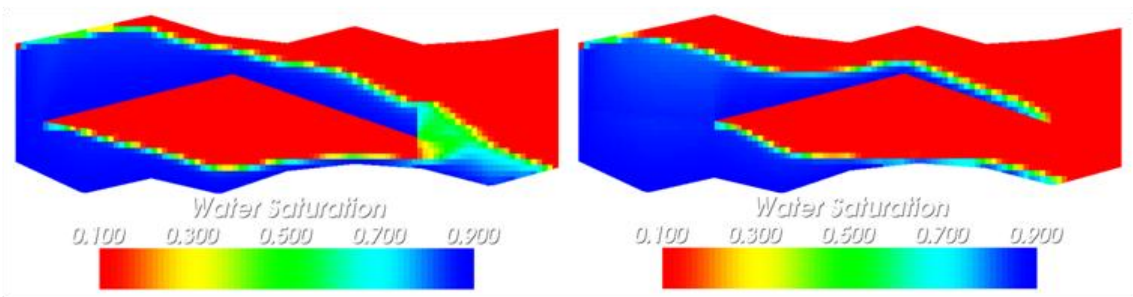

Figure 5.51: Saturation maps for pinchouts of maximum size and different xH @ t=1000 *Days*

Variation of head point height and the rotation angle displaces the boundary between lower and upper layers and consequently makes one layer shrunk and another expanded. Remembering the porosity and permeability contrast between two oil bearing layers, this would alter production rates and breakthrough times. Indeed their influences on production history would be much more perceptible in case of larger porosity and permeability contrasts between the layers surrounding the pinchout.

History matching seeks models minimising the misfit function defined in Eq. 5.5. NA with the following set of input parameters is employed to optimise pinchout geometry:

n_{s_i}	n_s	n_r	Iterations	Total Simulations
200	16	8	150	2600

Table 5.16: NA input parameters for history matching of pinchout geometry

Figure 5.52 shows the decreasing trend of misfits proving the convergence of NA which leaves an average misfit value of 1.23 after 2600 runs of simulator.

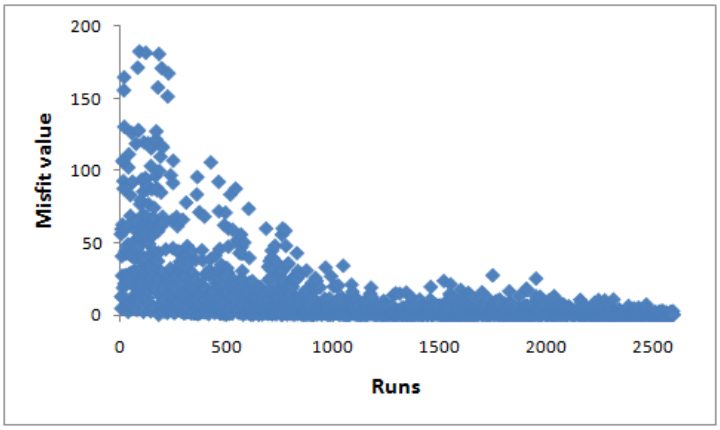

Figure 5.52: Convergence of NA in history matching of pinchout

History matching finds the best model after 2547 runs of simulator with the misfit of 0.016. The geometrical pinchout specifications of the maximum likelihood model and truth case has been compared schematically in figure 5.53 and the models built with these pinchout geometries have been shown in figure 5.54. Closefitting accordance between maximum likelihood model and truth case is observed with respect to their head point location and total length. Also the horizontal location of head point in history-matched model satisfactorily approaches the corresponding true value.

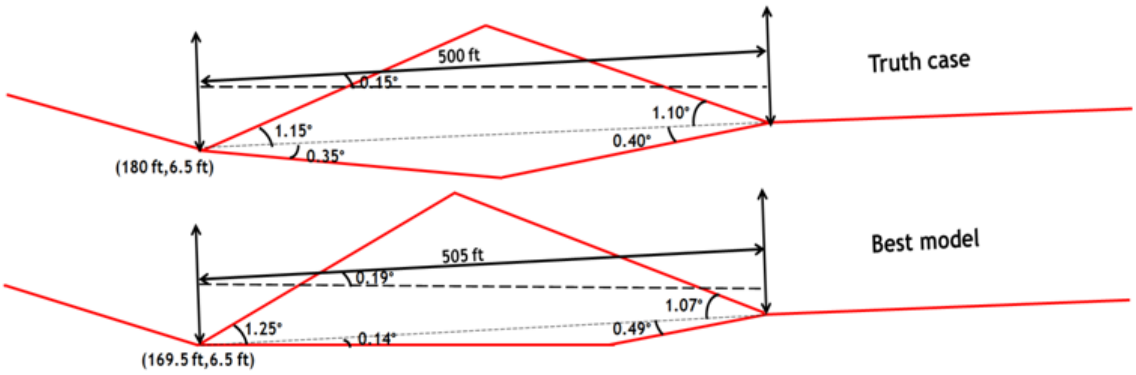

Figure 5.53: Pinchout geometry compared between the best model and the truth case

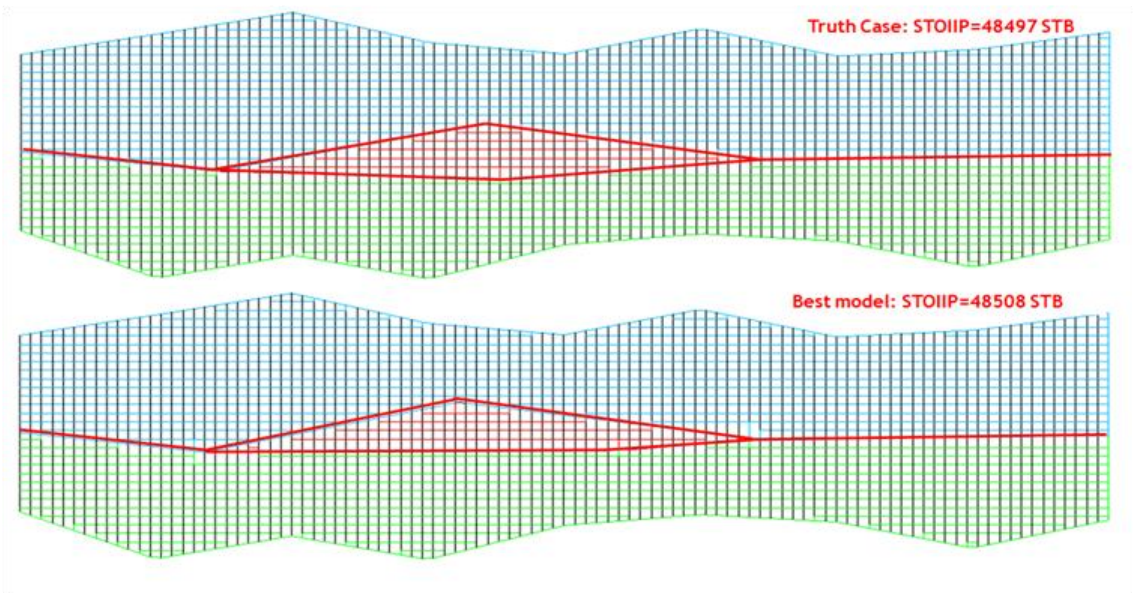

Figure 5.54: Schematic comparison between maximum likelihood and true pinched out models

Extent of upper layer influences flow behaviour more than lower layer extent, because STOIIP and overall flow conductivity are mainly provided by more porous more permeable layer (upper layer). Therefore production profiles are more sensitive to upper opening angles than lower angles, as their variation displaces the boundaries of upper layer. This explains why upper opening angles in maximum likelihood model are very similar to corresponding values in truth case, while there exist larger discrepancies between lower opening angles in best model and truth case. However summation of interior opening angles at head and tail points (oA=uHA+lHA+uTA+lTA) in best

model (1.96°) is slightly less than corresponding value for the truth case (2.0°) which countervails to some extent larger total length of best model (TL=505 *ft*) in contrast with truth case (TL=500 *ft*) and leads into almost the same pinchout size. Accordingly maximum likelihood model leaves an STOIIP of 48508 *STB* which is just 0.02% above its true value.

If truth case holds a pinchout thicker or as thick as its confining layers (like the pinchout of maximum prior size discussed here), STOIIP defined by the pinchout geometry of NA-optimised models determines the misfit from observed data and the side-effects of pinchout geometry on gravity force or disturbing the water front become indistinct. Thereafter the uncertainty in pinchout geometry increases, because different sets of pinchout parameters having the same pinchout size would lead into almost the same misfits regardless of pinchout location (xH, hH) and individual parameters defining pinchout orientation and inclination (rA, opening angles).

NA-sampled values of pinchout parameters have been individually plotted versus runs of simulator in figure 5.55. Centre of NA convergence range per each parameter has been tagged with red dotted straight line, while black dotted arrows show true parameters. Narrowest convergence range is obtained for the pinchout total length with the true value coinciding with its centre. A bit wider convergence range but still with the centre matching the true value has been achieved for head point height. This would rank the total length and head point height as the first and second simplest parameters to be history matched which respectively control pinchout dimension and the proportion of upper and lower layers from total reservoir thickness. Slightly larger difference between centre of convergence range and the true value have been observed for *x*-coordinate of head point and rotation angle, while still NA converges in a relatively narrow range.

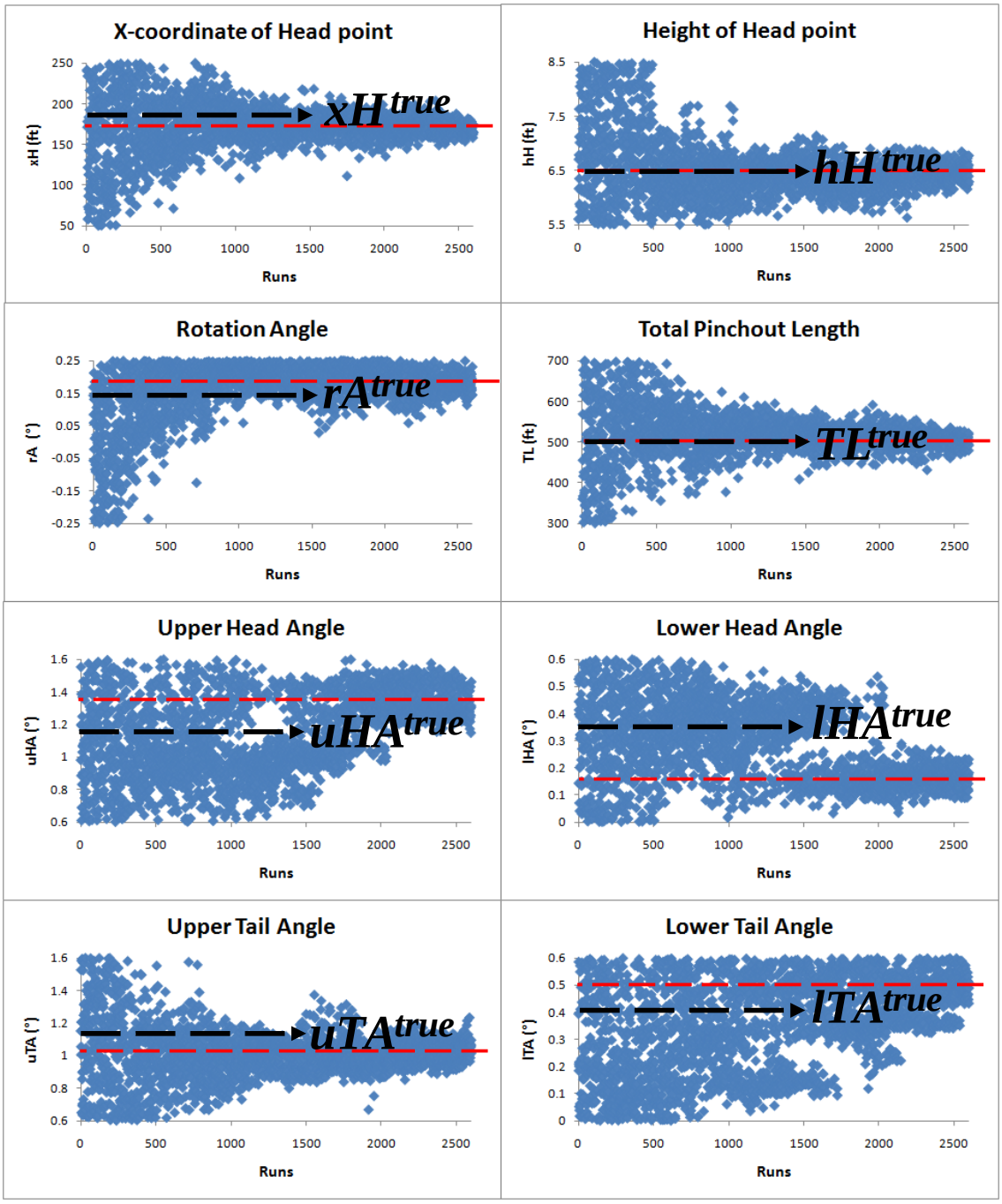

Figure 5.55: History matching trail for the pinchout geometrical parameters

Broad convergence regions for all interior opening angles might be attributed to their convolved impacts on pinchout dimension, gravity potential and thicknesses of upper and lower confining layers. Though among them, narrowest convergence range and smallest difference between centre of convergence range and true value are obtained for upper tail angle. Increase in upper tail angle affects:

1) The pinchout dimension and upper layer thickness resulting in reduced production rates and delayed water breakthrough,
2) The contribution of gravity potential to advancement of upper water semi-front after apogee point resulting in more efficient displacement and higher production rates. (The higher "uTA", the more favourable downward slope and the faster water front advancement)

These conflicting effects make production behaviour be more sensitive to upper tail angle in contrast with other opening angles and consequently lead into simpler history matching of upper tail angle.

However the predominant effect of opening angles is on pinchout dimension, thus production profiles are relatively unbiased to the pinchout opening directions at head and tail points. Total opening angles at head and tail points (HA and TA) are defined as the sum of upper and lower ones at corresponding points. History matching trails for total opening angles depicted in figure 5.56 demonstrate rather narrow NA-convergence ranges with their centres closefitting to the true values. This certifies the smaller uncertainty associated with total opening angles compared with individual directional opening angles.

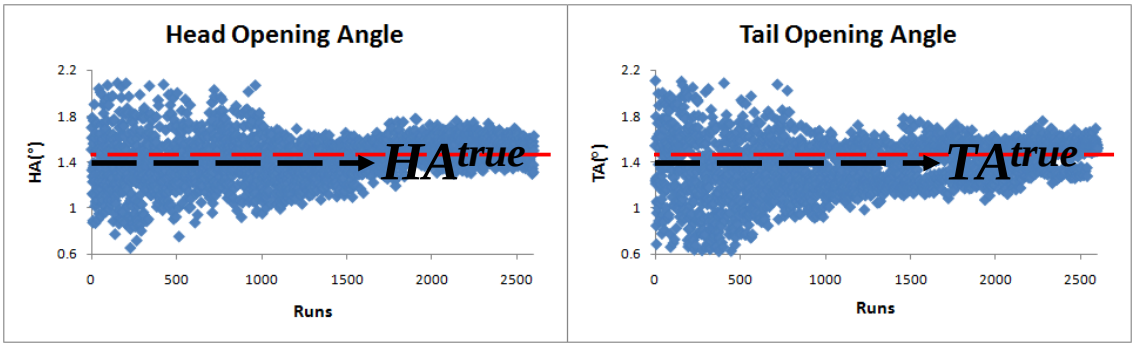

Figure 5.56: History matching trail for the pinchout opening angles at head and tail points

5.3.3 Quantifying the Uncertainties of Pinchout

Posterior probability densities calculated with NAB routine are converted to CDF values. CDF values have been plotted over the prior uncertainty ranges of each parameter in figure 5.57, where the bounds of posterior credible interval (interpolated p10 and p90 values), the posterior median (interpolated p50) were displayed. It clearly shows true values have been captured within the relevant credible intervals.

Low sensitivity of production to directional opening angles (except upper tail angle) is re-affirmed by linear variation of their corresponding CDFs over the prior ranges which is induced by proximity of mean values to the prior ranges mid-points and large standard deviations. So the posterior data are almost evenly distributed around the mean value and posterior inference does not considerably deduct the uncertainties associated with directional opening angles. CDF curves for other parameters are mainly skewed to the right of middle point of prior ranges, where the true values are located. The most compacted CDF curve is observed for the pinchout total length in which CDF varies from 0% to 100% in almost a quarter of prior uncertainty range. Narrowing index along with the values of variation coefficient, kurtosis and skewness for PPD have been given in table 5.17 per each parameter.

	xH	hH	rA	TL	uHA	lHA	uTA	lTA
NI (%)	54.98	34.15	58.96	76.30	24.28	32.97	42.56	26.66
CV (%)	19.92	10.40	75.93	7.03	23.94	49.73	20.17	50.28
Kurt	-0.58	-0.52	0.36	0.07	-1.01	-1.09	-0.39	-1.28
Skew	-0.01	0.50	-0.68	0.23	0.00	-0.10	0.10	0.00

Table 5.17: Important statistical measures calculated for pinchout geometrical specifications

The maximum percentage of uncertainty reduction occurs for the total length where the posterior credible interval is less than one-fourth of prior confidence interval, while more than 50% constriction of prior confidence interval for rotation angle and head point x-coordinate signifies their diagnosable impact on production behaviour. As an exception, uncertainty range for upper opening angle at tail point has been narrowed down by more than 40%.

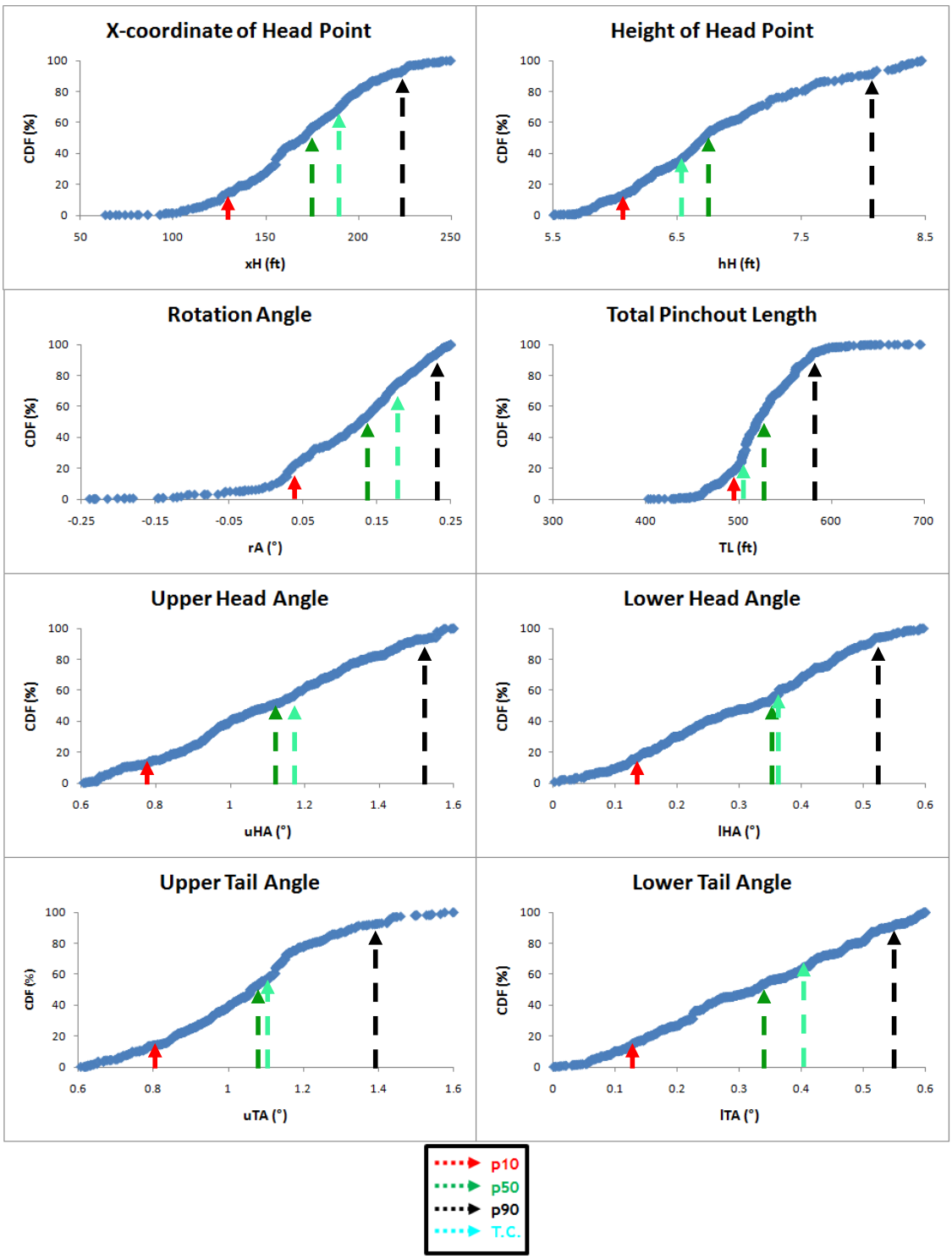

Figure 5.57: CDF for pinchout parameters used to determine bounds of credible interval

Representative models of pinchout built with combining the p10 values of each parameter or the p90 values, are shown in figure 5.58 along with the truth case and a pinchout comprised from median values (p50 values). As shown pinchout built with

medians, approximately conforms to the truth case such that its slightly smaller interior opening angles have been counterbalanced with its larger total length. Such a small difference between the truth case and model built with medians implies that values in the posterior uncertainty ranges are almost evenly distributed around the true values.

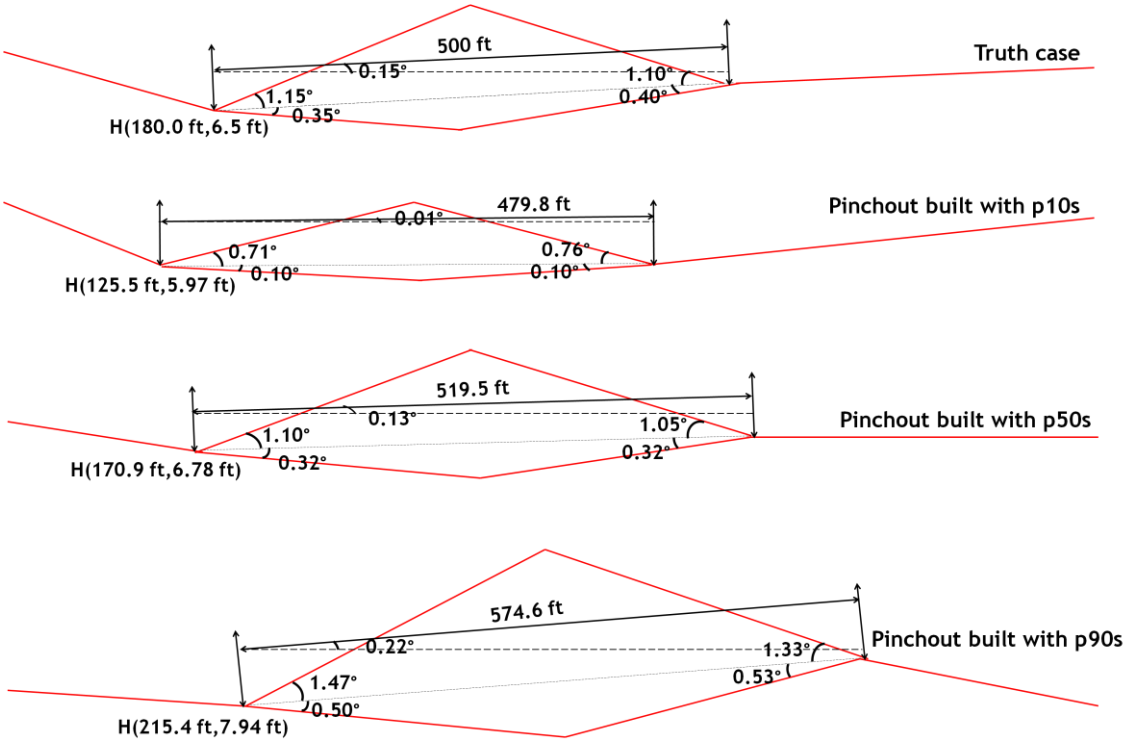

Figure 5.58: Pinchout geometry compared among the models built with p10s, p50s, p90s and the truth case

Reservoir models created with pinchout geometries shown in figure 5.58 are depicted in figure 5.59 to display the dimensions of pinchouts in different cases relative to other layers. Also one can see how other layers are influenced by resizing or displacing the pinchout. As anticipated almost identical values of STOIIP are obtained for truth case and model built with medians.

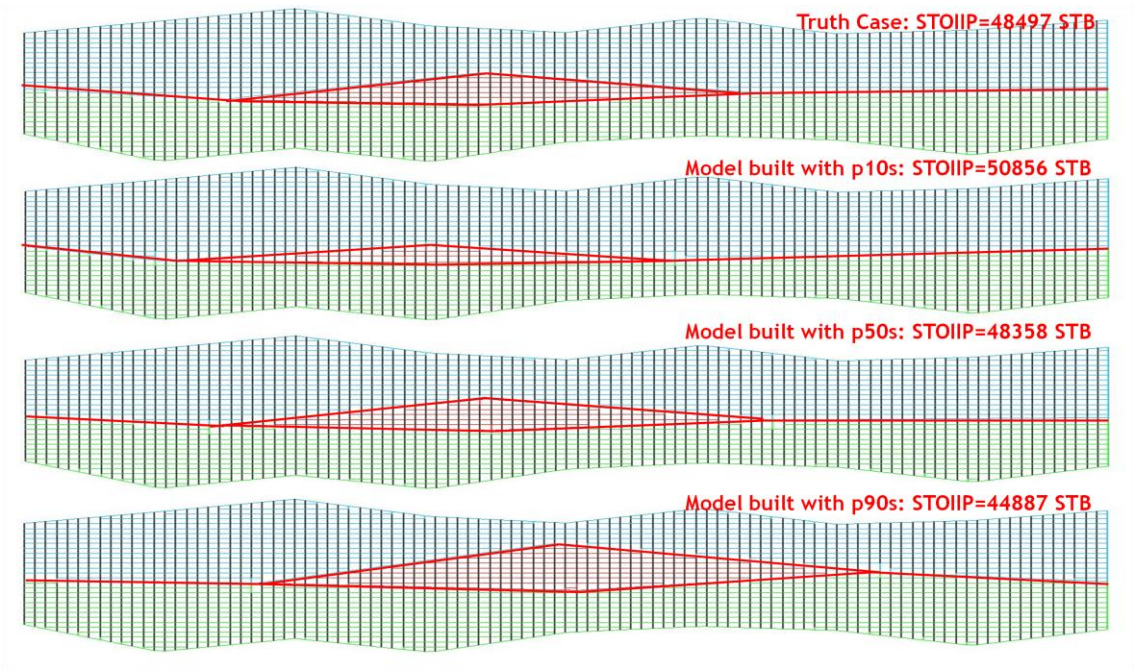

Figure 5.59: Truth case versus models with extreme posterior structural uncertainties for pinched-out model

To examine the impacts of posterior inference on restricting the production uncertainties, a representative ensemble offering the extreme geometrical uncertainties in credible intervals is constructed. Obtained oil and water production profiles shown in figures 5.60 and 5.61 show a much narrower variation range in contrast with similar profiles provided at prior. Although the gap between profiles for minimum and maximum pinchout size is still retained, but it has been shrunk to about 20% of its initial value.

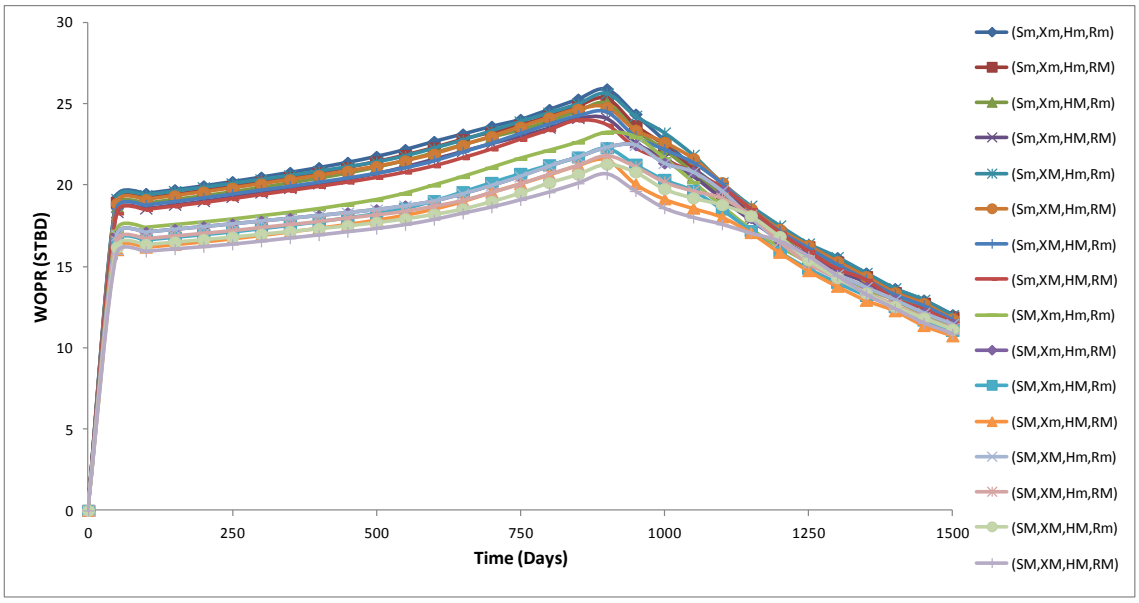

Figure 5.60: The posterior uncertainties of oil production for pinched out model

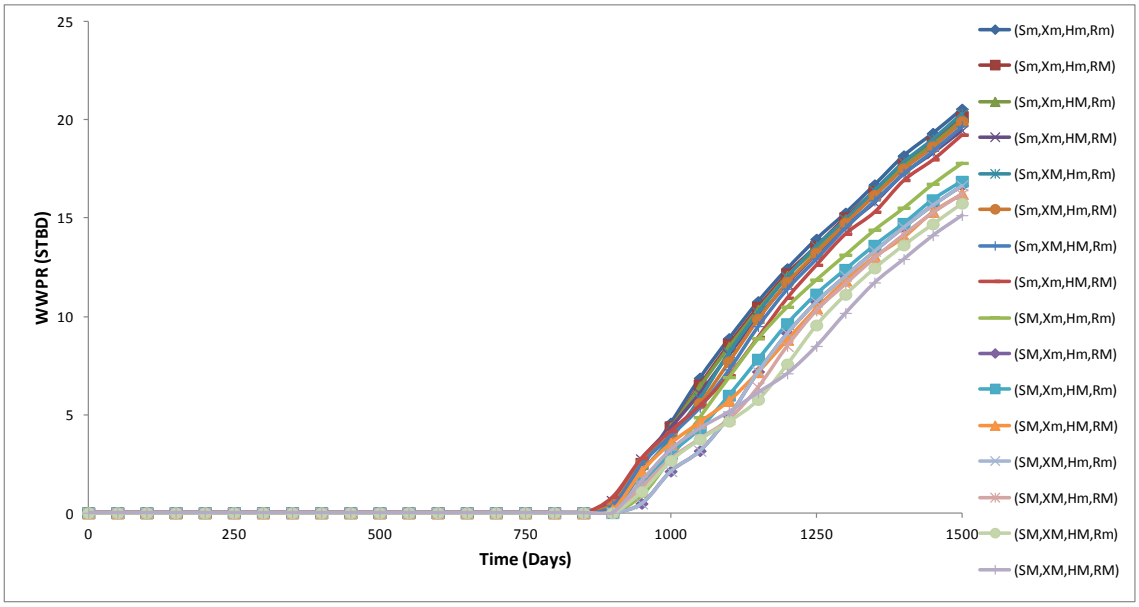

Figure 5.61: The posterior uncertainties of water production for pinched out model

Pinched out layer has a very small value of porosity, so as shown in figure 5.59, variation of its geometry and location results in considerable alteration of oil volume. To investigate the uncertainties associated with oil volume CDF values are plotted against the corresponding STOIIP. In figure 5.62, CDF values are given over the prior uncertainty range. Compacted CDF curve expresses the impact of posterior inference on

narrowing down the STOIIP uncertainty range to a marginal interval of $[45345\ STB, 49768\ STB]$.

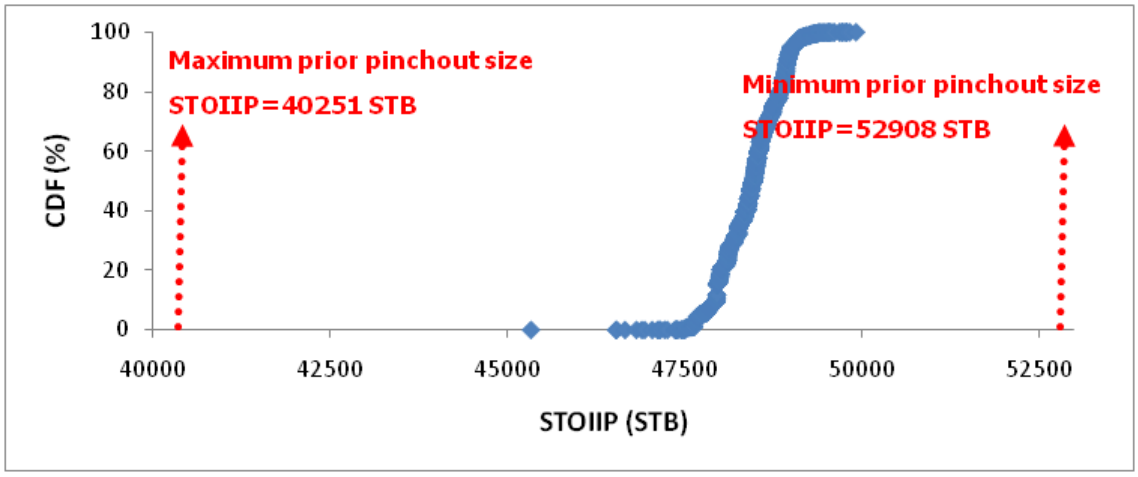

Figure 5.62: CDF distribution on prior range of STOIIP for pinched out model

As depicted in figure 5.63, STOIIP of truth case falls within the bounds of posterior uncertainty range of STOIIP $[p10 = 47963.33\ STB, p90 = 48958.25\ STB]$ and agrees with median value of STOIIP ($p50 = 48484.12\ STB$).

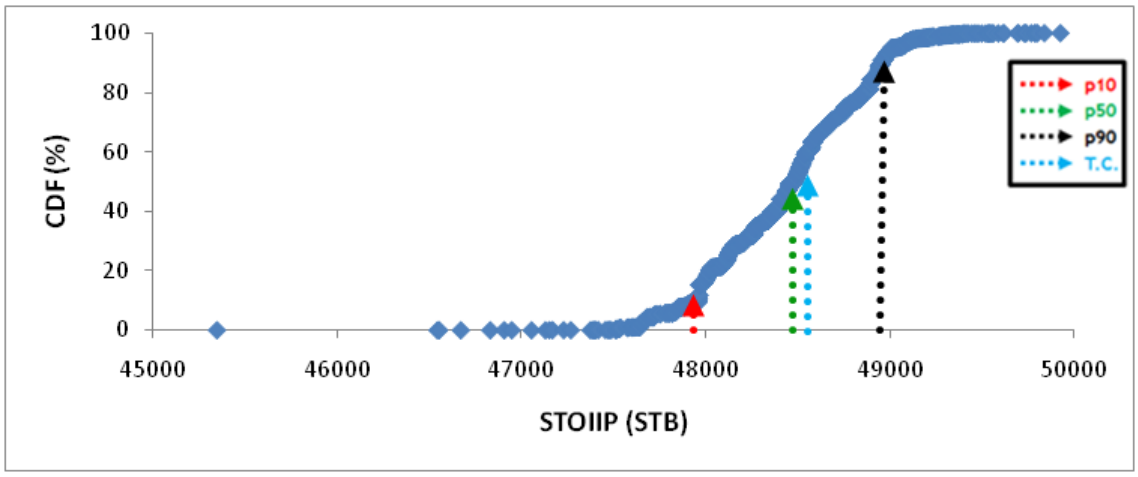

Figure 5.63: CDF distribution on posterior range of STOIIP for pinched out model

5.4 Comparative Study of Improvement in Reservoir Forecasting With Different Gridding and Flux Approximation Approaches

The preference of our hybrid Cartesian Cut Cell/extended EMPFA (CCC/EEMPFA) over the conventional approaches can be testified by comparing the corresponding uncertainty quantification results. Here we perform the history matching and uncertainty quantification on the similar pinchout geometry as studied in sections 5.3. The previous results are compared with those obtained for two other approaches:

a) Structured stair-stepped gridding with TPFA (SSS/TPFA)

b) Corner point grid geometry with MPFA O-method (CPG/MPFAO)

We take note that history matching (HM) and uncertainty quantification (UQ) are accomplished using stochastic methods of sampling through the uncertain parameters space, in effect comparison between different approaches must be made based on several repetitive runs of the history matching and uncertainty quantification processes for each approach. We carry out the history matching and uncertainty quantification 15 times for each gridding/flux approximation approach and make our inferences and judgements based on average values obtained from these 15 runs of HM and UQ. To numerically demonstrate the fulfilment of main propositions of history matching, we need to compare three approaches in terms of their variation of numerical errors over ensemble of models created in history matching. The approach with least variance of numerical error is the most preferable, because it leads into more reliable history matching results due to keeping the numerical errors almost equal over the ensemble of models. The convergence studies in the same way as section 4.5 are performed on the models created during history matching with three approaches.

Numerical Approach	Mean(L_2^{ep})	Variance(L_2^{ep})	Mean(L_2^{ev})	Variance(L_2^{ev})
CCC/EEMPFA	4.26	0.73	0.032	0.0033
SSS/TPFA	4.19	0.63	0.025	0.0031
CPG/MPFAO	4.81	1.54	0.039	0.0075

Table 5.18: Variation of Potential and Velocity error norms over the models created during history matching process

The mean and the variance of error norms for three sets of models simulated with different approaches have been given in table 5.18. As shown in table 5.18, Cartesian Cut Cell/EEMPFA approach leaves small variance of error norms comparable to that of stair-stepped gridding with TPFA, while for corner point geometry with MPFA O-method the error norms are spread over a wider range. This re-affirms that corner point geometry creates models with different gridding patterns and different trends of numerical error. However Cartesian Cut Cell method brings about minimal modifications to the structured gridding and in effect allows varying comfortably the structural geometry without altering the numerical errors. Moreover the mean value of error norms for our hybrid approach and stair-stepped gridding with TPFA are almost the same. This implies that using optimised quadrature parameters for extended EMPFA applied on degenerate irregular cells leads into as precise results as those of TPFA over the regular Cartesian cells.

Considering the fact that Cartesian Cut Cell method/EMPFA approach can translate conformally the evolving pinchout geometry into the grid without significantly disturbing the numerical error, it is anticipated that the best quality of history matching and uncertainty quantification results are obtained for this approach. We compare three approaches in terms of enhancement of forecasts on reservoir oil in place and production. The representative ensemble offering the extreme geometrical uncertainties after posterior inference (as described in section 5.3) is created for three approaches and the oil and water production profiles for these three ensembles (similar to figures 5.60 and 5.61) are calculated. The averaged difference between highest and lowest rates is regarded as a measure of reduced posterior production uncertainties. Also the posterior uncertainty over oil in place can be obtained from CDF distribution versus oil volume and the Width of updated Credible Interval (WCI) is used as a measure of any approach proficiency for narrowing down the STOIIP uncertainty. Table 5.19 gives these measures of updated uncertainty ranges for each approach.

Numerical Approach	WCI(q_w)	WCI(q_o)	WCI(STOIIP)
CCC/EEMPFA	2.28	3.55	1034
SSS/TPFA	3.21	4.37	1191
CPG/MPFAO	3.58	5.16	1286

Table 5.19: Measures of widths of updated credible intervals for different numerical approaches

The key finding of this table is that our Hybrid Cartesian Cut Cell/EMPFA approach can improves significantly the reservoir forecasting. As it provides narrower uncertainty intervals of fluid production and STOIIP compared to conventional numerical approaches. We believe such an enhancement can be explained with:

a) Ability of Cartesian Cut Cell method to decouple the pinchout geometry from its mapping onto the grid.

b) Promoted accuracy of numerical fluxes provided by extended EMPFA over irregular cells in the vicinity of geological structure.

In effect, we believe that our hybrid Cartesian Cut Cell/EMPFA approach can assist to come up with more reliable reservoir forecast with highly reduced structural uncertainties. It certifies the correct response of simulation outputs to the alteration of structures geometry, therefore the quality of optimisation results is improved and the chance that history matched geological models be good representatives of subsurface structures is increased. The augmented quality of misfit response surface would boost the reliability of posterior inferences made on ensemble of history matched models.

Chapter 6

Modelling and Quantification of Structural Uncertainties for Multiple Intersecting Geological Structures

In Chapter 5, the uncertainty quantification framework equipped with the hybrid Cartesian Cut Cell/EMPFA approach was employed to perform history matching on several synthetic models of single geological structures and investigate the relevant structural uncertainty. In this chapter we extend the application of our proposed method for history matching and uncertainty quantification of more complex models including any arbitrary combinations of typical geological structures (faults, pinchouts, bedding layers).

The specific goals of this chapter are as followings:

1. To show the practicability and robustness of using hybrid Cartesian Cut Cell/EMPFA approach to history match of more realistic proof-of-concept structural models with possibility of geological structures intersection.
2. To study the impact of combined structural uncertainties on history matching results by comparing with models of lone structures.
3. To investigate the uncertainty of predictions made by an ensemble of history-matched models.
4. To comprehend the importance of interpretation of the posterior inference results with reservoir engineering analysis of dependency of flow behaviour to different structural parameters.

The general flowchart for quantifying the structural uncertainties of multiple intersecting structures is almost the same as one for single structures (as depicted in figure 5.2 in chapter 5), with slight modifications in applying the Cartesian Cut Cell method for reshaping cells affected by introducing the new geometrical instances of structures at each step of history matching. The modified flowchart for multiple intersecting structures has been given in figure 6.1. Unlike the current state of art for handling structural uncertainty, our approach would provide the narrowed down credible intervals for STOIIP and recovery as well as pictorially confining the variability in shape and topology of geological structures. Moreover conventional approaches of Uncertainty Quantification suffer from the need for general regridding or disturbing the grid architecture for a structure evolving during history matching process.

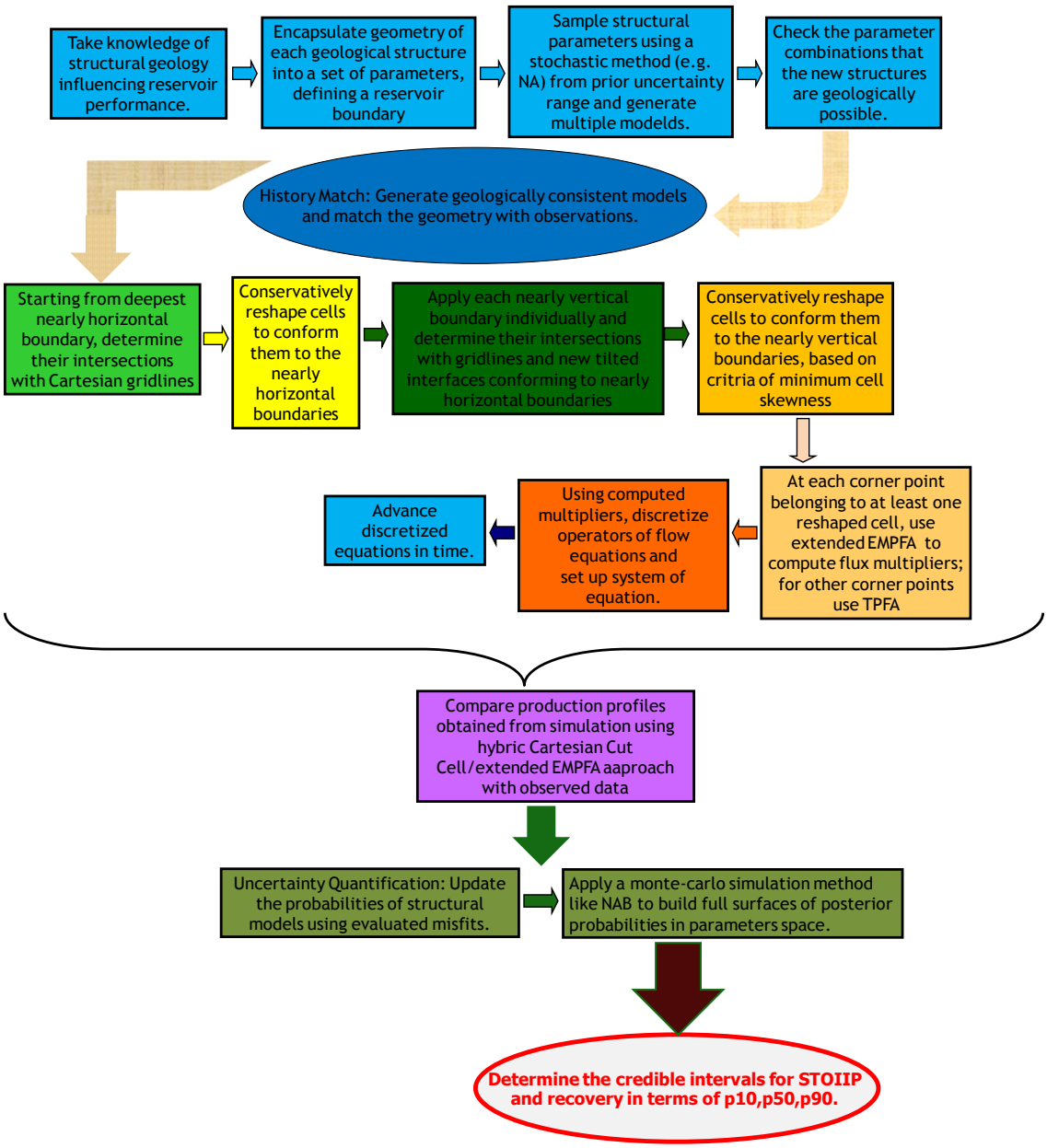

Figure 6.1: The general procedure for history match and uncertainty quantification of multiple intersecting geological structures assisted by hybrid CCC/EEMPFA approach

6.1 Simultaneous Quantification of the Uncertainties of Reservoir Layer Boundaries and Faults

6.1.1 Case Description

Uncertainty constraints of all uncertain intersecting surfaces of a multi-layered faulted reservoir model are demanded. The model is a two-dimensional vertical cross section of a reservoir comprised of three stratigraphic layers of different porosities and permeabilities and varying thicknesses along the axial extension of the model. Reservoir has been cut through with two normal faults with opposite slopes such that both faults dip towards the centre of middle block which is on the footing wall side for both faults. Middle block is depressed because of up-thrown blocks on the hanging walls of both faults. Model has been extended 1000 *ft* in horizontal direction and its normal width is 112 *ft*. The initial uniform pressure and connate water saturation are 100 *psia* and 0.1 respectively. Two injection and production wells have been completed on the left and right extremes of the model. In table 6.1, permeabilities and porosities for each layer has been given where the layers are indexed upward starting from the deepest layer.

Layer	$K_h\,(Darcys)$	$K_v\,(Darcys)$	$\phi\left(volume/volume\right)$
1	0.1	0.02	0.15
2	0.2	0.04	0.20
3	0.3	0.06	0.25

Table 6.1: Rock properties for uncertain multilayer faulted model

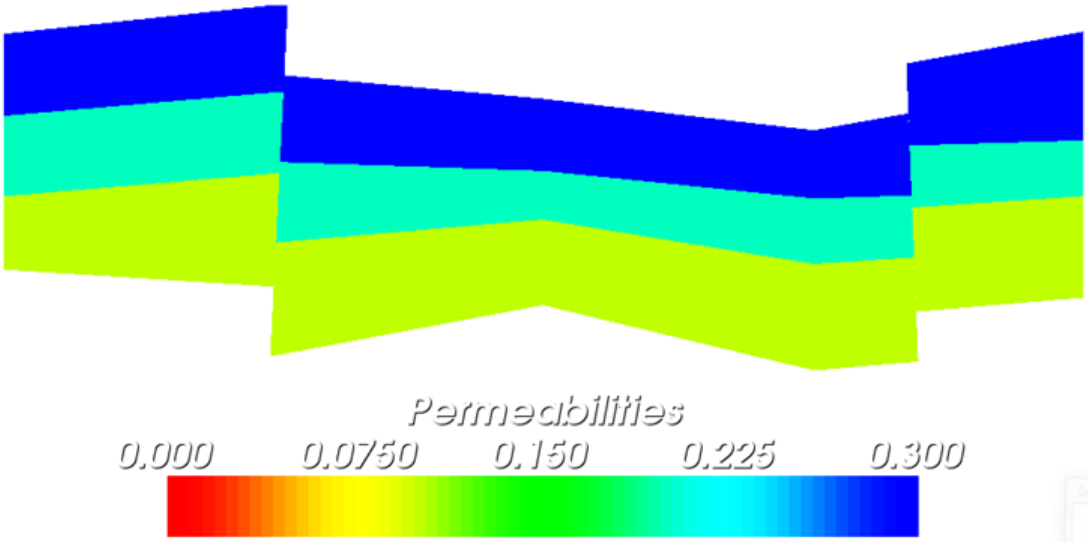

Figure 6.2: Horizontal permeability map for multilayer faulted model

6.1.1.1 Parameterisation of Boundaries of Reservoir Layers

Trend of layer boundaries is recognised from significant horizons detected in seismic map or interpolated from available outcrop data. Considering the straight plane passing through the picked depths of each layer boundary as the reference trend, seismic picked trend of layer boundary is fluctuating around reference trend, creating extrema with respect to the datum. Half width of prior uncertainty range for height of each point is assumed to be given by the height difference between the seismic-picked trend and straight reference trend. In this way variation of heights within the prior confidence interval is limited to one side of reference straight trend. Consequently the typical shape of layer boundary is preserved as like as the seismic-picked trend and just its peakedness changes such that the extrema get amplified or get rounded. This is shown in figure 6.3.

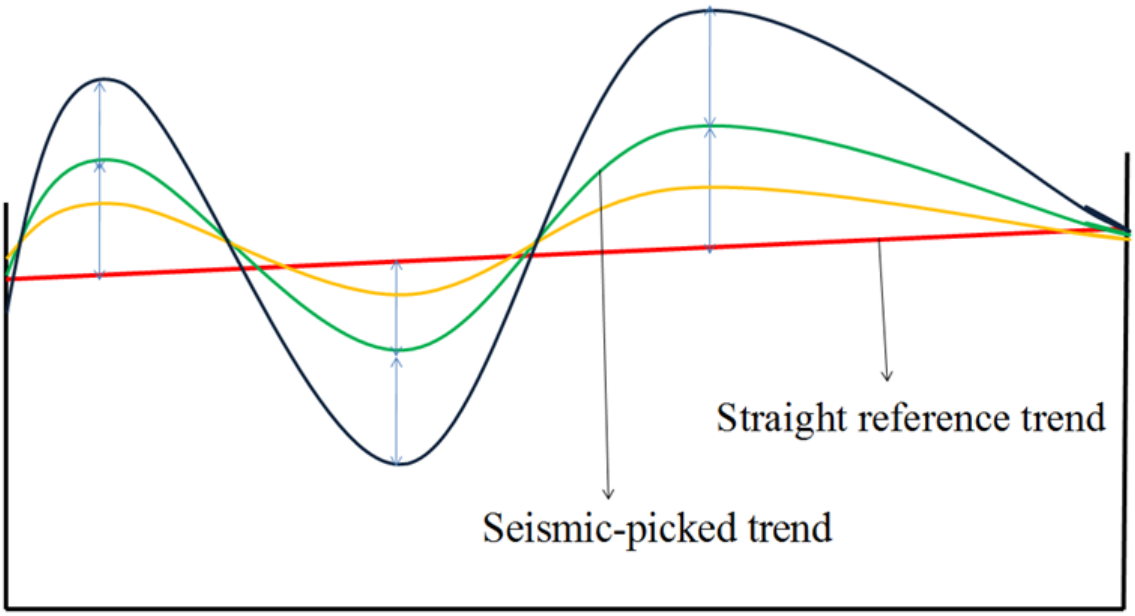

Figure 6.3: Variation of layer boundary with altering the amplitude at extrema

However the prior uncertainty ranges at each point are dependent on the local deviation of seismic-picked trend from straight reference trend. So one can write:

$$prior\ range\ half\text{-}width(x_i) = R(x_i) = 0.9\left|h^{spt}(x_i) - h^{srt}(x_i)\right| \quad (6.1),$$

in which $h^{spt}(x_i)$ and $h^{srt}(x_i)$ stand for the height of seismic-picked trend and straight reference trend at x_i. According to Eq. 5.2 given in Chapter 5, the seismic-picked layer boundary is obtained itself from random perturbation imposed on the true layer boundary. Hopefully true layer boundary lies within the prior uncertainty range when the optimisation algorithm employed in history matching process finds a trend with deviations from seismic-picked trend equal to the negative of the already imposed perturbations at corresponding points. It means:

$$h^{true}(x_i) \in \left[h^{spt}(x_i) - R(x_i), h^{spt}(x_i) + R(x_i)\right] \quad (6.2).$$

The seismic-picked heights, imposed perturbations and the radius of prior uncertainty ranges some $x_i's$ in the horizontal extension of reservoir are given in tables 6.2, 6.3, 6.4, 6.5 for layer boundaries 1 to 4 indexing upward from base horizon to top horizon.

$x_i(ft)$	15	250	500	750	985
$h^{spt}(x_i)(ft)$	-1.13	-3.31	1.07	-3.67	-1.94
$e(x_i)(ft)$	0	0.69	1.01	-0.25	0
$R(x_i)(ft)$	0	1.78	2.34	1.73	0

Table 6.2: Seismic-picked trend of 1st layer boundary along with corresponding prior ranges

$x_i(ft)$	15	250	500	750	985
$h^{spt}(x_i)(ft)$	5.85	7.59	8.84	6.01	7.43
$e(x_i)(ft)$	0	0.24	1.14	-0.13	0
$R(x_i)(ft)$	0	1.22	1.98	0.93	0

Table 6.3: Seismic-picked trend of 2nd layer boundary along with corresponding prior ranges

$x_i(ft)$	15	250	500	750	985
$h^{spt}(x_i)(ft)$	13.27	15.69	13.87	10.86	12.64
$e(x_i)(ft)$	0	-0.38	0.59	1.06	0
$R(x_i)(ft)$	0	2.31	0.82	1.73	0

Table 6.4: Seismic-picked trend of 3rd layer boundary along with corresponding prior ranges

$x_i(ft)$	15	250	500	750	985
$h^{spt}(x_i)(ft)$	20.86	23.88	20.04	18.76	22.43
$e(x_i)(ft)$	0	-0.50	1.08	-0.55	0
$R(x_i)(ft)$	0	2.37	1.44	2.96	0

Table 6.5: Seismic-picked trend of 4th layer boundary along with corresponding prior ranges

The true values of geometrical specifications of fault-1 and fault-2 along with their corresponding prior uncertainty ranges are listed in table 6.6 and table 6.7:

	Truth case	Prior range
X-coordinate of fault entrance point (*ft*)	250	100-450
Fault slope (*ft/ft*)	2.0	1.25-6.25
Fault throw (*ft*)	6.4	0.0-10.0

Table 6.6: Truth case and prior guess of uncertainty ranges for fault-1 in multi-layer model

	Truth case	Prior range
X-coordinate of fault entrance point (*ft*)	845	600-950
Fault slope (*ft/ft*)	-2.5	-6.25--1.25
Fault throw (*ft*)	4.6	0.0-10.0

Table 6.7: Truth case and prior guess of uncertainty ranges for fault-2 in mutli-layer model

The transmissibility multipliers are assumed to be constant along the faulting plane and equal to 0.80 for both faults. Though assessing of fault uncertainty would be restricted to its geometry and doesn't include transmissibility multiplier unlike most works on uncertainty quantification of faults.

6.1.2 History Matching of the Geometry of Layer Boundaries and Faults

The production profiles obtained from running the simulator for the truth case is regarded as the observed data and neighbourhood algorithm is employed to sample through the prior uncertainty ranges of all parameters and seek for models minimising the discrepancy with the observed production data. Input parameters of NA are given in table 6.8:

n_{s_i}	n_s	n_r	Iterations	Total Simulations
500	20	10	500	10500

Table 6.8: NA input parameters for simultaneous history matching of faults and layer boundaries

Lowest misfit of 0.171 has been achieved after 10469 simulations, while NA leaves an average misfit of 301 over all models. Comparing this with the average misfits obtained in Chapter 5 for the history match of single uncertain surfaces, raised uncertainty due to convolved uncertainties of multiple intersecting surfaces would be signified. Maximum likelihood model has been depicted along with the truth case in figure 6.4. Model with the lowest misfit have STOIIP of 44526 *STB* closely fitting to true value of 44660 *STB* oil originally in place. Geometry of fault-2 has been better history matched compared to fault-1, resulting in a throw of 4.53 *ft* against the true value of 4.60 *ft* and x-coordinate of 730 ft against the true value of 845 *ft*. One can attribute this to shorter distance of fault-2 to the production which makes the fault-2 more influential on the flow behaviour.

History matched fault-1 has a totally different geometry from the truth case, but it has the same impact on flow behaviour. Because while the smaller throw of maximum likelihood model reduces gravity potential easing the oil displacement, shorter distance of fault-1 from the injection well causes the water front before considerable gravity segregation enters the second block through a larger contact surface between segments of more porous more permeable upper and middle layer. This would counterbalance the negative impact of smaller throw on flow and makes water front advances faster

through the second block. Also it is noticeable that in the maximum likelihood model, segments of upper and middle layers in the second block are thicker than same layers in the truth case. Remembering the higher permeability of these two layers compared with the lower layer, their higher thickness deducts the gravity segregation and enhances the vertical sweep efficiency in the second block.

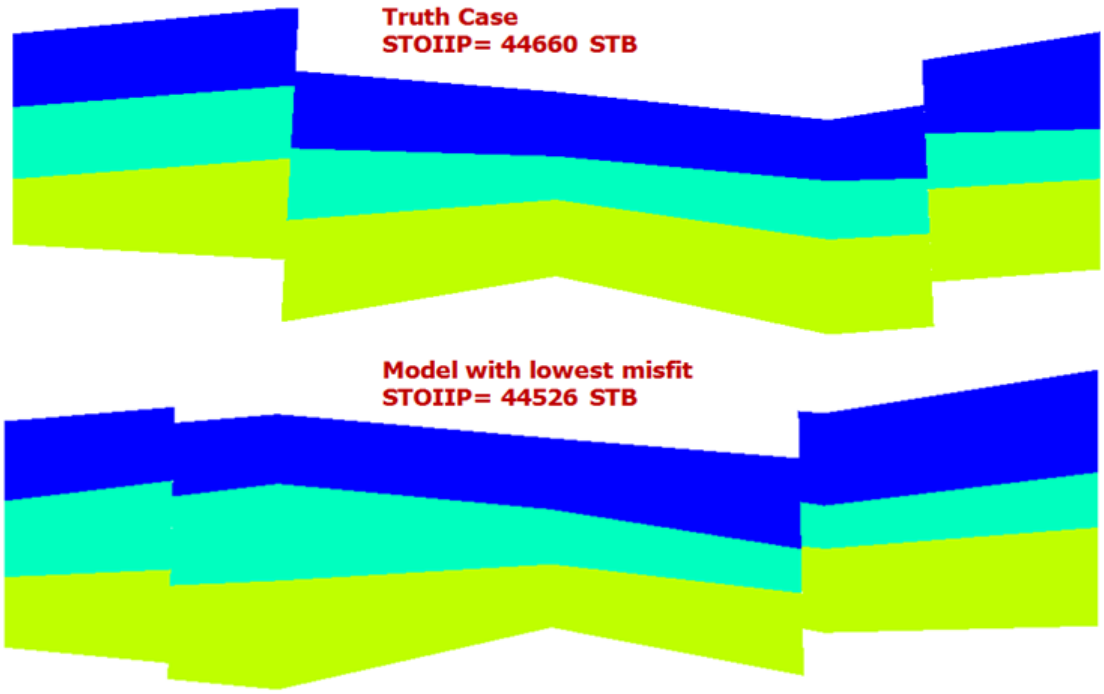

Figure 6.4: Maximum likelihood model vs. truth case for uncertain faults and layer boundaries

Indeed discrepancy between the history matched model and truth case is more remarkable in comparison with what has obtained for single uncertain surfaces in Chapter 5. This indicates that the history matched models become less trustable when the number of uncertain surfaces desired to be history matched increases. As the total resultant flow behaviour can be explained with different sets of geometry of uncertain surfaces and it cannot be interpreted with single independent impacts of individual surfaces. Evidently wider posterior credible intervals are anticipated for the multiple uncertain surfaces.

One can filter the ensemble of sampled models by NA by narrow margins about the true values to find the model with the closest set of geometrical parameters to the truth case. Thus we start with small values of $\alpha \in [0,1]$ and search in the ensemble for the models whose all heights are in the interval $\left[(1-\alpha)h_j^{true}(x_i),(1+\alpha)h_j^{true}(x_i)\right]$ for $i=1,2,3$ and $j=1,2,3,4$. Although individual heights with arbitrary small distance from true height can be found, but even by increasing α to unity, we didn't find any model with heights confined in desired margins all together. This demonstrates the difficulty of history matching of heights highlighted by considering the well-balanced (n_r/n_s) ratio which should expectedly allows for good exploration of search space. However taking into consideration the stronger impact of layer thicknesses on flow rather than boundary heights, we change the filter to narrow margins about the true thicknesses $\left[(1-\alpha)TH_j^{true}(x_i),(1+\alpha)TH_j^{true}(x_i)\right]$. For $\alpha=0.8$, we can find 39 models with desired thicknesses. Among these models we are interested in one with closest set of fault parameters (*FP*) to true parameters, thus we need to minimise the least square term $\sum_{j=1,i=1}^{j=2,i=3}\left(FP_i^j - FP_i^{j,true}\right)^2$ over the ensemble of 39 models. We pay attention that the model with minimised difference from true fault parameters has relatively small misfit of 28. The model has been compared schematically with truth case in figure 6.5.

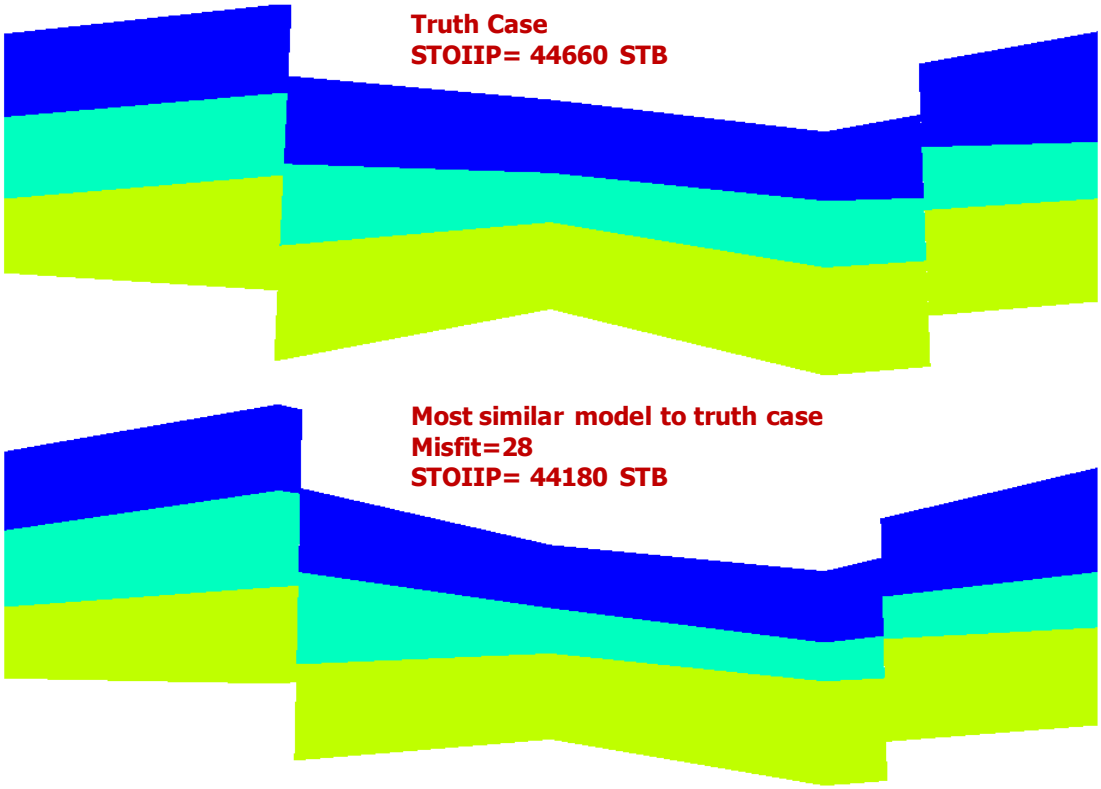

Figure 6.5: Most geometrically similar model to the truth case compared with truth case for uncertain faults and layer boundaries

This model has been obtained after 154 iterations of NA. Its very close STOIIP to the truth case and small misfit implies that this model is in the low misfit region of high-dimensional parameter space. However, very few models with similar layer thicknesses and fault parameters can be found in the history matching output ensemble. This recalls the similar situation for IC-fault model studied thoroughly by Erbas [2007] where the misfit surface have sharp local minima with respect to fault throw which makes sampling algorithms entrapped in regions far from low misfit regions of a 3-D parameter space. Considering local minima becomes much more problematic for higher dimensions of parameter space, we believe similar phenomena occurs for NA here and possible local minima prevent from refining properly the region around the closest model to truth case found in initial iterations. We believe in this problem misfit surface has local minima with respect to fault parameters specially fault-1 which conduct the sampling toward regions with poor match to structures of truth case. This observation motivates the need for using more powerful sampling or optimisation algorithms

capable of navigating the search space in a way that less entrapment occurs despite the curse of dimensionality and the matter of local minima.

NA sampling trails of uncertain heights have been depicted individually for layer boundaries in figures 6.6, 6.7, 6.8, 6.9. Red dotted horizontal line shows centre of NA-convergence range, while true heights have been marked with black dotted arrows.

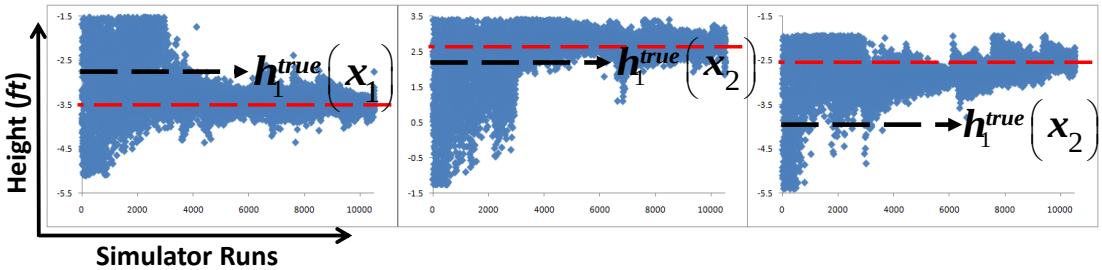

Figure 6.6: History matching trail over the heights of 1st layer boundary

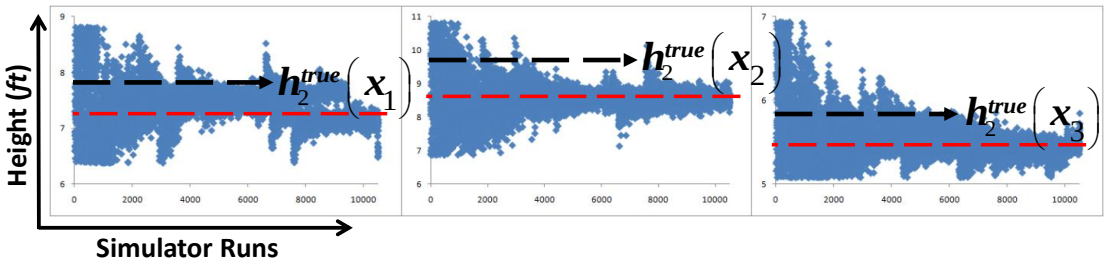

Figure 6.7: History matching trail over the heights of 2nd layer boundary

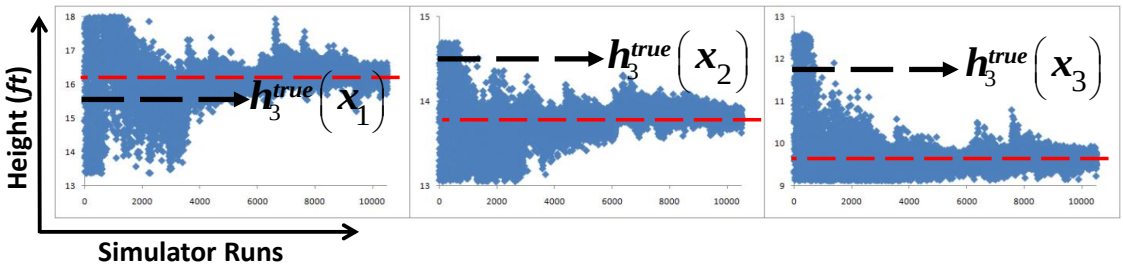

Figure 6.8: History matching trail over the heights of 3rd layer boundary

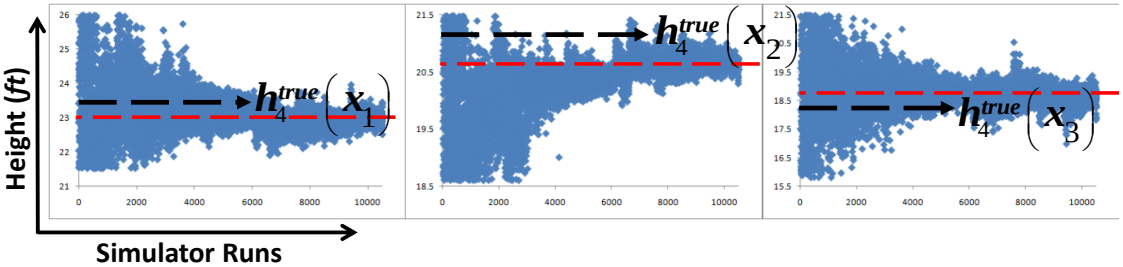

Figure 6.9: History matching trail over the heights of 4th layer boundary

More precise interpretation can be made on the history matching trails drawn for the resultant layer thicknesses as depicted in figures 6.10, 6.11, 6.12. NA converges to models with first layer thinner than the truth case over the second and third block located after first height-estimating point x_1, while converged second layer is thicker than the truth case in the middle of model axial extension .This would retard the gravity segregation for the water front when it enters the second block and compensates the reduced potential due to smaller offset of fault-1 in contrast with truth case. Remembering longer distance of fault-2 from the production well in the NA-converged models, before reaching the water front to the fault-2, a larger oil volume remains unswept in the third block in contrast with truth case. Considering depression of second block against the third block, water front is likely to advance mostly through the less-porous lower layers of the third block. However this negative effect on displacement efficiency is countervailed with larger thickness of 3rd layer at third block and smaller thicknesses of two other layers.

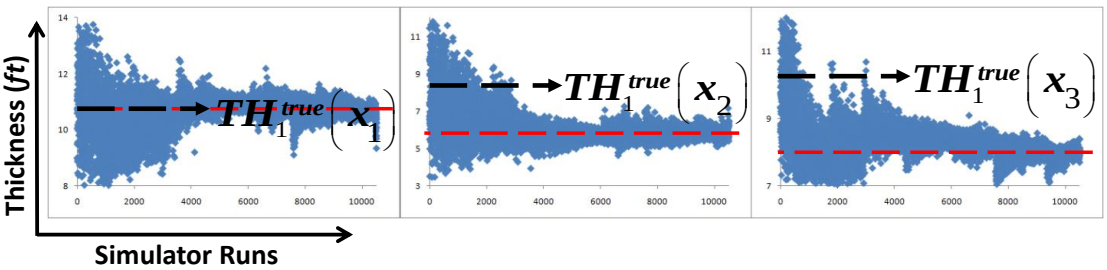

Figure 6.10: History matching trail for the thickness of 1st layer

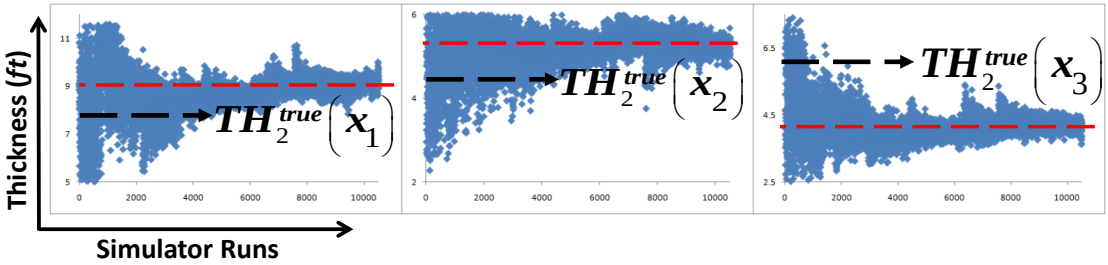

Figure 6.11: History matching trail for the thickness of 2nd layer

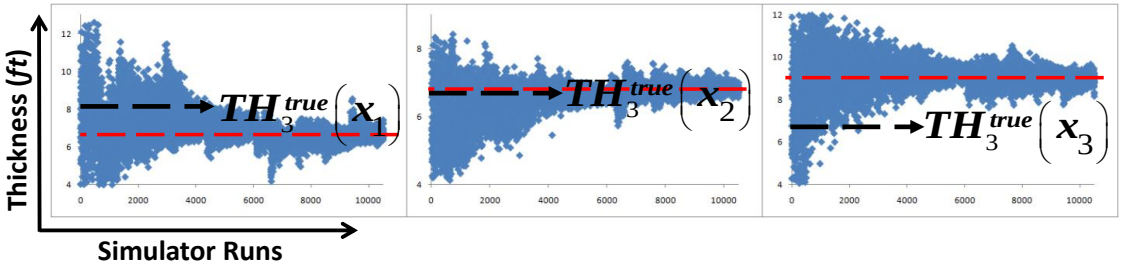

Figure 6.12: History matching trail for the thickness of 3rd layer

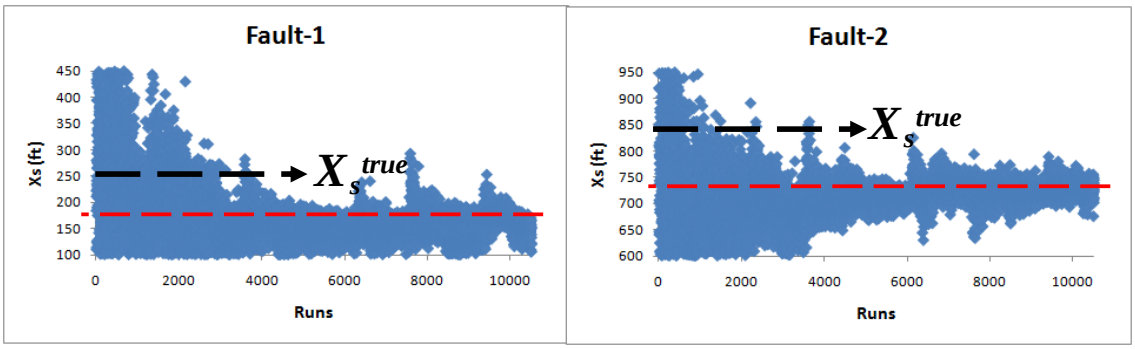

Figure 6.13: History matching trail of entrance location for both faults

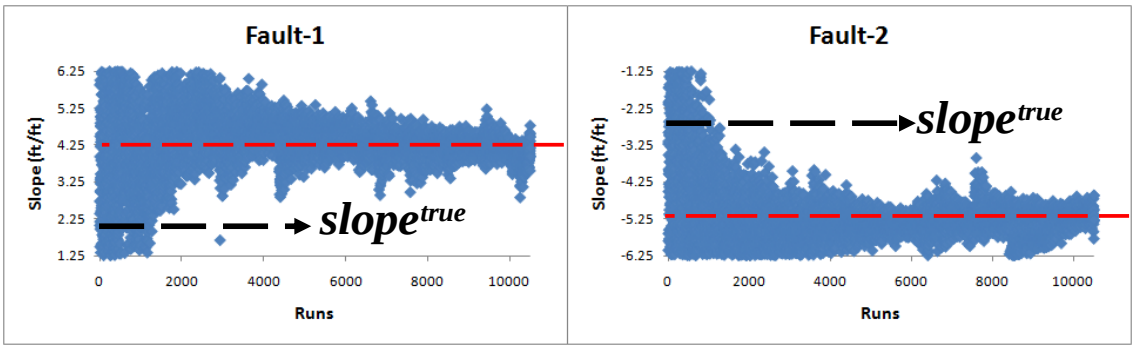

Figure 6.14: History matching trail of fault slope for both faults

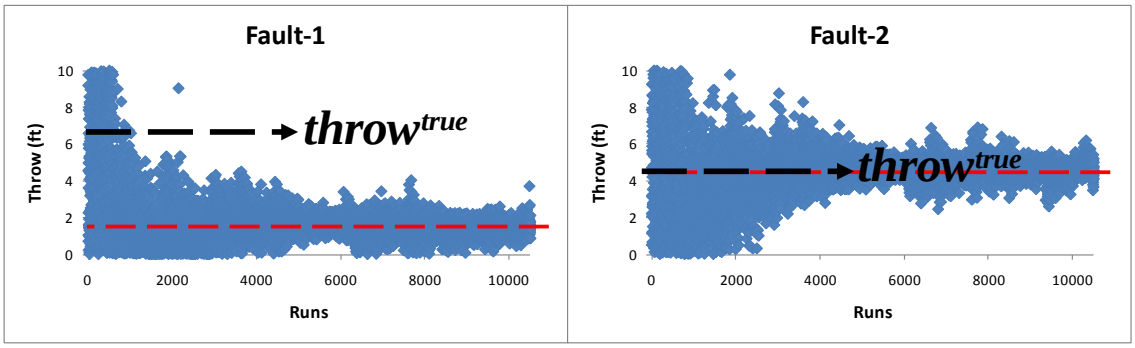

Figure 6.15: History matching trail of throw for both faults

6.1.3 Quantifying the Uncertainties of Faults and Layer Boundaries

NAB routine is conducted to reconstruct the posterior probability densities and then posterior Bayesian inference is done for determining the bounds of credible interval from the CDF values obtained from integrating the posterior probability densities. For layer boundaries, trends passing through the p10s and p90s can schematically display the bounds of posterior range of uncertainty for the corresponding. As shown in figures 6.16 to 6.19, truth case lies mostly within the credible interval.

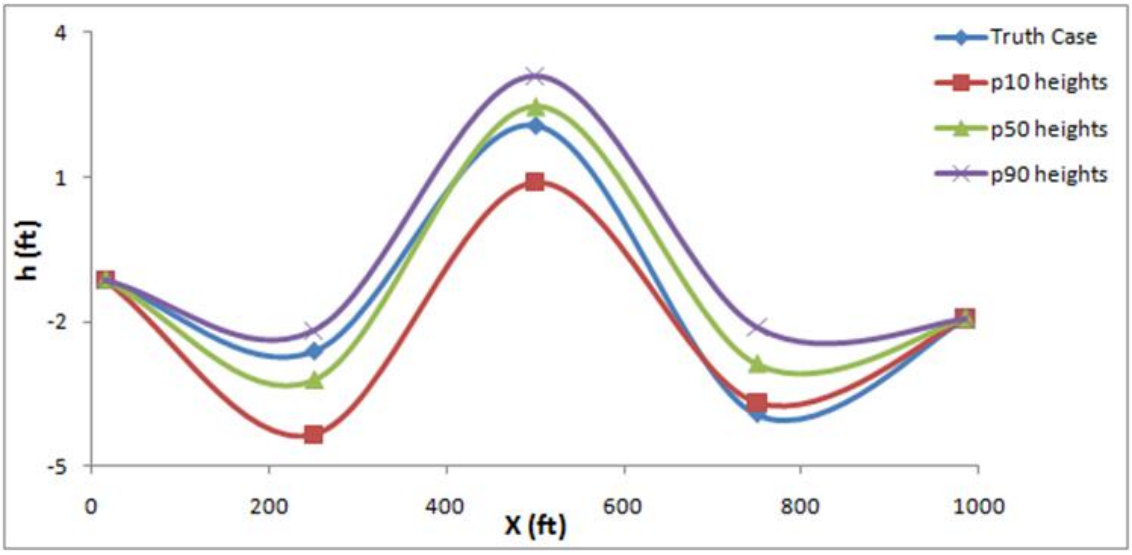

Figure 6.16: Posterior credible interval for the 1st layer boundary compared with truth case

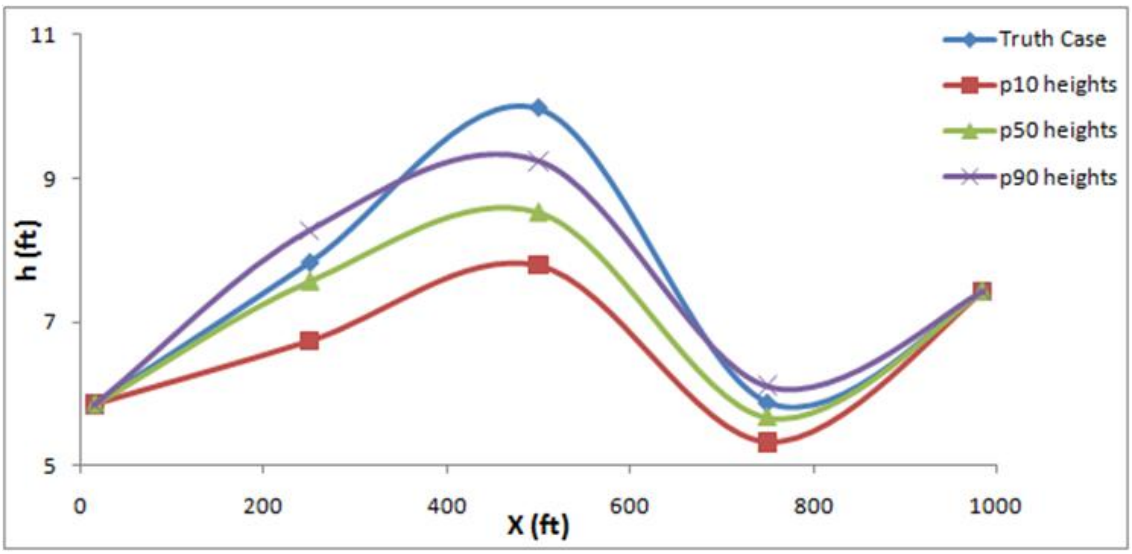

Figure 6.17: Posterior credible interval for the 2nd layer boundary compared with truth case

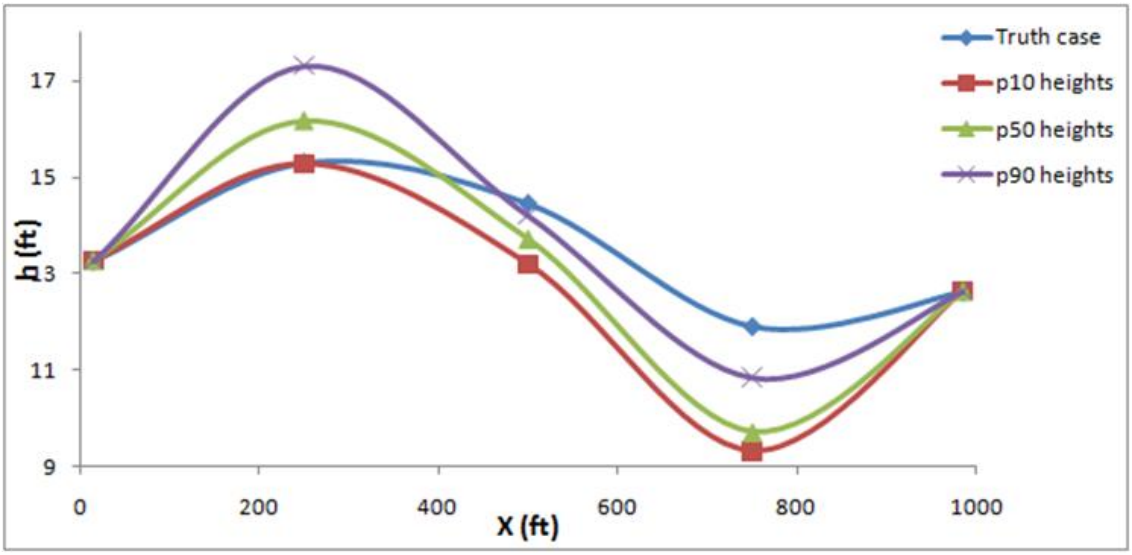

Figure 6.18: Posterior credible interval for the 3rd layer boundary compared with truth case

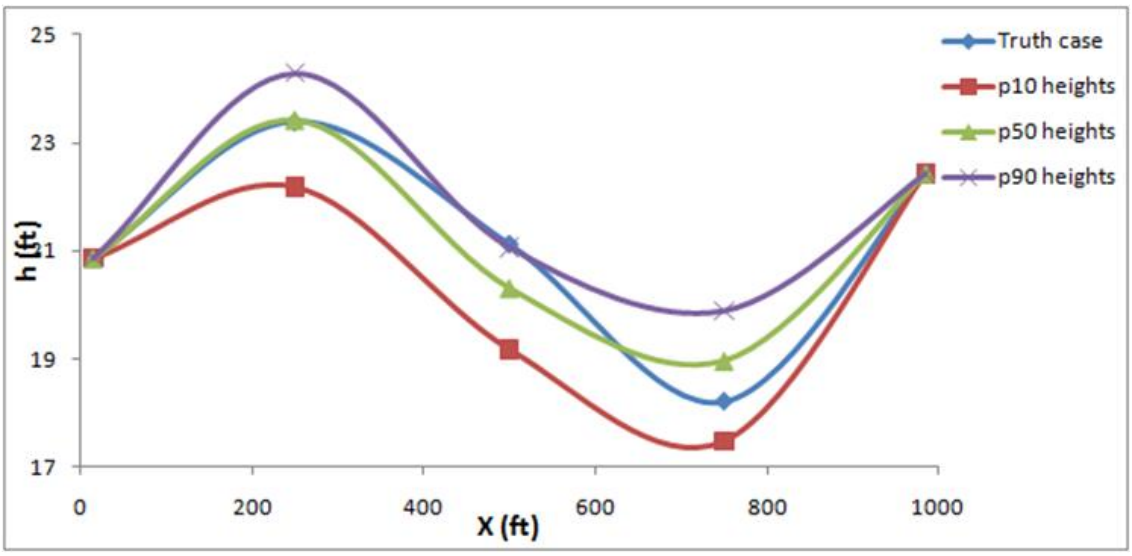

Figure 6.19: Posterior credible interval for the 4th layer boundary compared with truth case

A spurious down-thrusting of credible interval with respect to truth case happens for the 2nd layer boundary around the middle of model axial extension. Similar phenomenon is observed for the 3rd boundary close to the right extreme of model. This indicates that displacing the boundary between two less permeable layers in the second block does not affect considerably the production for maximum likelihood models. Truth cases of 1st and 4th layer boundaries (reservoir top and base horizons) are captured completely within their corresponding credible intervals. One can interpret this as the immense impact of top and base horizons geometry on the production behaviour in comparison with other layer boundaries. As the reformation and displacement of reservoir horizons may extend the reservoir into the non-porous rock formation or shrink the reservoir by leaving out some parts of porous rocks, while changing the inter-layers boundaries just increase or decrease the porosity values of active cells. Therefore what dominantly controls the STOIIP and production profiles is the total thickness of reservoir confined within the first and last layer boundaries.

Indeed narrower credible intervals are expected for top and base horizons in contrast with inter-layers boundaries. However as the porosity contrast (and probably permeability contrast) increases between layers sharing a boundary, STOIIP and production behaviour become more sensitive to variation of that layer and posterior

inference leaves less uncertainty over its geometry. This is somehow the case for the pinchout where its overlapping boundaries are too influential on flow like top and base horizons. The narrowing indices for the heights per each horizon (defined by Eq. 5.7 from chapter 5), are given per each layer boundary in table 6.9.

x-coordinate	$x_1 = 250\ ft$	$x_2 = 500\ ft$	$x_3 = 750\ ft$
Nar. Idx. (1st layer boundary) (%)	39.50	53.02	54.76
Nar. Idx. (2nd layer boundary) (%)	37.02	63.54	57.73
Nar. Idx. (3rd layer boundary) (%)	55.91	38.13	55.84
Nar. Idx. (4th layer boundary) (%)	55.63	34.75	59.29

Table 6.9: Percentage of uncertainty reduction for each height per each boundary

Generally smaller narrowing indices are obtained in the middle of model axial extension, demonstrating the reduced effect of layers geometry on production. Two large narrowing indices (coloured as red in table 6.9) occur for 2nd and 3rd boundaries where the true height is located outside the credible interval, implying that narrowed down updated credible interval might be a result of inability of misfit variables to monitor the impacts of variation of corresponding uncertain parameter. For example here, an observation well drilled in the middle of model axial extension can monitor the water saturation build-up and take more effectively the impacts of inter-layers boundaries into the consideration.

Figure 6.20 represents a schematic comparison between the truth case and models offering the extreme variations of uncertain surfaces after posterior inference. STOIIP for three typical models built with p10s, p50s and p90s are in a very narrow range around the true STOIIP. Such a remarkable agreement indicates that the flow behaviour dictated by imposed faults into the models is more influenced with the SOTOIIP.

The throw of “fault-1” lies outside the credible interval. In case of more precise location of faults determined by seismic, it is very likely that throw of fault-1 is captured within the credible interval. On the other hand, throw of fault-2 is captured within the credible interval. In general, due to small permeability contrast between bedding layers, the impact of fault throw on reservoir interconnectivity and hence flow behaviour would be reduced. So it is expected that the truth case of closer fault to the production well has more significant influence on flow behaviour.

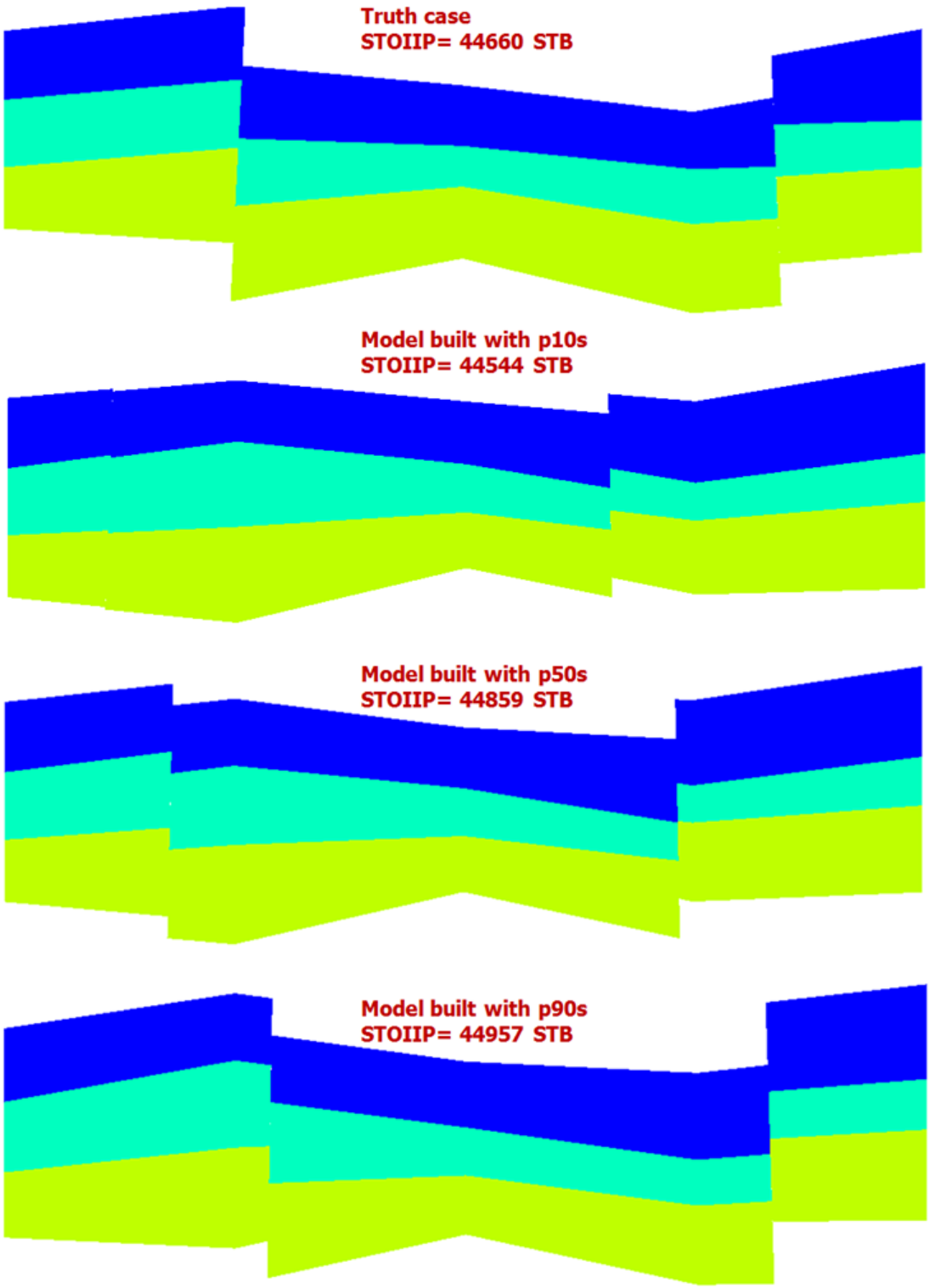

Figure 6.20: The variation of uncertain boundaries and fault within the credible interval

6.2 Simultaneous Quantification of the Uncertainties of Pinchouts and Faults

6.2.1 Case Description

It is desired to simultaneously quantify the structural uncertainties of intersecting surfaces of pinchout and fault. The model is a two-dimensional vertical cross section of a reservoir containing a pinched out layer with reduced porosity of 0.02 and a negligible permeability of 0.00000002 *Darcy*. Rock properties for two stratigraphic layers confining the pinchout have been set constant and equal together. Their corresponding porosity and permeability are 0.20 and 0.20 *Darcy*. Two normal faults with positive offsets separate the oil bearing formation into three blocks, such that the middle block has been downthrown. Model dimensions in horizontal and normal directions are 1000 *ft* and 112 *ft*, while model thickness varies in axial direction according to fixed heights of top and base horizons given in table 6.10. Two injection and production wells are opened to flow on the left and right extremes at well flowing pressures of 150 *psia* and 50 *psia* respectively.

$x_i(ft)$	15	125	250	375	500	625	750	875	985
$h^{base}(x_i)(ft)$	0.13	-0.06	1.58	-0.93	1.7	1.18	1.66	0.71	0.43
$h^{top}(x_i)(ft)$	19.36	18.02	17.58	18.74	17.87	17.12	17.66	18.09	19.43

Table 6.10: Heights of top and base horizons for faulted pinched out model

Tables 6.11 and 6.12 provide the true values of two faults parameters and their corresponding prior uncertainty ranges, where “fault-1” and “fault-2” stand for faults closer to the left and right extremes respectively. Narrower uncertainty ranges are selected for fault parameters in contrast with multi-layer model discussed in section 6.1. Also in table 6.13, the truth case and prior uncertainty ranges of involved pinchout have been given.

	Truth case	Prior range
X-coordinate of fault entrance point (*ft*)	256	150-350
Fault slope (*ft/ft*)	1.38	1.0-2.0
Fault throw (*ft*)	4.35	2.0-6.0

Table 6.11: Truth case and prior ranges for fault-1 in pinched out faulted model

	Truth case	Prior range
X-coordinate of fault entrance point (*ft*)	828	750-900
Fault slope (*ft/ft*)	-0.78	-1.25--0.75
Fault throw (*ft*)	4.53	1.0-5.0

Table 6.12: Truth case and prior ranges for fault-2 in pinched out faulted model

Pinchout parameters	Truth case	Prior range
xH (*ft*)	173.0	50-250
hH (*ft*)	6.03	5.5-8.5
rA (°)	-0.15	-0.25-0.25
TL (*ft*)	500.0	350-650
uHA (°)	0.83	0.7-1.2
lHA (°)	0.22	0.1-0.4
uTA (°)	0.90	0.7-1.2
lTA (°)	0.21	0.1-0.4

Table 6.12: Truth case and prior ranges for pinchout in pinched out faulted model

6.2.2 History matching of Pinchout and Fault Geometrical Specifications

Oil and water production profiles are obtained for truth case in a period of 1500 *Days*. Effects of uncertainties with fault and pinchout on predicted production profiles can be investigated with running the simulator for models enjoying the extreme values on prior uncertainty ranges. Production profiles for two representative models offering the maximum structural uncertainty along with the observed profiles are depicted in figures 6.21 and 6.22 for oil and water phases respectively.

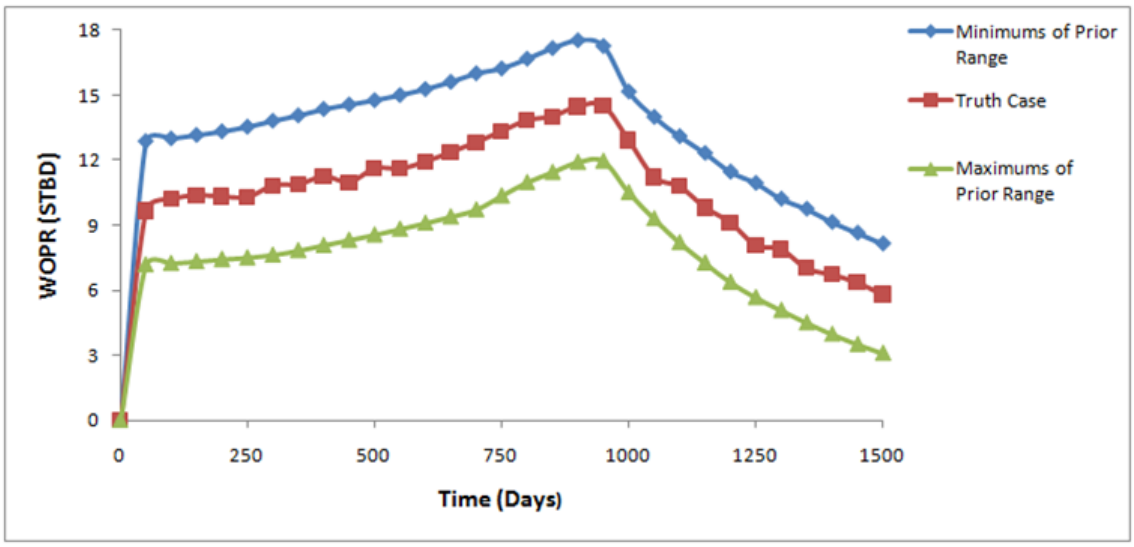

Figure 6.21: Variation of WOPR in prior uncertainty ranges for faulted pinched out model

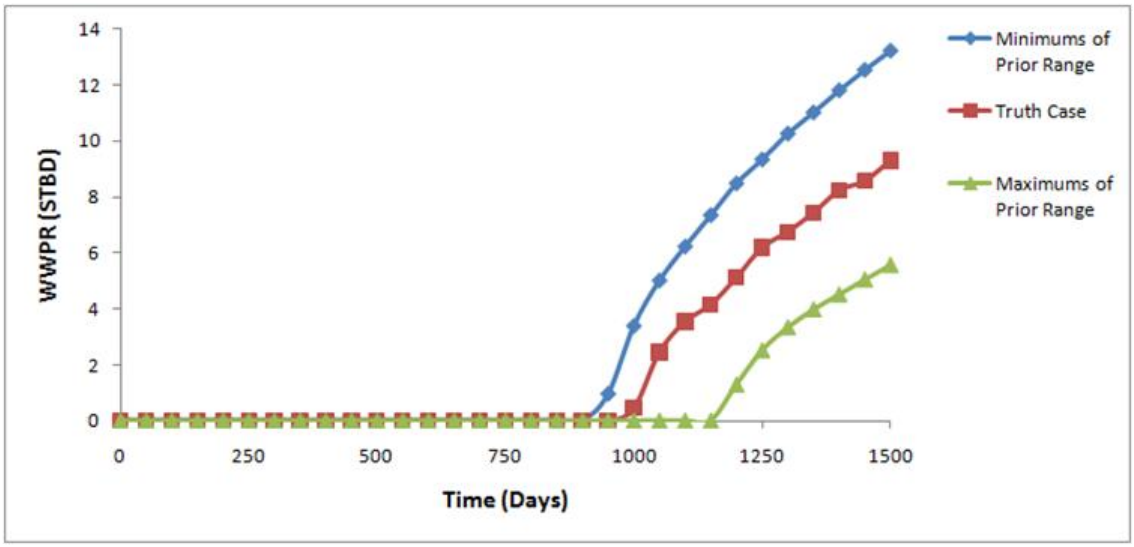

Figure 6.22: Variation of WWPR in prior uncertainty ranges for faulted pinched out model

Higher production rates and earlier breakthrough are corresponding to minimum pinchout extent leading to maximum STOIIP, however fault parameters picked at their minimum prior ranges have much less effect of production behaviour. This might be verified by very similar production rates from models having the minimum pinchout size combined with alternating values of fault parameters on extremes of prior ranges.

However it seems that at a fixed set of pinchout parameters, water breakthrough time is dependent mainly on the throws of two faults, while it is influenced at a smaller order of magnitude by the locations of faults. The larger throws of fault-1 and smaller throws of fault-2 eventuate in earlier breakthrough. Because such a combination of offsets for two faults maximizes the gravity potential reserved for both phases and accelerates the advancement of water front. Also a delay in water breakthrough is predicted when the faults are displaced away from the wells at extremes of models. Closer fault-1 to the injection well exerts the gravity potential provided by positive offset on a more piston-like water front, so both semi-fronts moving in layers encompassing the pinchout move faster in second block. One the other hand, remembering the negative slope of fault-2, water front has to overcome the counteractive gravity potential along the fault-2 plane when it enters the third block. Thereafter closer fault-2 to the production well is equivalent to a water front decelerated by negative slope of fault-2 in a shorter distance before entering the production well, so water front breaks through earlier. Constant rock properties throughout the layers confining the pinchout make the impacts of fault geometry on potential field more distinctive and interpretable.

The following set of input parameters of NA has been employed to sample through the prior uncertainty ranges and minimize the misfit function:

n_{s_i}	n_s	n_r	Iterations	Total Simulations
200	20	10	150	3200

Table 6.13: NA input parameters for simultaneous history matching of faults and pinchout

NA finds a maximum likelihood model after 3089 iterations with a misfit of 0.21, while it returns an average misfit of 182 over all models. Smaller average misfit in contrast with the multi-layer faulted model (discussed in section 1) indicates that production profiles are much more influenced by the variation of pinchout geometry rather than by variation of permeable layers thicknesses and as a result NA finds the maximum likelihood models after less number of simulations. In figure 6.23, the parameters of

maximum likelihood model have been compared with the true parameters within the scaled prior range. “PO”,”F1”,”F2” stand respectively for pinchout, fault-1 and fault-2.

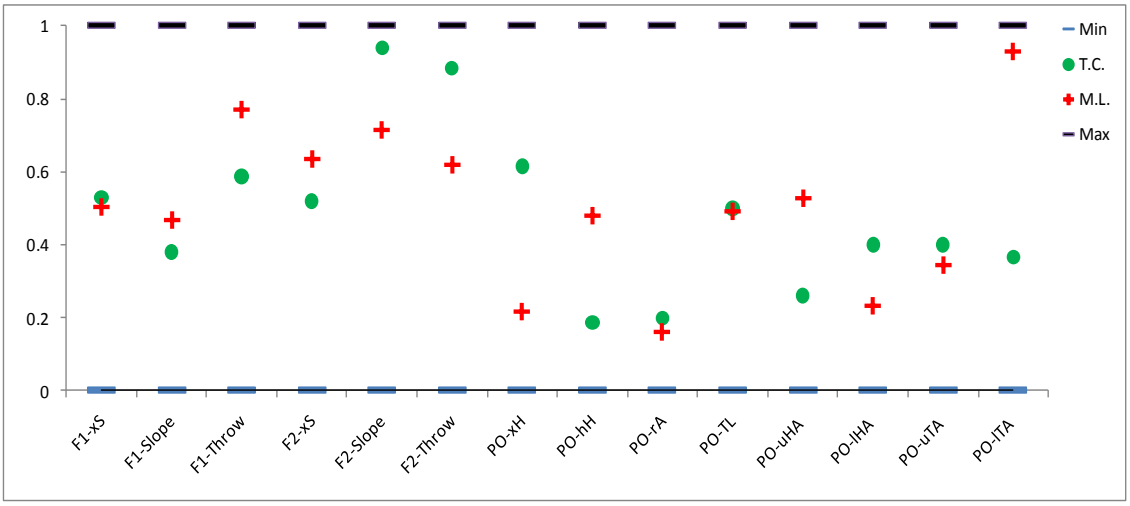

Figure 6.23: Comparison between parameters of maximum likelihood model and truth case within the relevant scaled prior ranges

The best closefitting agreements are observed pinchout total length, pinchout rotation angle and the location of fault-1. The good matching of first parameter (PO-TL) is explained with its substantial effects on pinchout extent (and consequently STOIIP). On the other hand PO-rA determines the thickness of layer beneath the pinchout at constant values of interior pinchout angles, such that if PO-rA is negative, the larger the absolute value of rotation angle leads into the thinner lower layer and leaves larger proportion of STOIIP in the layer above the pinchout. Thus at more negative PO-rA, less gravity segregation and higher vertical sweep efficiency are anticipated. In contrary more positive PO-rA results in smaller vertical sweep efficiency, because in addition to a thicker lower layer, counter-clockwise rotated pinchout enforces the upper water semi-front to overcome an elevated gravity barrier.

Very good match of fault-1 location and acceptable match for location of fault-2 are explained with their considerable influence on deviation of water front from piston-like shape. Also a relatively good match for PO-uTA is obtained in contrast with other

pinchout opening angles. As we discussed in Chapter 5, this is due to remarkable contribution of downward oriented geometry of upper pinchout branch on advancement of water front in upper layer.

However summation of interior opening angles for maximum likelihood model (2.38°) is a bit larger than corresponding value for truth case (2.16°). So remembering almost identical PO-TL for M.L. and T.C. models, a larger pinchout extent and consequently smaller STOIIP is expected for M.L. model. This can be seen in figure 6.24 where the geometries of maximum likelihood model and truth case have been compared. Maximum likelihood has been assigned for a model with larger F1-Throw and smaller F2-Throw compared with truth case, thus better vertical sweep efficiency is anticipated for M.L. model. This can explain how M.L. model with smaller STOIIP (32449 *STB*) in contrast with true STOIIP (32551 *STB*) can reproduce the observed production profiles.

Figure 6.24: Maximum likelihood model vs. truth case for uncertain faults and pinchout

6.2.3 Quantifying the Convolved Structural Uncertainties of Faults and Pinchouts

Posterior Bayesian inference is performed on CDF values constructed by running NAB routine to create updated uncertainty envelops for each uncertain parameter. In figures 6.25 and 6.26, cumulative posterior probability has been plotted over the prior uncertainty ranges. All true values of fault-1 and pinchout lie within the updated uncertainty range, while for fault-2 true values of slop and throw are not captured within the bounds of credible interval. This observation and relatively narrower credible intervals for fault-1 in contrast with fault-2 demonstrates more profound dependency of flow behaviour on geometry of fault-1. What makes fault-1 more influential than fault-2 is it closeness to the pinchout, such that:

1. Fault-1 is intersected with the pinchout. So at a fixed geometry of pinchout, the location and throw of fault-1 control the effective conductivity across the fault plane, as their variation changes the thickness of pinched out layer at fault plane. While at fault-2 plane regardless of its geometry the flow conductivity remains constant.
2. Sealing effect of pinchout prevents downward cross flow between layers confining the pinchout, so gravity potential provided by the positive offset and positive slope of fault-1is translated into the flow behaviour more remarkably compared with negative gravity potential reserved by fault-2. Because more efficient displacement in upper layer closer to fault-1 is expected.
3. Throw of fault-1 determines the height offset between two interrupted portions of pinchout in first and second blocks. At higher throws of fault-1, it is more likely that water semi-fronts formed in first block reunify in the second block and continue to advance in upper layer along the pinchout body. Thus oil in layer beneath the pinchout remains unswept and depending on relative thicknesses of pinchout confining layers, displacement efficiency would be impacted.

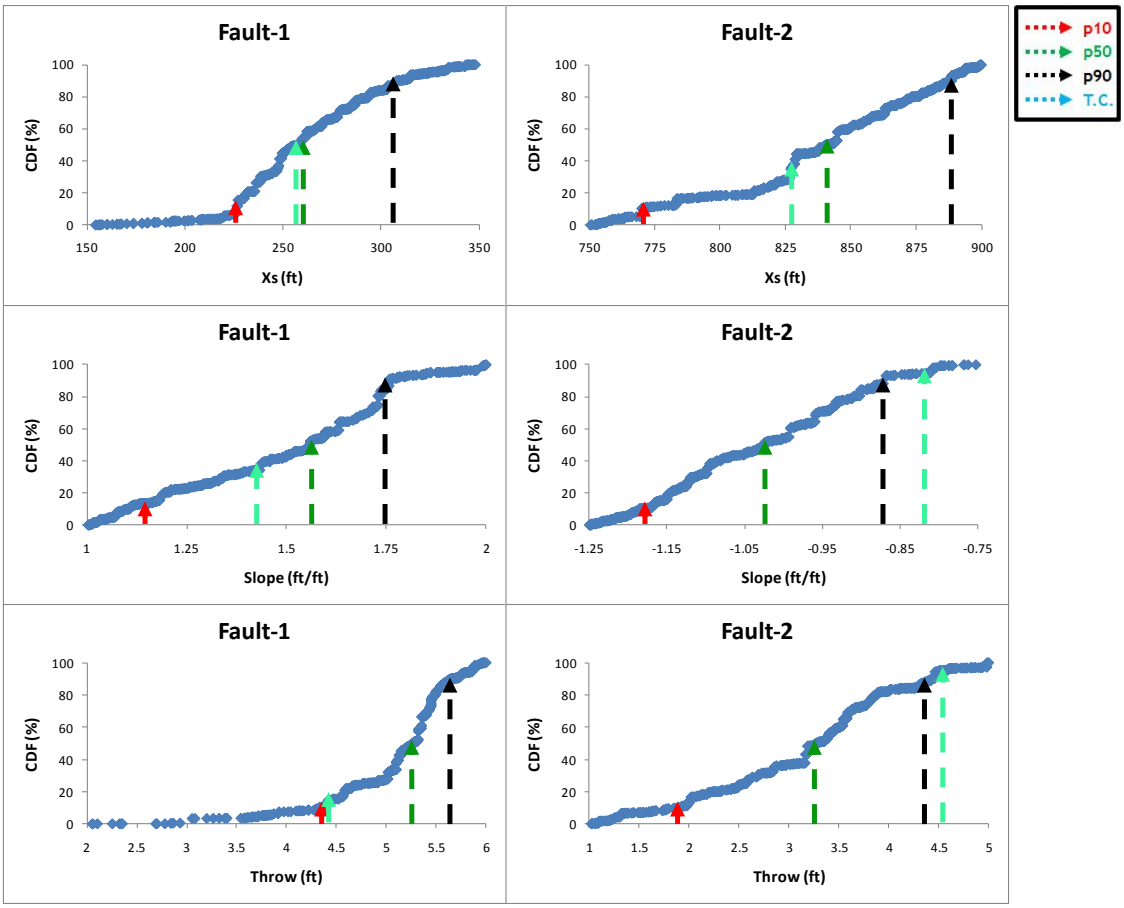

Figure 6.25: CDF for geometrical parameters of fault-1 and fault-2 used to determine their corresponding Bayesian credible interval

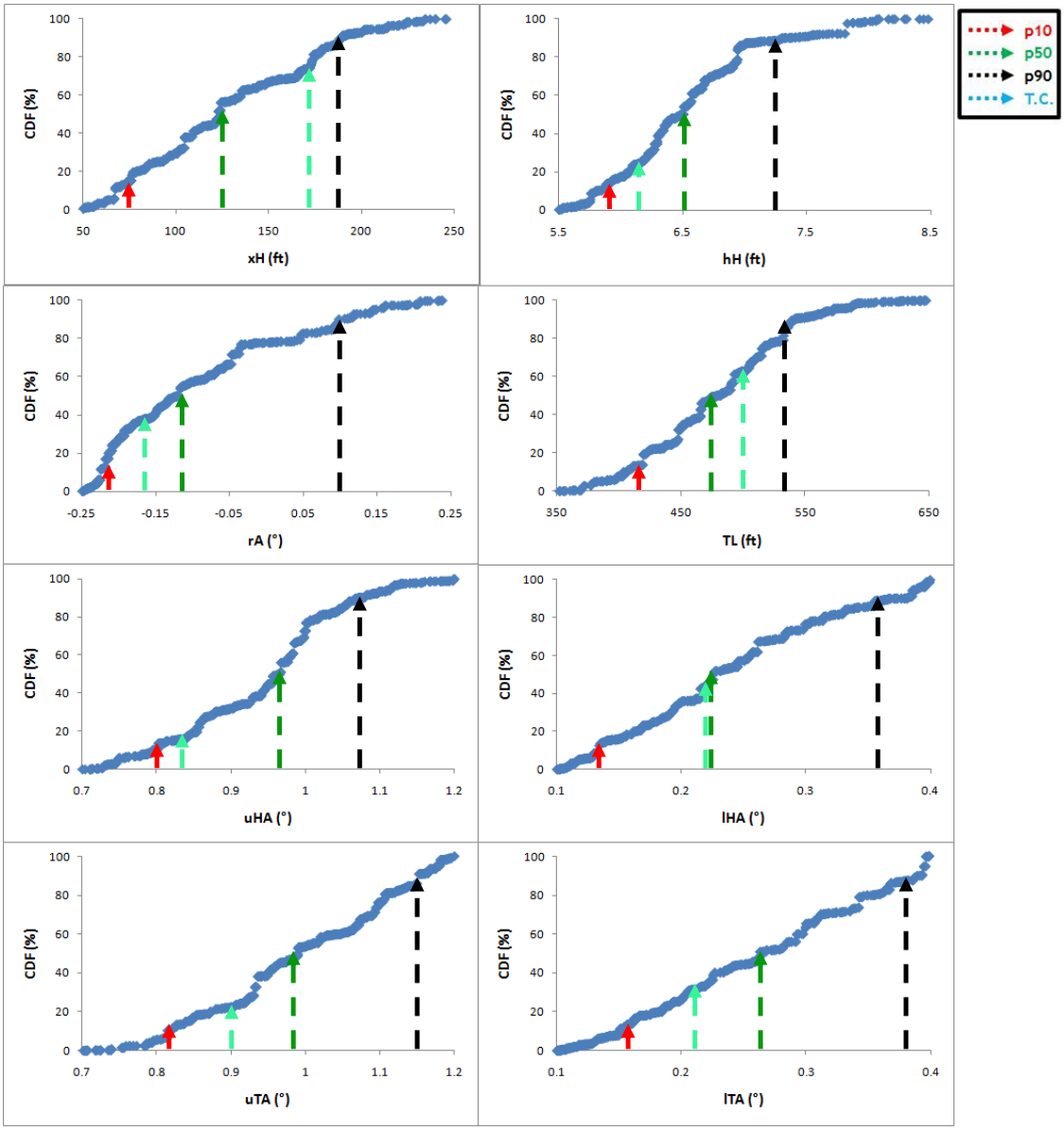

Figure 6.26: CDF for geometrical parameters of pinchout used to determine their corresponding Bayesian credible interval

However for pinchout all true values of geometrical parameters have been captured within the credible interval. The narrowest credible interval among them is observed for TL and hH. Narrow credible interval for the total length of pinchout is explained with its considerable impact on the pinchout size and consequently on oil in place. The height of head point determines the vertical thickness of lower permeable layer in the middle block exposed to lower semi-front, as at a constant throw of fault-1 the higher the head point of pinchout would be equivalent to thicker connection between left and middle block across the lower permeable layer and consequently a more efficient oil

displacement across the lower permeable layer is expected, while at lower values of hH it is more likely that lower semi-front moves above the pinchout in the middle block and leaves oil in the lower permeable layer unswept leading to a delayed gravity segregation and better displacement in upper layer. However the convolved impacts of other pinchout parameters on flow behaviour especially in presence of two faults makes their individual influences less recognisable and results in almost linear variation of their corresponding CDF at posterior along the parameter interval. For example in absence of any other intersecting fault, more downward rotated pinchout (more negative rA) has a single impact on reduction of gravity segregation and better oil displacement in upper layer, On the contrary in presence of an intersecting fault (fault-1) more negative rA facilitates advancement of lower semi-front above the pinchout and increases the chance for remaining oil unswept in lower permeable layer.

A schematic comparison of truth case with models built with p10, p50, p90 values of geometrical parameters of uncertain surfaces has been given in figure 6.27. A good agreement is observed between truth case and model built with p50s in terms of STOIIP, while model built with p50s is less elongated in horizontal direction, but has larger opening angles. Also model built with p50s provides relatively good approximations of fault-1 parameters.

Effects of simultaneous pinchout and faults uncertainties on oil in place can be investigated with plotting CDF of models in posterior versus their corresponding STOIIPs (depicted in figure 6.28). Reduced uncertainty over STOIIP ([p10=31969 *STB*,p90=33117 STB]) is remarkable, but in comparison with an uncertain pinched out model devoid of intersecting fault, less narrowing of credible interval after posterior inference is attained. This demonstrates that although reservoir volume is not dependent on fault geometry, but in presence of any uncertain surface which affects the volume of oil bearing layers, fault geometrical uncertainty impacts the posterior forecasts of oil volume in the place. This is mainly because the impression of flow behaviour from geometry of pinchouts or other layers gets obscured with introduction of any intersecting fault. Such an elevated uncertainty results in less updated information taken

from history-matched models and consequently wider ranges of Bayesian credible intervals

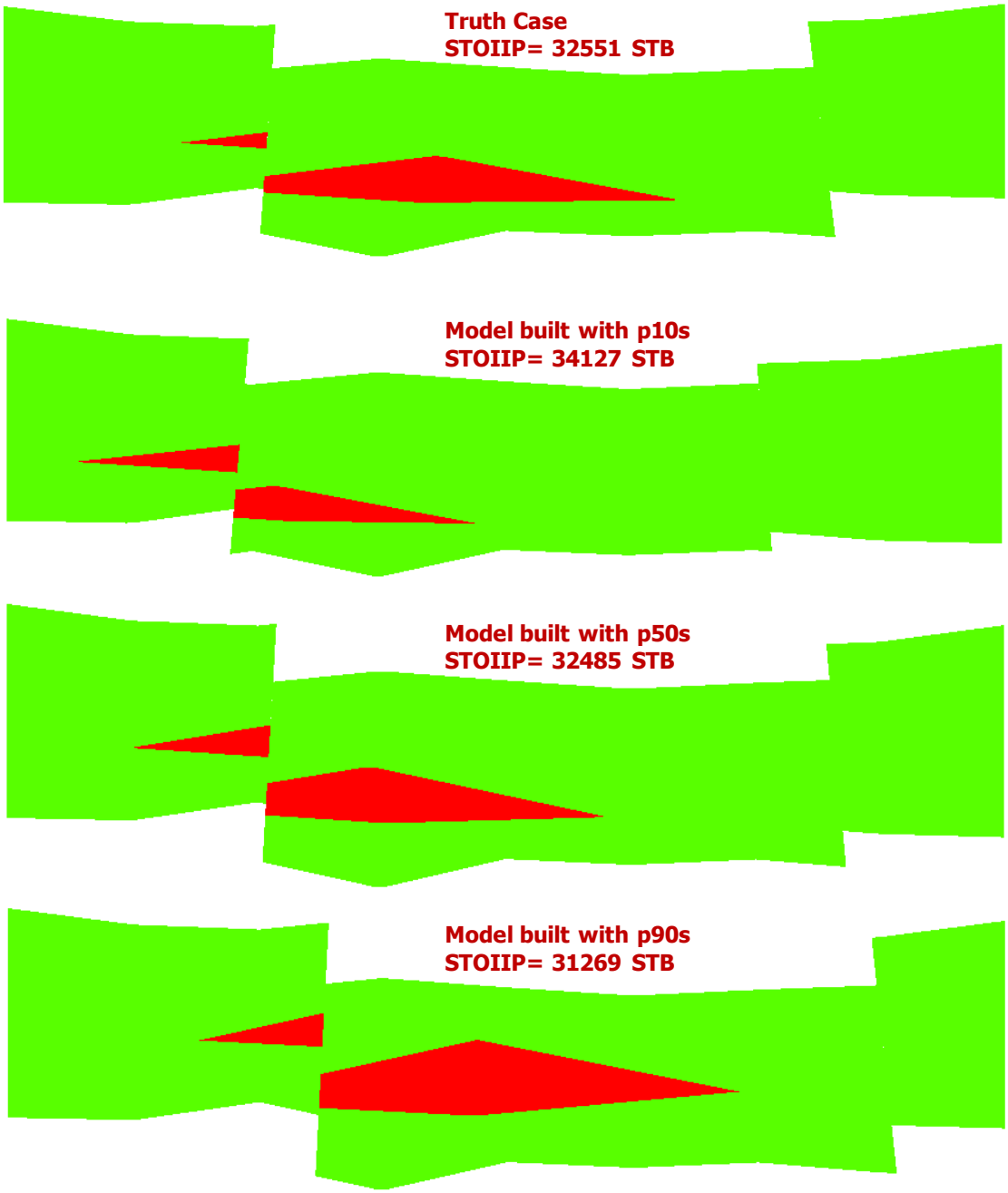

Figure 6.27: Extreme variation of uncertain faults and pinchout within the credible interval compared with truth case

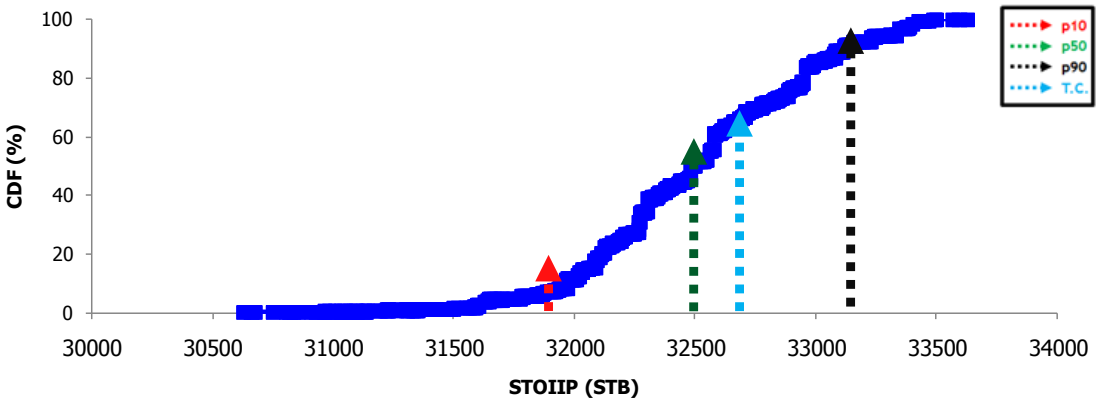

Figure 6.28: CDF distribution on posterior range of STOIIP for pinched out faulted model

The augmented uncertainty due to the inclusion of sharply-dipped structures can be seen by comparing the posterior variation ranges of oil and water production (depicted in figure 6.29 and 30) by the relevant prior ranges (depicted in figures 6.21 and 6.22). The reduction of gap between highest and lowest rates at posterior compared with prior is evaluated about 40% of prior gap. Remembering the shrinkage the of relevant gaps for the pinched out model (discussed in section 5.3.3 of chapter 5) to 20% of its prior value, one can conclude that as the structural complexity increases, the posterior inference leaves less confined uncertainty ranges and hence less reliable forecasts can be made about the production profiles.

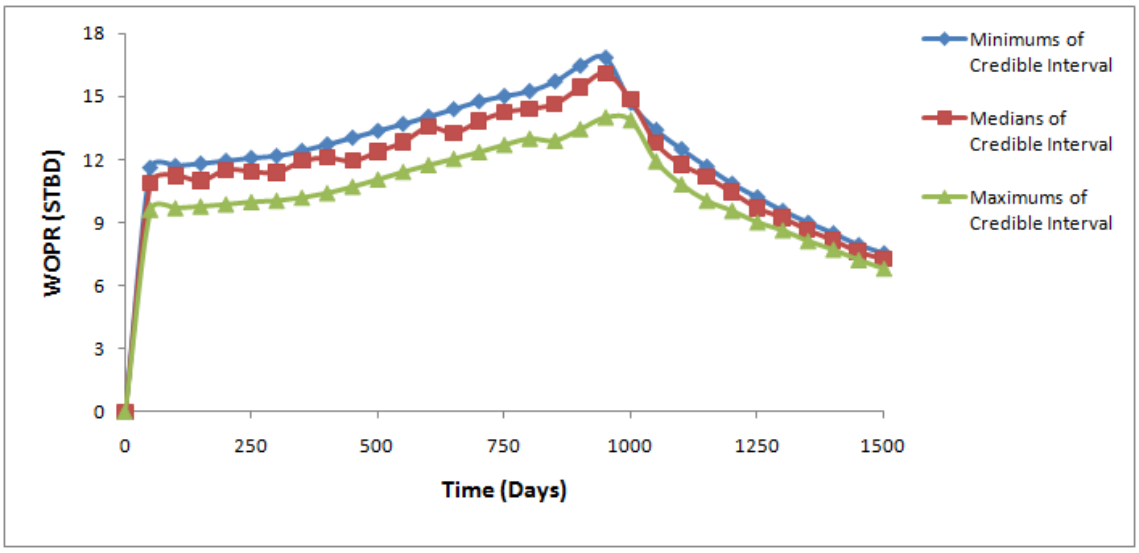

Figure 6.29: Variation of WOPR in the posterior credible interval for faulted pinched out model

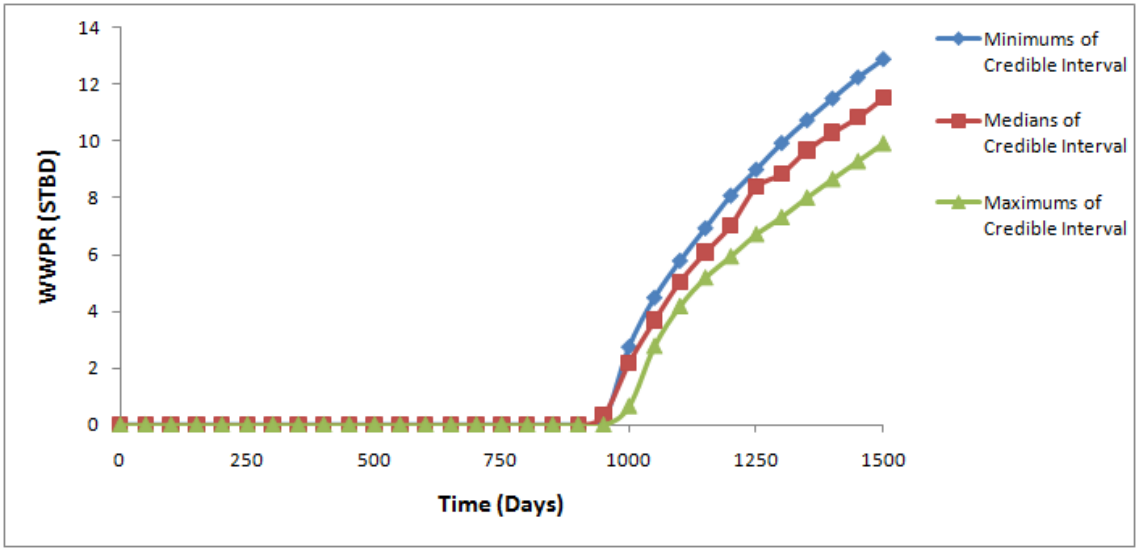

Figure 6.30: Variation of WWPR in the posterior credible interval for faulted pinched out model

The general conclusion of this chapter is that history matching of geological structures becomes intensely harder when combinations of intersecting uncertain structures are involved in history matching problem. We believe that more robust optimisation techniques can handle more effectively the raised uncertainty of multiple intersecting structures.

Chapter 7

Conclusions and Future Works

Our main aim in this research was to handle large scale reservoir uncertainties in terms of their modelling and quantification. The research was conducted towards the design of an approach assisting the dynamic variation of uncertain structures during the history matching process to study the corresponding structural uncertainties. The proposed hybrid Cartesian Cut Cell/EMPFA approach removes the necessity for rebuilding the reservoir model at each step of history matching process and gives the flexibility to handle geological structures of normal geometrical complexities coming about in petroleum reservoirs. Indeed there is the potential to extend the work beyond this thesis for tackling more complex geological structures like intersecting fault, discrete fracture networks or very sharply dipped bedding planes. Such a helpful tool was implemented in terms of a C++ computer program (SUQIB) including a convolved grid pre-processor and reservoir simulator for 2-D models. This program supersedes the commercial reservoir simulators in the general uncertainty quantification framework previously developed at Heriot-Watt University and makes it capable to handle structural uncertainty problems. Such an improvement is more highlighted knowing that no other approach yet has been introduced for automatic history matching of geological structures without disturbing the reservoir model. While in our proposed approach the geometry of geological structures is decoupled from its representation onto the computational grid. Cartesian Cut Cell method lets the reservoir model to be fixed to a

Cartesian background grid during the history matching process and incorporates the updated geometries of geological structures at each step of history matching into the reservoir model with displacing and reforming the immersed boundaries as the representation of uncertain geological surfaces on grid.

The robustness and functionality of proposed approach have been testified by performing history matching and uncertainty quantification for several 2D models possessing some typical geometrically parameterised geological structures. Both cases of models having single structure or multiple intersecting structures have been studied.

In this chapter, we summarise the undertaken works and put forward the conclusions drawn from our research. Also we recommend some promising directions of research as the future works.

7.1 Key Findings

Our key findings will be presented in two parts: (1) Performance of Hybrid Cartesian Cut Cell/EMPFA approach, (2) Concluding remarks about the uncertainties of large scale structures.

7.1.1 Performance of Hybrid Cartesian Cut Cell/EMPFA Approach

Difficulties of flow simulation for models involving geological structures arise from their complex geometries which complicates the well resolved mesh generation. Apart from drawbacks of using body-fitted regridding techniques for history matching of geological structures (discussed in details in chapter 1, 3), they might eventuate in very ill-posed solution matrices. Strongly curved interfaces coupled with high grid aspect ratios turn up in the vicinity of geological structures and body-fitted gridding spreads this undesirable grid geometry into the bulk of reservoir far from any geological structures. Moreover the strong heterogeneities of petrophysical properties across geological structures and high permeability anisotropies increase the condition number

of solution matrix as a measure of difficulty of its solving. The proposed Hybrid Cartesian Cut Cell/extended EMPFA approach can relieve some of these problems and possibly provides a more easily solvable solution matrix.

The main advantages brought by Cartesian Cut Cell are as followings:

1. When it is applied for history matching of geological structures, it guarantees the fulfilment of a main proposition of uncertainty quantification framework which assumes almost equal simulation errors for the ensemble of sampled models. Also by removing the need for general regridding, it accelerates the process. This saving of computational time would be more remarkable in case of 3D models involving more complex geological structures.
2. Cartesian cut cell method restricts the occurrence of strongly deformed cells to the immediate adjacency of structures and prevents from spreading out the complex geometry of geological structures into the bulk of reservoir model where the media is well represented with rectangular Cartesian grids. Therefore the total number of cells exhibiting curved faces would be considerably reduced. As a result usual “Two Point Flux Approximation” with proven monotonicity can be used for most of cells instead of using complex flux reconstruction schemes like “Multipoint Flux Approximation” or “Mimetic Finite Difference” with limited and conditional monotonicity. Resulting solution matrix with much smaller condition number is more likely to yield a physical solution free of spurious oscillations.
3. Multiple intersecting geological structures are properly incorporated into the grid with subtle implementation of Cartesian cut cell method. Multistep cutting the cells out of Cartesian grid by geological structure follows the same consequence of geological events creating structures (sedimentation, erosion, faulting, folding). Therefore reservoir Compartmentalisation is well honoured by cut cells.
4. The emergence of unfavourable grid geometries with practically zero volume and very high grid aspect ratio is avoided by “Cell Merging” idea in the cost of obtaining few non-neighbour connections. As a result stability of solution would be increased by avoiding such large volume contrasts between neighbour cells.

Complex patterns of structures intersections, sharply dipped beddings with sudden curvature change along their planes (wavy beddings) or very faulted zones can increase the geometrical complexity of reservoir model and leads to a dramatic increase in the possible cell-boundary intersection states. A successful implementation of Cartesian Cut Cell Method requires the comprehensive identification of all these possibilities in a way that a geometrically consistent breakage of Cartesian cells into their sub-cells belonging to different compartments is assured. The general idea of "Cell Merging" can be adapted for any degree of complexity to create geology honouring cells with favourable grid aspect ratios even in presence of intersecting structures (e.g. fault intersecting pinchout, fault intersecting layer boundaries and so forth). For example small cut cells with bilinear or highly curved faces (e.g. cells in the vicinity of extreme points of a pinchout) can be merged to an adjacent cell to reduce the overall cell skewness.

The degeneracy of reformed cells after truncating them with the surface of geological structure necessitates the use of a multipoint flux approximation technique. We employed a modified version of Enriched Multipoint Flux Approximation with promoted accuracy due to assigning individual bilinear potential distributions throughout the sub-volumes of cells sharing a common vertex. This scheme was demonstrated to be very beneficial for flow simulation on geological models as explained in followings:

1. It was shown that with suitable choice of quadrature parameters for a point-wise EMPFA scheme, monotonic results with negligible spurious oscillations can be obtained for a wide range of anisotropies and grid aspect ratios. We have verified that for the studied typical structures (as the good representatives of subsurface reality), QM-matrix criteria can be met by using "Extreme Anisotropic Quadrature".
2. EMPFA scheme was shown to be convergent and consistent over a benchmark model involving all geological structures studied in this thesis. Super-linear and linear convergence rates were obtained for potential and flux approximation respectively. Although error estimates calculated over the irregular cells (cells cut by geological surfaces) were larger than corresponding values for whole the region, but almost the same convergence rates as corresponding values calculated over whole the model are obtained for irregular cells. Thus EMPFA

can maintain desirable accuracy comparable to second order accuracy of finite volume method over Cartesian grid even for complex geological structures.

3. Using EMPFA, the unfortunate effect of other MPFA approaches (MPFA-O, MPFA-L) on non-matching cells is avoided and obtaining non-zero transmissibility and consequently non-zero flux is assured for any face shared by two cells having non-zero permeability. Such an advantage is more highlighted along the fault plane or along the pinchout surface, where even if permeability at each of involved cells diminishes to zero, a non-zero flux is obtained across the face shared by active cells. As a result, the overall reservoir interconnectivity which is substantially affected by faults geometry in horizontal direction and by pinchout geometry in vertical direction will be precisely translated into the flow simulation.

All discussed advantages of extended EMPFA are very beneficial in the context of uncertainty quantification. The promoted accuracy in flux approximation certifies the correct response of simulation outputs to the alteration of structures geometry. Therefore the quality of optimisation results is improved and the chance that history matched geological models be good representatives of subsurface structures is increased. Moreover the reliability of posterior inferences made on ensemble of history matched models will be boosted because of a misfit response surface with augmented quality. It is expected that consistent credible intervals are obtained for the geometrical parameters of different structures (narrower credible intervals for more effective parameters and wider ones for less effective parameters).

7.1.2 Concluding Remarks about the Uncertainties of Large Scale Structures

We have used general uncertainty quantification framework equipped with Cartesian Cut Cell/EMPFA approach to history match and quantify the structural uncertainties of several benchmark models involving some typical geological features like fault, pinchout and layer boundaries. The results were presented in Chapter 5 for non-intersecting structures and in Chapter 6 for multiple intersecting structures. The conclusions presented in the followings although were made based on these synthetic

cases, but they are applicable for more complex models as well, because the studied models include two-dimensional projections of most geological features found in underground reservoirs.

1. Geometry of sharply dipped geological structures (faults or wavy bedding truncations) primarily influences the overall horizontal reservoir interconnectivity, while the vertical interconnectivity is mainly impressed by the geometry of gently dipped structures (pinchouts, non-steep bedding layers). On the other hand, due to high anisotropy ratios $\left(K_h/K_v\right)$ governed in petroleum reservoirs, flow takes place mostly in horizontal direction through the cell thinner interfaces. As a result individual geometrical parameters of faults are more easily history matched compared with those of pinchouts or reservoir horizons and accordingly their corresponding uncertainties are more considerably reduced after posterior inference.
2. Production predictions are significantly influenced by the volume of oil in place (STOIIP) which is dictated only by the location of gently dipped geological structures especially top and basin horizons. Therefore the average depth along trend of history matched layer boundaries (especially top and basin horizons) well concurs with the truth case. This accordance is amplified for the thickness of individual layers (especially for the total reservoir thickness bordered between top and basin horizons). On the contrary, the history matched local geometry (local curvature, local orientation, etc) of gently dipped geological structures differs a lot from truth case. In this regard, following points are worth mentioning:
    a. Accumulative impact of geometrical parameters determines the volume of oil in place, therefore models having different geometries of geological structures but comprising the same volume of oil in place display similar production behaviours. As a result:
        i. STOIIP predicted by history matching is reliable and prior uncertainty of reservoir volume is substantially reduced after posterior inference.
        ii. Uncertainty over individual geometrical parameters (like the depths along the bedding planes) is not narrowed down too much after posterior inference. However one can regroup these parameters in a way that resulting parameters are more

representative of volume enclosed by structure rather its geometry, such a re-parameterisation is likely to be ensued by faster convergence of history matching and narrower credible intervals for individual geometrical parameters.

iii. Uncertainty over the local geometry of bedding planes becomes more sever far away from wells and spurious down-throwing or uplifting might be developed, where local geometry is almost ineffective on production.

b. Running the optimisation method in a more exploitative mode is more preferred for bedding planes or pinchouts, as it would improve the quality of STOIIP prediction by refining the sampling through regions with very good fit into production data.

3. The impact of fault geometry on overall reservoir interconnectivity (especially in horizontal direction) is intensified as the permeability contrast between reservoir layers is increased. Therefore the fault uncertainty reduction after posterior inference is more remarkable for models with stronger cross permeability contrasts. However the optimisation of fault geometry for layered models is an ill-posed problem and is likely to be entrapped at local minima. Thus more explorative modes are recommended for fault history matching in layered models with stronger cross permeability variation.
4. Among fault parameters, fault throw is well history matched and its corresponding uncertainty interval is more narrowed down, explained by its more significant impact on reservoir interconnectivity. However fault location is likely to be predicted with an acceptable approximation, especially in presence of uncertain beddings or pinchouts, where the location of fault affects both reservoir compartmentalisation and interconnectivity. Fault dip is the most difficult parameter to be history matched which still remains uncertain after Bayesian inference. However for higher reservoir thickness and stronger cross layer permeability contrast, better prediction of fault dip is expected due to elevated impact of fault dip on reservoir horizontal interconnectivity.
5. Pinched out (eroded) layers might impose a very strong permeability disparity in vertical direction which dramatically alters the horizontal reservoir interconnectivity. As a result, true local geometry of pinchouts is more likely to be predicted with narrowed down uncertainty in comparison with axially

extended layers. Therefore apart from the volume enclosed by pinchout, the predicted values of the horizontal location, the depth and the orientation of pinchout are expected to adequately approximate the true values.

6. The discrepancy among production profiles for an ensemble of models picked from posterior credible interval can show how well the structural uncertainties have reduced. Production profiles for this ensemble are overlapping and converging to the observed production profiles when uncertain structures only affect the oil in place (like top and bottom horizons). However when structures affecting reservoir interconnectivity are introduced into the framework of uncertainty quantification, production profiles tend to diverge. This shows that the inherent uncertainties associated with sharply-dipped structures (faults) are more persistent and the forecasts performed based on posterior inference made on these structures remains wider uncertainty ranges relative to less inclined structures.
7. As the complexity of structural system rises, its associated uncertainty increases as a result of superposition of uncertainties of individual geological structures especially in case of networks of intersected sharply-dipped and gently-dipped structures. Due to convolved and unrecognisable impacts of intersecting structures on flow behaviour, fault uncertainties broadens uncertainty ranges for reservoir volume and future production rates, even though reservoir volumetric factors are not affected by faulting pattern and geometry.

Uncertain Structures in Synthetic models	STOIIP Estimation Enhancement	Recovery Forecast Enhancement
Top and Basin Horizon	7.2%	0.4%
Fault	-	16.2%
Pinchout	7.6%	21.5%
4 Layer + 2 Fault	11.7%	36.8%
Pinchout +2 Fault	9.3%	28.6%

Table 7.1: Narrowing indices given for uncertainty ranges on STOIIP and recovery after posterior inference maid on studied models having structural uncertainties

The overall conclusion of this thesis is that taking the structural uncertainties into account can considerably improve the reliability of our estimates about the volume of oil in place. Moreover reduction of uncertainties about the geometry and location of geological structures substantially helps to make unfailing decisions about field development plans like infill drilling, water flood scenarios or enhanced oil recovery strategies. Adjustment of tuning parameters of optimisation methods and interpretation of posterior inference outcomes must be carried out with an exhaustive reservoir engineering analysis on uncertain geological structures.

7.2 Future Work

Our recommendations about the open scopes of research beyond this PhD are listed as below:

1. The future research should be focused on more realistic models and hence the implemented Cartesian Cut Cell method should be extended to three-dimensional problems. For this aim all the different possibilities of boundary-cell cutting status must be determined. However to reduce the dependency of flux reconstruction on the geometry of degenerate cells which complicates achieving monotonic potential distributions, it is recommended to adapt EMPFA method for problems with discontinuities across irregular boundaries. For this purpose, trilinear potential approximation must be enforced throughout each sub-cell cut by boundaries. The corresponding trilinear coefficients should be obtained by fulfilling the flux and potential continuity condition across several points along the boundary plane enclosed between faces of corresponding parent cell. It seems that ideas inspired by the *Sharp Interface Finite Volume* developed by Oevermann et al. [2006, 2009] can be utilised to increase effectiveness of EMPFA scheme for flux computing over cells cut by boundaries with reduced necessity to explicit reshaping of cut cells.
2. In this thesis we studied the layered reservoirs with vertical porosity and permeability variations. However for fully heterogeneous models, the effects of displacing and deforming the reservoir boundaries (geological structures) on the geostatistical simulations must be investigated. It seems that geostatistical simulation should be performed on individual compartments enclosed by

reservoir boundaries independently. Nevertheless recreating the permeability realisations at each step of history matching must be avoided by mapping from a permeability distribution at a reference representation of each compartment to an updated geometry of corresponding compartment.

3. To extend this work for a given fine scale model, it is recommended to reconstruct fluxes in coarse scale by means of *Variable Compact Multipoint Method* developed by Gerritsen et al. [2006], Lambers et al. [2008] and Chen et al. [2009]. This scheme when is combined with a local or global upscaling method yields upscaled adjusted by enforcing the M-matrix condition for the the resulting solution matrix. However the method works well only for a certain range of problems away from very high anisotropy ratio and large off-diagonal terms of full tensor. Reduced simulation error due to well translated sub-grid heterogeneity into the coarse scale is another advantage of this method.
4. Any future research moving toward more realistic models has to consider putting more geological realism into the initial prior knowledge of geological structures and possibly multiple prior structural realisations.

References

Aarnes, J.E., Krogstad, S., Lie, K.A. [2008], Multiscale mixed/mimetic methods on corner-point grids, Computational Geoscience, 12(3), 297-315

Aavatsmark, I. [2002], Introduction to multipoint flux approximation for quadrilateral grids, Computational Geoscience, 6, 405–432

Aavatsmark, I. [2008], Comparison of monotonicity for some multipoint flux approximation methods. In: Finite Volumes for Complex Applications, Editors: Eymard R., Hérard J.-M. 5, Wiley-ISTE, New York

Aavatsmark, I., Barkve, T., Bøe, Ø., Mannseth, T. [1994], Discretization on non-orthogonal, curvilinear grids for multi-phase flow, Proceedings of the 4th European Conference on the Mathematics of Oil Recovery, Røros, Norway, 7-10 June

Aavatsmark, I., Barkve, T., Bøe, Ø., Mannseth, T. [1996], Discretization on non-orthogonal, quadrilateral grids for inhomogeneous, anisotropic media, Journal of computational physics, 127 , 2–14

Aavatsmark, I., Barkve, T., Bøe, Ø., Mannseth, T. [1998], Discretization on unstructured grids for inhomogeneous, anisotropic media. Part I: Derivation of the methods, SIAM Journal on Scientific Computing, 19, 1700–1716

Aavatsmark, I., Barkve, T., Bøe, Ø., Mannseth, T. [1998], Discretization on unstructured grids for inhomogeneous, anisotropic media. Part II: Discussion and numerical results, SIAM Journal on Scientific Computing, 19, 1717–1736

Aavatsmark, I., Multipoint flux approximation methods for quadrilateral grids [2007-A], 9th International Forum on Reservoir Simulation, Abu Dhabi, 9-13 December

Aavatsmark, I., Eigestad, G.T., Heimsund, B.-O., Mallison, B.T., Nordbotten, J.M., and Øian, E. [2007-B], A new finite volume approach to efficient discretization on challenging grids, SPE 106435, Proceeding of SPE Reservoir Simulation Symposium, Houston, 26-28 February

Aavatsmark, I., Eigestad, G.T., Klausen R. A., Wheeler, M. F., Yotov, I. [2007-C], Convergence of a symmetric MPFA method on quadrilateral grids, Computational Geoscience, 11, 333–345

Aavatsmark, I., Eigestad, G.T., Nordbotten, J.M. [2006], A compact MPFA method with improved robustness, EAGE Paper B019, Proceeding of 10th European Conference on the Mathematics of Oil Recovery, Amsterdam, The Netherlands, 4 - 7 September

Aavatsmark, I., Reiso, E., Teigland, R. [2001], Control-volume discretization method for quadrilateral grids with faults and local refinements, Computational Geosciences, 5, 1–23

Aftomis, M.J., Berger, M.J., Adomavicius, G. [1999], A parallel Cartesian approach for external aerodynamics of vehicles with complex geometry, Proceedings of the thermal and fluids analysis workshop, NASA Marshall Spaceflight Centre, Huntsville, Alabama, USA

Aftomis, M.J., Berger, M.J., Melton J.E. [1995], Adaption and surface modelling for Cartesian mesh methods, AIAA Paper 95-1725-CP, Jun 1995

Aftomis, M.J., Berger, M.J., Melton J.E. [1997], Robust and efficient Cartesian mesh generation for component based geometry, Technical Report for AIAA-97-0196, US Air Force Wright Laboratory

Aftomis, M.J., Berger, M.J., Melton, J. E. [1998], Robust and efficient Cartesian mesh generation for component-base geometry, AIAA Journal, 36(6), 952-960

Al Rougha, H.B., Al-Henshiri, M.Y., Khouri, N., Arisaka, K., Sultan, A. [2004], Integration of 3-D Seismic & Dynamic Data Improves Interpretation of Structural Features, SPE 88692-MS, ZADCO, Abu Dhabi, UAE

Alpak, F.O. [2010], A Mimetic Finite Volume Discretization Method for Reservoir Simulation, SPE Journal, 15 (2), 436-453

Anterion, F., Eymard, R., Karcher, B. [1989], Use of Parameter Gradients for Reservoir History Matching, SPE 18433, Symposium on Reservoir Simulation, Houston, Texas, USA, February 6-8

Arbogast, T., Dawson, C.N., Keenan, P.T., Wheeler, M.F., Yotov, I. [1998], Enhanced cell-centered finite differences for elliptic equations on general geometry, SIAM Journal on Scientific Computing, 19, 404–425

Arbogast, T., Wheeler, M.F., Yotov, I. [1997], Mixed finite elements for elliptic problems with tensor coefficients as cell centered finite differences, SIAM Journal on Numerical Analysis, 34 (2), 828-852

Arbogast, T., Wheeler, M.F., Yotov, I. [1997], Mixed finite elements for elliptic problems with tensor coefficients as cell-centered finite differences, SIAM Journal on Numerical Analysis, 34, 828–852

Arnold, D.P. [2009], Geological Paramterisation: Techniques and Philosophies, PhD Thesis, Institute of Petroleum Engineering, Heriot Watt University, Edinburgh, UK

K. Aziz, A. Settari [1979], Petroleum Reservoir Simulation, Elsevier Applied Science Publishers, New York

Baddeley, M.C., Curtis, A., Wood, R.A. [2004], An introduction to prior information derived from probabalistic judgements: elicitation of knowledge, cognative bias and herding. In A Curtis and R Wood, editors, Geological Prior Information: Informing Science and Engineering, 239, Geological Society, London, England

Banks, A., Vincent, J., Wudi, C. [2007], A Review of Particle Swarm Optimization, Part 1: Background and Development, Natural Computing, 6, 467-484

Barber, RW. [1992], Solving the shallow water equations using a non-orthogonal curvilinear coordinate system, In Falconer RA, editor. Hydraulic and environmental modelling: coastal waters, Pressed by Ashgate, 1992:469-480

Barker, J.W., Cuypers, M., Holden, L. [2001], Quantifying Uncertainty in Production Forecasts: Another Look at the PUNQ-S3 Problem, SPE 74707, SPE Journal, 6(4), 433-441

Beghein, C., Resovsky, J., Trampert, J. [2002], P and S Tomography Using Normal-Mode and Surface Waves Data with a Neighbourhood Algorithm, Geophysics journal, 149, 646-658

Beghein, C., Trampert, J. [2004], Probability Density Functions for Radial Anisotropy From Fundamental Mode Surface Wave Data and the Neighbourhood Algorithm, Geophysics Journal, 157, 1163-1174

Behrenbruch, P., Turner, G., Backhouse, A. [1985], Probabilistic Hydrocarbon Reserves Estimation: A Novel Monte Carlo Approach, SPE 13982, Offshore Europe Conference, Aberdeen, 10-13 September

Bianco, A., Cominelli, A., Dovera, L., Naevdal, G., Valles, B. [2007], History Matching and Production Forecast Uncertainty by Means of the Ensemble Kalman Filter: a Real Field Application, SPE 107161, SPE Europec/EAGE Annual Conference and Exhibition held in London, United Kingdom, 11–14 June

Birchenko, V., Demyanov, V., Konopczynski, M,. Davies, D. [2008], Impact of Reservoir Uncertainty on Selection of Advanced Completion Type, SPE 115744, Annual Technical Conference and Exhibition, Denver, Colorado, USA, 21-24 September

Bissell, R.C., Sharma, Y., Killough, J.E. [1994], History Matching Using the Method of Gradients: Two Case Studies, SPE 28590-MS, SPE Annual Technical Conference and Exhibition, New Orleans, Louisiana, 25-28 September

Blockley, D., Godfrey, P. [2000] Doing it Differently: Systems of Rethinking Construction, Thomas Telford, London, 2000

Bonet-Cunha, L., Oliver, D.S., Redner, R.A, Reynolds, A.C [1998] A Hybrid Markov Chain Monte Carlo Method for Generating Permeability Fields Conditioned to Multiwell Pressure Data and Prior Information, SPE 50991, SPE Journal, volume 3, issue 3, 261-271

Bond, C.E., Gibbs, A.D., Shipton, Z.K., Jones, S. [2007], What do you think this is? Conceptual uncertainty in geoscience interpretation, GSA Today, 17(11), 4–10

Brodie, K., Fettes, D., Harte, B., Schmid, R. [2007], Structural terms including fault rock terms. Recommendations by the International Union of Geological Sciences Subcommission on the Systematics of Metamorphic Rocks

Caffarelli L., Cabré, X. [1995], Fully Nonlinear Elliptic Equations, American Mathematical Society

Cai, Z., Jones, J., McCormick, S.F., Russell, T. [1997], Control volume mixed finite element methods, Computational Geoscience, 1, 289–315

Caumon, G., Strebelle, S., Caers, J., Journel, G. [2004], Assessment of Global Uncertainty for Early Appraisal of Hydrocarbon Fields, SPE 89943, Annual Technical Meeting and Exhibition, Houston, Texas, USA, 26-29 September

Causon, D.M., Ingram, D.M., Mingham, C.G. [2001], A Cartesian cut cell method for shallow water flows with moving boundaries, Advances in Water Resources, 24, 899-911

Causon, D.M., Ingram, D.M., Mingham, C.G., Yang, G., Pearson, R. [2000], Calculation of shallow water flows using a Cartesian cut cell approach, Advances in Water Resources , 23, 545–562

Cerv, V., Menvielle, M., Pek, J. [2007], Stochastic Interpretation of Magnetotelluric Data, Comparison of Methods, Annals of Geophysics, volume 50, number 1

Chappell, N.A., Lancaster, J.W. [2007], Comparison of Methodological Uncertainties within Permeability Measurement, Hydrological Processes, 21, 2504-2514

Chen, Q.-Y., Wan, J., Yang, Y., Mifflin, R.T. [2008], Enriched multi-point flux approximation for general grids, Journal of computational physics, 227, 1701–1721

Chen, T., Gerritsen, M.G., Lambers, J.V., Durlofsky, L.J. [2010], Global variable compact multipoint methods for accurate upscaling with full-tensor effects, Computational Geoscience, 12(3), 399-416

Chen, W., Gavalas, G., Wasserman, M. [1973], A New Algorithm for Automatic History Matching, SPE 4545, SPE-AIME 48th Annual Fall Meeting, Las Vegas, USA, 30 September - 3 October

Childsa, C., Walsha, J.J., Wattersona, J. [1997], Complexity in fault zone structure and implications for fault seal prediction, Hydrocarbon Seals - Importance for Exploration and Production, Norwegian Petroleum Society Special Publications, 7, 61-72

Chou, S.-H., Kwak, D.Y., Kim, K.Y. [2001], A general framework for constructing and analyzing mixed finite volume methods on quadrilateral grids: the overlapping co-volume case, SIAM Journal on Numerical Analysis, 39 (4), 1170–1196

Christie, M., Blunt, M. [2001], Tenth SPE Comparative Solution Project: A Comparison of Upscaling Techniques, SPE 66599, Reservoir Simulation Symposium, Houston, Texas, 11-14 February

Christie, M., Demyanov, V., Erbas, D. [2006-A], Uncertainty Quantification for Porous Media Flows, Journal of Computational Physics, 217, 143-158

Christie, M., Demyanov, V., Pickup, G.E., O'Sullivan, A., Arnold, D., Erbas, D., Okano, H., Valjak, M. [2006-B], Uncertainty Quantification and Geological Parameterization, DEVEX Conference, Aberdeen, UK, 12-13 May

Christie, M., Glimm, J., Grove, J.W., Higdon, D.M., Sharp, D.H, Wood-Schultz, M.M. [2005], Error Analysis and Simulations of Complex Phenomena, Los Alamos Science, 29, 6-25

Christie, M., Macbeth, C., Subbey, S. [2002], Multiple History Matched Models for Teal South, The Leading Edge, March, 286-289

Cignoni, P., Rocchini, C., Scopigno, R. [1998], Metro: Measuring Error on Simplified Surfaces, Computer Graphics Forum, 17(2), 167-174

Coirier, W.J., Powell K.G. [1993], An accuracy assessment of Cartesian mesh approaches for the Euler equations, Journal of Computational Physics, 117, 121-131

Cortez, R. [2000], A vortex/impulse method for immersed boundary motion in high Reynolds number flows, Journal of Computational Physics, 160, 385-400

Crumpton, P.I., Shaw, G.J., Ware, A.F. [1995], Discretization and multigrid solution of elliptic equations with mixed derivative terms and strongly discontinuous coefficients, Journal of computational physics, 116 , 343–358

De Zeeuw, D., Powell, K.G. [1993], An adaptively refined Cartesian mesh solver for Euler equations, Computational Physics, 104, 56-68

Downton, J.E., Gray., D., Zuk, T. [2007], Visualizing AVAZ Parameter Estimates with Uncertainty Due to Noise, EAGE 69th Conference and Exhibition, London, UK, 11-14 June

Durlofsky, L.J. [1994], Accuracy of mixed and control volume finite element approximations to Darcy velocity and related quantities, Water Resources Research, 30 (4), 965–973

Edwards, M.G. [1995], Symmetric, flux continuous, positive definite approximation of the elliptic full tensor pressure equation in local conservation form, 13th SPE Reservoir Simulation Symposium, San Antonio, Texas, USA, 12-15 February

Edwards, M.G., Rogers, C.F. [1998-A], Finite volume discretization with imposed flux continuity for the general tensor pressure equation, Computational Geoscience, 2, 259–290

Edwards, M.G. [1998-B], Cross Flow, Tensors and finite volume approximation with deferred correction, Computer Methods in Applied Mechanics and Engineering, 151, 143–161

Edwards, M.G. [1999], Split Tensor Discretization Operators Coupled with Quasi K-Orthogonal Grids, SPE 51903, Proceeding of SPE Reservoir Simulation Symposium, Houston, Texas, USA, 14-17 February

Edwards, M.G. [2000], M-matrix flux splitting for general full tensor discretization operators on structured and unstructured grids, Journal of computational physics, 160, 1–28

Edwards, M.G. [2001], Split Full Tensor Discretization Operators on Structured and Unstructured Grids in Three Dimensions, SPE 66358, Proceeding of SPE Reservoir Simulation Symposium, Houston TX, USA, 11-14 February

Edwards, M.G. [2006], Higher-resolution hyperbolic-coupled-elliptic flux-continuous CVD schemes on structured and unstructured grids in 3-D, International Journal for Numerical Methods in Fluids, 51, 1079–1095

Edwards, M.G., Rogers, C.F. [1994], A flux continuous scheme for the full tensor pressure equation, Proceedings of 4th European Conference on the Mathematics of Oil Recovery, Røros, Norway, 7-10 June

Edwards, M.G., Zheng H. [2011], Quasi M-Matrix Multifamily Continuous Darcy-Flux Approximations with Full Pressure Support on Structured and Unstructured Grids in Three Dimensions, SIAM Journal on Scientific Computing, 33(2), 455–487

Edwards, M.G., Zheng, H. [2008], A quasi-positive family of continuous Darcy-flux finite volume schemes with full pressure support, Journal of computational physics, 227, 9333–9364

Edwards, M.G., Zheng, H. [2010], Double-families of quasi-positive Darcy-flux approximations with highly anisotropic tensors on structured and unstructured grids, Journal of computational physics, 229, 594–625

Eigestad, G.T., Aavatsmark, I., Espedal, M. [2002-A], Symmetry and M-matrix issues for the O-method on an unstructured grid, Computational Geosciences, 6, 381–404

Eigestad, G.T., Aavatsmark, I., Reiso, E., Reme, H., Teigland, R. [2002-B], MPFA methods applied to irregular grids and faults, Computational Methods in Water Resources, 47, 413-420

Eigestad, G.T., Klausen R.A. [2005], On the convergence of the multi-point flux approximation O-method: Numerical experiments for discontinuous permeability, Numerical Methods for Partial Differential Equations, 21, 1079-1098

Elabed, S. [2003], Analysis of the Neighbourhood Algorithm Applied to History Matching Under Uncertainty, Technical Report, Heriot Watt University, Institute of Petroleum Engineering

Elkins, L.F. [1972], Uncertainty of Oil in Place in Unconsolidated Sand Reservoirs - A Case History, SPE 3789-PA, Journal of Petroleum Technology, 24(11), 1315-1319

Erbas, D. [2006], Sampling Strategies for Uncertainty Quantification in Oil Recovery Prediction, PhD Thesis, Institute of Petroleum Engineering, Heriot Watt University, Edinburgh, UK

Evensen, G., [1993], The Ensemble Kalman Filter: theoretical formulation and practical implementation Ocean Dynamics, 53, 343–367

Evensen, G., Hove, J., Meisingset, H.C., Reiso, E., Seim, K.S., Espelid, Ø. [2007], Using the EnKF for Assisted History Matching of a North Sea Reservoir Model, SPE 106184, 2007 SPE Reservoir Simulation, Symposium, held in Woodlands, Texas, USA, 26–28 February

Fedkiw, R., Aslam, T., Merriman, B. and Osher, S. [1999-A], A Non-Oscillatory Eulerian Approach to Interfaces in Multi-material Flows (The Ghost Fluid Method), Journal of Computational Physics, 152, 457-492

Fedkiw, R., Aslam, T. and Xu, S. [1999-B], The Ghost Fluid Method for Deflagration and Detonation Discontinuities, Journal of Computational Physics, 154, 393-427

Friedel, T., Tewari, R., Rasidi, T.G., Flew, S., Strasser, R., Trebolle, R., Belfield, W., Caretta, F. [2009], Efficient Uncertainty Management Workflow for Brownfield Redevelopment, SPE 125673, SPE/EAGE Reservoir Characterization and Simulation Conference, Abu Dhabi, UAE, 19-21 October

Friis H.A., Edwards M. G. and Mykkeltveit, J. [2008], Symmetric Positive Definite Flux-Continuous Full-Tensor Finite-Volume Schemes on Unstructured Cell Centered Triangular Grids, SIAM Journal of Scientific. Computation, 31(2), 1192-1220

Gamerman, D. [1997], Markov Chain Monte Carlo, Stochastic Simulation for Bayesian Inference, Chapman & Hall CRC, USA

Gavalas, G.R, Shah, P.C., Seinfeld, J.H. [1976], Reservoir History Matching by Bayesian Estimation, SPE 5740, SPE Journal, volume 16, number 6, 337-350

Gazet, S., Chavanne, E., Khalaf, A. [2009], Evaluating the Impact of Geophysical Uncertainties on Gross Rock Volume in a Low Relief Carbonate Field, Offshore Abu Dhabi, SPE 125573, SPE/EAGE Reservoir Characterization and Simulation Conference, Abu Dhabi, UAE, 19-21 October

Gelman, A., Carlin, J.B., Stern, H.S., Rubin, D.B. [1995], Bayesian Data Analysis, London: Chapman and Hall. First edition, 1995

Gerritsen, M.G., Lambers, J.V., Mallison, B.T. [2006], A variable and compact MPFA for transmissibility upscaling with guaranteed monotonicity, Proceedings of the 10th European Conference on the Mathematics of Oil Recovery, Amsterdam, The Netherlands, 4–7 September

Gerritsen, M.G., Lambers, J.V., Mallison, B.T. [2008], Accurate local upscaling with variable compact multipoint transmissibility calculations, Computational Geoscience, 12(3), 399–416

Gilks, W. R., Richardson, S., Spiegelhalter, D.J. [1996], Markov Chain Monte Carlo In Practice, Chapman & Hall

Gomez, S., Gosselin, O., Barker, J.W. [2001], Gradient-Based History Matching With a Global Optimization Method, SPE 71307-PA, SPE Journal, 6(2), 200-208

Griffith, B.E., Peskin, C.S. [2005], On the order of accuracy of the immersed boundary method, Higher order convergence rates for sufficiently smooth problems, Journal of Computational Physics, 208, 75–105

Hajizadeh, Y. [2011], Population-Based Algorithms for Improved History Matching and Uncertainty Quantification of Petroleum Reservoirs , PhD Thesis, Institute of Petroleum Engineering, Heriot Watt University, Edinburgh, UK

He, C., Edwards, M.G., Durlofsky, L.J. [2002], Numerical calculation of equivalent cell permeability tensors for general quadrilateral control volumes, Computational Geoscience, 6(1), 29–47

Heinemann, Z.E., Brand, C.W., Munka, M., Chen, Y.M. [1991], Modelling Reservoir Geometry with Irregular Grids, SPE Reservoir Engineering, 225-232

Holden, L., Mostad, P., Nielsen, B.F., Gjerde, J., Townsend, C., Ottesen, S. [2003], Stochastic Structural Modelling, Mathematical Geology, 35(8), 899-314

Holger, H.H., Stützle, T. [2004], Stochastic Local Search Foundations and Applications, Morgan Kaufmann, Elsevier, 2004

Hou, T.Y., Li, Z., Osher, S., Zhao, H. [1997], A Hybrid Method for Moving Interface Problems with Application to the Hele–Shaw Flow, Journal of Computational Physics, 134, 236-252

Hyman, J.M., Shashkov, M. [1997], Natural discretizations for the divergence, gradient, and curl on logically rectangular grids, Computers & Mathematics with Applications, 33, 81–104

Irving, A.D., Chavanne, E., Faure, V., Buffet, P. , Barber, E. [2010-A], An uncertainty modelling workflow for structurally compartmentalized reservoirs, Geological Society, London, Special Publications, 347(1), 283 - 299

Irving, A., Robert, E. [2010-B], Optimisation of Uncertain Structural Parameters Using Production and Observation Well Data, SPE Conference Paper 131463-MS, SPE EUROPEC/EAGE Annual Conference and Exhibition, Barcelona, Spain, 14-17 June

Iwegbue, M., Appah, D., Ogwo, E.A. [2007], Crude Oil Metering Experience in the Niger-Delta, SPE 111906, Nigeria Annual International Conference and Exhibition, Abuja, Nigeria, 6-8 August

Jansky, J., Plicka, V., Novotny, O. [2007], Determining a 1-D Velocity Model of the Uppermost Crust from P and S Arrival Times Using the Neighbourhood Algorithm, Synthetic Test, Acta Geodyn, Geomater, volume 4, number 2, 146, 5-12

Ji, H., Lien, F.S., Yee, E. [2006], A robust and efficient hybrid cut-cell/ghost-cell method with adaptive mesh refinement for moving boundaries on irregular domains, Computer Methods in Applied Mechanics and Engineering, 198, 432-448

Ji, H., Lien, F.S., Yee, E. [2006], An efficient second-order accurate cut-cell method for solving the variable coefficient Poisson equation with jump conditions on irregular domains, International Journal for Numerical Methods in Fluids, 52 , 723-746

Jia, H., Lienb, F-.S., Yeec, E. [2010], Numerical simulation of detonation using an adaptive Cartesian cut-cell method combined with a cell-merging technique, Computers & Fluids, 39(6), 1041-1057

Johansen, H., Colella, P. [1998], A Cartesian grid embedded boundary method for Poisson's equation on irregular domains, Journal of Computational Physics, 147, 60-85

Kennett, B. [2006], Non-Linear Methods for Event Location in a Global Context, Physics of the Earth and Planetary Interiors, 158, 46-54

King, M.J., Mansfield, M. [1997], Flow Simulation of Geologic Models, SPE 38877, SPE Annual Technical Conference and Exhibition, San Antonio, USA, 5-8 October

Klausen R.A., Winther, R. [2006-A], Convergence of multipoint flux approximations on quadrilateral grids, Numerical Methods for Partial Differential Equations, 22, 1438–1454

Klausen R.A., Winther, R. [2006-B], Robust convergence of multi point flux approximation on rough grids, Numerical Mathematics, 104, 317–337

Klausen, R., Russell, T. [2004], Relations among some locally conservative discretization methods which handle discontinuous coefficients, Computational Geoscience, 8 (4), 341–377

Knipe, R J. [1997], Juxtaposition and seal diagrams to help analyze fault seals in hydrocarbon reservoirs, AAPG Bulletin, 81(2), 187-195

Koppen, M. [2004], No-Free-Lunch Theorems and the Diversity of Algorithms, IEEE Congress on Evolutionary Computation, CEC, 19-23 June 2004, Portland, USA

Lai, M.-C., Li, Z.L., [2001], A remark on jump conditions for the three-dimensional Navier-Stokes equations involving an immersed moving membrane, Applied Mathematics Letters, 14, 149-154

Lai, M.-C., Li, Z.L., [2001], The Immersed Interface Method for the Navier–Stokes Equations with Singular Forces, Journal of Computational Physics, 171, 822–842

Lai, M.-C., Peskin, C.S. [2000], An immersed boundary method with formal second order accuracy and reduced numerical viscosity. Journal of computational physics, 160, 705-719

Lambers, J.V., Gerritsen, M.G. [2008], Spatially-varying compact multi-point flux approximations for 3-D adapted grids with guaranteed monotonicity, Proceedings of the 11th European Conference on the Mathematics of Oil Recovery, Bergen, Norway, 8–11 September

Lazinica, A. [2009], Particle Swarm Optimization, InTech Educational Publishing, ISBN 978-953-7619-48-0

Lee, S.H., Durlofsky, L.J., Lough, M.F., and Chen, W.H. [1998], Finite Difference Simulation of Geologically Complex Reservoirs with Tensor Permeabilities, SPE Reservoir Evaluation & Engineering, 567-574

Leveque, R.J., Chaoming, Z. [1997], The immersed interface method for acoustic wave equations with discontinuous coefficients, Wave Motion, 25, 237-263

LeVeque, R.J., Li, Z. [1994], The Immersed Interface Method for Elliptic Equations with Discontinuous Coefficients and Singular Sources, SIAM Journal on Numerical Analysis, 31, 1019-1044

Lever, H [2007], Private communications

Li, R., Reynolds, A.C., Oliver, D.S. [2003], History Matching of Three-Phase Flow Production Data, SPE 87336-PA, SPE Journal, 8(4), 328-340

Li, Z. [1994], The Immersed Interface Method: A Numerical Approach for Partial Differential Equations with Interfaces, Ph.D. thesis, University of Washington, USA

Li, Z. [1996], A note on immersed interface methods for three dimensional elliptic equations, Computers & Mathematics with Applications, 31, 9-23

Li, Z., Soni, B. [1999-A], Fast and accurate numerical approaches for Stefan problems and crystal growth, Numerical Heat Transfer, Part B Fundamentals, 35, 461-478

Li, Z., Zhao, H., Gao, H. [1999-B], A numerical study of electro-migration voiding by evolving level set functions on a fixed cartesian grid, Journal of Computational Physics, 152, 281-304

Lipnikov, K., Shashkov, M., Svyatskiy, D., Vassilevski, Yu. [2008], Monotone finite volume schemes for diffusion equations on unstructured triangular and shape-regular polygonal meshes, Journal of computational physics, 227, 492–512

Lipnikov, K., Svyatskiy, D., Vassielvski, Yu. [2010], A monotone finite volume scheme for advection-diffusion equations on unstructured polygonal meshes, Journal of computational physics, 229, 4017-4032

Lipnikov, K., Manzinib, G., Svyatskiya, D. [2011], Analysis of the monotonicity conditions in the mimetic finite difference method for elliptic problems, Journal of Computational Physics, 230(7), 2620-2642

Liu, H., Krishnan, S., Marella, S., Udaykumar, H.S. [2005], Sharp interface Cartesian grid method II: A technique for simulating droplet interactions with surfaces of arbitrary shape, Journal of Computational Physics, 210, 32–54

Mantica, S., Cominelli, A., Mantica, G. [2002], Combining Global and Local Optimization Techniques for Automatic History Matching Production and Seismic Data, SPE 78353, SPE Journal, Volume 7, Number 2, 123-130

Manzocchi, T., Walsh, J., Nell, P., Yielding, G. [1999], Fault transmissibility multipliers for flow simulation models, Petroleum Geoscience, 5, 53—63

Marella, S., Krishnan, S., Liu, H., Udaykumar, H.S., Sharp interface Cartesian grid method I: An easily implemented technique for 3-D moving boundary computations, Journal of Computational Physics, 210, 1–31

McCorquodale, P., Colella, P., Johansen, H. [2001], A Cartesian grid embedded boundary method for the heat equation on irregular domains, Journal of Computational Physics, 173, 620-635

Metropolis, N., Rosenbluth, A.W., Rosenbluth, M.N., Teller, A.H.; Teller, E. [1953], Equations of State Calculations by Fast Computing Machines, Journal of Chemical Physics 21 (6), 1087–1092

Mlacnik, M.J., Durlofsky, L.J. [2006], Unstructured grid optimization for improved monotonicity of discrete solutions of elliptic equations with highly anisotropic coefficients, Journal of computational physics, 216, 337–361

Nævdal, G., Mannseth, T., Vefring, E.H. [2002], Near-Well Reservoir Monitoring Through Ensemble Kalman Filter, SPE 75235, SPE/DOE Improved Oil Recovery Symposium, Tulsa, USA, April 13-17

Nicotra, G., Godi, A., Cominelli, A., Christie, M. [2005], Production Data and Uncertainty Quantification: A Real Case Study, SPE 93280, Reservoir Simulation Symposium, Houston, USA, 31 January-2 February

Nordbotten, J.M., Aavatsmark, I., Eigestad, G.T. [2007], Monotonicity of control volume methods, Numerical Mathematics, 106, 255–288

Nordbotten, J.M., Eigestad, G.T. [2005], Discretization on quadrilateral grids with improved monotonicity properties, Journal of computational physics, 203, 744–760

Oevermann, M., Klein, R. [2006], A Cartesian grid finite volume method for elliptic equations with variable coefficients and embedded interfaces, Journal of Computational Physics, 219, 749–769

Oevermann, M., Scharfenberg, C., Klein, R. [2009], A sharp interface finite volume method for elliptic equations on Cartesian grids, Journal of Computational Physics 228, 5184–5206

Okabe, A. [1992], Spatial tessellations: concepts and applications of Voronoi diagrams, Wiley series in probability and mathematical statistics

Oliver, D.S. [1996], Multiple Realizations of the Permeability Field from Well-Test Data, SPE 27970, SPE Journal, volume 1, number 2, 145-154

Oliver, D.S., He, N., Reynolds, A.C [1996], Conditioning Permeability Fields to Pressure Data, European Conference for the Mathematics of Oil Recovery (ECMOR), Leoben, Austria

Ouenes, A., [1993], A New, Fast Parallel Simulated Annealing Algorithm for Reservoir Characterization, New Mexico Petroleum Recovery Research Center; Saad, Naji, SPE 26419-MS,SPE Annual Technical Conference and Exhibition, , Houston, Texas, USA, 3-October

Pal, M., Edwards, M.G., Lamb, A.R. [2006-A], Convergence study of a family of flux-continuous, finite-volume schemes for the general tensor pressure equation, International Journal for Numerical Methods in Fluids, 51, 1177–1203

Pal, M., Edwards, M.G. [2006-B], Flux-Splitting Schemes for improved monotonicity of discrete solution of elliptic equation with highly anisotropic coefficients, Proceeding of European Conference on Computational Fluid Dynamics (ECCOMAS CFD 2006), Egmond aan Zee, The Netherlands, 5–8 September

Pal, M., Edwards, M.G. [2006-C], Family of flux-continuous finite-volume schemes with improved monotonicity, Proceedings of the 10th European Conference on the Mathematics of Oil Recovery, 4–7 September

Palatnik, B.M. , Aanonsen, S.I., Zakirov, I.S., Zakirov, E.S. [1994], New Technique to Improve the Efficiency of History Matching of Full-Field Models, 4th European Conference on the Mathematics of Oil Recovery, Borås, Norway, 7-11 June

Peskin, C.S. [1972], Flow patterns around heart valves: A digital computer method for solving the equations of motion, Ph.D. thesis, Albert Einstein College of Medicine, Available at: http://www.umi.com/hp/Products/DisExpress.html, Order Number 7230378

Peskin, C.S. [1977], Numerical analysis of blood flow in the heart, Journal of computational physics, 25, 220–252

Peskin, C.S. [1981], Vortex dynamics of the aortic sinus, In Mathematical Aspects of Physiology (Hoppensteadt FC, ed.), Vol. 19 of Lectures in Applied Mathematics, 93-104

Peskin, C.S. [1982], The fluid dynamics of heart valves: Experimental, theoretical, and computational methods, Annual Review of Fluid Mechanics, 14, 235-259

Peskin, C.S. [1987], Numerical analysis of blood flow in the heart, Computational Physics, 25, 220-252

Peskin, C.S. [2002], The immersed boundary method [2002], Cambridge University Press, Printed in the United Kingdom, DOI: 10.1017/S0962492902000077

Ponting, D.K. [1989], Corner Point Geometry in Reservoir Simulation, 1st Joint IMA/SPE European Conference on the Mathematics of Oil Recovery, Cambridge University, England, 25-27 July

Popinet, S. [2003], Gerris: a tree-based adaptive solver for the incompressible Euler equations in complex geometries, Journal of Computational Physics, 190, 572-600

Portellaand, R.C.M., Prais, F. [1999], Use of Automatic History Matching and Geostatistical Simulation to Improve Production Forecast, SPE 53976-MS, Latin American and Caribbean Petroleum Engineering Conference, Caracas, Venezuela, 21-23 April

Qian, L., Causon, D.M., Ingram, D.M., Mingham, C.G. [2001], A Cartesian cut cell method for incompressible viscous flows, Proceeding of European Conference on Computational Fluid Dynamics (ECCOMAS CFD 2001), Southend-on-Sea, UK, 2001

Rankey, E.C., Mitchell, J.C. [2003], Interpreter's corner that's why it's called interpretation: Impact of horizon uncertainty on seismic attribute analysis, The Leading Edge, 22, 820

Rivenæs, J.C., Otterlei, C., Zachariassen, E., Dart, C., Sjøholm, J. [2005], A 3-D stochastic model integrating depth, fault and property uncertainty for planning robust wells, Njord Field, offshore Norway, Petroleum Geoscience, 11, 57–65

Røe, P., Abrahamsen, P., Georgsen, F., Syversveen, A.R. [2010], Flexible Simulation of Faults, SPE Annual Technical Conference and Exhibition, Florence, Italy, 19-22 September

Rojas, T. [2010], Private Communications

Roma, A.M., Peskin, C.S., Berger, M.J. [1999], An adaptive version of the immersed boundary method, Journal of Computational Physics, 153(2), 509–534

Romero, C., Carter, J., Gringarten, A., Zimmerman, R. [2000], A Modified Genetic Algorithm for Reservoir Characterization, SPE 64765, International Oil and Gas Conference and Exhibition, Beijing, China 7-10 November

Salhi, M.A., Van Rijen, M., Wei, L., Dijk, H. [2005], Structured Uncertainty Assessment for Fahud Field through the Application of Experimental Design and Response Surface Methods, SPE Conference Paper 93529-MS, SPE Middle East Oil and Gas Show and Conference, Kingdom of Bahrain, Mar 12 - 15

Sambridge, M. [1999-A], Geophysical Inversion with a Neighbourhood Algorithm, Part 1: Searching Parameter Space, Geophysical Journal International, 138, 479-494

Sambridge, M. [1999-B], Geophysical Inversion with a Neighbourhood Algorithm - II Appraising the Ensemble, Geophysical Journal International, 138, 727-745

Samson, P., Dubrule, O., Euler, N. [1996], Quantifying the Impact of Structural Uncertainties on Gross-Rock Volume Estimates, SPE Conference Paper 35535-MS European, 3-D Reservoir Modelling Conference, Stavanger, Norway, 16-17 April

Schaaf, T., Coureaud, B., Labaune, F. [2009], Joint Structural and Petrophysical History Matching Leads to Global Geological Stochastic Reservoir Models, Joint EUROPEC/EAGE Conference and Exhibition, Amsterdam, The Netherlands, 8-11 June

Schulze-Riegert, R., Axmann, J., Haase, O., Rian, D., You, Y. [2001], Optimization Methods for History Matching of Complex Reservoirs, SPE 66393, Reservoir Simulation Symposium, Houston, Texas, USA, 11-14 February

Seiler, A., Aanonsen, S.I., Evensen, G., Lia, O. [2010-B], An Elastic Grid Approach for Fault Uncertainty Modelling and Updating Using the Ensemble Kalman Filter, SPE Conference Paper 130422-MS, SPE EUROPEC/EAGE Annual Conference and Exhibition, Barcelona, Spain , 14-17 June

Seiler, A., Aanonsen, S.I., Evensen, G., Rivenæs, J.C. [2010-A], Structural Surface Uncertainty Modeling and Updating Using the Ensemble Kalman Filter, SPE Journal Paper 125352-PA, 15(4), 1062-1076

Seiler, A., Rivenæs, J.C., Aanonsen, S.I., Evensen, G., [2009], Structural Uncertainty Modelling and Updating by Production Data Integration, SPE Conference Paper 125352-MS, SPE/EAGE Reservoir Characterization and Simulation Conference, Abu Dhabi, UAE, 19-21 October

Shashkov, M., Steinberg, S. [1996], Solving diffusion equations with rough coefficients in rough grids, Journal of computational physics, 129, 383–405

Sivia, D.S. [1996], Data Analysis-A Bayesian Tutorial, Claredon Press, Oxford

Slater, G., Durrer, E. [1970], Adjustment of Reservoir Simulation Models to Match Field Performance, SPE 2983, 45th Annul Fall Meeting, Houston, Texas, USA, 4-7 October

Sousa, S., Maschio, C., Schiozer, D. [2006], Scatter Search Metaheuristic Applied to the History-Matching Problem, SPE 102975, Annual Technical Conference and Exhibition, San Antonio, Texas, USA, 24-27 September

Spall, J.C. [2003], Introduction to Stochastic Search and Optimization: Estimation, Simulation, and Control, Wiley. ISBN 0471330523

Sperrevik, S., Gillespie, P., Fisher, Q., Halvorsen, T., Knipe, R. [2002], Empirical estimation of fault rock properties, Hydrocarbon Seal Quantification, 11, 109-125

Stephen, K., MacBeth, C. [2006], Reducing Reservoir Prediction Uncertainty Using Seismic History Matching, SPE 100295, EUROPEC/EAGE Annual Conference and Exhibition, Vienna, Austria, 12-15 June

Stephen, K., Shams, A., MacBeth, C. [2007], Faster Seismic History Matching in a UKCS Reservoir, SPE 107147, EUROPEC/EAGE Annual Conference and Exhibition, London, United Kingdom, 11-14 June

Subbey, S., Christie, M., Sambridge, M. [2003], A Strategy for Rapid Quantification of Uncertainty in Reservoir Performance Prediction, SPE 79678, Reservoir Simulation Symposium, Houston, USA, 3-5 February

Suzuki, S., Caumon, G., Caers, J. [2008], Dynamic data integration for structural modeling: model screening approach using a distance-based model parameterization, Computational Geoscience, 12(1), 105-119

Thomas, K., Hellums, L., Reheis, G. [1971], A Nonlinear Automatic History Matching Technique for Reservoir Simulation Models, SPE 3475, 46th Annual Fall Meeting, New Orleans, USA, October 3-6

Thore, P., Shtuka, A., Lecour, M., Ait-Ettajer, T., Cognot, R. [2002], Structural uncertainties: Determination, management, and applications, Geophysics, 67(3), 840-852

Tornberg, A.K, Engquist, B. [2003-A], Regularization techniques for numerical approximation of PDEs with singularities, Journal of Scientific Computing, 19, 527–552

Tornberg, A.K, Engquist, B. [2003-B], The segment projection method for interface tracking, Communications on Pure and Applied Mathematics, 56, 47–79

Tornberg, A.K, Engquist, B. [2004], Numerical approximations of singular source terms in differential equations, Journal of Computational Physics, 200, 462–488

Tucker, P., Pan, Z. [2000], A Cartesian cut cell method for incompressible viscous flow, Applied Mathematics and Computation, 24, 591–606

Udaykumar, H.S., Kan, H.-C., Shyy, W., Tran-Son-Tay, R. [1997], Multiphase dynamics in arbitrary geometries on fixed Cartesian grids, Journal of Computational Physics, 137, 366-405

Udaykumar, H.S., Marella, S., Krishnan, S. [2003], Sharp-interface simulation of dendritic growth with convection benchmarks, International Journal of Heat and Mass Transfer, 46 (14), 2615–2627

Udaykumar, H.S., Mittal, R., Rampunggoon, P., Khanna, A. [2001], A Sharp Interface Cartesian Grid Method for Simulating Flows with Complex Moving Boundaries, Journal of Computational Physics, 174, 345–380

Udaykumar, H.S., Mittal, R., Rampunggoon, P. [2002], Interface tracking finite volume method for complex solid–fluid interactions on fixed meshes, Communications in Numerical Methods in Engineering, 18 (2), 89–97

Udaykumar, H.S., Mittal, R., Shyy, W. [1999], Computation of Solid-fluid phase front computations in the sharp interface limit on fixed grids, Journal of Computational Physics, 153, 535-574

Valjak, M. [2008], Automated history matching using real-life reservoirs; improved the accuracy of reservoir performance forecasts, PhD Thesis, Institute of Petroleum Engineering, Heriot-Watt University, Edinburgh, UK

Verma, S., Aziz, K., A control volume scheme for flexible grids in reservoir simulation, SPE 37999, SPE Reservoir Simulation Symposium, Dallas, Texas, 8-11 June

Vincent, G., Corre, B., Thore, P. [1998], Managing Structural Uncertainty in a Mature Field for Optimal Well Placement, SPE Conference Paper 48953, SPE Annual Technical Conference and Exhibition, New Orleans, 27–30 September

Watson, A., Lee, W. [1986], A New Algorithm for Automatic History Matching Production Data, SPE 15228, Unconventional Gas Technology Symposium, Louisville, USA, May 18-21

Wedan B, South Jr. J.C. [1983], A method for solving the transonic full potential equation for general configurations, AIAA Paper 83-1889

Wen, X.-H., Durlofsky, L.J., Lee, S.H., Edwards M.G. [2000], SPE 62928, Full Tensor Upscaling of Geologically Complex Reservoir Descriptions, SPE Annual Technical Conference and Exhibition, , Dallas, Texas, USA, 1-4 October

Williams, N., Lond, D. [2006], Kutubu – A Rethink, SPE 101123, Asia Pacific Oil and Gas Conference and Exhibition, Adelaide, Australia, 11-13 September

Wu, X.H., Parashkevov, R.R. [2009], Effect of Grid Deviation on Flow Solutions, SPE Journal, 14(1), 67-77

Yang, G., Causon, D.M., Ingram, D.M. [2000], Calculation of compressible flows about complex moving geometries using a 3-D Cartesian cut cell method, International Journal for Numerical Methods in Fluids, 33, 1121–1151

Yang, G., Causon, D.M., Ingram, D.M., Saunders, R., Batten, P. [1997], A Cartesian cut cell method for compressible flows: Part A. Static body problems, Aeronautical Journal, 101 (1001), 47–56

Yao, H., Beghein, C., van der Hilst, R. [2009], Surface Wave Array Tomography in SE Tibet from Ambient Seismic Noise and Two-Station Analysis – II. Crustal and Upper-Manle Structure, Geophysics Journal, 173, 205-219

Ye, T., Mittal, R., Udaykumar, H.S. [1999], An Accurate Cartesian Grid Method for Viscous Incompressible Flows with Complex Immersed Boundaries, Computational Physics, 156, 209-240

Zhang, Y., Oliver, D.S. [2009], History Matching Using a Hierarchical Stochastic Model with the Ensemble Kalman Filter: A Field Case Study, SPE 118879-MS, SPE Reservoir Simulation Symposium, the Woodlands, Texas, USA, 2-4 February